



HAL
open science

Structural basis of outer-mitochondrial membrane mitofusin-guided fusion

Raphaëlle Versini

► **To cite this version:**

Raphaëlle Versini. Structural basis of outer-mitochondrial membrane mitofusin-guided fusion. Biochemistry, Molecular Biology. Sorbonne Université, 2023. English. NNT: 2023SORUS653. tel-04616890

HAL Id: tel-04616890

<https://theses.hal.science/tel-04616890>

Submitted on 19 Jun 2024

HAL is a multi-disciplinary open access archive for the deposit and dissemination of scientific research documents, whether they are published or not. The documents may come from teaching and research institutions in France or abroad, or from public or private research centers.

L'archive ouverte pluridisciplinaire **HAL**, est destinée au dépôt et à la diffusion de documents scientifiques de niveau recherche, publiés ou non, émanant des établissements d'enseignement et de recherche français ou étrangers, des laboratoires publics ou privés.

Thèse de Doctorat

Domaine: Biophysique computationnelle

École doctorale Chimie-Physique et Chimie Analytique de Paris Centre - ED 388

Laboratoire de Biochimie Théorique UPR-9080 - Institut de Biologie Physico-Chimique CNRS

Laboratoire des Biomolécules UMR 7203 - Sorbonne Université CNRS ENS

Structural basis of outer-mitochondrial membrane mitofusin-guided fusion

Présentée par

Raphaëlle Versini

Pour obtenir le grade de docteur en sciences de Sorbonne Université sous la direction
de Patrick Fuchs et Antoine Taly

Thèse soutenue le 18 Décembre 2023 devant le jury composé de:

Pr. Zoe Cournia	Academy of Athens	Rapportrice
Pr. Alexandre Bonvin	Utrecht University	Rapporteur
Dr. Isabelle Callebaut	CNRS	Examinatrice
Dr. David Taresté	INSERM	Examinateur
Dr. Patrick Fuchs	Université Paris Cité	Directeur de thèse
Dr. Antoine Taly	CNRS	Directeur de thèse



SORBONNE
UNIVERSITÉ

ACKNOWLEDGEMENTS

I extend my deepest gratitude and appreciation to everyone who has supported me throughout this enriching journey of completing my doctoral research.

I wish to acknowledge the Agence Nationale de la Recherche (ANR) for their financial support, without which this research would not have been possible. Their investment in my work has been pivotal in ensuring its successful completion.

I am also thankful to the members of my doctoral committee, Pr. Zoe Cournia, Pr. Alexandre Bonvin, Dr. Isabelle Callebaut, and Dr. David Taresté, to be a part of my defense jury and for the expertise they bring to this academic endeavor. Your insightful suggestions significantly contributed to the enhancement of this manuscript. David (and Anais :)), working together on mitofusins has been a truly enjoyable collaboration, and I look forward to the possibility of collaborating again in the future. Alexandre, thank you for this amazing internship in 2019. The wonderful atmosphere within the Haddock team played a significant role in strengthening my love for structural bioinformatics and research. Anne Lopes, thank you for your participation in my thesis committee and your valuable insights during these events.

I would like to express my sincere appreciation to my advisors as well, Patrick Fuchs and Antoine Taly, for their guidance, mentorship, and continuous support during this research. Working with you has been the most fulfilling and rewarding experience of my academic and professional life. You are both great teachers, and your guidance and support was invaluable throughout this period. I will remember fondly our scientific conversations, as well as the debates about the differences between Totoro and Goldorak. Patrick, your attention to detail, dedication to teaching and your constant ability to be available for your Ph.D students is deeply inspiring. I loved our many conversations about science or just about our daily life and aspirations (which was most of our conversations lets be honest :p), and I hope we'll still have many more in the future! Antoine, your wise insights over the scientific discoveries as well as academic world has been instrumental in shaping my three years of Ph.D and I will definitely remember them throughout my career. Your reaction to Patrick's confusion over Japanese animation was endlessly entertaining! I hope we will get to talk again in the future, whether it is about science, or board games and D&D. You are both a great source of inspiration.

I am grateful to my colleagues and fellow researchers at the Laboratoire des Biomolécules (LBM) and the Laboratoire de Biochimie Théorique (LBT), whose collaborative spirit and intellectual discussions enriched my research experience. Hubert, Charles, and Jérôme, I look forward to discussing climbing with you again and hope we can all visit Murmur Pantin together one day. Thank you to my friends at LBT, Afra, Julie, Sélène, Zakarya, Jules, and Sujith, I hope we will get many more evenings of theater, board games, or just nice chatting. Mario, thank you for all the support and the geeky/nerdy talks, I hope we will get many more and that one day I will also get to see you as a Dungeon Master. Thank you to all my friends at LBM, Marine, Yadira, Maya, Edward and Leiman, your kindness and support has been instrumental throughout these years. Marta, I rarely met someone with whom I felt such an immediate

connection as a friend. I am so happy you are a part of my life, my sweet italian Marta, and I look forward to a lasting friendship. Paula, your amazing charisma has always inspired me. You are my big sister and I have looked up to you and admired you throughout my Ph.D. Thank you for reintroducing me to climbing. I have enjoyed our numerous late evening talks and I hope we will have many more in the future. Steph, I could not have asked a better person to start my Ph.D. with. I grew and matured with you, my Ph.D twin, and you were truly one of the most important support throughout these years. Thank you for all the amazing fun times, but also for always being there for me through the hard times of the Ph.D. (and life!!), with all the needed long and sometimes sad conversations. I hope we will get many more, good or bad, I know we will be there for each other in the future.

Emile, mon amour, mon chaton, merci pour ton soutien (et ta patience!) en cette fin de thèse, ainsi que pour tout les câlins, les bon repas et tes petites attentions pendant les moments difficiles.

Je tiens aussi a exprimer ma gratitude envers ma famille, pour leurs encouragements, leur amour et leur confiance inébranlables en mes capacités. Merci à mon grand-frère, ma grande soeur, ma belle-soeur et mes neveux. Merci à mes quatre parents, ma mounette, mon papou, ma Fred et mon petit gros. Merci à mon chat, Coccinelle, pour toujours me rappeler le plus important dans la vie, manger, dormir et mordre maman quand elle oublit les deux premiers.

Thank you all for being an integral part of my academic journey.

ABSTRACT

The Ph.D project is the structural study of mitofusins (Mfn1/2 in humans and Fzo1 in yeasts) using mainly modeling-based methods such as molecular dynamics or structure prediction methods based on artificial intelligence (mainly AlphaFold). This project is a part of an ANR (MITOFUSION) shared between different partners (Laboratoire de Biochimie Théorique: Antoine Taly, Marc Baaden, Laboratoire des Biomolécules: Patrick Fuchs, Laboratoire de Biologie Moléculaire et Cellulaire des Eucaryotes: Mickaël Cohen, Institut de Psychiatrie et Neurosciences de Paris: David Tareste) whose goal is to understand the structure-function relationships of the mitofusin.

Mitochondria form a complex network inside the cells, undergoing continuous fusion and fission events. These processes shape mitochondrial dynamics and are essential for the maintenance, function, distribution and inheritance of mitochondria. The morphology of the latter therefore respond to the ever-changing physiological changes of the cell. The large GTPase involved in the tethering and fusion of the mitochondrial outer membranes (OM) are transmembrane proteins called mitofusins. The mitofusins Mfn1 and Mfn2 can be found in mammals. Fzo1 (Fuzzy Onion 1) is the unique mitofusin homologue in *Saccharomyces cerevisiae*. The mitochondrial inner membrane fusion and crista organisation is mediated by human OPA1 (Optic Atrophy 1) and yeast Mgm1 (Mitochondrial Genome Maintenance 1).

Mitochondrial fusion dysfunction is related to several neurodegenerative disorders, such as Parkinson, Alzheimer and Huntington diseases. As a matter of fact, research has shown that mutations in Mfn2 induce the development and progression of muscular dystrophies, such as Charcot-Marie-Tooth Type 2A, the most common form of axonal CMT disease. The exact mechanism by which the mitofusins contributes to mitochondria dysfunction as well as the exact molecular fusion mechanism is not fully understood yet. Overall, mitochondrial fusion plays an important role in CMT2A, it is thus of paramount importance to get a full understanding of the process at the molecular level.

The structure of both Mfn1 and Mfn2 was partially solved, the transmembrane domain being excluded, and no solved structure are available for Fzo1. With our ANR partners, we decided to work on the yeast version of Mitofusin (named Fzo1) as it is a good model (of homology with human Mfn1 and Mfn2) as yeast are convenient hosts for testing how other protein partners are involved in the process (e.g. Ugo1). Fzo1 is embedded in the mitochondrial OM as it possesses two transmembrane domains, exposing N- and C- terminal portions towards the cytosol and a loop towards the intermembrane space. On the N-terminal side can be found two coiled-coil heptad repeats (HRs) domains, HRN (in yeast only) and HR1, flanking a GTPase domain. A third coiled-coil heptad repeats domain HR2 is on the C-terminal portion. Some models of Fzo1 were built based on the mitofusin related bacterial dynamin-like protein (BDLP). BDLP is involved in membrane remodelling and exists in two conformational states, a closed compact version which changes to an opened extended structure, upon GTP-binding, on which the built models were based.

The goal of the Ph.D is to update the model of Fzo1 built in 2017, by working on the transmembrane domains using multiscale molecular dynamics, and then update the overall structure using artificial intelligence methods. Another project consisted in studying the amphipathic helix of HR1 domain of Mfn1 (MfnA-AH), test its membrane binding capabilities. Initially, we employed coarse-grained simulations, establishing a robust foundation for evaluating the predictive capacity of the MARTINI family of force fields. Using other simulations ran with the penetratin, we were able to provide a comparative analysis for the AH-membranes interactions in the MARTINI force-fields. The Mfn1-AH was then further characterized using all-atom simulations.

RÉSUMÉ

Le projet de doctorat porte sur l'étude structurale des mitofusines (Mfn1/2 chez l'homme et Fzo1 chez la levure) en utilisant principalement des méthodes basées sur la modélisation telles que la dynamique moléculaire ou les méthodes de prédiction de structure basées sur l'intelligence artificielle (principalement AlphaFold). Les mitochondries forment un réseau complexe à l'intérieur des cellules, subissant des événements continus de fusion et de fission. Ces processus façonnent la dynamique mitochondriale et sont essentiels pour l'entretien, la fonction, la distribution et l'héritage des mitochondries. La morphologie de ces dernières répond donc aux changements physiologiques constants de la cellule. Les grandes GTPase impliquées dans l'ancrage et la fusion des membranes externes de mitochondrie sont des protéines transmembranaires appelées mitofusines. Les mitofusines Mfn1 et Mfn2 se trouvent chez les mammifères. Fzo1 (Fuzzy Onion 1) est l'homologue unique de Mfn1/2 chez la levure *Saccharomyces cerevisiae*. La fusion de la membrane interne mitochondriale et l'organisation des crêtes sont médiées par l'OPA1 humaine (Atrophie Optique 1) et la Mgm1 de la levure (Maintenance du Génome Mitochondrial 1).

La dysfonction de la fusion mitochondriale est liée à plusieurs troubles neurodégénératifs, tels que Parkinson, Alzheimer et la maladie de Huntington. En effet, il a été montré que les mutations dans Mfn2 induisent le développement et la progression de dystrophies musculaires, telles que la maladie de Charcot-Marie-Tooth de type 2A, la forme la plus courante de la maladie CMT axonale. Le mécanisme exact par lequel les mitofusines contribuent à la dysfonction mitochondriale, ainsi que le mécanisme moléculaire exact de la fusion, ne sont pas encore entièrement compris. Dans l'ensemble, la fusion mitochondriale joue un rôle important dans la CMT2A, il est donc d'une importance capitale de comprendre pleinement le processus au niveau moléculaire.

Les structures de Mfn1 et Mfn2 ont été partiellement résolues, le domaine transmembranaire étant exclu, mais aucune structure résolue n'est disponible pour Fzo1. Fzo1 est intégré à la membrane externe de mitochondrie avec ses deux domaines transmembranaires, exposant les parties N- et C-terminales vers le cytosol et une boucle vers l'espace intermembranaire. Du côté N-terminal, on trouve deux domaines de répétitions en heptad (HRs), HRN (présent uniquement chez la levure) et HR1, flanquant un domaine GTPase. Un troisième domaine HR, HR2, se trouve dans la partie C-terminale. Certains modèles de Fzo1 ont été construits avec comme template la protéine bactérienne de type dynamin-like (BDLP). BDLP est impliquée dans le remodelage des membranes et existe sous deux états conformationnels, une version compacte fermée qui passe à une structure étendue ouverte lors de la liaison au GTP, sur laquelle les modèles construits étaient basés.

L'objectif du doctorat est de mettre à jour le modèle de Fzo1 construit en 2017, en travaillant dans un premier temps le domaine transmembranaire à l'aide de dynamiques moléculaires à plusieurs échelles. Nous avons ensuite travaillé sur le modèle de Fzo1 en entier, notamment à l'aide de méthode d'intelligence artificielle. Un autre projet a consisté à étudier l'hélice amphipathique du domaine HR1 de Mfn1 (MfnA-AH), à tester ses capacités de liaison à la membrane. Initialement, nous avons utilisé des simulations gros grains, établissant ainsi une base solide pour évaluer la capacité prédictive de la famille de champs de force MARTINI. En utilisant d'autres simulations réalisées avec la pénétratine, nous avons pu fournir une analyse comparative des interactions AH-membranes dans les champs de force MARTINI. Mfn1-AH a ensuite été caractérisé plus en détail à l'aide de simulations tout-atomiques.

CONTENTS

List of Figures	VI
List of Tables	X
1 Introduction	1
1.1 The vital role of mitochondria in cell function	2
1.1.1 Mitochondria structure and function	2
1.1.2 The mitochondrial life cycle : engaging fusion and fission machinery	4
1.1.3 A word on mitochondrial membranes lipidic composition	6
1.2 Membrane fusion and diverse examples	9
1.2.1 Main stages of the fusion process	10
1.2.2 The example of SNARE fusion	11
1.2.3 Viral protein fusion	13
1.3 The membrane-remodeling properties of the dynamin superfamily proteins	14
1.3.1 Evolutionary conserved structural features of DSPs	16
1.3.2 Bacterial dynamin-like proteins bears striking similarities with mitofusins	18
1.4 Mitofusins are key players of outer mitochondrial fusion	22
1.4.1 Mitochondrial dynamics machinery	23
1.4.2 The role of mitofusins in mitochondrial dysfunction and associated pathologies	27
1.4.3 Mitofusins share structural similarities with the dynamin superfamily	28
1.5 Using computational simulations to gather insights into membrane fusion	34
1.5.1 Investigation of preliminary conditions favorable for membrane fusion	34

1.5.2	Analysis of the full fusion process through molecular dynamics	35
1.6	Thesis aim	37
2	Material and Methods	40
2.1	Fundamental Concept of Molecular Dynamics	41
2.1.1	Representation Accuracy	41
2.1.2	The Force-Field	43
2.1.3	Molecular Dynamics Algorithm	46
2.1.4	Periodic Boundary Conditions	47
2.1.5	Energy of the system	48
2.1.6	Thermodynamic Ensembles	49
2.1.7	Molecular Dynamics Protocol	51
2.2	Coarse-Grained Molecular Dynamics: two versions of the MARTINI force-fields	53
2.2.1	MARTINI2: The coarse-grained model tailored for proteins	54
2.2.2	MARTINI3: mitigating overaggregation issues from MARTINI2	56
2.3	Temperature-Replica Exchange Molecular Dynamics	59
2.4	Advancing molecular modeling: Revolutionizing protein structure prediction with AlphaFold	63
3	Molecular dynamics based prediction of Fzo1 transmembrane domains structure	65
3.1	Introduction	66
3.2	Materials and Methods	68
3.2.1	Coarse-Grained conformational sampling	69
3.2.2	All-Atom refinement of the model	71
3.2.3	AlphaFold2 predictions	73
3.3	Results	74
3.3.1	The association of transmembrane helices is reproducible with two coarse-grained force fields	74
3.3.2	Protonation of Lys716 interferes with the formation of a stable TM1-TM2 dimer	75
3.3.3	Protonation of Lys716 acts as a switch for remodeling the TM1-TM2 interface .	75
3.3.4	The TM domain energy landscape quantifies Lys716-mediated dimer de-stabilization	76
3.3.5	Charged Lys716 destabilizes the membrane	78
3.3.6	Replica exchange MD provides a refined atomistic model and verifies stable TM assembly	78

3.3.7	Experiments show that the polar residue 716 is crucial for mitochondrial respiration in yeast	81
3.4	Discussion	82
3.4.1	The TM1-TM2 interface is robust across force fields and levels of representation	82
3.4.2	How can we interpret TM1 expulsion from the membrane with Martini 3?	83
3.4.3	Extensive multiscale simulations yield a new structural model of the Fzo1 TM domain improving over previous predictions	84
3.4.4	An independent Fzo1-Ugo1 complex prediction matches the novel TM domain fold	85
3.4.5	Could Fzo1 TM domain play an active role in membrane fusion?	86
3.5	Conclusion	87
3.6	Supplementary Material	88
3.7	Supplementary Results	89
4	A case by case study of the protein-membrane interactions of MARTINI2 and MARTINI3 force-fields	95
4.1	Introduction	96
4.2	Materials and Methods	100
4.2.1	Software details	101
4.2.2	Systems setup	101
4.2.3	Scaling of water beads non-bonded interactions in MARTINI3	102
4.2.4	Simulation parameters	102
4.2.5	Analysis details	103
4.3	The penetratin has a more realistic behavior in MARTINI3 simulations	105
4.4	The behavior of Mfn1-AH exhibits distinct dissimilarities between MARTINI2 and MARTINI3.	110
4.5	Discussion	113
4.5.1	Martini3 membranes exhibit a reduced level of compactness in membranes . . .	113
4.5.2	The MARTINI3 simulations of the penetratin shows good agreement with experimental data	114
4.5.3	Insufficient role of Packing Defects in driving membrane binding of amphipathic helices: Insights from Mfn1-AH	115
5	Computational investigation of the insertion of an Mfn1-HR1 domain amphipathic helix	118
5.1	Introduction	119
5.2	Materials and Methods	122

5.2.1	Preliminary 300 ns simulations	123
5.2.2	Membrane analysis simulations	124
5.2.3	Computational strategy for studying Mfn1-AH / membrane interaction further	124
5.2.4	T-REMD of Mfn1-AH in water (REMD-water)	124
5.2.5	T-REMD of Mfn1-AH with membrane (REMD-helix and REMD-folding)	125
5.2.6	Analysis	126
5.3	Mfn1-AH leads to thinning of the membrane	128
5.4	Mfn1-AH is more structured and stable in a DOPE membrane	132
5.5	Structural dynamics of Mfn1-AH: Unfolding, Insertion, and Folding processes in water and membrane environments	134
5.5.1	Unfolding process of Mfn1-AH in water	134
5.5.2	The insertion process of Mfn1-AH in a POPC:DOPE bilayer	135
5.5.3	The folding process of Mfn1-AH in a POPC:DOPE bilayer	136
5.6	Discussion	137
5.6.1	Can Mfn1-AH fold into the membrane on its own ?	137
5.6.2	Has Mfn1-AH fusion inducing properties?	138
5.7	Appendix	140
6	Exploring the mitofusin conformational landscape with AlphaFold	143
6.1	Introduction	144
6.2	Materials and methods	144
6.3	AlphaFold provides a new type of cis-dimerization conformation involving the coiled-coil domains in the interactions	145
6.3.1	AlphaFold exclusively produces mitofusins structures in an open conformation, unsuitable with membrane tethering mechanism	145
6.3.2	The AF models are validated by the available experimental data	149
6.3.3	New models involving fusion partners Ugo1 shed new light on cross-type cis-dimer	151
6.4	A specific MSA provides additional insights into TM domain interactions and structure prediction	154
6.5	Conclusion	155
6.6	Appendix	158
7	Conclusion	164
7.1	Production of a TM domain structure fitting mitofusins small loops	165
7.2	A first preliminary study of Mfn1-AH	167

7.3	This Ph.D work gave us valuable insights on the MARTINI3 force-field	168
7.4	A new cross-type cis-dimer is unveiled by AlphaFold predictions	170
7.5	What's next ?	172

Bibliography		174
---------------------	--	------------

LIST OF FIGURES

1.1	Mitochondrion morphology	2
1.2	Mitochondrial network	3
1.3	Schematic summary of mitochondrial metabolism	4
1.4	Mitochondrial functions within the cell	5
1.5	Mitochondrial contacts with other organelles within the cell	9
1.6	Lipid bilayer fusion	10
1.7	Structures of SNARE	11
1.8	SNARE conformation cycle during vesicle docking and membrane fusion	12
1.9	SNARE-mediated fusion according to the stalk hypothesis	13
1.10	Structural snapshots toward membrane fusion	13
1.11	Dynamin-superfamily members in animals and plants	14
1.12	GTP-binding motifs	16
1.13	Modular architecture of dynamin family members	17
1.14	Crystal structures of BDLP in GDP-associated and nucleotide-free conformations	19
1.15	BDLP is a GTPase capable of decorating and tubulating liposomes	20
1.16	The GTP and Lipid-Induced Conformation Changes	21
1.17	A polymerization/depolymerization model for fusion and fission	22
1.18	Regulation of mitochondrial morphology through fusion and fission	23
1.19	Mitochondrial fission	24
1.20	Domain structures of mitochondrial fusion and fission components	26
1.21	Solved Mitofusins structures	30
1.22	Fzo1 models produced by De Vecchis et al. in 2017 [1] and Brandner et al. in 2019 [2]	31

1.23	Working models for the molecular mechanisms of Mitofusin in OM fusion	32
1.24	Putative Fzo1 trans tethering complex	33
1.25	Demonstration of packing defects and protrusion analysis	35
1.26	Branching reaction pathway for vesicle fusion	36
1.27	Stages of SNARE-mediated membrane fusion revealed by simulations	37
2.1	Spatiotemporal resolution of various biophysical techniques	42
2.2	Various representation precision used in molecular dynamics	43
2.3	Potential Energy terms illustration	43
2.4	Non-bonded interactions	45
2.5	Leap Frog algorithm	47
2.6	Periodic Boundary Conditions (PBCs).	48
2.7	Scheme depicting the various stages within an MD Protocol.	51
2.8	Energy minimization main concepts	52
2.9	Energy minimization of 3 water molecules	52
2.10	MARTINI mapping	54
2.11	Description of MARTINI2 particles	55
2.12	Description of MARTINI3 particles	57
2.13	Boltzmann distribution of the Potential Energy of each replica of an T-REMD simulation	60
2.14	Illustration of the T-REMD method	61
2.15	Free energy landscapes and the effects of temperature	62
2.16	Analysis of REMD	63
2.17	AlphaFold model architecture	64
3.1	Protocol	68
3.2	TM1-TM2 contacts determined using Martini 3 and best model extraction	77
3.3	TM domain prediction based on REMD simulations	79
3.4	The polarity of K716 is essential for Fzo1 function	81
3.5	AlphaFold2 prediction of Fzo1 in interaction with Ugo1	85
S3.1	Distance between the center of mass of the two TM domains, as a function of time	89
S3.2	Effect of the TM domain on lipid properties relevant for fusion	90
S3.3	Position of TM1 relative to TM2 colored as a function of the free energy	90
S3.4	PCA colored as a function of the free energy for the MARTINI simulations	91
S3.5	Conformations of the TM domain during the REMD simulations	91

S3.6	Supplementary results of the REMD	92
S3.7	Comparison of the PCA between AA and CG simulations	92
S3.8	Fzo1 model predicted with AlphaFold2	93
S3.9	TM domain sequence alignments from eucaryotic mitofusins	94
4.1	Comparison of a Coarse-Grained system with its All-Atom version	97
4.2	Lateral association of embedded amphipathic helices	98
4.3	Improving packing and reducing protein stickiness	99
4.4	Stick representation of the lipids used in this chapter	100
4.5	Quantification of lipid packing defects	105
4.6	Characterization of penetratin membrane binding	106
4.7	Membrane thickness analysis of the penetratin	107
4.8	Membrane analysis of penetratin systems	108
4.9	Distribution of the residues of the penetratin in the membrane	109
4.10	Membrane analysis of the Mfn1-AH simulations	111
4.11	Distribution of the residues of Mfn1-AH in the membrane for the MARTINI2 membrane-peptide systems	112
4.12	Study of the driving force in membrane-Mfn1-AH interactions	113
4.13	MARTINI3 scaled results	116
5.1	Experimental investigation of the interaction between Mfn1-AH and lipid bilayer structure	120
5.2	Description of Mfn1's amphipathic helix properties	121
5.3	Phases of amphipathic helix / membrane interaction	122
5.4	Schematic description of all three REMD carried out for this project	124
5.5	Mfn1-AH effect on the membrane global properties	129
5.6	The impact of Mfn1-AH on the order parameter of the lipid tails	130
5.7	The impact of Mfn1-AH on the membrane surface properties	131
5.8	Mfn1-AH stability in POPC and POPC:DOPE membranes	132
5.9	REMD-helix : Ensemble of Mfn1-AH conformations at 310K	133
5.10	REMD-water: Evolution of the helicity content as a function of time	134
5.11	REMD-folding: Study of replica 4	135
5.12	REMD-folding: Secondary structure evolution of replica 4	136
5.13	REMD-folding: Folding process of Mfn1-AH	137
5.14	Liposome-liposome docking and fusion by HR1 of Mfn1	138
S5.1	Area per lipid as a function of time during classical simulations at 310K	140

S5.2	REMD-helix : Analysis per replica	141
S5.3	REMD-folding : Analysis per replica	142
6.1	AlphaFold model of Fzo1	146
6.2	AlphaFold model of human mitofusins Mfn1 and Mfn2	147
6.3	AF dimeric models of human and yeast mitofusins	149
6.4	Experimental structures aligned with the Alphafold models	150
6.5	AF structure prediction of mitofusins fusion regulators	151
6.6	AF tetrameric models of mitofusins and solute carriers Ugo1/SLC25A46	153
6.7	Models produced with AF provided with a custom MSA	155
S6.1	TM domain alignment of the mitofusins used for the custom MSA	159
S6.2	AlphaFold monomeric models of mitofusins	162
S6.3	AlphaFold oligomeric models of mitofusins	163
7.1	Homology modeling of mitofusins transmembrane domains	166
7.2	Proposed mechanism based on AF models	171
7.3	Updated cis-dimer model of Fzo1	172

LIST OF TABLES

1.1	Outer mitochondrial membrane phospholipidic composition	7
1.2	Inner mitochondrial membrane phospholipidic composition	8
1.3	Fatty acid composition of mitochondria in <i>S. cerevisiae</i>	8
1.4	Functions of dynamin-superfamily members	15
2.1	MARTINI2 Interaction Matrix	55
2.2	MARTINI3 Interaction Matrix	58
3.1	Plasmids used in this study	74
3.2	<i>Saccharomyces cerevisiae</i> strains used in this study	74
3.3	Cluster populations from the CG Martini simulations	76
4.1	EphA1 and ErbB1 TM domain dimerization free energy ΔG_{DIM} (in kJ/mol)	98
4.2	Summary table of the simulation systems	101
4.3	Summary table of the membrane thickness for the Mfn1-AH systems	110
5.1	Summary table of the simulation systems	122
6.1	Summary table of the models produced with AlphaFold	144
S6.1	Summary table of the sequences selected for a custom alignment	158
S6.2	Distances in Å between the closest residues of mitofusins monomers in mitofusins dimers	160
S6.3	Distances in Å between monomers of the tetramers	161

CHAPTER 1

INTRODUCTION

1.1 The vital role of mitochondria in cell function

Mitochondria are organelle whose most prominent role is to provide the cell with metabolic energy in the form of ATP generated by oxidative phosphorylation. Mitochondria, being semi-autonomous organelles, possess their own genetic material (mtDNA) and machinery for protein synthesis. They are unique organelles due to their two distinct membranes. Mitochondria form a complex network inside the cells, undergoing continuous fusion and fission events, independently of the host cell's division. These processes shape mitochondrial dynamics and are essential for the maintenance, function, distribution and inheritance of mitochondria. The morphology of the latter therefore respond to the ever-changing physiological changes of the cell [3].

1.1.1 Mitochondria structure and function

The presence of mitochondria within cells is believed to originated from an endosymbiotic event, wherein an ancestral host cell established a symbiotic relationship with an α -proteobacterial ancestor with an oxidative respiratory system. Over time, this symbiosis evolved into the mitochondria we observe in modern cells [4, 5]. Furthermore, a large fraction of genes coding for mitochondrial proteins have been transferred in the nucleus and require synthesis in the cytoplasm before being imported into the mitochondria [5, 6].

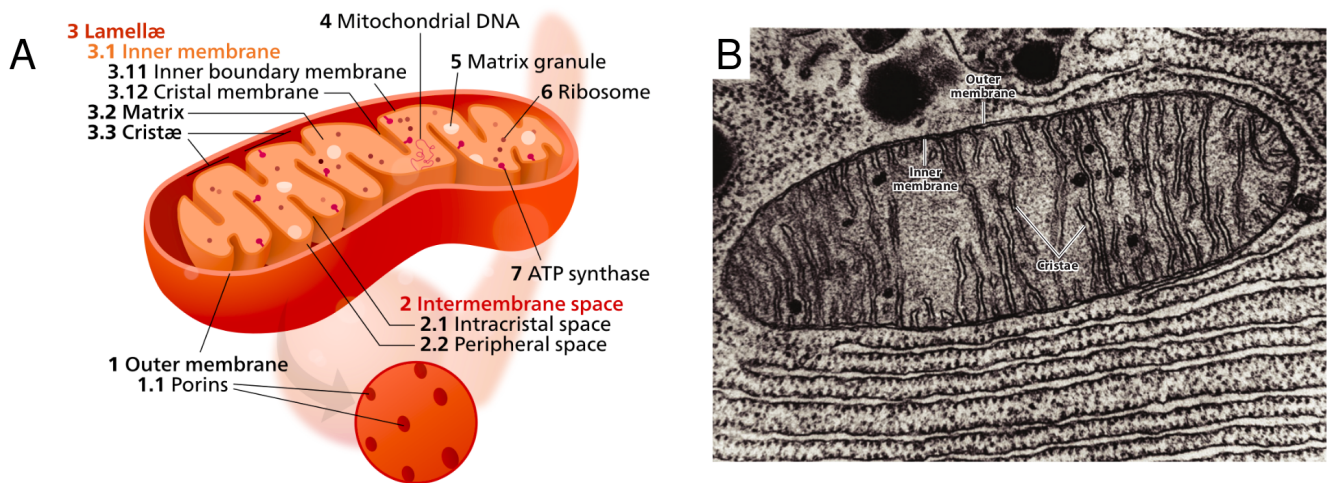


Figure 1.1: **Mitochondrion morphology.** (A) Schematic representation of a mitochondrion (<https://en.wikipedia.org/wiki/Mitochondrion>). (B) Thin-section electron micrograph of a mitochondrion from a bat pancreatic cell, which shows the different membrane structures of the mitochondrion: OM, IM, and cristae. Taken from [7].

The architecture of mitochondria was first revealed using electron microscopy in 1950s [8]. The organelle is composed of two membranes, the outer membrane (OM) and inner membrane (IM), separated by the intermembrane space (IMS) (Figure 1.1). The environment located inside the IM is called the matrix and harbours the mtDNA, existing in multiple copies. It is the site of organellar DNA replication,

transcription, protein biosynthesis and numerous enzymatic reactions. The high pH of the matrix (7.9 to 8) creates trans-membrane electrochemical gradient that drives ATP synthesis [9]. The IM is characterized by a larger surface area than the OM as it is folded into lamellar and tubular structures, called cristae, which protrude into the matrix and bears the respiratory chain complexes [10, 11]. Nonetheless, the description of mitochondria as given in Figure 1.1 (a scheme of a mitochondrion, showed as one individual bean-shaped organelle) is actually misleading, as the mitochondria are highly dynamic organelles which build large interconnected intracellular networks [12] (Figure 1.2).

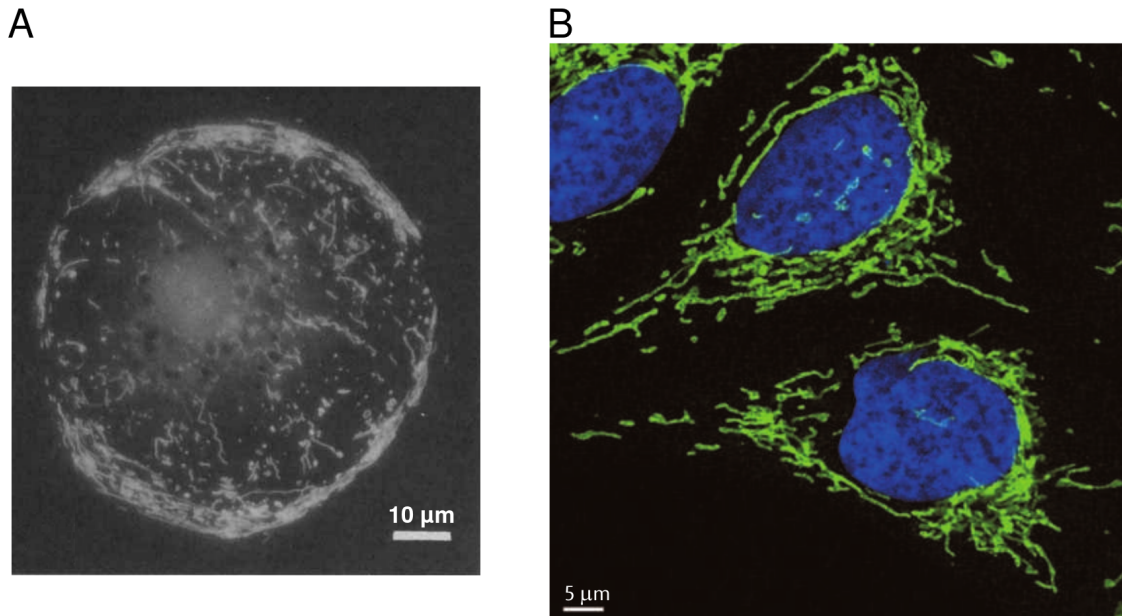


Figure 1.2: **Mitochondrial network.** (A) Mitochondrial network of endothelial cell. Taken from [12]. (B) Confocal microscopy of human osteosarcoma cells (U2OS). Mitochondria are in green, and Nuclei in blue. Taken from [3].

As mentioned previously, cristae serve as the site where oxidative respiration occurs, which provides ATP to the cell [13]. In the initial stage, pyruvate is generated from a glucose molecule, within the cytosol as a starting point. The pyruvate then enters the mitochondria, is converted in acetyl-CoA which is then processed by the citric acid cycle. Acetyl-CoA can also be converted through an alternative pathway involving fatty acids and the citric acid cycle can be provided with amino-acids as well. The cycle yields carbon dioxide as well as NADH and FADH₂, as well as a small amount of ATP. The generated NADH and FADH₂ then enter the electron transport chain located in cristae. The electron located in the molecules are transferred to the Electron Transport Chain (ETC), leading to the pumping of protons (H⁺) in the IMS, conferring an electrochemical gradient to the IM. The electrochemical gradient drives protons (H⁺) to flow back into the mitochondrial matrix through ATP synthase, which powers the synthesis of ATP from adenosine diphosphate (ADP) and inorganic phosphate (Pi) in a process called oxidative phosphorylation [14].

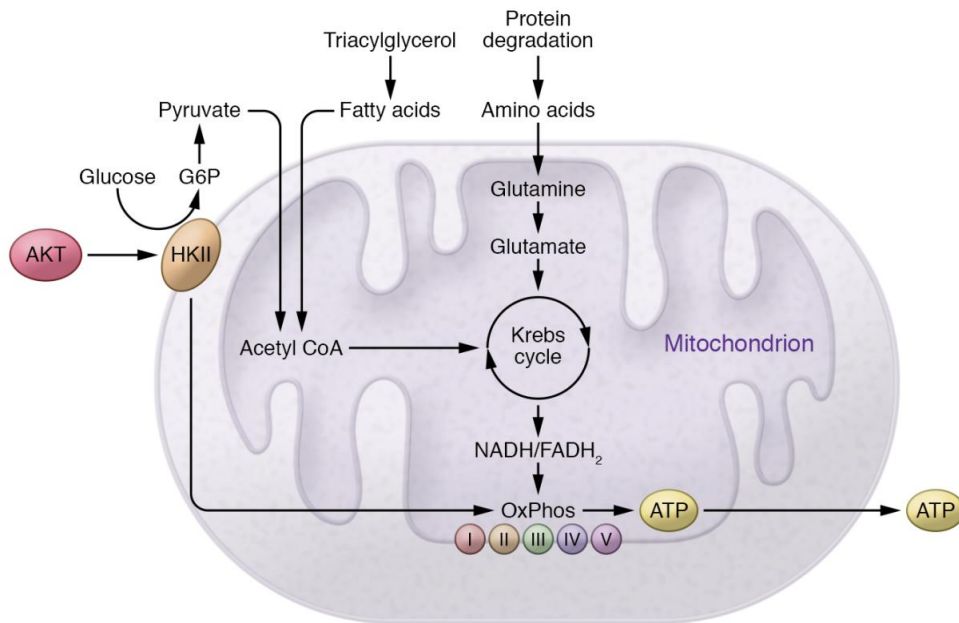


Figure 1.3: **Schematic summary of mitochondrial metabolism.** Taken from [14].

1.1.2 The mitochondrial life cycle : engaging fusion and fission machinery

As most of the genes of the mitochondrial proteins are located in the nucleus, proteins have to be imported from the cytosol for the mitochondria to function properly. These proteins are unfolded and transported inside of the mitochondria or its membranes, thanks to chaperones and signals recognized by receptors. They can then be folded and often inserted into membranes, and assembled with cofactors and other proteins to macromolecular complexes. Furthermore, mitochondrial biogenesis also involves the incorporation of mitochondrion-synthesized and imported membrane lipids, the amplification of the mitochondrial genome and the translation of mitochondrion-encoded proteins [15, 16, 17].

Mitochondrial cellular functions are described in Figure 1.4. Throughout the cell life cycle, this organelle undergoes numerous events of fusion and fission. Damaged organelles are removed, while functioning portions of the network can be distributed to other sections of the cell. Finally, one of the roles of mitochondria is to release the factor triggering the apoptosis of the cell.

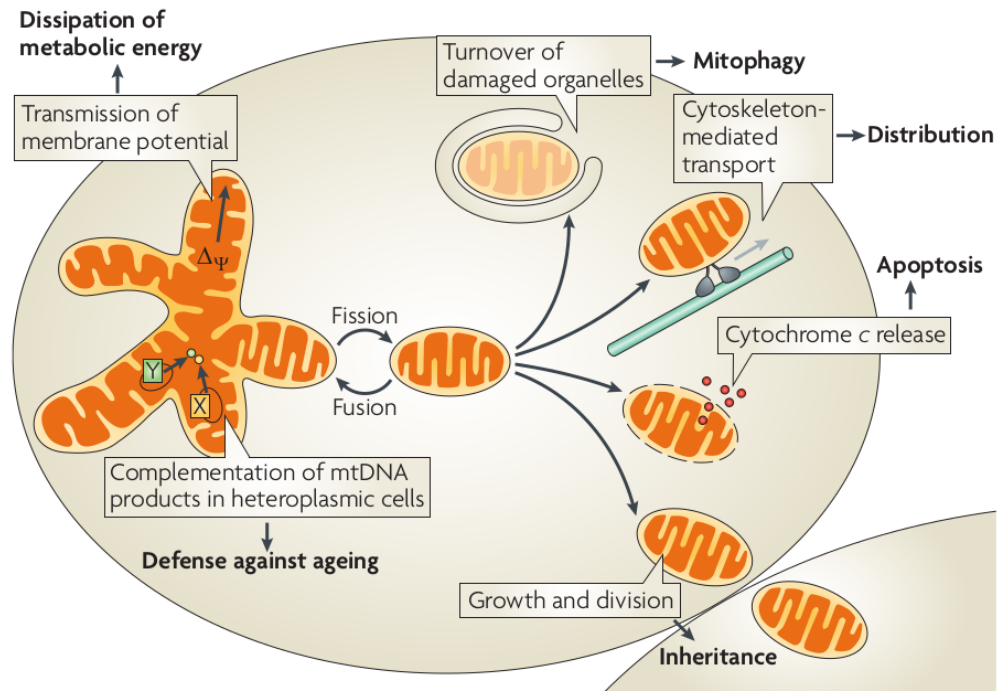


Figure 1.4: **Mitochondrial functions within the cell.** Fusion and fission processes play crucial roles in a variety of cellular mechanisms. Division is essential for tasks such as organelle inheritance and distribution during cell division, the release of pro-apoptotic factors from the intermembrane space, intracellular transport facilitated by the cytoskeleton, and the removal of damaged organelles through mitophagy. Fusion, on the other hand, is of particular significance in addressing the decline of respiratory functions due to aging by enabling the complementation of mitochondrial DNA (mtDNA) gene products in heteroplasmic cells. Taken from [3].

Mitochondrial inheritance. Mitochondria are not generated de novo but instead are inherited through cell division. During cell proliferation, the number of mitochondria need to increase, then fragment when entering mitosis and undergo cytokinesis for a partitioning of the organelles in a stochastic manner [18, 19]. Therefore, mitochondrial fission plays a critical role in this phase. In yeast, mitochondria are inherited in an ordered manner by cytoskeleton-dependent bud-directed transport [20]. However, mitochondrial fission inevitably produces organelles lacking mtDNA, leading to mitochondrial heterogeneity and dysfunction of the organelle, if fusion is impaired [21]. It is thus a fundamental mechanism of the cell, that will ensure that the mitochondrial genome and gene products are replenished before functionality is lost [22].

Mitochondrial distribution and morphology fit specific requirements of the cells. Mitochondria are localized in different parts of the cell, and its distribution depends on division, as it is necessary to spread the mitochondrial network throughout the cell. It is most important in large and extended cells, such as neurons, with high energy demand structures such as dendritic spines and synapses [23]. Another example of cells with specific needs would be muscles cells, in which mitochondrial filaments connect a dense layer of mitochondria in the oxygen-rich cell periphery with mitochondria in the oxygen-poor

core of the muscle fibre, thereby forming a continuous network. This structural organisation allows for production of ATP in remote parts of the cell to fuel molecular motors during muscle contraction [24]. Thus, concerted activities of the mitochondrial fusion and fission machineries shape the mitochondrial compartment and adapt it to the specific requirements of the cells.

Mitochondrial quality control and ageing. Some byproducts of ATP production are reactive oxygen species (ROS), which are known to induce mutations and lesions in DNA, as well as degradation of protein and lipids [25]. Long exposure to ROS will lead to an accumulation of mtDNA mutations which will result into a loss of functional respiratory chain complexes. A decline of bioenergetic capacity and eventually age-associated pathologies and death will then be observed [26]. However, as various solitary mitochondria can accumulate different mtDNA mutations, fusion between these defective organelle enables the exchange of genetic material and the production of functional proteins, thus restoring mitochondrial activity through genetic complementation [27]. Another mechanism that contribute to keeping healthy mitochondria is the process of autophagy (or mitophagy in the case of mitochondria), which is self-degradation of cellular components that are harmful or no longer required. A double-membrane autophagosomes sequester organelles or portions of cytosol and fuse with lysosomes or vacuoles for breakdown by resident hydrolases [28]. It was shown that mitochondrial fission and selective fusion may contribute to removal of damaged mitochondria, thereby initiating a quality control mechanism [29, 30, 31]. In fact, removal of fusion will result in a decline of respiratory capacity.

Role of mitochondrial fission in apoptosis. Apoptosis is a programmed cell death process that occurs in multicellular organisms. During apoptosis, cells undergo a series of well-defined morphological and biochemical changes that lead to their orderly and controlled elimination. A key step of apoptosis is OM permeabilization, which releases cytochrome c and other pro-apoptotic factors from the intermembrane space into the cytosol to trigger downstream cell death pathways. Additionally, mitochondrial fragmentation has been shown to be induced early in the apoptotic pathway [32], and inhibiting fusion has been shown to induce apoptosis [33]. However, fragmentation of mitochondria alone does not induce apoptosis, as additional stimuli is needed.

1.1.3 A word on mitochondrial membranes lipidic composition

Mitochondria are characterized by two membranes, the outer membrane (OM) and inner membrane (IM), both defined by different composition and functions. The IM can be split into two main categories, the inner boundary membrane, running parallel to the OM, and the cristae, invaginations of the IM, providing an enlarged surface area for ATP production. These membranes outline and divide two subcompartments, the intermembrane space and the matrix. The OM is smooth and generally permeable, freely traversed by ions and small, uncharged molecules through pore-forming membrane proteins (porins) [34]. Any larger molecules, especially proteins, have to be imported by special translocases. The IM is by contrast a membrane in the strictest sense, as even small solutes like ions and metabolic substrates cannot pass through it without the help of carrier proteins. It is where oxidative phosphorylation takes place, in a suite

of membrane protein complexes that create the electrochemical gradient across the inner membrane, or use it for ATP synthesis. Among subcellular fractions, the mitochondria exhibit the highest abundance of protein-rich lipid bilayers. In comparison to other organelles, the phospholipid to protein and sterol to protein ratios within mitochondrial membranes are relatively low. The IM specifically showcases the lowest ratio, with a protein:lipid mass ratio of 75:25. This is in contrast to the OM, which maintains a more balanced ratio of 50:50 between proteins and lipids [35, 36].

The OM and IM exhibit differences not only in terms of their functions and membrane proteins but also in their phospholipid compositions. Both are mainly composed of phosphatidylcholine (PC) and phosphatidylethanolamine (PE), and in lower proportions we find anionic phospholipids such as phosphatidylinositol (PI), phosphatidylserine (PS), phosphatidic acid (PA) and cardiolipin (CL) (Tables 1.1 and 1.2). CL is specific to mitochondria and is in its highest proportions in the IM. Sterols and sphingolipids are found at very low amount. While there is general agreement on the phospholipids involved, their specific proportions are still a topic of debate, and various proportions can be found in the literature (Tables 1.1 and 1.2). Different studies and experimental techniques used for lipid analysis have contributed to discrepancies in reported lipid compositions. As there is variations in sample sources, species, tissues types and methodologies, divergence has been observed. The dynamic nature of mitochondrial membranes and their lipid composition further adds complexity to the understanding of this topic. Nevertheless, studies have revealed that both membranes primarily consist of C18 and C16 aliphatic chains, with little (one) to no saturations (Table 1.3).

Table 1.1: **Outer mitochondrial membrane phospholipidic composition.** Phosphatidylethanolamine (PE), phosphatidylcholine (PC), phosphatidylinositol (PI), phosphatidylserine (PS), phosphatidic acid (PA) and cardiolipin (CL).

Organism	PE %	PC %	PI %	PS %	PA %	CL %	Ref
Rat liver	27.5 ± 1.7	54.7 ± 3.1	13.4 ± 2.3	2.1 ± 0.5	0.4 ± 0.5	0.3 ± 0.3	[37]
Mouse liver	26.8	40.9	9.1	< 0.1	nd	4.0	[38]
<i>Neurospora crassa</i>	32.7 ± 2.6	50.2 ± 1.6	9.2 ± 1.1	0.6 ± 0.2	0.7 ± 0.4	3.1 ± 0.5	[37]
<i>S. cerevisiae</i>	32.6	45.6	10.2	1.2	4.4	5.9	[35]
<i>S. cerevisiae</i>	34 ± 1	44 ± 2	14 ± 1	4 ± 1	1 ± 1	5 ± 1	[36]
<i>S. cerevisiae</i>	33	46	10	1	4	6	[39]

Table 1.2: **Inner mitochondrial membrane phospholipidic composition.** Phosphatidylethanolamine (PE), phosphatidylcholine (PC), phosphatidylinositol (PI), phosphatidylserine (PS), phosphatidic acid (PA) and cardiolipin (CL).

Organism	PE	PC	PI	PS	PA	CL	Ref
	%	%	%	%	%	%	
Mouse liver	26.5	35.1	5.0	< 0.1	nd	18.0	[38]
<i>S. cerevisiae</i>	24.0	38.4	16.2	3.8	1.5	16.1	[35]
<i>S. cerevisiae</i>	24 ± 1	37 ± 2	14 ± 1	3 ± 1	2 ± 1	13 ± 1	[36]
<i>S. cerevisiae</i>	24	38	16	4	2	16	[39]

Table 1.3: **Fatty acid composition of mitochondria in *S. cerevisiae*.** 16:0, Palmitic acid; 16:1, Palmitoleic acid; 18:0, Stearic acid; 18:1, Oleic acid; 20:0, Arachidic acid.

Organism	14:0/1	16:0	16:1	18:0	18:1	Ref
<i>S. cerevisiae</i>		18	44	4	34	[40]
<i>S. cerevisiae</i>	<2.0	9.0	32.6	1.5	50.1	[41] 30°C
<i>S. cerevisiae</i>	<2.0	12.0	26.4	4.7	51.3	[41] 35°C

There is also discrepancies in the proportions of cholesterol (mammals) or ergosterol (yeast) in both membranes. In yeast, the OM generally has a low content of sterols, accounting for approximately 1% of all the lipids [36, 39, 35]. However, the percentage of sterols in the IM has been found to vary significantly, ranging from 2.5% or 7% [36, 39] to 25% [35]. Overall, it is assumed to have about 10% of cholesterol within the organelle [42].

The unique composition of phospholipids in mitochondrial membranes serves specific functions. Notably, cardiolipin (CL), a significant lipid specific to mitochondria, plays a crucial role in their structure, function, and diverse cellular processes. Indeed, CL has been demonstrated to be indispensable for mitochondrial protein transport and is involved in cofactor integration and the respiratory chain. Additionally, CL localizes around cristae, and its deficiency significantly impacts mitochondrial morphology by leading to enlarged mitochondria and disrupted or absent cristae structure. CL is also involved in the fusion and fission processes of mitochondria, as certain proteins involved in these processes have demonstrated an affinity for this phospholipid [43].

Another function that serve the mitochondrial membranes, and more precisely the outer membrane (OM), is the engagement in the extensive network of interactions with membranes of other organelles, establishing contact sites (Figure 1.5). The best characterized interaction is the ER-mitochondria interaction, which was first discovered when ER membrane patches were biochemically isolated attached to the OMM [44]. Contacts with plasma membranes, as well as lipid droplet, endosomes and lysosome have also been reported [45]. Finally, communications between peroxysome and mitochondria have been documented, as the fusion machinery of mitochondria in yeast appears to be involved in tethering these two membranes together [46]. Crosstalk between these two organelles is supported by the fact that di-

verse metabolic processes depend on their concerted action, such as β -oxidation of fatty acids, bile acid synthesis and maintenance of cellular ROS homeostasis [47]. Furthermore, they share the same machinery involved in their division [45]. The interactions and the key players are described in more detail in section 1.4.1 of the Introduction.

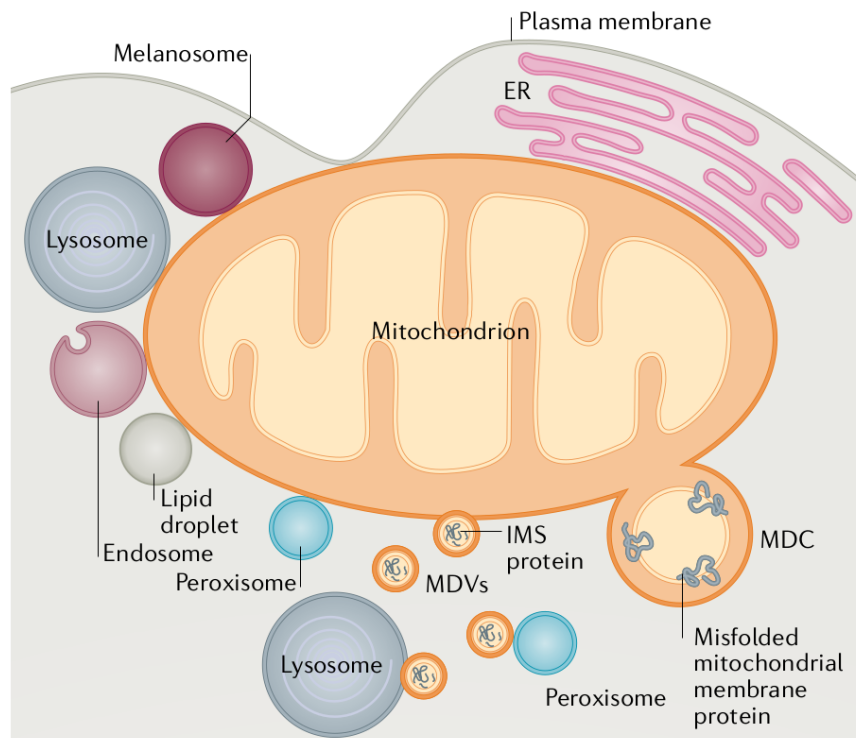


Figure 1.5: **Mitochondrial contacts with other organelles within the cell.** The outer mitochondrial membrane (OMM) forms intricate networks of interactions with various organelles, including membrane contact sites with the endoplasmic reticulum (ER), plasma membrane, lysosomes, endosomes, lipid droplets, peroxisomes, and melanosomes. These sites of membrane contact play a regulatory role in governing the functions of mitochondria. Moreover, mitochondria release mitochondrial-derived vesicles (MDVs) and mitochondrial-derived compartments (MDCs), which incorporate components from the mitochondria. MDVs facilitate communication with other organelles, such as lysosomes and peroxisomes, while MDCs are instrumental in mitochondrial quality control by eliminating misfolded proteins from mitochondrial membranes. Taken from [45].

1.2 Membrane fusion and diverse examples

In our study of the mitochondrial fusion mechanism, we first intend to investigate the main steps of membrane fusion, along with notable examples documented in the literature, such as the SNARE mechanism of fusion and viral peptide fusion. In fact, many disparate fusion reaction seem to share some main mechanistic motifs.

1.2.1 Main stages of the fusion process

To initiate membrane fusion (Figure 1.6), it is necessary to bring the two bilayers into close proximity, allowing interactions between proximal leaflets and minimizing the energy associated with hydration repulsion. Subsequently, the interface between the hydrophilic and hydrophobic regions of the bilayers is destabilized [48, 49]. This destabilization is followed by the formation of a hemifusion stalk phase involving the proximal leaflets. Hemifusion is defined as the state in which the outer membrane leaflets are already continuous, but no aqueous connection has formed. From the stalk, either a fusion pore appears, or a stalk expansion leads to the hemifusion diaphragm, which will then yield a fusion pore itself [49]. The initially separated volumes by the apposed membranes have now established an aqueous connection through the fusion pore. At this final stage, the fusion pore enlarges, resulting in the complete fusion of the lipid bilayers.

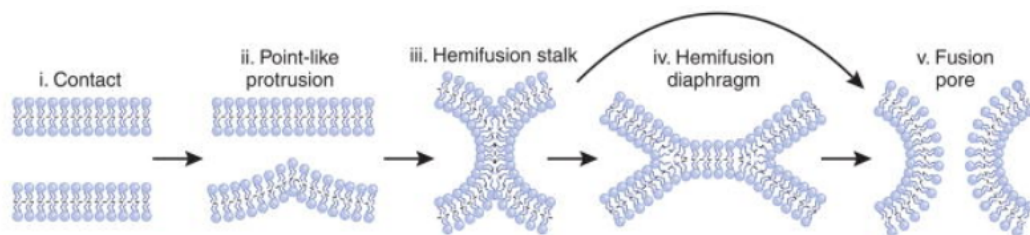


Figure 1.6: **Lipid bilayer fusion.** Dashed lines represent the boundaries of the hydrophobic surfaces of monolayers. Taken from [49].

Fusion is sensitive to membrane lipid composition. As a matter of fact, different lipid type demonstrate variation in their molecular shape, which will then impact the overall shape of the membrane [50]. The curvature of the membrane is greatly influenced by its lipid composition, and one such lipid that plays a role in curvature is phosphatidylethanolamine (PE). PE, being a cone-shaped phospholipid, can modulate the shape of the membrane, thereby affecting the arrangement of lipids within the bilayer and exposing hydrophobic regions of the membrane to the surrounding solvent [49]. These lipid packing defects and negative intrinsic curvature of PE could then favor interactions between proximal leaflets, reducing the energy barrier of creating the hemifusion stalk phase [51, 52]. Furthermore, highly curved membranes are more prone to fuse with one another. In addition, the role of membrane tension in advancing beyond early fusion intermediates was showed in 2002 by Malinin and collaborators [53].

Most cases of membrane fusion actually necessitate proteins. These proteins possess specific structural features that allow them to interact with and modify lipid bilayers, often promoting membrane tethering, insertion into the lipid bilayer, and inducing fusion. Additionally, these proteins can undergo conformational changes triggered by various cues, such as changes in pH or the presence of other factors, to initiate fusion. The structures of these proteins and the mechanisms involved can vary depending on their localization within the cell and/or the specific organism to which they belong.

1.2.2 The example of SNARE fusion

Fusion serves as a significant mechanism that enables communication between various compartments within the cell, as discussed earlier. These various organelles can also communicate through the exchange of trafficking vesicles. Additionally, these vesicles facilitate communication between the cell and its surrounding environment. SNARE (soluble N-ethylmaleimide-sensitive factor attachment protein receptor) proteins have been identified as key elements to mediate fusion in the the trafficking steps of the secretory pathway [54]. SNARE proteins form a superfamily of small proteins with 25 members in *Saccharomyces cerevisiae*, 36 members in humans and 54 members in *Arabidopsis thaliana*.

A characteristic of the SNARE is the SNARE-motif, an evolutionary conserved stretch of 60–70 amino acids that are arranged in heptad repeats (HR). Their domain organisation is described in Figure 1.7A, and their crystal structure is in Figure 1.7B. The heptad repeats patterns consists of layers of hydrophobic and polar residues that contribute to the formation of coiled-coil structures. The coiled-coil structure allows SNARE proteins to interact with each other, bringing the membranes in close proximity and facilitating the fusion process. These hydrophobic layers contain an 'O' layer of three highly conserved glutamine (Q) residues and one highly conserved arginine (R) residue, classifying the contributing SNARE motifs into Qa-, Qb-, Qc- and R-SNAREs [55, 56]. In a functional SNARE fusion machinery, one of each of the four SNAREs is involved, with R-SNAREs situated on the vesicle membrane and Q-SNAREs located on the target membrane. In addition to the SNARE motifs, a transmembrane domain is often present at the C-terminal end, and independently folded domains are often located N-terminal to the SNARE motif. The latter domain often vary between subgroups of SNAREs.

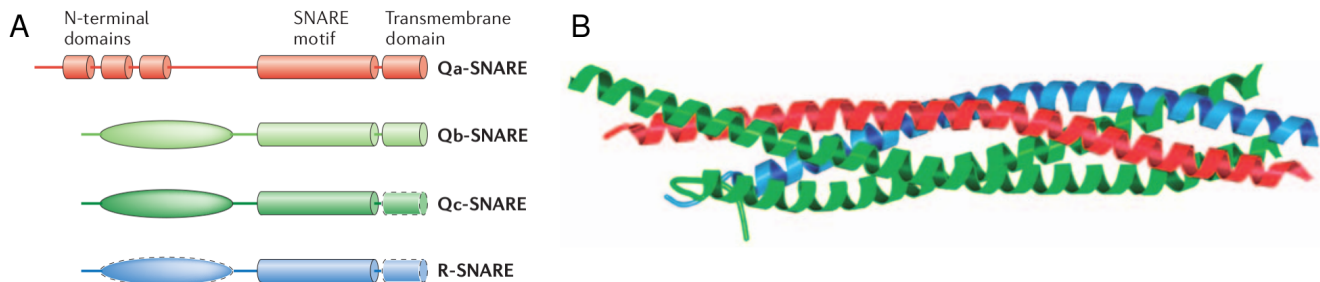


Figure 1.7: **Structures of SNARE.** (A) Schematic domain organisation of SNARE proteins. Dashed domain borders highlight domains that are missing in some subfamily members. Qa-SNAREs have N-terminal antiparallel three-helix bundles. The various N-terminal domains of Qb-, Qc- and R-SNAREs are represented by a basic oval shape. (B) Crystal structure of the SNARE motifs solved in 1998 [57]. (A), (B) Adapted from [58].

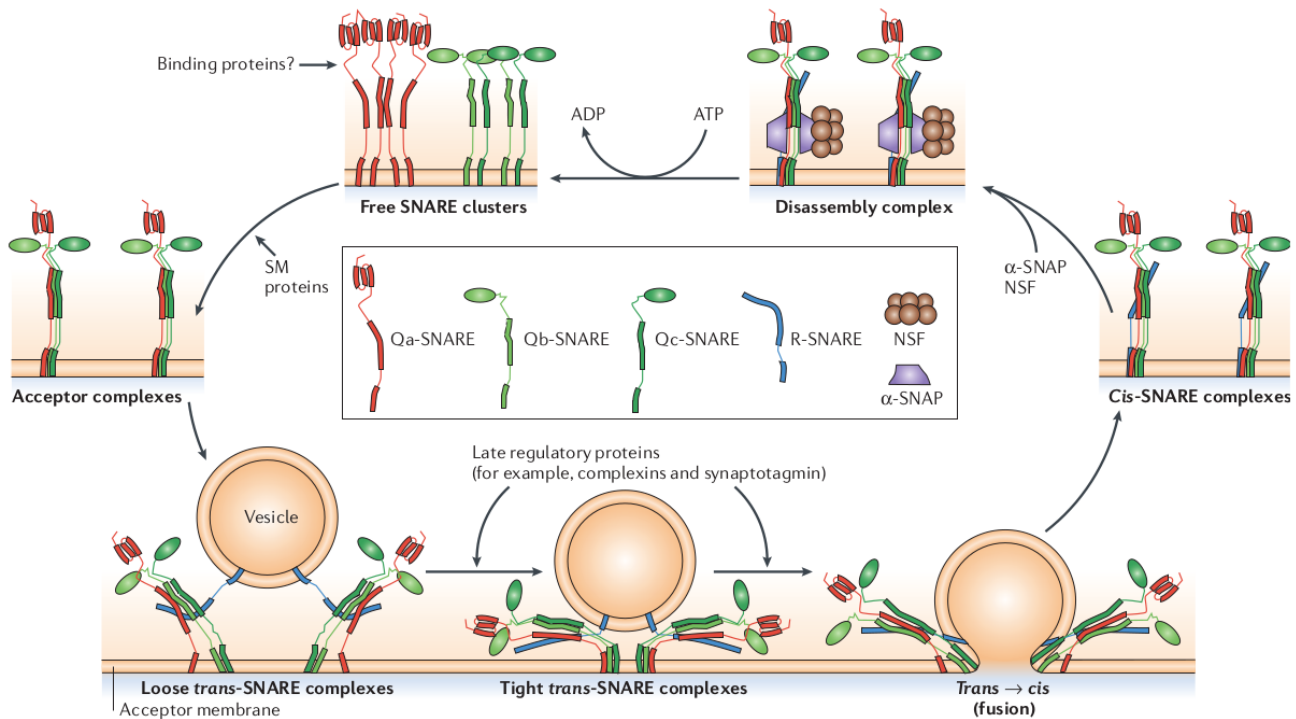


Figure 1.8: **SNARE conformation cycle during vesicle docking and membrane fusion.** Example considering three Q-SNAREs on an acceptor membrane and an R-SNARE on a vesicle. Taken from [58].

Free, meaning uncomplexed SNAREs (left top row, Figure 1.8), are constantly generated within the membrane [58]. These Q-SNAREs are free to interact with other Q-SNAREs in order to then dock and fuse vesicles. The uncomplexed SNAREs are then able to assemble through their SNARE motif, forming defined and partially helical Qabc intermediates (left middle row, Figure 1.8) [59]. This assembly process might require SM proteins. Acceptor complexes are then able to interact with R-SNAREs through the N-terminal SNARE motif. A first loose state is formed, which anchors the vesicle to the membrane, followed by a tight state, which leads to a close connection of the membranes that are destined to fuse, and initiates the membrane merger (bottom row Figure 1.8). A detailed SNARE membrane fusion mechanism can be seen in Figure 1.9. Following the membrane tethering phase through the tight trans-SNARE complexes, the stalk phase is stabilized, followed by the hemifusion diaphragm and the fusion pore. The initial trans-SNARE complexes are now in cis-configuration (right middle row Figure 1.8). These cis-SNARE complexes can be targeted by the NSF protein (N-ethylmaleimide-sensitive factor) together with SNAPs (soluble NSF attachment proteins) that function as cofactors (right top row, Figure 1.8), and will disassemble the cis-SNARE complex. The R- and Q-SNAREs are separated and sorted (for example, by endocytosis), and can now be recycled for other fusion processes [48, 58].

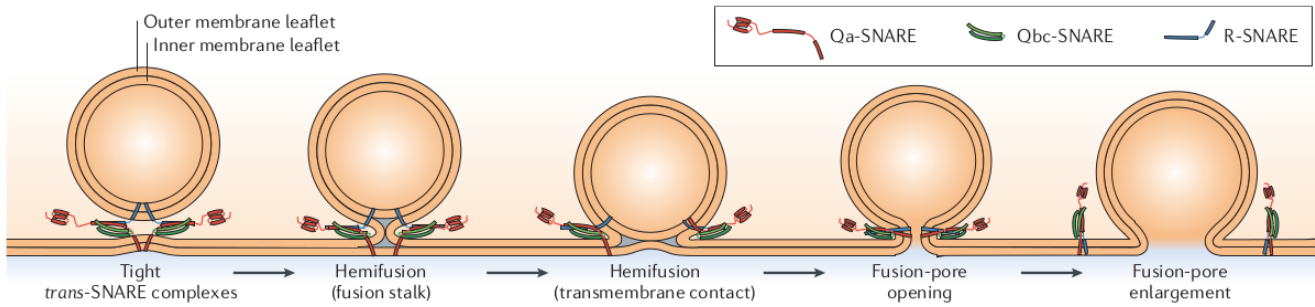


Figure 1.9: SNARE-mediated fusion according to the stalk hypothesis. Taken from [58].

1.2.3 Viral protein fusion

Another example of protein induced fusion, is viral protein fusion. The virus is able to bind then fuse with the host cell membrane, in order for the nucleocapsid to enter the cytoplasm [48]. The membrane fusion mechanism involving the binding of influenza hemagglutinin (HA) receptor is one of the most well-understood processes [60]. This single “universalist” protein mediate all steps of the fusion reaction, from the binding leading to close proximity of the membranes, to the fusion pore.

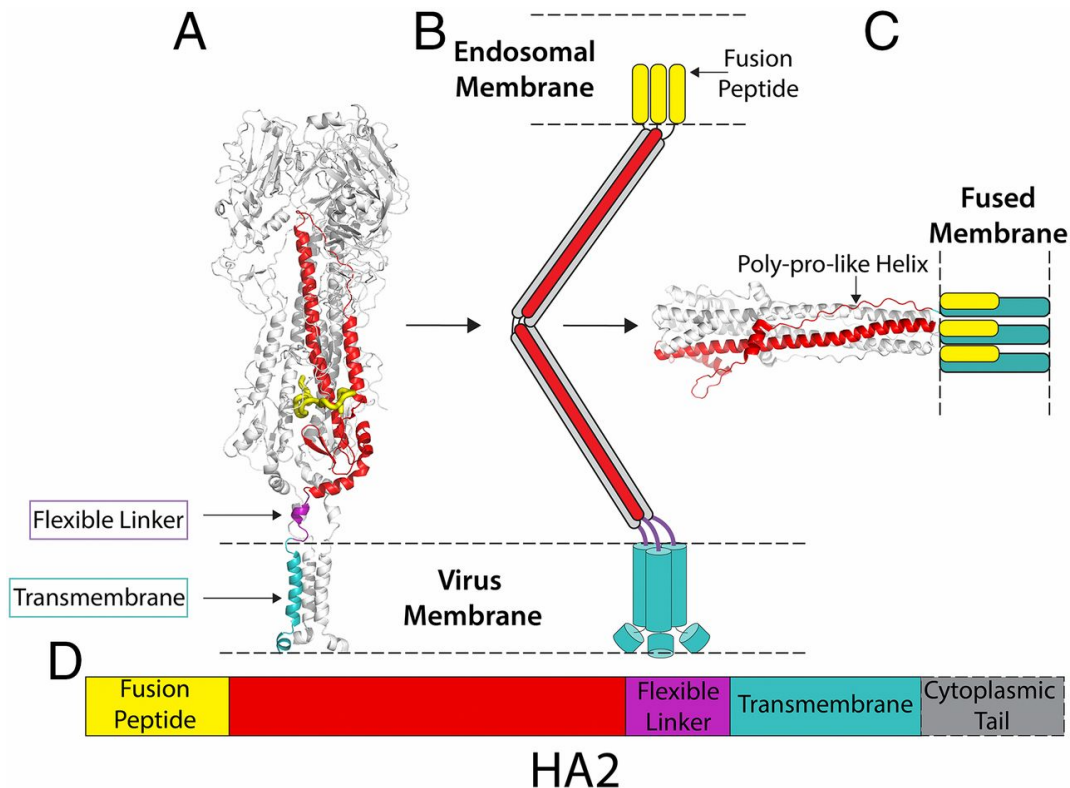


Figure 1.10: **Structural snapshots toward membrane fusion.** (A) The structure of straight full-length HA from cryo-EM. (B) Schematic representation of possible fusion intermediate. (C) The structure of fusion HA2, with modeled membrane anchor and fusion peptide colocalized in a fused membrane. (D) A color-coded diagram showing the location of the different regions of HA2 in its primary structure. Taken from [61].

Prior to the viral budding from its host cells, the fusion proteins undergo proteolytic cleavage, which leads to the formation of an N-terminal globular region and a metastable C-terminal segment (Figure 1.10). The fusion peptide is liberated from its buried position and exposed, towards the targeted membrane. The activated fusion peptide inserts into the hydrophobic interior of the target membrane. The fusion protein can have various fusion-activating conditions, such as low pH or high temperature [60, 62].

1.3 The membrane-remodeling properties of the dynamin superfamily proteins

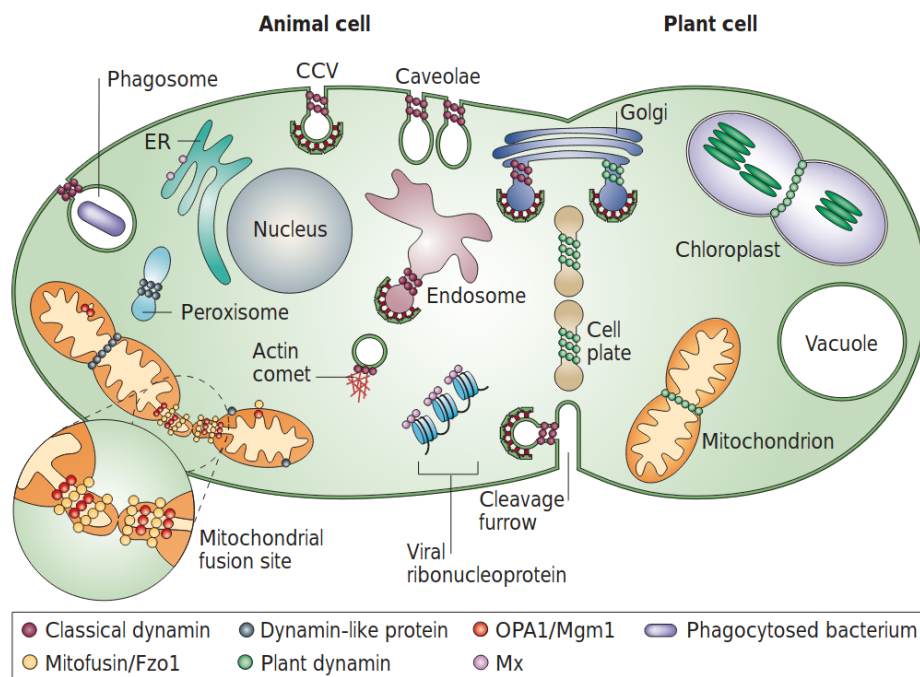


Figure 1.11: **Dynamin-superfamily members in animals and plants.** Classical dynamins (shown in maroon) are a group of dynamin proteins responsible for participating in various processes, including clathrin-coated vesicle (CCV) formation at the plasma membrane, cleavage furrow, Golgi, and endosomes. They are also involved in non-clathrin-mediated budding events at caveolae and phagosomes. In contrast, dynamin-related proteins encompass a broad spectrum of dynamin homologues. Dynamin-like proteins (depicted in grey) play a crucial role in the division of organelles like mitochondria and peroxisomes. The OPA1 family, represented in red, and the mitofusin family in yellow, contribute to the reorganization of mitochondria, particularly in processes related to mitochondrial fusion. As a result, they often counteract the functions of dynamin-like proteins. The Mx family, shown in pink, is typically induced by interferons and provides resistance against RNA viruses. Additionally, plants possess a variety of dynamin proteins, indicated in light green. While some of these plant dynamin proteins perform similar roles to their animal counterparts, such as participating in CCV budding, others have unique functions specific to plants, such as involvement in cell plate formation or chloroplast division. Taken from [63].

As described before, fusion and fission are essential mechanism for the survival of the cell. Just as SNAREs are established to be essential for vesicle-fusion mechanism, dynamins have an essential role in vesicle fission as well as organellar membrane-remodeling events or even whole-cell division (cytokinesis) [63, 64]. Furthermore, their functions can also be related to viral resistance, as members of this family exhibit membrane-dependent and membrane-independent activities [64].

Table 1.4: **Functions of dynamin-superfamily members.** Adapted from [64]

Cellular function	Protein (abbreviation)	Organism
Endocytic vesicle fission and intracellular vesicle trafficking	Dynamin 1-3 (Dyn1-3)	mammals
	Dynamin-related protein 1 (Drp1)	mammals
	Vacuolar protein sorting 1 (Vps1p)	yeast
	Dynamin-related protein 2A/B (DRP2A/B)	plants
	Dynamin-related protein 1A/E (DRP1A/E)	plants
Mitochondrial fission	Drp1	mammals
	Dyn2	mammals
	Dynamin-related GTPase (Dnm1p)	yeast
	DRP3A/B	plants
Mitochondrial fusion	Mitofusins 1/2 (Mfn1/2)	mammals (OM)
	Fuzzy onions 1 (Fzo1)	yeast (OM)
	Optic atrophy 1 (OPA1)	mammals (IM)
	Mitochondrial genome maintenance 1 (Mgm1p)	yeast (IM)
Peroxisomal fission	Drp1	mammals
	Dnm1p	yeast
	DRP3A	plants
	DRP5B (ARC5)	plants
ER tubule fusion	Atlastins (ATL1-3)	mammals
	Sey1p	yeast
	Root hair defective 3 (RHD3)	plants
Chloroplast division	DRP5B (ARC5)	plants
Cell division (cytokinesis)	Dyn2	mammals
	DRP1A-E	plants
	DRP5A	plants
Viral resistance	Myxovirus resistance A/B (MxA/B, 1/2)	mammals
	Guanylate binding proteins (GBPs)	mammals
	DRP4A-D	plants

Dynamins can be found ubiquitously across various cellular compartments (Figure 1.11, Table 1.4). Classical dynamins can be found participating in vesicle fission at the plasma membrane, cleavage furrow, Golgi and endosome (clathrin-coated vesicles), as well as at caveolae and phagosomes (non-clathrin-mediated budding events). Dynamin-like proteins, OPA1/Mgm1 and mitofusins are involved in mitochondrial and peroxysome reorganization. Plants contains many additional dynamins involved in membrane reorganisation, similar to those found in yeast and mammals, which functions on the membranes of mitochondria, CCVs but chloroplast and cell plate as well. The Mx family is a type of dynamins that is

not involved in membrane dynamic, as it is involved in the resistance against RNA viruses. Human MxA localizes to the smooth endoplasmic reticulum and also interacts with viral ribonucleoproteins.

1.3.1 Evolutionary conserved structural features of DSPs

Dynamins are characterized by their GTPase domain. However, the mere presence of a GTPase domain in a protein does not automatically classify it as a dynamin. The proteins of this superfamily are classified as 'large GTPases', which distinguish them from small Ras-like and other regulatory GTPases, such as the α -subunits of heterotrimeric G-proteins and translation factors of protein biosynthesis [63]. The larger GTPase domain as well as their oligomerization-dependent GTPase activation, their low GTP-binding affinities, the presence of additional domains and the ability of many members of the dynamin family to interact with lipid membranes are distinctive attributes of the dynamin superfamily. In fact, these protein also comprise a middle domain (MD) as well as a GTP effector domain (GED) that are involved in oligomerization and stimulation of GTPase activity. MD and GED are both part of an helical bundle called *stalk* and connected to the GTPase via the Bundle Signaling Element (BSE) [65]. The binding of phospholipids is facilitated by distinct structural elements positioned between the *stalk* helices. Classical dynamins employ a pleckstrin homology domain (PH) to bind to the membrane. In contrast, other dynamin-like proteins (DLPs) utilize different mechanisms, such as transmembrane helices (TM) or exposed loops (L4, helix 9), isoprenylation sites (CaaX), and paddle domains (Pad) [66] (Figure 1.13).

The dynamin GTPase domain is significantly larger (about 300 aa) than that of Ras-related GTPases (about 180 aa). This domain contain the GTP-binding motifs (G1-G4) that are needed for guanine-nucleotide binding and hydrolysis [67] (Figure 1.12). This binding ability gives another distinguishing feature to DSP, which is the capacity to homodimerize in a nucleotide-regulated manner [67], mediated in by interactions between the GTPase domain, the middle domain and the GED. One GTP molecule is bound per GTPase domain, with the sequences participating in the binding spread overall the domain. The G1 motif coordinates the phosphates, and the threonine in the G2 motif is involved in catalysis. The glycine in the G3 motif forms a hydrogen bond with the γ -phosphate of GTP. The less conserved G4 motif is involved in base and ribose coordination, through a conserved aspartate [67].

Atlastin	VSVAGAFRK GKS FLMDFMLRY	NEPL T GF S WR	AVLLM DTQ GTFDSQSTL	IFLVR DW
BDLP	LLVL GDMKR GKS TFLNALIGE	VN PCT AVLTV	GIEIV DSP GLNDTEARN	LVNA WDQ
Dynamin1	I AVVGGQ S AGK SSVLENFVGR	SGIV T RRPLV	NLTL V DLPGMTKVPVGD	VIT K LDL
EF1 α	IVVIGHV D SG K STTTGHLIYK	ERGI T IDISL	YVTI D APGHRDFIKNM	GVN K MDS
FZ01	VFIT G DVNT GKS ALCNSLLKQ	QL PCT NVFSE	DISL ID SPGLN MS LSLQT	V V KK F DK
GBP1	VAIV G LYRT GKS YLMNKLAKG	VQ SHT KGIWM	ILVLL D TEGLGDVEKGD	V W TL R DF
IIGP1	VAVT G ET G SG K SSFINTLRGI	GA A KTGVVEV	NVV F WDLPGIGSTNFPP	VRT K VDS
MFN1	V A FF G RT S SG K SSVINAMLWD	IG H IT N CFLS	DLV L V D SPGTDVTT E LD	L N NR W DA
MFN2	V A FF G RT S N G KSTVINAMLWD	IG H IT N CF L R	DLV L M D SPGIDVTT E LD	L N NR W DA
MX1	I A VI G DQ S SG K SSVLEALS G V	SGIV T RCPLV	DLT L ID L PGIT R VAVGN	IL T K P DL
OPA1	V V V G DQ S AG K T S VLEAMIAQA	GEM M T R SPVK	R M V L V D LP G VINTV T SG	V L T K V D L
	Gxxxx GKS T	T	Dxx G	NK x D T

Figure 1.12: **GTP-binding motifs.** The key residues are shown in orange. All sequences are for human proteins, except Fz01 which is the yeast *Saccharomyces cerevisiae* protein, BDLP is the bacteria *Nostoc punctiforme* protein, and IIGP1 is the mouse protein.

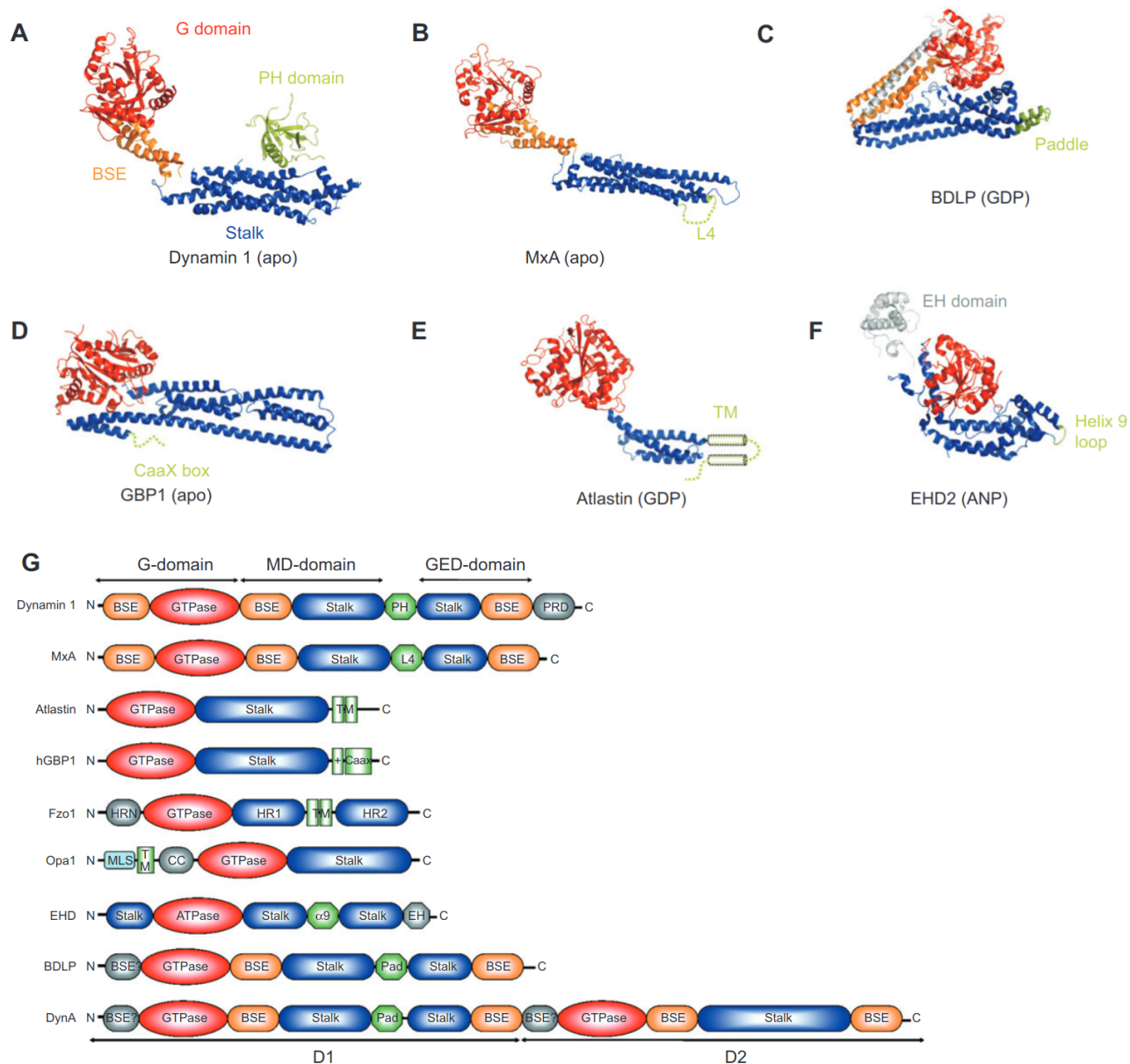


Figure 1.13: Modular architecture of dynamin family members. Dynamin (A, pdb code 3SNH), MxA (B, 3SZR), BDLP (C, 2J68), GBP1 (D, 1DG3), atlastin (E, 3Q5D), EHD2 (F, 2QPT). (A – F) display the modular organization of DSPs, highlighting the consistent domain arrangement they share. Present in all DSPs is the nucleotide-binding domain (referred to as the G domain and shown in red), a helical stalk domain (depicted in blue), and a lipid-binding module (illustrated in green). (G) Overview of the Modular Domain Structure. The conventional domain terminology is indicated above (comprising the G domain, MD, and GED domains). The lipid-binding elements encompass pleckstrin homology domains (PH), transmembrane helices (TM), or exposed loops (L4, helix 9), isoprenylation sites (CaaX), and paddle domains (Pad). The bundled signaling components are shown in orange (BSE). A unique instance is the bacterial DLP DynA, discovered in firmicutes, which is a fusion of two DLPs. Here, only the initial DLP domain (D1) contains a membrane-affiliated paddle domain. Mitofusins like Fzo1 are equipped with coiled-coil domains, potentially analogous to the stalk domains found in other DLPs. Opa1 features an N-terminal mitochondria localization signal (MLS) followed by a transmembrane helix. The coiled-coil motif (CC) within Opa1 might serve as bundled signaling elements (BSEs). Taken from [66].

Conformational reorganization play a crucial role in the functioning of dynamins. As a matter of fact, research has indicated that BDLP and other bacterial dynamin-like proteins undergo conformational changes [65, 68, 69], shifting from an 'open' extended conformation to a 'closed' constrained conformation. Considering the significant sequence and structural conservation of BDLP with the proteins Mfn1 and Fzo1, it is assumed that these mitochondrial fusion proteins undergo strong conformational changes as well. Similar shifts, from an elongated to a constricted conformation, have been observed for atlastins [70] and the yeast counterpart Sey1 [71], as well as for fission involved DSPs [72]. In fact, studies have demonstrated that conformational changes in Dnm1 [73] and Drp1 [74] lead to constriction of lipid tubes, thereby inducing membrane fission [75]. This change has been observed within the BSE, in a movement called a 'powerstroke' [76, 77]. Such a movement has also been observed for the antiviral protein MxA [78]. The transition from one state to the other has been shown to be driven by either GTP binding, GTP hydrolysis, membrane binding, or the process of dimerization itself, depending on the DSP [77].

1.3.2 Bacterial dynamin-like proteins bears striking similarities with mitofusins

Bacterial dynamins, referred to as bacterial dynamin-like proteins (BDLPs), are a group of proteins present in bacteria that exhibit both structural and functional similarities to eukaryotic dynamins. In fact, numerous bacterial species harbor genes encoding dynamin-like proteins, which share the closest resemblance to the Fzo1/mitofusins class of dynamins (in charge of OM fusion) [65, 1]. Numerous bacterial species, such as *N. punctiforme*, possess multiple dynamin genes, often found arranged in tandem. This genomic organization suggests a close functional relationship between the genes, with some species even having a fusion of two dynamin genes containing two GTPase domains.

A noteworthy example of such a two-headed bacterial dynamin is the protein encoded by the *ypbR* locus in *Bacillus subtilis*, which is referred to as DynA (Figure 1.13G). The protein is composed of two main subunits D1 and D2 and was shown to tether to membranes, through the D1 subunit [79], but optimal activity was only achieved with the full length protein [80]. The subunit was demonstrated to promote GTP-independent fusion as well. During these processes, GTP hydrolysis may not be necessary to provide the energy for fusion through mechanical force. Instead, GTP likely serves a regulatory role, determining whether and how a dynamin complex tethers membranes and transitions into its fusogenic state [79]. Moreover, recent findings appear to support the role of DynA in membrane surveillance and protection against pore-forming agents [80].

Because of the evolutionary connection between mitochondria and bacteria, along with the similarities observed between DynA and mitofusins, there is speculation that the mitofusin family originated from an ancestor present in the protomitochondrion [81].

The *N. punctiforme* BDLP mediates protein curvature

N. punctiforme has a bacterial dynamin-like protein referred to as BDLP, which structure has been solved first in 2006 [65]. This protein, shown to be interacting with membranes, is composed of a GTPase

domain, as well as stalk and BSE domains, sharing a similar domain architecture with mitofusins (Figure 1.13C,G). Indeed, stalk and BSE are structurally organized as coiled-coil, similar to the heptad repeat domains of mitofusins (PDB ID: 1T3J [82]). BDLP possess a membrane binding domain called a paddle (Figure 1.13C,G). Contrary to the transmembrane domains of mitofusins, the paddle domain is only able to interact with one of the two leaflets, and does not span through the entire membrane. The protein is in fact highly soluble in solution without detergent [65]. The closed compact monomeric and dimeric structures can be seen in Figure 1.14 [65]. A nucleotide-free structure can also be observed (Figure 1.14), showing a significant conformational changes with respect to the GDP-binding state : (i) the active site within the GTPase domain rearranges, (ii) the helices 15, 16 and 17 (resid 412–449) realign with the paddle domain when the nucleotide is released, as they were formerly perpendicular to the paddle domain.

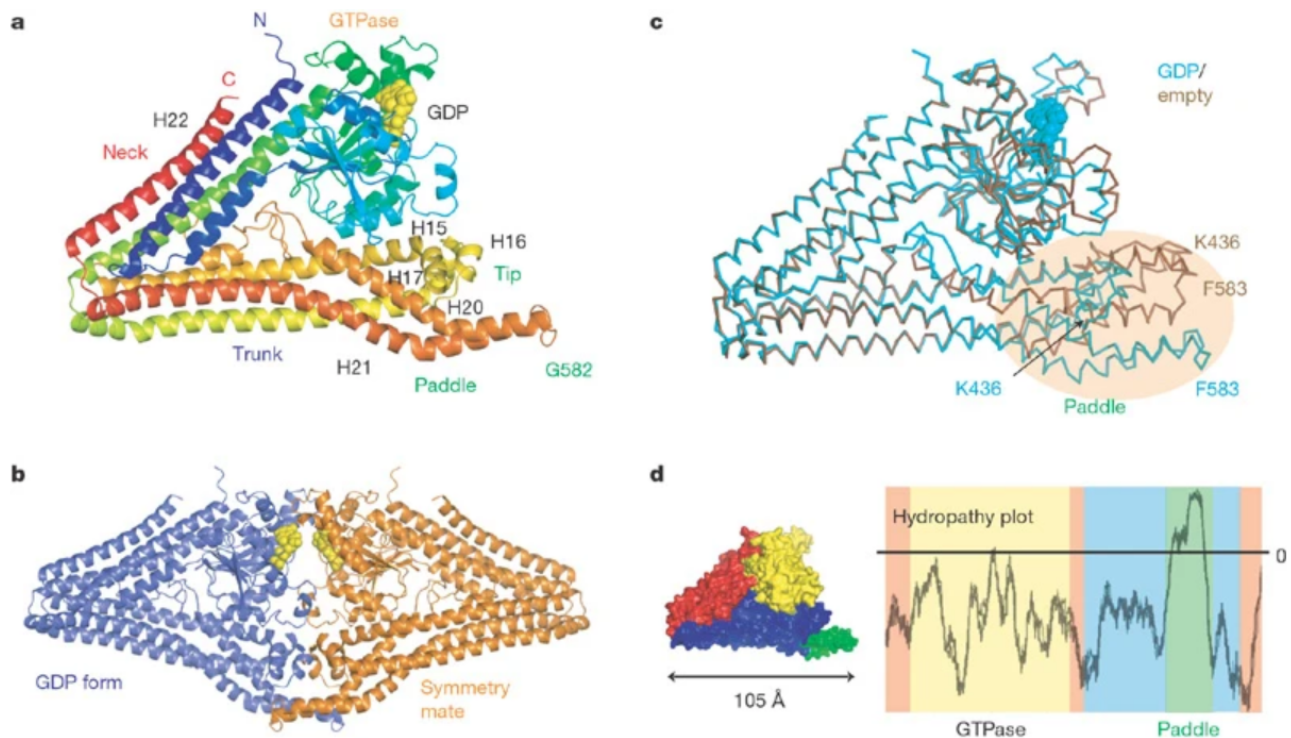


Figure 1.14: Crystal structures of BDLP in GDP-associated and nucleotide-free conformations. (a) The BDLP-GDP monomer colored as function of the domain assignment. The monomer is rainbow-coloured from the N (blue) to the C (red) terminus. (b) GDP binding promotes homodimerization. (c) Main chain superposition showing structural reorganization between the GDP-bound and nucleotide-free states. Note the significant conformational change at the paddle domain. (d) Surface plot of the GDP monomer coloured as a function of the main regions: yellow, GTPase domain; red, neck region; blue, trunk region; green, paddle region (left). Similarly colour-coded hydropathy plot (TMpred) strongly predicts that the paddle region (residues 572–606) is transmembrane (right). Taken from [65].

As described for other dynamins, the dimeric version of BDLP structure shows interactions between the two GTPase domains forming a compact diamond-shaped [65]. However, as the paddle domain is not

bound and anchored to a membrane, we observe interactions involving this domain. In this conformation, BDLP is probably unable to bind to membranes, which suggests an important intramolecular rearrangement on which the region between *neck* and *trunk* acts as a hinge that opens and markedly extends the molecule on GTP or lipid binding.

It is still complicated to determine the biological role of BDLP. However, cryo-EM reconstruction (Figure 1.15) shows compatibility with the hypothesis that BDLP controls the lipid curvature in an second open elongated conformation [68]. In this work, it is shown that BDLP forms a tightly packed helical surface coating (50 nm diameter) (Figure 1.15B) around a lipid tube (Figure 1.15A). The protein seems to be involved in membrane shaping functions.

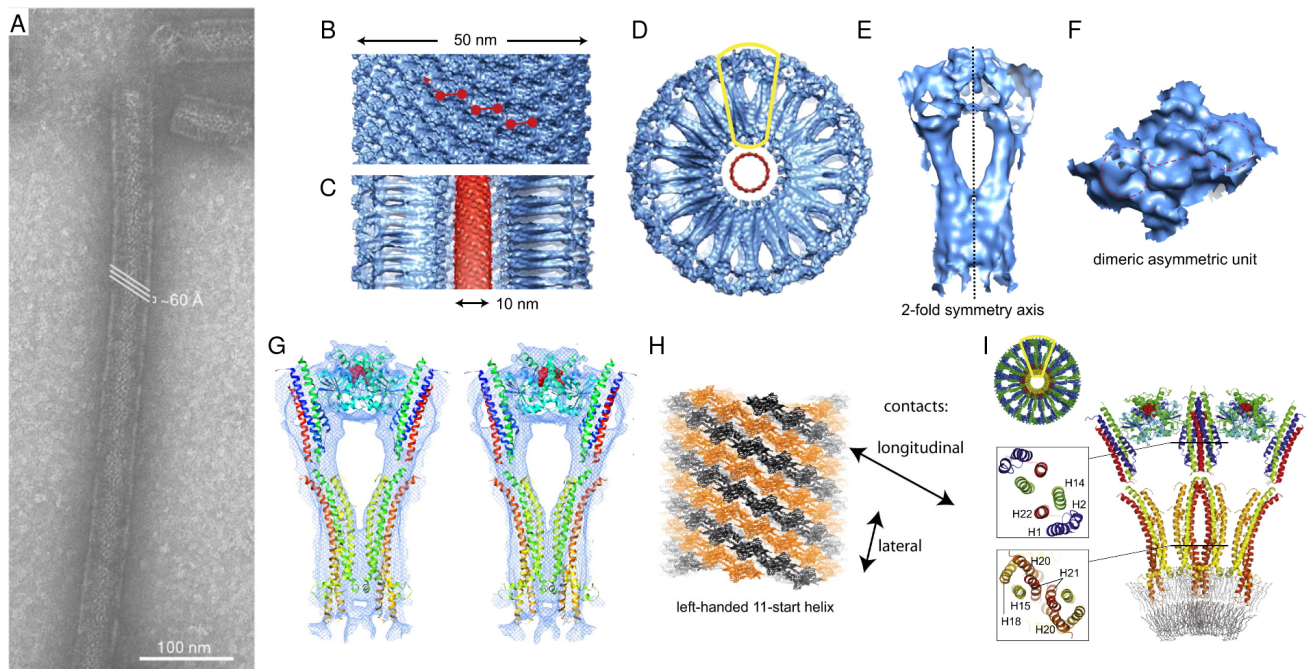


Figure 1.15: BDLP is a GTPase capable of decorating and tubulating liposomes. (A) BDLP tubulating *E. coli* lipid liposomes. Taken from [65] (B) Density surface overview of the native BDLP tube reconstruction. Red dumbbells show zigzag arrangement of the dimeric asymmetric unit. (C) As in (B), but sliced along the tube axis exposing the globular outer layer, inner radial spokes, and lipid tube core (red). (D) As in (B), but showing the tube in cross-section to the helix axis. The lipid core is in red. (E) Close-up view of region outlined in yellow in (D), showing surface detailing of the asymmetric unit and two-fold symmetry. (F) As in (B), but a close-up view of the asymmetric unit showing surface detail. (G) Close-up stereo image of region outlined in yellow in (D), showing the fit of two BDLP molecules that form the dimeric asymmetric unit of the reconstruction. (H) Molecular interpretation of the images in (A) and (B), showing the longitudinal 11-start left-handed rise. (I) Model of the helical BDLP filament in cross-section to the helix axis showing a fitted lipid bilayer. A standard outer leaflet (5 nm bilayer thickness) is modeled for size comparison only. Shown close up are protein-protein contacts between a pair of asymmetric units. The focus is on interaction between the central neighboring *neck* and *trunk* helices. From (B) to (I), taken from [68].

The compact structure of BDLP-GDP bound [65] does not fit the elongated shape in Figure 1.15D,E

which means that the first solved structure need to be adapted to the latter shape (Figure 1.15G) [68]. Two pairs of chain breaks in the model : a first pair at helices 13/14 Asp360 and helices 21/22 at Arg656, and another at Gly68 and Gly309 located at the interface between the *neck* and the GTPase domain (Figure 1.16). The outcome of this process yields distinct GTPase, *neck*, and *trunk* domains, which can be fitted into the density as rigid bodies, with little demand for further adjustment to the atomic model (location of the *neck* and *trunk* in the compact structure can be seen in Figure 1.14d). The dimer of two open conformation BDLP shows dimerization through the GTPase domains, as well as proximity between the *trunks* (Figure 1.15G). Furthermore, the molecular interpretation of the packed helical coating of BDLPs in Figure 1.15B, 1.15H and 1.15I, shows that the coiled-coil domains can also be involved in the interactions between the BDLP monomers forming the surface coating.

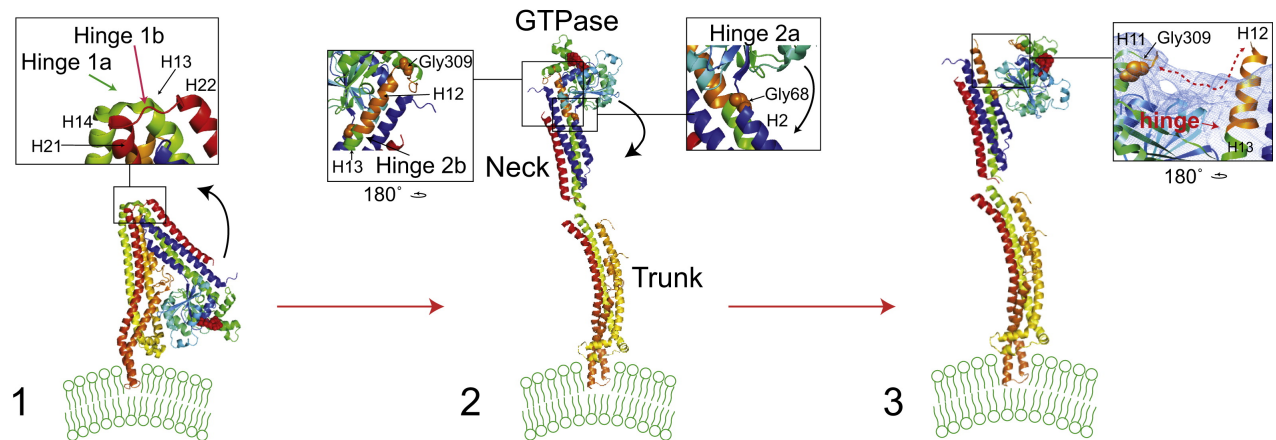


Figure 1.16: The GTP and Lipid-Induced Conformation Changes. A three-step conformational transition between the closed conformation [65] and the open conformation model [68]. The sequence of domain rearrangements is unknown and shown arbitrarily. Two movements are involved, first involving hinges 1a and 1b, then the reorganization of the GTPase domain involving hinges 2a and 2. Taken from [68].

From these two studies [65, 68] hypothesis of the function of BDLP and its mechanism were drawn (Figure 1.17). In solution BDLP probably exists as a dimer as seen in Figure 1.14. Binding to GTP probably triggers conformational changes in concert with the insertion of the paddle domain in the outer leaflet of the membrane. The protein is now able to polymerize on the surface of the membrane resulting in a coated lipid bilayer (Figure 1.15). Once a sufficient number of proteins are assembled, the accumulation of binding energy forces the membrane into significantly higher curvature, resulting in the formation of narrow tubes. Subsequently, GTP is hydrolyzed which induces instability in the structure, followed by depolymerization of the entire protein coat. The lipid bilayers remain in an energetically unfavorable state. There are three possible scenarios to alleviate this transition state (Figure 1.17A) : (i) the system relaxes, going back to the initial state; (ii) membrane fission occurs; (iii) if membranes belong to different surfaces, fusion occurs (side view in Figure 1.17B).

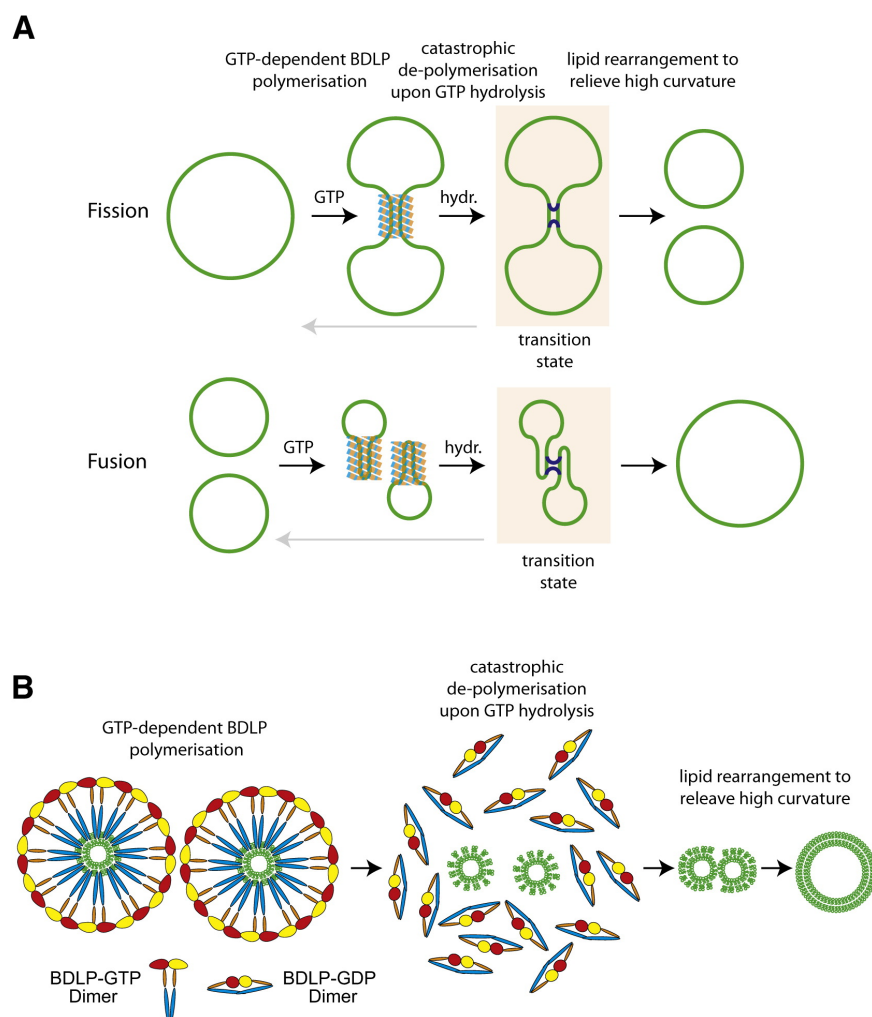


Figure 1.17: Hypothesis of a polymerization/depolymerization model for fusion and fission. (A) Diagram illustrating the distinct phases of BDLP/dynamin-mediated fission and fusion. The assembly process is triggered by GTP binding, leading to a substantial increase in curvature. Upon hydrolysis to GDP, there's a disruptive disassembly phase, resulting in a transition state. This state can either revert to the initial state (indicated by the gray arrow) or progress by rearranging the membrane connections (depicted in blue). When these membranes are part of the same surface, this leads to fission. In cases where the membranes are associated with two distinct surfaces (such as two vesicles), the outcome is fusion. (B) A more intricate illustration of the same model as depicted in (A), viewed from a lateral perspective. The tubulation process induces significant curvature by inserting the paddle into the outer leaflet through the pure displacement of lipids and/or compression of the lipid tails. Following disassembly, this leaves the bilayer in an unstable condition, which can be resolved by merging two (or more) structures into one, resulting in reduced curvature. Taken from [68].

1.4 Mitofusins are key players of outer mitochondrial fusion

Mitochondrial membranes dynamics are managed by members of the dynamin-superfamily (Table 1.4). Due to its unique double-membrane structure, the fission and fusion processes of mitochondria are more complex compared to those of the plasma membrane and other organelles. The intricate interplay be-

tween the inner and outer mitochondrial membranes during fission and fusion requires a coordinated regulation of various proteins and factors to ensure the proper functioning and dynamics of these essential organelles.

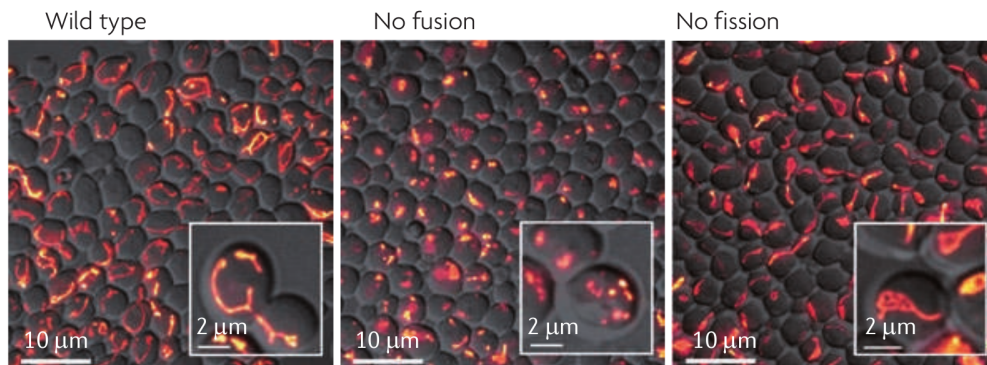


Figure 1.18: **Regulation of mitochondrial morphology through fusion and fission.** In budding yeast, mitochondria appear as branched and tubular organelles (shown in the left panel). However, in mutants where the fusion component Fzo1 is absent, multiple small mitochondrial fragments are observed. These fragments result from mitochondrial fission occurring in the absence of fusion, as depicted in the central panel. In contrast, mutants lacking the fission component Dnm1 exhibit a network-like structure of highly interconnected mitochondria (depicted in the right panel). Taken from [3].

1.4.1 Mitochondrial dynamics machinery

Mitochondrial fission machinery

The fission of mitochondria is primarily carried out by the dynamin-related protein 1 (DRP1) in mammals and Dnm1 in yeast (Figures 1.19 and 1.20). Cells lacking the protein have a highly interconnected mitochondrial network, formed by ongoing fusion in the absence of fission activity. The protein is soluble and comprises an N-terminal GTPase, a middle domain, and a C-terminal GTPase effector domain, all of which participate in its self-assembly process (Figure 1.20). When fission starts (in mammals), the protein is recruited by one of the following receptors, causing it to translocate from the cytosol to the outer membrane (OM) : mitochondrial fission factor (MFF), mitochondrial dynamics protein of 49 kDa (MID49), MID51 and mitochondrial fission 1 protein (FIS1) [83]. After binding, DRP1 undergoes oligomerization, which leads to formation of linear polymers on the OM stabilized by the interaction with the receptors. In yeast, Fis1 (Figure 1.20) primarily acts as a recruiter for Dnm1, facilitating its attachment to the mitochondrial membrane. This recruitment does not involve a direct interaction between Fis1 and Dnm1; instead, it is mediated by Mdv1 and Caf4, two proteins that lack mammalian homologs [84].

It is important to note at this stage that mitochondrial fission occurs in the vicinity of the smooth ER, which wraps around mitochondria (Figure 1.19) [85]. At contact sites between ER and mitochondria, DRP1 collaborates with actin-nucleating proteins (inverted formin 2 (INF2), and formin-binding protein spire 1C) leading to the accumulation of actin, which precedes DRP1 recruitment to sites of fission.

Assisted by the initial accumulation of actin filaments, DRP1 undergoes oligomerization and initiates membrane constriction through GTP hydrolysis, ultimately resulting in mitochondrial fission [86, 87].

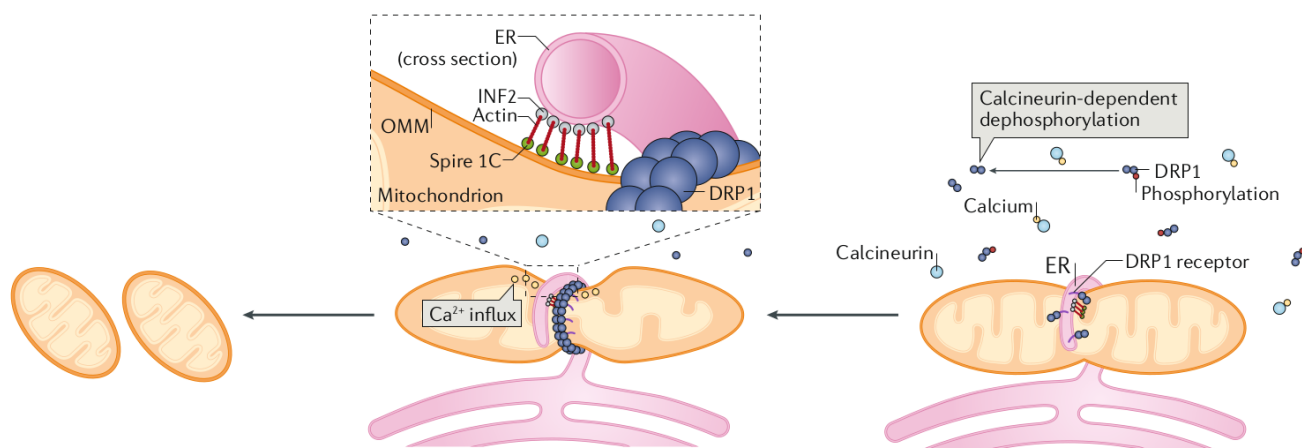


Figure 1.19: **Mitochondrial fission.** Mitochondrial fission is primarily regulated by dynamin-related protein 1 (DRP1). Fission is initiated by the dephosphorylation of DRP1 by calcineurin, leading to its recruitment to the mitochondrial surface, where it binds to its specific receptors. This recruitment often occurs at regions where the endoplasmic reticulum (ER) wraps around the mitochondria. Once recruited, DRP1 undergoes oligomerization and initiates membrane constriction through GTP hydrolysis. The process is further supported by actin polymerization at the interface between the ER and mitochondria, a process facilitated by the actin-nucleating proteins INF2 and spire 1C. The accumulation of actin filaments can drive the initial constriction of mitochondria, thus facilitating subsequent DRP1 polymerization. Adapted from [45].

The described mechanism only involves the OM. However, our understanding of inner membrane (IM) fission remains limited. It is proposed that after GTP hydrolysis, constriction of dnm1 spirals may subsequently lead to the simultaneous severing of both mitochondrial membranes [3]. However, a separate machinery for constriction and/or division cannot be excluded. Possible candidates are Mdm33 in yeast [88], and MTP18 in mammals [89]. However, their implication in IM and mitochondrial fission is still debated [90].

Mitochondrial fusion machinery

As mitochondria are composed of two membranes OM and IM, the fusion process involves four membranes in total. The first membrane involved in the process is the OM, followed by the fusion of the IM.

As mentioned before, the large GTPase family involved in the tethering and fusion of the OM are transmembrane proteins called mitofusins [91] (Figure 1.20). The first known mediator of mitochondrial fusion was discovered in 1997 through molecular genetic analysis of the male sterile fuzzy onions (fzo) mutant in *Drosophila melanogaster* [92]. This protein is the founding member of a conserved protein family, termed mitofusins, that has members in yeast [93, 94], worms [95] and mammals [96]. The mam-

malian mitofusins are Mfn1 and Mfn2 [97, 98]. Mitofusins in yeast and mammals exhibit a comparable domain structure. Being part of the dynamin superfamily, they are equipped with a large GTPase domain, but are also composed of two transmembrane regions embedded in the OM, and multiple heptad repeat (HR) domains. Mammal mitofusins Mfn1 and Mfn2 have two HR domains, whereas the yeast mitofusin Fzo1 contains one more, placed at the N-terminal section of the protein (Figure 1.13). These proteins feature a short loop in the intermembrane space, while the majority of the protein faces the cytosol [99, 98].

The IM fusion is involving other sets of dynamin related proteins. In yeast, the large GTPase Mgm1 (Figure 1.20) is required for inner membrane tethering and fusion, as well as cristae organisation [100]. It possesses an N-terminal mitochondrial targeting sequence that is cleaved by matrix-processing peptidase (MPP) upon import. A large Mgm1 isoform consists of an N-terminal transmembrane domain, which anchors the protein in the inner membrane, while the major portion is located in the intermembrane space. A subset of Mgm1 molecules undergoes further processing during import by the rhomboid-related membrane protease Pcp1, resulting in a short isoform lacking the transmembrane anchor. In both isoforms a GTPase domain, a GTPase effector domain and several heptad repeats can be found [101]. The mammalian orthologue of mgm1 is the optic atrophy protein 1 (OPA1) [102] (Figure 1.20). OPA1 exists in eight isoforms, which are produced through alternative splicing and alternative processing at two cleavage sites situated between the N-terminal transmembrane domain and the first heptad repeat [103]. Furthermore the structure of OPA1 was recently solved using cryoEM [104, 105], showing the DLP-like structure of the molecule (presence of a stalk, BSE and membrane interacting domain) and suggesting rearrangement of the structure during the IM fusion process.

When inner membrane fusion is hindered (by mutating OPA1 or Mgm1 for example), outer membrane fusion can still proceed independently of inner membrane fusion. This suggests that the fusion machineries in the mitochondrial outer and inner membranes can operate separately from one another. However, there is substantial evidence indicating that mitofusins interact with the fusion machinery within the inner mitochondrial membrane (IM). Indeed, a functional link between factors involved in OM and IM fusion is not unexpected, as these processes are coordinated. Yeast mutants with insertions between the transmembrane regions of Fzo1 exhibit a distinct loss of Fzo1 interactions with the inner membrane, leading to significant deficiencies in mitochondrial fusion [99]. Therefore, the intermembrane space loop of Fzo1 plays a crucial role in coordinating double-membrane fusion [99]. Indeed, studies have demonstrated a strong association of Mgm1 with Fzo1. Furthermore, it has been proposed that the absence of Mgm1 leads to a modified conformation of Fzo1, as suggested by Wong et al. [106]. Similarly, a possible functional dependence between Mfn1 and Opa1 was noted as in cells deficient in Mfn1, OPA1 could promote mitochondrial fusion [102]. This observation is potentially supported by a proposed topology for human mitofusins, proposing that the C-terminal end is exposed to the mitochondrial intermembrane space (IMS) [107].

In yeast exists Ugo1, a 58 kDa protein, which is embedded in the OM, with its N-terminal end

facing the cytosol and the C-terminal facing the intermembrane space (IMS) [108]. It has been suggested that Ugo1 plays a coordinating role in OM and IM fusion, as it can interact with both Fzo1 and Mgm1, creating a scaffold for the assembly of a fusion complex [109]. Further studies have demonstrated Ugo1's involvement in both outer and inner membrane fusion [110], as well as interactions with Fzo1 [106, 109], further emphasising the contacts between OM and IM through the fusion machinery of the organelle. Interestingly, no equivalent of Ugo1 protein has been identified in mammals. However, the exposure of the human mitofusin to the IMS [107] could potentially compensate for the absence of Ugo1 in humans, as discussed previously [111].

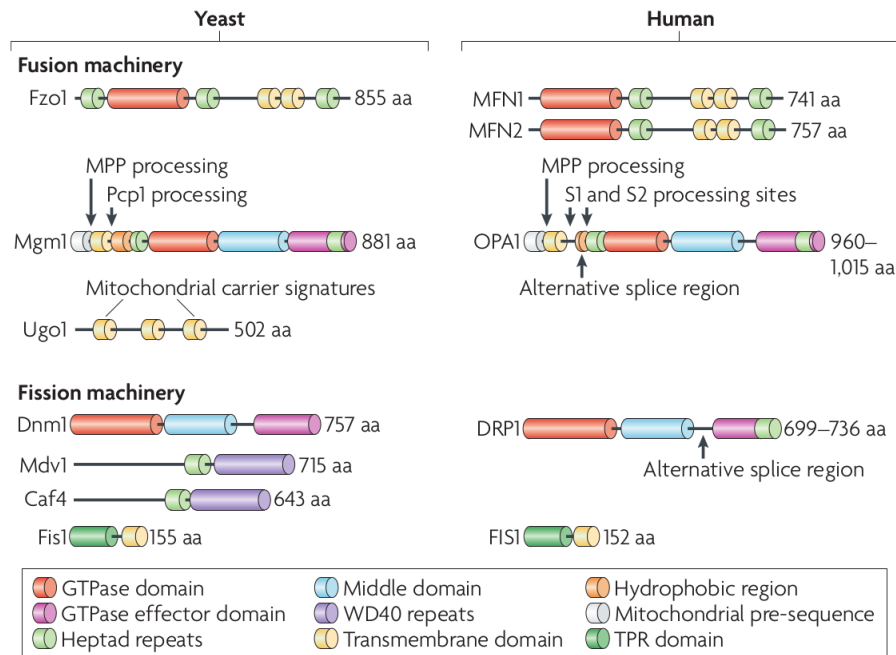


Figure 1.20: Domain structures of mitochondrial fusion and fission components. The core components of the mitochondrial fusion machinery in yeast are Fzo1 and mitofusins MFN1 and MFN2 in mammals for the outer membrane ; and Mgm1 in yeast and optic atrophy protein 1 (OPA1) in mammals for the inner membrane. These proteins are connected by the yeast-specific outer membrane protein Ugo1. The soluble protein Dnm1 (dynamin-related protein 1 (DRP1) in mammals) is recruited to mitochondria by the outer membrane protein mitochondrial fission 1 (Fis1; FIS1 in mammals). Two yeast-specific proteins, mitochondrial division protein 1 (Mdv1) and Caf4, serve as adaptors. The lengths of the yeast and human proteins (numbers of amino acids) and important processing and splice sites are indicated. Matrix-processing peptidase (MPP) removes matrix-targeting sequences following import; Pcp1 is a membrane protease involved in alternative processing of Mgm1; OPA1 is processed by different proteases, at two sites S1 and S2. Proteins are not drawn to scale. TPR, tetratricopeptide repeat. Taken from [3].

Mitofusins and membrane interactions with other organelles

The OM plays a vital role in cellular operations. Notably, it serves as a hub for signaling processes and is engaged in an extensive network of interactions with various other cellular compartments, establishing membrane contact sites [45], as described earlier in Figure 1.5 and section 1.1.3 of the Introduction. In

fact, while their primary role is related to mitochondrial fusion and regulation of mitochondrial morphology, there is evidence suggesting that mitofusins may have secondary roles.

As mentioned before, the best studied interaction would be between mitochondria and ER. We have already mentioned that mitochondrial fission spatially localizes at sites of proximity to the ER [85] (Section 1.4.1), involving the mitochondrial fission machinery in the tethering process. For instance, the presumed DRP1 receptor, FIS1, plays a role in regulating connections with the ER [112]. However, the two organelle have also their membranes tethered by protein bridges involving mitofusins, establishing mitochondria–ER contact sites (MERCs) [113]. Among the proteins involved, the mitofusin Mfn2 has been described as a key MERC tether, which homo-oligomerize as the protein is both embedded in ER and the OM (there have been descriptions of hetero-oligomer tethering between MFN2 and MFN1 as well) [113, 114, 45].

Interactions between mitochondria and plasma membranes as well have been observed in mammary stem cells. This connection is achieved through the interaction between MFN1 and a pool of protein kinase C isoform- ζ localized at the plasma membrane [115]. Mfn2 plays a role in mitochondria-plasma interactions as well [116], as it is involved in the regulation of Ca²⁺ influx from the extracellular medium.

Finally, the last noted interaction with organelles involving mitofusins is the mitochondria-peroxisome interactions. As a matter of fact, the two organelle share metabolic processes (such as β -oxidation of fatty acids and bile acid synthesis), as well as division machinery components (DRP1, MFF and FIS1) [47]. When it comes to membrane interactions, Fzo1 has been noted to serve as a tether for peroxisomes and mitochondria in yeast [46], paralleling Mfn2 tethering with ER. Similar to other mitochondrial protein such as Fis1, Fzo1 was found to be co-localized with peroxisome [46]. Hence, it was suggested that tethering was mediated by homotypic interactions between mitochondrial Fzo1 and peroxisomal Fzo1. However interactions between the protein and another set of proteins on the peroxisome could not be excluded.

1.4.2 The role of mitofusins in mitochondrial dysfunction and associated pathologies

Mitochondrial fusion dysfunction is related to several neurodegenerative disorders, such as Parkinson, Alzheimer and Huntington diseases [117, 118]. As a matter of fact, research has shown that mutations in Mfn2 induce the development and progression of muscular dystrophies, such as Charcot-Marie-Tooth Type 2A, the most common form of axonal CMT disease [119, 120]. This syndrome affects the peripheral nerves and is characterised by muscle weakness, hyporeflexia and sensory loss in the lower limbs [121, 122]. The exact mechanism by which the mitofusins contributes to mitochondria dysfunction as well as the exact molecular fusion mechanism is not fully understood yet. Overall, mitochondrial fusion plays an important role in CMT2A, it is thus of paramount importance to get a full understanding of the process at the molecular level.

Moreover, mitochondrial disorder can also cause cancer [123] and it has been shown that mitochondria could be a target for cancer therapy [124, 125]. Metabolic changes in mitochondria induced by mitofusins mutants or their loss of activity seem to participate in the development of certain types of cancer [126], making mitofusins a suitable candidate as a target for cancer treatment. As a matter of fact, recent research has shown that specifically Mfn 1 and Mfn2 may also play a role in the development and progression of cancer. Studies have found that Mfn1 and Mfn2 are often linked to various types of cancer, including breast [127], liver [128], lung [129], cervical [130] and colon cancer [131], and that their dysregulated expression is associated with increased cell proliferation, invasion, and resistance to chemotherapy. Regulating the activity of mitofusins has been shown to reduce the growth and spread of cancer cells in preclinical studies. Therefore, mitofusins are considered promising targets for cancer therapy [127, 128, 129, 130, 131]. However, these therapies will have to cater to the specific cancer treated as each might benefit from different states of the mitochondrial network [132]. Interestingly, it was shown in liver cancer's case [128] that inhibition of mitochondrial fusion triggered apoptosis in the cancerous cells.

1.4.3 Mitofusins share structural similarities with the dynamin superfamily

Mitofusins topology and domains composition

Such as other members of the dynamin superfamily, mitofusins are characterized by three distinct structural domains [133]. The first one is the GTPase domain characterized by low nucleotide affinity, and which binds and hydrolyzes GTP. The two other structural domains are helical bundles, paralleling the *neck* (or BSE domain) and the *trunk* (or stalk) found in BDLP and described in section 1.3.2 of the Introduction. Furthermore, mitofusins have their *neck* and *trunk* region containing two heptad repeat (HR) domains, HR1 and HR2 (see Fzo1 in Figure 1.13G, and Mfn1/2 in Figure 1.21). In yeast, Fzo1 possesses a third homologous region (referred to as HRN), situated at the N-terminal position relative to the GTPase domain [1].

In addition to the previously mentioned domains, mitofusins also possess domains involved in interactions with lipids. This domain is frequently observed in dynamins, often taking the form of pleckstrin homology (PH) domains, transmembrane (TM) domains, or a paddle region (Figure 1.13G). Indeed, the yeast mitofusin Fzo1 was found to contain two transmembrane helices, spanning the OM twice and exposing both the N- and C-terminals of the protein in the cytosolic region, as supported by studies such as Fritz et al. (2001) [99] and Rojo et al. (2002) [98]. Subsequently, this domain configuration was also confirmed for the human orthologues [96, 82, 134]. However, this representation is challenged for the human mitofusins, where Mattie et al. (2018) [107], proposed a single TM domain exposing the protein C-terminal to the mitochondrial IMS. Consequently, it remains feasible for humans and other vertebrates to potentially exhibit two distinct topological arrangements, as suggested by Cohen and Tareste in 2018 [111].

Experiments conducted on the different domains revealed specific properties linked to each of them.

The heptad repeat (HR) domains were indeed subjected to thorough investigation. These hydrophobic HR motifs are predicted to adopt coiled-coil structures [62] and are believed to have a pivotal role in tethering two mitochondria during the docking phase preceding fusion [82, 135]. Such HRs were shown to be crucial for the fusion process of various proteins such as viral fusion proteins [60] and SNAREs [55, 56, 136]. In the case of mitofusins, Mfn1 HR1 domain promotes bilayer fusion [135], possibly by inducing instability in the lipid bilayer and generating lipid packing defects. The HR2 domain has also undergone detailed examination, with structural data (PDB: 1T3J [82]) revealing two HR2 region forming an antiparallel coiled-coil structure spanning a length of 9.5 nm [82]. From this discovery it was hypothesized that this domain would mediate tethering of mitochondria, supported by the extensive aggregation of mitochondria in a HR2-dependent manner observed when the GTPase domain was removed [82]. Electron microscopy of these aggregated mitochondria revealed a 16nm between opposing OMs [82], while electron cryo-tomography of mitochondria isolated from *Saccharomyces cerevisiae* revealed an approximate 8 nm gap between the outer membranes [137]. Finally, it is also interesting to note that the topology proposed by Mattie et al. (2018) for Mfn1/2 shows HR2 exposed to the intermembrane space (IMS) [107]. These two states could potentially facilitate the coordination between the OM and IM during fusion, serving a role similar to that of Ugo1 in yeast [111]. This function might work in conjunction with the UGO1-like protein SLC25A46 [138]. The different fusion hypotheses arising from these findings will be discussed later.

Structural study of mitofusins

The detailed molecular mechanisms involving the mitofusins remain largely unknown. In fact, little is known on the structure of mitofusins. However, the structure of Mfn1 has been partially elucidated through X-ray diffraction, revealing its monomeric form in 2017 (PDB GTP-bound: 5GOF, PDB GDP-bound: 5GOE, PDB nucleotide-free: 5GO4, Figure 1.21C) [139]. Additionally, two dimeric conformations were identified in 2017 (PDB: 5GOM, Figure 1.21D) [139] and 2018 (PDB: 5YEW, Figure 1.21E) [140]. The overall monomeric structure of the protein was consistent with the dynamin superfamily and more specifically BDLP [139, 65]. The structures highlighted the significance of G domain dimerization, which is controlled by guanine nucleotides, in the process of membrane fusion facilitated by mitofusin. Upon GTP loading, there is a possibility of inducing a conformational change, transitioning from the 'closed' state, characterized by tethering constraints, to the 'open' state, which permits tethering [139]. The second dimeric structure showed that there is a rearrangement of the structure, between the *neck* and the GTPase domain [140] (for a clear description of the '*neck*', '*trunk*' and GTPase see Figure 1.14). It is also proposed that the assumed mechanisms can also be applied to Mfn2.

Mfn2 was partially solved as well in 2019 in a monomeric conformation (PDB GDP-bound: 6JFK, PDB nucleotide-free: 6JFL, PDB Mfn2-T111D: 6JFM, Figure 1.21F) [141]. The structure is very similar to Mfn1 and BDLP. Similar to other dynamin superfamily members, MFN2 possesses key characteristics such as domain organization and G domain-mediated dimerization. However, unlike most other members, MFN2 exhibits a hydrolyze-but-not-dissociate feature, maintaining a low GTP turnover rate

that seems crucial for its cellular function. Furthermore, the study investigated the impact of Thr111 phosphorylation in MFN2 [141]. The crystal structure of a phosphorylation mimic MFN2IM(T111D) revealed that the phosphorylated residue, Asp111, blocks the GTP-binding groove in the P-loop (G1 motif), disrupting the binding affinity for guanine nucleotides. This suggests that phosphorylation at Thr111 directly inactivates MFN2 and inhibits its role in mitochondrial fusion.

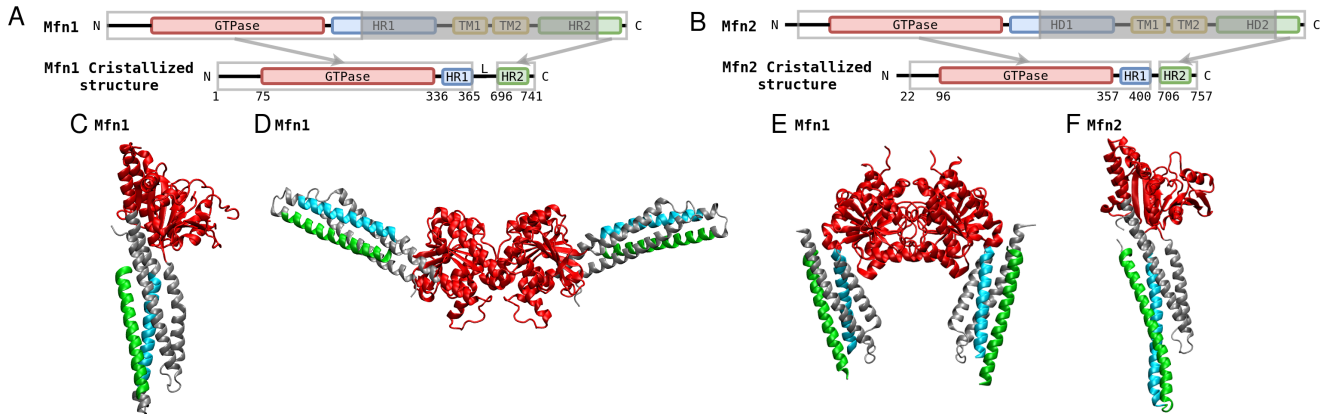


Figure 1.21: Solved Mitofusins structures. (A) Schematic representation showing the organization of Mfn1 based on full-length Mfn1. GTPase, GTPase domain in red; HR1/2, heptad repeat 1/2 in blue/green; TM, transmembrane region in orange. Borders of each element are indicated by residue numbers. (B) Schematic representation showing the organization of MFN2 based on full-length MFN2. G domain, GTPase domain; HD1/2, helical domain 1/2; TM, transmembrane region. Borders of each element are indicated by residue numbers. (C) Partial monomer of Mfn1 (PDB: 5GOF) [139]. (D) Dimer conformation of Mfn1 (PDB: 5GOM) [139]. (E) Closed dimer conformation of Mfn1 (PDB: 5YEW) [140]. For both (B) and (C), the domains are colored according to (A). In grey is represented the portions of the sequences not assigned to a specific domain. (E) Structure of the partial monomer of Mfn2 (PDB: 6jfk) [141], the domains are colored according to (D). In grey is represented the portions of the sequences not assigned to a specific domain.

Given the similarity between the mitofusins and BDLP, a few models were built based on the solved structures of BDLP [65, 68], and it is proposed that mitofusins change conformation from an open to closed conformation. The possible conformations of mitofusins have been studied using a combination of techniques, ranging from homology modeling to threading [133]. In 2013 [142], researchers constructed an initial model of the yeast mitofusin Fzo1 by using the closed conformations of BDLP as a template. Additionally, they created a model of a truncated version of Fzo1, which lacked the transmembrane (TM) domain, and built it on the open conformation of BDLP [142].

Using similar approaches, a model of Mfn2 was subsequently proposed in 2016 [143]. In this model, a conformational change was proposed before tethering/fusion involving the unfolding of the HR2 domain. However, this hypothesis contrasts with the conformational switch observed in BDLP and other DRPs that have been studied [65, 68, 69], and its thermodynamic stability has not been tested. As a result, this model overlooked the established importance of the mitofusin GTPase domain in mitochon-

drial fusion [65, 68, 137]. Nevertheless, a short peptide (residues 367–384) designed to disrupt intramolecular HR1–HR2 interactions was found to rescue mitochondrial morphology in murine embryonic fibroblasts and cultured neurons expressing either a Mfn2 mutant or the naturally occurring human Charcot–Marie–Tooth type 2A (CMT2A) mutant [143]. However, it remains uncertain whether the model proposed in the study is the sole explanation for the experimental findings. In more recent work, a model of mitofusin 2 has been developed, incorporating data from BDLP and Mfn1, and subsequently tested through a brief molecular dynamics simulation [144]. The studies suggested that a distinct paddle domain, in addition to the TM domain, was positioned above the hydrophobic layer.

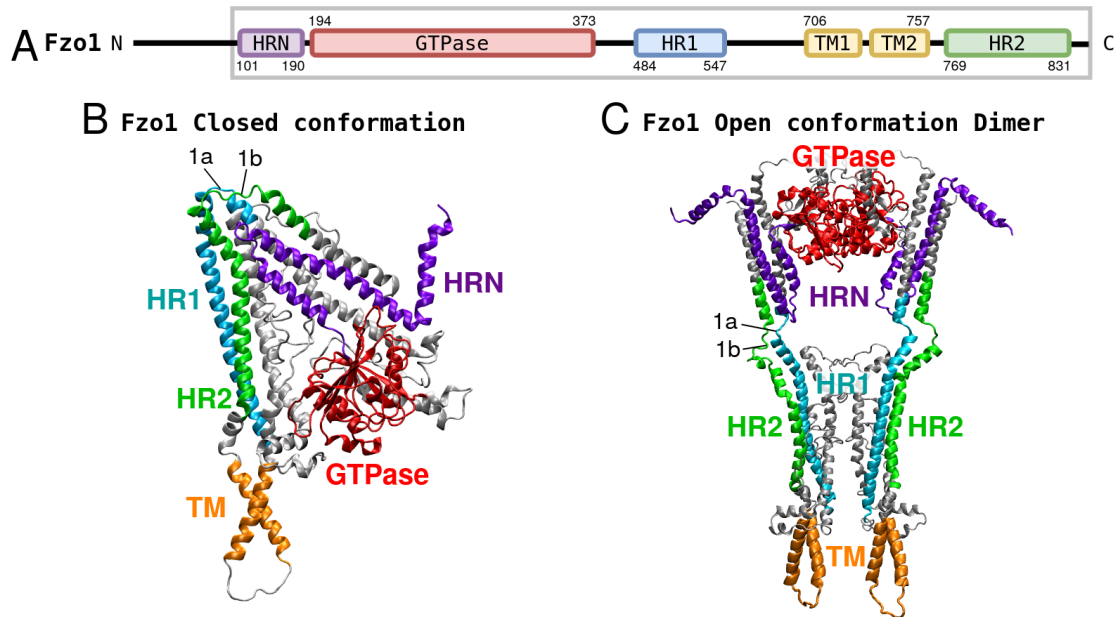


Figure 1.22: **Fzo1 models produced by De Vecchis et al. in 2017 [1] and Brandner et al. in 2019 [2].** (A) Schematic representation showing the organization of Fzo1. GTPase, GTPase domain in red; HRN, heptad repeat of the N-terminal section in purple; HR1/2, heptad repeat 1/2 in blue/green; TM, transmembrane region in orange. Borders of each element are indicated by residue numbers. (B) Closed monomeric conformation of Fzo1 produced by [1]. (C) Open dimeric conformation produced by [2]. For both (B),(C) the domains are colored according to (A). In grey is represented the portion of the sequences not assigned to a specific domain. Hinges 1a (in HR1) and 1b (in HR2) are represented.

After the initial endeavor to model Fzo1 [142], a subsequent model was constructed, which not only enhanced the overall structure but also improved the conformation of the transmembrane domain [1]. Importantly, this revised model was validated using experimental data and dynamically assessment within a membrane environment via MD simulations [1]. The closed conformation of the model is shown in Figure 1.22B and open conformation is shown in Figure 1.22C. The latter conformation was built in 2019 using the closed conformation [2]. This work stands as the most comprehensive and intricate model of mitofusins available to date, encompassing both HB1 and HB2 helical bundles. Within this framework, the architectural structure of Fzo1 is revealed, offering a precise depiction of its helical segments. Notably, HR1 and HR2 are not contiguous but exhibit localized bends at hinges 1a/b, reminiscent of the

flexible hinges observed in BDLP [65, 68]. Furthermore, the HR2 segment situated within Fzo1 trunk is exposed to the solvent and may be accessible for trans-tethering interactions [1]. In this context, HR2 could potentially play a role in membrane tethering, as previously suggested for Mfn1 [82].

Current hypothesis of fusion mechanisms involving mitofusins

The overall fusion mechanism of mitofusins remains elusive. Brandt et al. 2016 [137] have detailed various conformations of outer mitochondrial membrane when fusion is proceeding, showing a tethering and docking ring stage before fusion. The OMs tethered intermediate were observed to be at a distance of about 6 to 8 nm. Macromolecular assembly was observed within the ring-shaped mitochondrial docking complex, which was hypothesized to be mitofusins. Out of these information and the structural analysis of mitofusins, many hypothesis on the mitochondrial fusion process were formed. As mentioned before, the GTPase is known to drive dimerization [68], while the heptad repeat domains were shown to participate in membrane tethering as well as membrane destabilization [82, 135, 111]. The fusion process is often thought to be involving mitofusins acting in trans to tether together adjacent mitochondrial target membranes. Such tethering may be mediated by the antiparallel association of the HR2 region, as well as the dimerization of the protein through the GTPase domain.

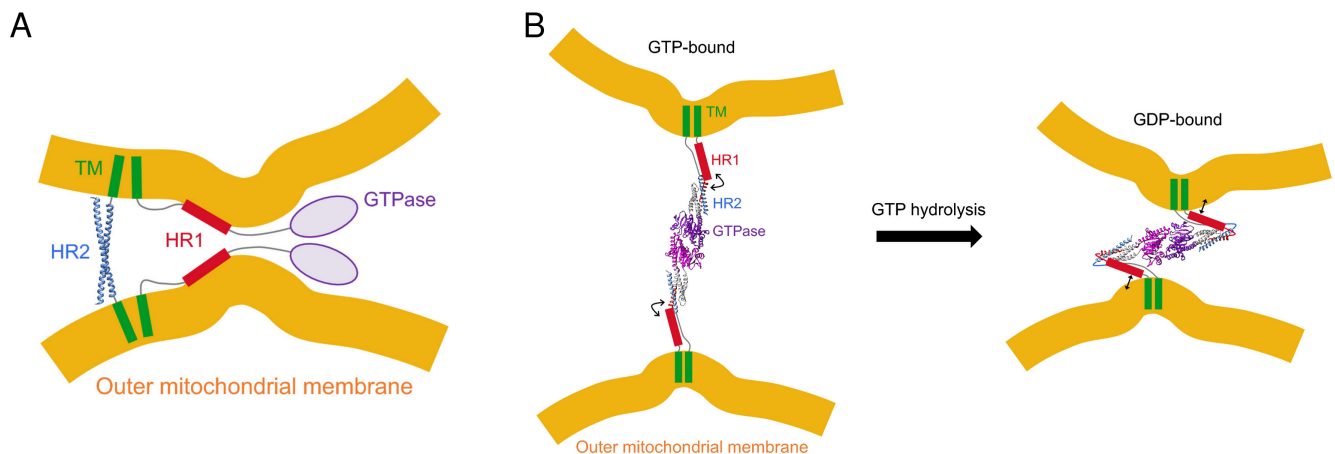


Figure 1.23: **Working models for the molecular mechanisms of Mitofusin in OM fusion.** Two possible scenarios for mitochondrial fusion were suggested by Daste and collaborator in 2018 [135]. These hypothesis are compatible with a membrane destabilization function of HR1 during fusion. (A) The HR2 domain is involved in mitochondrial docking through the formation of antiparallel coiled-coil dimers that bring opposing mitochondrial membranes at 10 nm from each other (PDB: 1T3J) [82]. The HR1 domain interacts with the lipid membrane (in cis or in trans), which brings outer mitochondrial membranes in closer proximity and perturbs their lipid bilayer structure, notably in membrane regions already displaying lipid packing defects. (B) Mitofusin-mediated mitochondrial docking occurs through GTP-dependent trans-dimerization of its GTPase domain followed by GTP hydrolysis driven open/closed conformational transition that pulls the membranes together (Protein PDB: 5GOM) [139]. In the closed conformation, the HR1 domain is perfectly placed to interact with the lipid bilayer surface and thus act as the molecular trigger for membrane merger. Crystallized sequences of Mfn1 in panels (A and B) are shown in ribbon representation and sequences with unknown structure are displayed as random coils or geometric shapes. The positions and orientations of the protein domains in the two panels are arbitrary. Taken from [135].

Daste et al. 2018 [135], proposed two mechanisms involving the human mitofusin Mfn1, shown in Figure 1.23. The first one rely on the trans association of the HR2 domains (Fig. 1.23A). This model also shows interactions of HR1 with the membrane, promoting fusion. However, the absence of dimerization through the GTPase domain and the HR2 relative to HR1, does not validate the structures solved in 2017 and 2018 [139, 140]. The second mechanism is in fact mainly based on the solved Mfn1 structures (Fig. 1.23B), and does not shown any interactions between HR2 domains. A conformational rearrangement occurs subsequent to trans-dimerization through the GTPase domain, which would position HR1 in a way that can destabilize the membrane. It is important to note that these two pathways are not mutually exclusive, and HR2 dimerization could occur as well with the structure proposed in Figure 1.23B. Furthermore, these two models do not take into account possible cis-dimerization [107] occurring during the dimerization process.

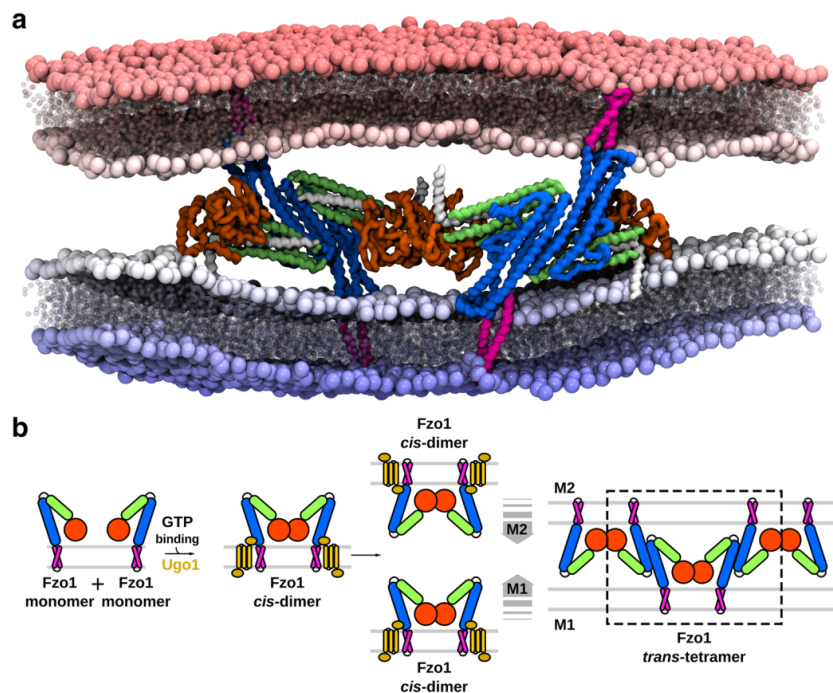


Figure 1.24: **Putative Fzo1 trans tethering complex.** (a) The system represents the final configurations of the putative Fzo1 trans tethering complex after a CG-MD simulation. The cis-interactions occur towards the GTPase domain. The trans interactions occur through the HRs (also called HBs) oriented in an antiparallel fashion as suggested for the human Mfn1 (Koshiba et al. 2004). GTPase domain, orange; HB1, blue; HB2 (or BSE), green; TM region, pink. The two bilayers represent two mitochondrial OM before fusion (M1 and M2 in (b)). Lipid head groups and tails are shown as spheres from red to blue according to the z -axis. Solvent is omitted for clarity. (b) Proposed Fzo1 fusion path. The color code is the same as in (a). Taken from [133]. Structure produced in [2].

Finally, in 2019 [2] membrane tethering models through cis and trans oligomers were investigated, taking advantage of the Fzo1 model produced in 2017 [1]. In this proposed model, two Fzo1 molecules would form oligomers in cis via their GTPase domain (Figure 1.24b). Within this cis-oligomer, the

HB2/trunk region would expose a hydrophobic spine from the HR2, available for trans interactions as described by De Vecchis et al. in 2017 [1]. Consequently, the spines of HRs would align in an antiparallel manner, consistent with the crystal structure of Mfn1 [82]. The model was subjected to coarse-grained simulation, revealing a 25% increase of the lipid-protein contact surface, attributed to the observed membrane curvature. Moreover, the tethering distance appeared to be about 5.5 to 9.5 nm throughout the simulation, which would agree with the observed 8 nm previously mentioned [137].

1.5 Using computational simulations to gather insights into membrane fusion

Efforts of many computational groups have been devoted to model the process of lipid bilayer fusion. Through computer simulations, it is possible to reveal which key physical properties the lipid layers must possess, as well as which external conditions could influence the mechanism [49]. Various methods of computer simulation exist, such as molecular dynamics, as well as Monte Carlo simulations or brownian-dynamics simulations. These computer experiments mimicking the lipid-water mixtures can have different degrees of accuracy. However, the propensity of the membranes to fuse and the intermediate structures emerging in the course of bilayer merger are directly ‘observed’ rather than derived by physical analysis. These tools were developed by fitting them to experimentally measured physical characteristics of lipid membranes, such as the bending and stretching moduli, the line tension of pores formed in the lipid bilayers, the rate of lateral diffusion of lipid molecules in the membrane plane, the rate of water permeation through the lipid bilayer matrix, and the temperatures of the lipid transition between the liquid and the crystalline phases and between different mesophases. It is implicit that fitting to these experimental values will make these tool suitable for describing the intramembrane energy changes in the course of the structural rearrangements accompanying the fusion process.

1.5.1 Investigation of preliminary conditions favorable for membrane fusion

To examine the merging capability of the membranes, different protocols were employed, and various parameters were observed and analyzed. As a membrane is more prone to undergo fusion when hydrophobic areas of the membrane are exposed to the solvent, the packing defects (Figure 1.25A) were studied in lipidic systems, involving lipids such as phosphatidylcholine (PC), phosphatidylethanolamine (PE) or diacylglycerol (DAG) [52, 145]. These analysis show that there is packing defect induced by conical lipids, such as PE and DAG, as well as by unsaturated carbon tails.

Another parameter that has been studied to assess the fusion capabilities of membranes is the presence of lipid tail protrusion in the membrane (Figure 1.25B). A protrusion event happens when a carbon atom from a lipid tail extends 0.1 nm above (or below, depending on the leaflet) its phosphorus atom, protruding into the polar layer [146, 147]. Two modes of protrusion were identified by Tahir and collaborators in 2016 [147]. The (i) "elbow" protrusion, which represented the majority of protrusions observed in planar bilayers, and corresponds to an hydrophobic atom near the lipid head extended into the solvent. In

contrast, (ii) "splay" protrusion involve the exposure of atoms near the end of a lipid tail, more prevalent in in curved vesicles or micelles. In fact, Larson and collaborators [146] have shown that protrusions increased in the presence of fusion inducing amphipathic helices. The scale to which the protrusions increased depended of the conformation of the helix, as well as the distance of the lipids to the peptide. Tahir et al. 2016 [147] showed an increased protrusion likelihood for curved membranes and suggested a significant effect of unsaturated lipids and the presence of proteins.

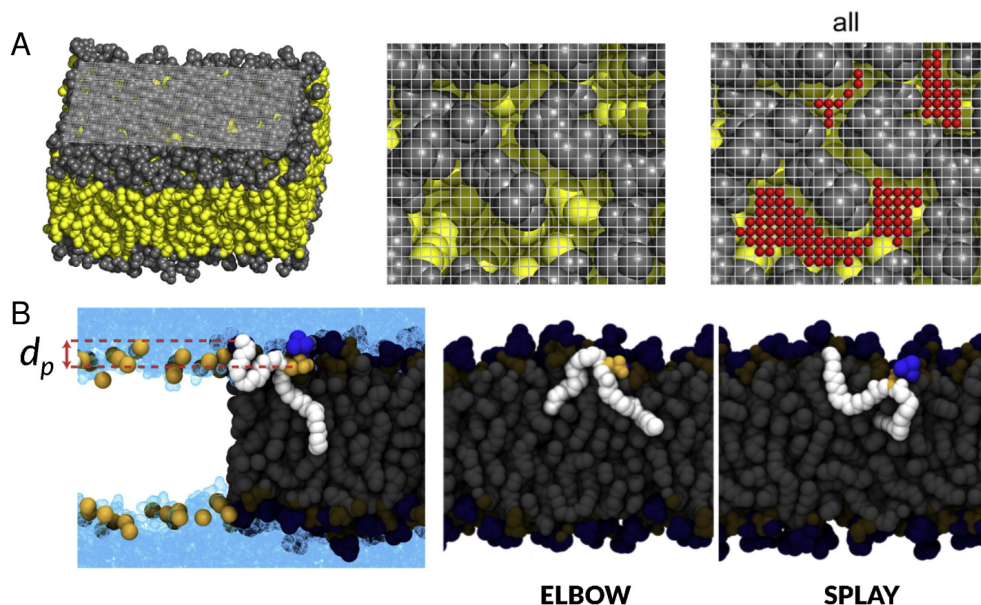


Figure 1.25: **Demonstration of packing defects and protrusion analysis.** (A) Example of packing defect analysis for a pure POPC bilayer. In all panels, the light gray grid represents the matrix M at 1 resolution. The aliphatic atoms are colored in yellow, and the other atoms are colored in gray (including polar head and glycerol group). Left, a three-dimensional view is shown. Middle, a top view is shown of a patch of upper leaflet. Right, the same top view as in the middle with the coordinates of the packing defects. Taken from [145]. (B) Left, example of protrusion and definition of the distance between a hydrophobic tail atom its phosphorus atom projected along the membrane normal (d_p). Two type of protrusion are showed : in the middle image is the "elbow" protrusion (lipid tail atom close to the phosphorus protruding), in the image on the right is defined the "splay" (end of lipid tail atom protruding). Taken from [147].

1.5.2 Analysis of the full fusion process through molecular dynamics

These studies [146, 147] hypothesized that the protrusions exist prior to the stalk phase. This starting phase of fusion, the stalk, was studied by Smirnova and collaborators in 2010 [148], and suggested that membranes would fuse via a prestalk intermediate favored at low hydration numbers. The prestalk intermediate is a state defined by a lipid adopting a conformation where its tail resides in the headgroup region of the layer to which the lipid belongs to. This lipidic conformation could correspond to a protrusion event. In this context, protrusion may promote the formation of the prestalk intermediate, subsequently facilitating the fusion process. Poojari et al. 2021 [149] showed, through free energies analysis, that the

inner leaflet of the plasma membrane was more prone to fusion. This finding prompted the study of a wide range of lipids and membrane composition, and their associated free energies of stalk formation. In fact, stalk formation was shown to be facilitated by increased tail disorder, lipids with negative intrinsic curvature (stabilizer of the large negative curvature of the stalk), while anionic headgroups would in fact be unfavorable [149]. In accordance to the prestalk phase favored by low hydration numbers, Smirnova et al. 2019 [150], showed that stalk stability increases with decreasing intermembrane distance. It was also shown that SNARE transmembrane domains favors the stalk phase, while PE lipids did not affect the stalk barrier [150]. However, the research did not dismiss the idea that PE lipids, owing to their conical shape, reduce the overall stalk barrier by influencing the membranes distance to one another through membrane curvature. A smaller head group would lead to increased exposure of the tails to the solvent, generally resulting in reduced repulsion between the membranes.

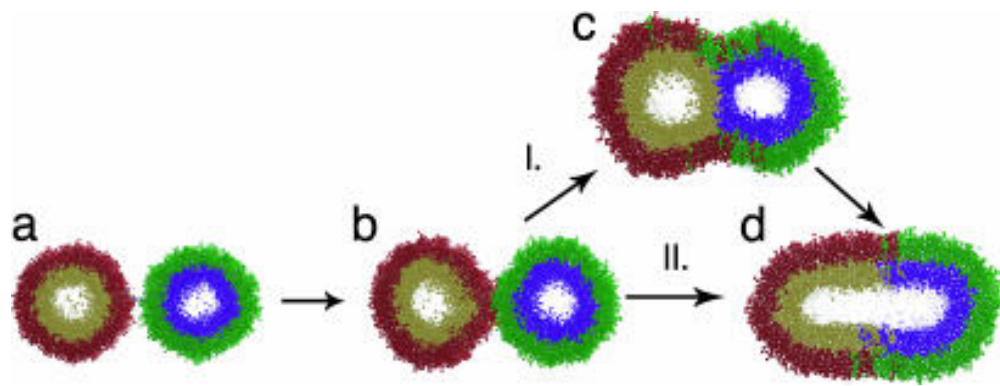


Figure 1.26: **Branching reaction pathway for vesicle fusion.** Pathway I illustrates the conventional progression from an initial unfused state (a) through an early intermediate resembling a stalk (b) and a hemifused late intermediate (c), ultimately leading to the fully fused state (d). Pathway II portrays an additional reaction route that emerged in simulations: the rapid transition from the stalk-like intermediate to the fully fused state. Lipids are color-coded to differentiate between the outer leaflets (in red and green) and the inner leaflets (in gold and blue) of each vesicle. Taken from [151].

Furthermore, the axially symmetric fusion stalk as the first lipidic bridge forming between fusion bilayers was confirmed through molecular dynamics simulation in atomic detail [152, 49]. The fusion behavior was able to be reproduced using atomistically detailed models, and specific features, such as lipid mixture were studied [153, 151, 152]. The simulations allowed to observe events that are complicated to observe by experimental techniques, such as the prefusion complex, and established that this reaction proceeds on a 6- to 9- μ s time scale, with a metastable hemifusion intermediate (Figure 1.26) [151].

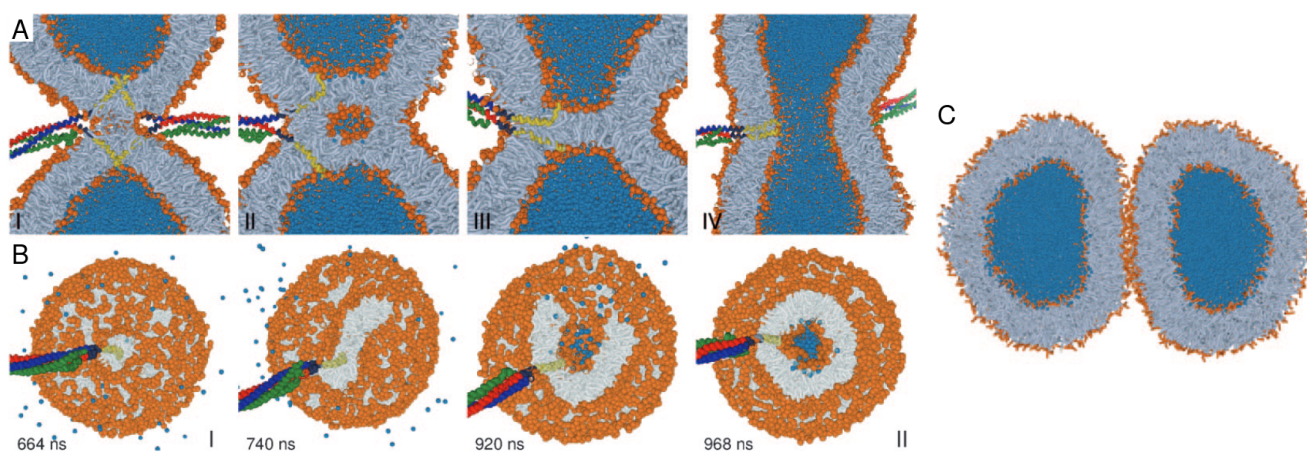


Figure 1.27: **Stages of SNARE-mediated membrane fusion revealed by simulations.** (A) I: Stalk, II: inverted micelle intermediate (IMI; single SNARE complex), III: Hemifusion-diaphragm (single SNARE complex), IV: fusion. (B) Cross-sections of the fusion plane showing the transition from stage I (stalk) to stage II (inverted micelle) in more detail. The stalk (664 ns), shows a worm-like expansion (740 ns) and eventually, after bending (920 ns), forms a closed ring that encapsulates exterior solvent forming an inverted micelle (968 ns). (C) SNARE-free control setup with the vesicles strongly pressed against each other. Taken from [154].

Finally, the SNARE fusion mechanism was detailed using coarse-grained molecular dynamics [154]. In fact, the simulations revealed multiple stages of membrane fusion (Figure 1.27A,B): (i) stalk formation phase, followed by (ii) an inverted micelle intermediate and (iii) the hemifusion diaphragm, and finally (iv) the fusion pore formation. Furthermore, in the absence of SNARE embedded in the membrane, the occurrence of the stalk phase was not observed under normal conditions, and even when the vesicles were pressed against each other (Figure 1.27C), it happened rarely. In contrast to the conventional hemifusion pathway (described previously in Figure 1.6) [49], the simulation revealed an inverted micelle stage: the stalk expanded in a manner resembling a worm's shape within the cross-section of the fusion plane, eventually closing and shaping into a ring that encloses an external solvent bubble. This study helped shifting the views on SNARE-mediated membrane fusion. In fact, the study showed the key role of the SNARE complex in the initiation of the fusion stalk as well as the opening of the fusion pore [154], in contrast to the previously described mechanism, confining the SNARE to the role of bringing the two membranes together. Furthermore, experimental data confirmed the contribution of SNARE into the stalk expansion and the formation of the pore [155], confirming that SNARE complexes play a role during all stages of fusion by helping overcoming subsequent fusion barriers.

1.6 Thesis aim

The goal of the Ph.D is to study the structures of mitofusins using mainly theory-based methods (molecular dynamics). This work mainly focuses on the mitofusin of *S. Cerevisiae* Fzo1, with the intent that the developed protocols can then be applied to the human mitofusin. This project is a part of an ANR project (MITOFUSION) shared between different partners (Laboratoire de Biochimie Théorique: Antoine Taly,

Marc Baaden, Laboratoire des Biomolécules: Patrick Fuchs, Laboratoire de Biologie Moléculaire et Cellulaire des Eucaryotes: Mickaël Cohen, Institut de Psychiatrie et Neurosciences de Paris: David Taresté) whose goal is to understand the structure-function relationships of mitofusins.

Chapter 3 studies the transmembrane domain of Fzo1. The work on mitofusins started in a Master 2 internship before the Ph.D, and focused on the transmembrane domain (TM) of fzo1 using multiscale molecular dynamics. This project was first meant to last for about 6 month. This region of the protein was initially described using the ab initio method PREDDIMER [156, 1]. In this first project, the goal was to undertake a physics-based investigation, using coarse-grained molecular dynamics, to sample the conformations of the helices in a membrane environment. After 6 month of internship, the conformations observed were in fact quite different to what PREDDIMER predicted. This finding, combined with (i) the newest version of the MARTINI force-field coming out in April 2021 and (ii) the aim to test protonation states of the basic conserved residue Lys716 (neutral and charged), compelled us to thoroughly study this section of the protein, using the multiple versions of the MARTINI force-field followed by all-atom simulations. Considering the improvement of the force-field with the 3rd version, we decided to use the main conformation produced by the MARTINI3 simulations with a neutral lysine for further all-atom simulations. Based on this model we ran some simulations using the enhanced sampling technique Temperature-Replica Exchange Molecular Dynamics (T-REMD) method [157]. In the end, we obtained a good structural candidate for the TM domain of Fzo1.

Chapter 4 presented was the comparative study of the two MARTINI force-fields (MARTINI2 and MARTINI3). One of the main changes made between the MARTINI2 and MARTINI3 versions of the force-field is the backbone definition of the helices (described in more detail in Section 2.2). In fact, helices were defined neutral in MARTINI2, while the backbone is fully considered as polar (including helices) in MARTINI3. Hence, helices are more hydrophilic in MARTINI3 systems, which compelled us to comparatively study the membrane-peptide interactions in the MARTINI force-fields, through two cases : the cell penetratin peptide penetratin, and the amphipathic helix located in the HR1 domain of Mfn1 (Mfn1-AH). This analysis stemmed from two collaborations, a first one on the penetratin with LBM colleagues Sophie Cribier and Nicolas Rodriguez, and a second one on Mfn1-AH with ANR collaborator David Taresté. Major differences were observed between the two force-field tested. Hence, we decide to study different membrane observables in order to assess the changes and limitations of the new version of the force-field.

Chapter 5 presented is the study of Mfn1-AH using all-atom molecular dynamics. This AH is located in the HR1 domain, which had been previously shown to promote fusion. This 18 residues amphipathic helix was hypothesized to confer the membrane-binding and fusion capacity to the domain [135]. As there are few experimental data on the properties and functions specific to the peptide, the goal of this project is to have an overview on the effects of this amphipathic helix on a membrane environment. This work is part of the overall goal to characterize the various elements necessary for outer membrane fusion, and more generally to learn about the fusion mechanism of mitofusins. This work uses regular all-atom

simulations, as well as the enhanced sampling technique T-REMD to provide insights on this peptide.

As a last project of the Ph.D, we started working on the structure of Fzo1 as a whole. We tested the AlphaFold2 [158] method for our protein. AlphaFold is a deep learning model developed by DeepMind, used to predict the 3D structure of proteins from their amino acid sequence, a long-standing challenge in structural biology [158]. AlphaFold achieved very good results in the critical assessment of protein structure prediction (CASP14) experiment, and outperformed other existing methods [159]. The neural network was trained using only supervised learning on experimental protein structure deposited in the Protein Data Bank, and is able to achieve remarkable accuracy. However, despite the very good performance it usually yields, the first Fzo1 model predicted by the machine learning method was not validated by all of the experimental data collected when the homology model was first established in 2017 [1]. Furthermore, the transmembrane domains of the protein are partially predicted as intrinsically disordered, opposing results of the secondary structure prediction. A first preliminary study of these models produced by AF are presented at the end of the manuscript (Section 6). An adjustment of some parameters, such as the multiple alignment sequence, which is usually produced by Alphafold2, have shown some improvement in the models produced.

CHAPTER 2

MATERIAL AND METHODS

2.1 Fundamental Concept of Molecular Dynamics

Molecular Dynamics (MD) stands out as the predominant method across the diverse Ph.D projects showcased in this manuscript. Employed within the realm of molecular modeling and simulations, this computational technique is geared towards investigating the temporal behavior and movements of atoms and molecules. By mathematically resolving the equations of motion rooted in classical mechanics, it delves into the study of various biomolecules. Here, its application involves the study of the behavior of diverse biomolecules, predominantly lipids and proteins, particularly those belonging to the mitofusin family. This technique will provide us insights into the dynamic behavior of systems at the atomic and molecular level.

2.1.1 Representation Accuracy

Molecular Dynamics has the capacity to provide detailed and valuable insights of a molecular model that may not be reachable through experiments, as illustrated in figure 2.1. Nonetheless, this computationally acquired information necessitates validation. Typically, this validation process requires a comparison with experimentally derived data.

Molecules in a molecular dynamics systems are represented by a set of particles linked to one another. Multiple representation can be used in molecular dynamics (Figure 2.2). Indeed, each force field establishes its own level of representation precision. The most straightforward approach to defining a molecule would involve depicting each individual atom within the molecule, a representation referred to as "all-atom". This detailed representation poses certain challenges, particularly when attempting to conduct simulations over extended time or when dealing with systems that encompass a vast number of atoms.

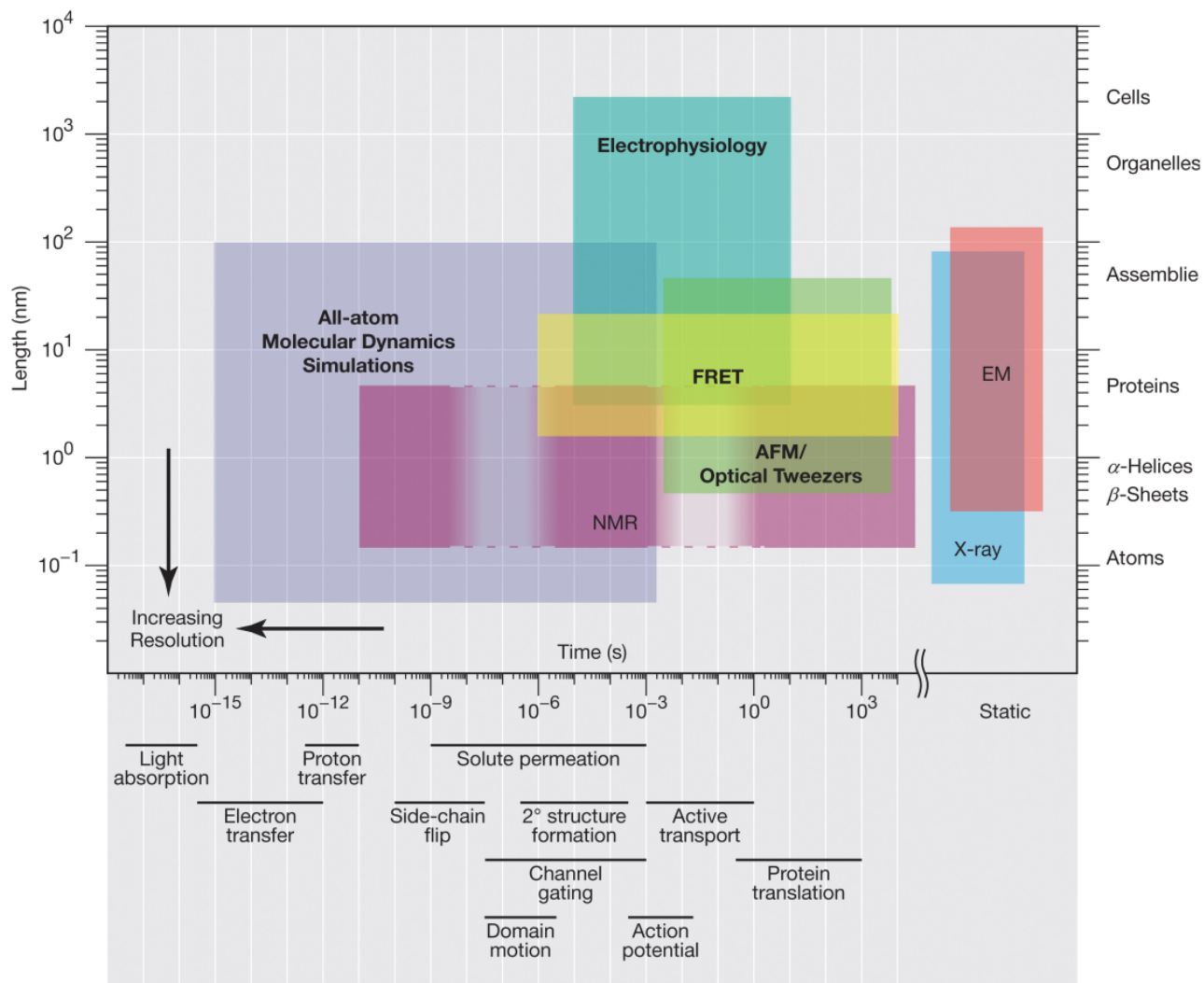


Figure 2.1: **Spatiotemporal resolution of various biophysical techniques.** The time scales of MD simulations are juxtaposed with those of experimental methods, highlighting a noteworthy discrepancy. MD simulations yield considerably shorter time scales in contrast to the more extensive time frames characteristic of experimental assays. Taken from [160].

Hence, alternative modes of representation are available, one of which is the "united-atom" approach. This approach simplifies the "all-atom" approach by treating groups of atoms as single entities, with each bead representing a heavy atom along with its associated aliphatic hydrogen atoms. This representation considers every atoms of the molecules besides the hydrogen atoms, reducing the complexity of the simulated systems. Finally, some of the most common representations are the "coarse-grained" representations, wherein several heavy atoms are combined into a single particle or bead. Notably, the MARTINI family of force fields holds prominence as the most widely employed, and has a mapping of 4 heavy atoms to 1 particle [161, 162, 163, 164].

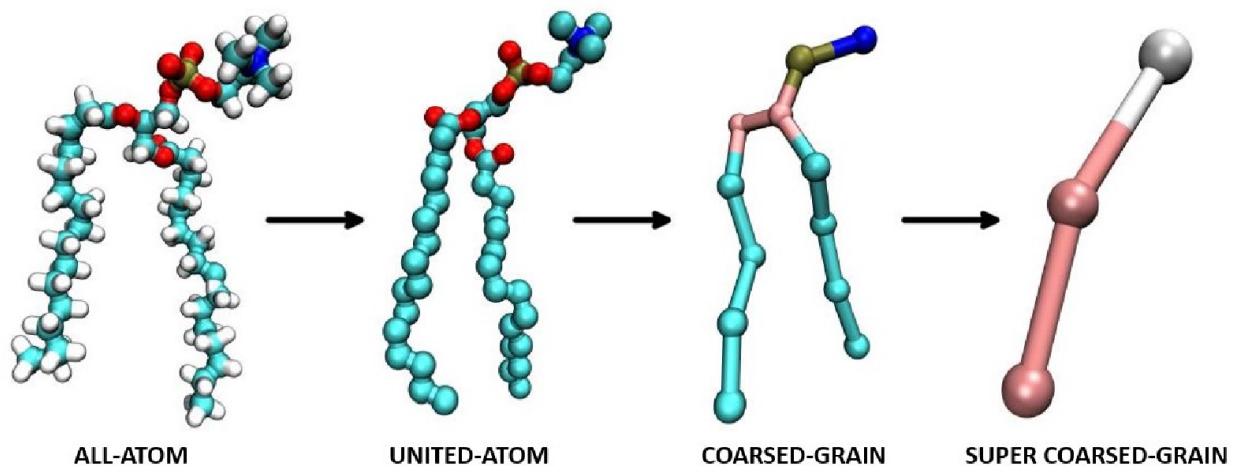


Figure 2.2: **Various representation precision used in molecular dynamics.** The example used for the various resolution is a Palmitoyl-Oleoyl-Phosphatidyl-Choline (POPC). Provided by Patrick Fuchs.

2.1.2 The Force-Field

The various particles composing the molecules in the systems are either bonded (particle belonging to the same molecule) or engaged in non-bonded interactions with one another. Force fields, which encompass a set of parameters and equations, provide the framework for quantifying and describing these interactions by evaluating the potential energy of the system. This potential energy dictates how the particles of the system interact with each other and allows the prediction of structural, thermodynamic, and kinetic properties. The potential energy is defined as a set of equations and parameters that determine the forces and energies associated with two classes of terms, bonded and non-bonded interactions (Figure 2.3 and Equation 2.1).

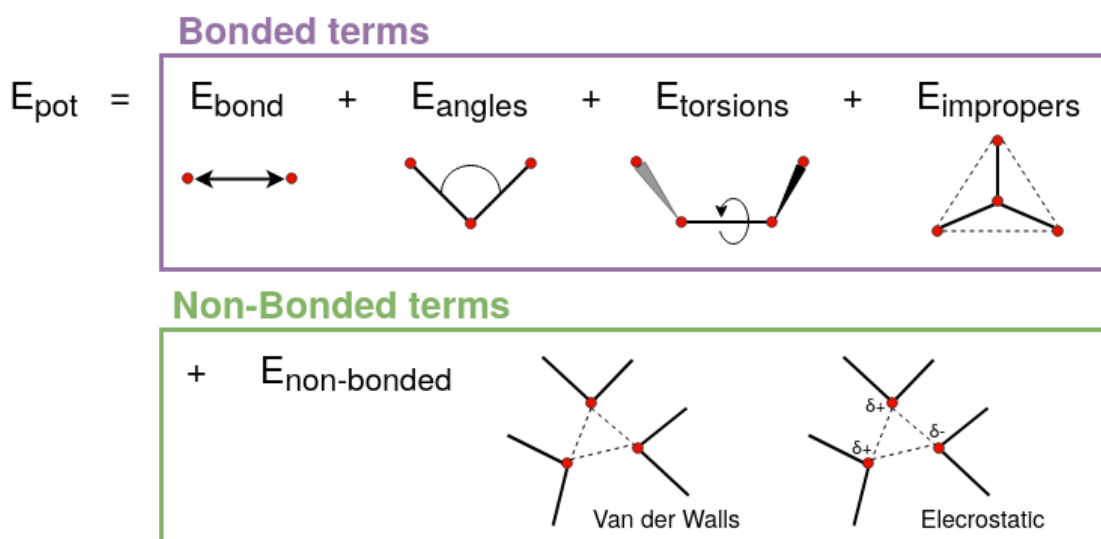


Figure 2.3: **Potential Energy terms illustration.**

There exists four distinct bonded terms: the bonds connecting two consecutive atoms, the angles formed by three consecutive atoms, the proper dihedral angles created by four consecutive atoms, and the improper dihedrals. The latter, referred to as improper dihedrals, involve angles between four atoms designed to maintain planarity within groups such as aromatic rings or to prevent molecules from inverting into their mirror images (for instance, a tertiary asymmetric carbon with a United-Atom representation). In contrast, the non-bonded terms encompass electrostatic and Van der Waals (VdW) interactions. The sum of both the bonded and non-bonded terms contributes to the system's potential energy calculation, thereby determining its overall potential energy:

$$\begin{aligned}
 E_{potential} &= E_{bond} + E_{angles} + E_{torsions} + E_{impropers} + E_{VdW} + E_{Electrostatic} \\
 E_{potential} &= \sum_{bonds} \frac{k_l}{2} (l - l_0)^2 + \sum_{angles} \frac{k_\theta}{2} (\theta - \theta_0)^2 \\
 &+ \sum_{dihedrals} \sum_{m=1}^M \frac{V_m}{2} [1 + \cos(m\omega - \gamma)] + \sum_{impropers} \frac{k_\Omega}{2} (\Omega - \Omega_0)^2 \\
 &+ \sum_{i=1}^{N-1} \sum_{j=i+1}^N 4\varepsilon_{ij} \left[\left(\frac{\sigma_{ij}}{r_{ij}} \right)^{12} - \left(\frac{\sigma_{ij}}{r_{ij}} \right)^6 \right] + \sum_{i=1}^{N-1} \sum_{j=i+1}^N \frac{q_i q_j}{4\pi\varepsilon_0 r_{ij}}
 \end{aligned} \tag{2.1}$$

The various elements are defined as:

Bonds: l is the distance between the atoms, l_0 is the equilibrium bond length and k_l is the force constant.

Angles: θ is the angle between the atoms, θ_0 the equilibrium angle and k_θ the force constant.

Dihedrals: V_m is the dihedral amplitude, m is the dihedral multiplicity ω is the dihedral angle and γ is a phase factor .

Impropers: k_ω is the force constant, ω is the improper angle value and ω_0 is the value at equilibrium.

VdW: i and j are the two atoms, ε_{ij} the Lennard-Jones well-depth, r_{ij} is the the distance between i and j , and σ the distance at which the Lennard-Jones equals zero.

Electrostatic: q_i and q_j are the partial atomic charges and ε_0 the permittivity of vacuum.

It's crucial to note that non-bonded interactions are not computed between atoms directly bonded or separated by two bonds. For atom pairs separated by three bonds, these non-bonded terms are modified, often referred to as 1-4 interactions. Typically, these 1-4 terms complement dihedral angles to achieve accurate dihedral distributions. The attenuation of 1-4 interactions concerning normal non-bonded interactions varies depending on the specific force field employed.

While the concept of computing non-bonded interactions for every imaginable pair of atoms might seem optimal, the practicality of implementing this approach becomes unfeasible when considering the

vast number of atoms used in typical simulations of biological systems, notably because it scales with the square of the total number of particles (N^2 complexity where N is the number of particles). In fact, due to the rapid decay of these interactions over interatomic distances, a cutoff distance is commonly implemented, which serves to exclude interactions beyond a certain range. Nevertheless, employing a finite cutoff distance introduces significant artifacts when dealing with highly charged systems, such as nucleic acids, lipids, and ionic liquids [165]. An adverse consequence is the accumulation of charged molecule pairs at the cutoff distance, a behavior that contradicts the intended simulation behavior. To address this issue, a widely accepted solution known as the Particle Mesh Ewald (PME) algorithm has gained prominence [166, 167]. This concept builds upon the foundational Ewald summation [168], incorporating optimizations to enhance computational efficiency.

The fundamental premise of PME involves computing contributions beyond the cutoff distance (as depicted in figure 2.4) through ingenious computational strategies. This is accomplished by assuming the simulation box to be replicated in all spatial directions, mimicking a crystal lattice. Electrostatic interactions are divided into two components: the initial part calculated in real space using the classical Coulomb law (as expressed in Equation 2.1), up to a relatively short cutoff (typically around 10 Å), and a subsequent part encompassing atoms beyond the cutoff, which is evaluated in Fourier space, similar to the treatment in a crystal lattice. To expedite the calculation of this latter part, a grid-based approach (hence the term "Mesh" in PME) is employed, allowing the utilization of the fast Fourier transform (FFT), which results in a computational complexity of $N\log(N)$ (where N denotes the number of atoms). In the scope of this thesis, PME is used for handling electrostatic interactions, while a switch function is applied for van der Waals interactions.

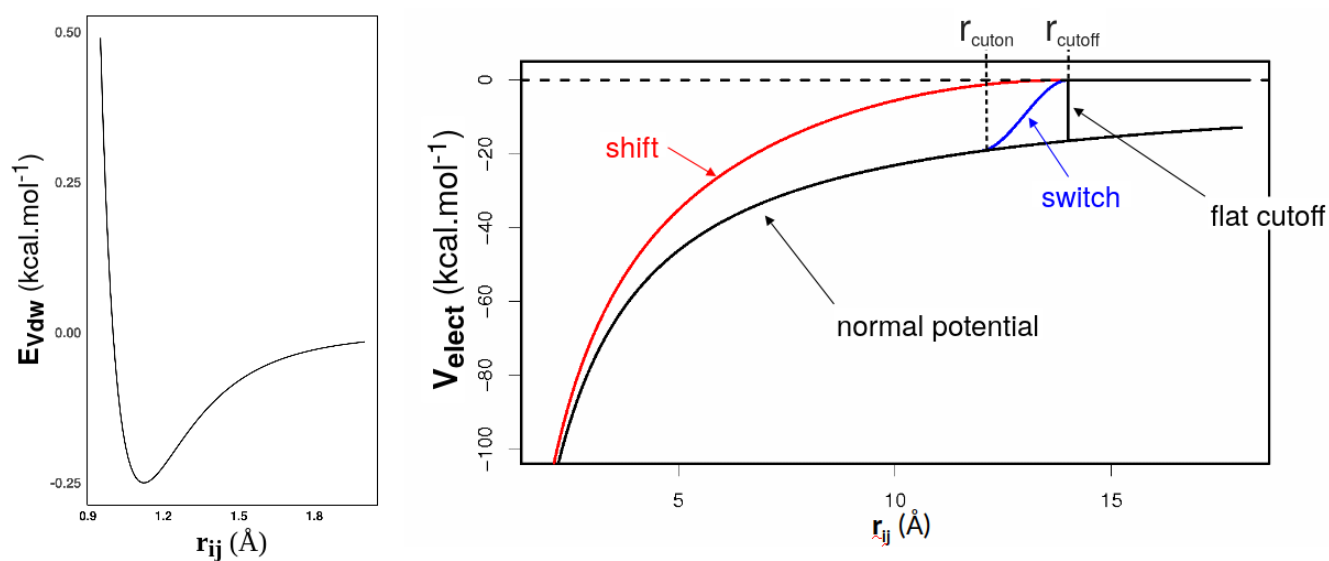


Figure 2.4: **Non-bonded interactions: Lennard-Jones potential and Coulomb law.** (A) The Lennard-Jones potential is shown. (B) Coulomb law representing the electrostatic interactions, with the application of the PME algorithm.

Each force-field have been developed to specialize in specific sets of molecules or macromolecules. Indeed, it is complicated for one force-field to fit all types of molecules. Hence, specific force-fields are developed for specific systems. For instance, AMBER [169] is tailored for nucleic acids and proteins, among other molecular categories. These FFs are typically referred to as "empirical" due to their reliance on simple functional forms (as seen in the above equation), often fine-tuned through calibration against experimental data and/or more advanced quantum calculations.

The molecular dynamics (MD) simulations presented in this manuscript employ two distinct FFs. The all-atom force-field CHARMM36 [170], chosen for its robustness and broad applicability across a wide range of molecules. On the other hand, MARTINI (2 and 3) [161, 162, 163, 164] is employed for coarse-grained (CG) simulations, a mode that simplifies systems and extends simulation timescales.

2.1.3 Molecular Dynamics Algorithm

In this section, vectors are written with bold face (e.g. \mathbf{r}_i), while scalars use regular font (e.g. m_i).

The fundamental concept behind MD is to numerically solve the equations of motion for each particle (atom or molecule) in a system, defined by a specific temperature, pressure and molecular composition. These equations are derived from classical mechanics and describe how the positions and velocities of particles change over time. As the force field (FF) evaluates the system's potential energy ($E_{\text{potential}}$, denoted as E), a simulation determines the force vector, $\mathbf{F}_i = (F_{ix}, F_{iy}, F_{iz})$, experienced by an atom i within the system. This force is derived from the potential energy E by calculating its gradient with respect to the atom's position vector $\mathbf{r}_i = (x_i, y_i, z_i)$:

$$\mathbf{F}_i = -\frac{\partial E}{\partial \mathbf{r}_i} \quad (2.2)$$

Subsequently, this force can be incorporated into Newton's second law equation:

$$\mathbf{F}_i = m_i \cdot \mathbf{a}_i \quad (2.3)$$

Consequently, the formulation of Newton's equation can be modified, considering that the particle i 's position corresponds to the second derivative of its acceleration \mathbf{a}_i :

$$\frac{\mathbf{F}_i}{m_i} = \frac{d^2 \mathbf{r}_i}{dt^2} \quad (2.4)$$

The equation 2.4 indicates that the position \mathbf{r}_i of a particle i after a small fraction of time δt , can be deduced from its mass m_i and the exerted force \mathbf{F}_i . The modified version of Newton's equation is a differential equation which can be solved either analytically or numerically. Solving the equation analytically means finding a functional expression that describes the relationship between an unknown function and its derivatives while satisfying the given equation and any initial or boundary conditions. This solution can

be applied to simple systems such as the harmonic oscillator. Most of the time the differential equation is solved numerically which involves using computational methods to approximate the solution rather than finding an exact analytical expression. This approach is better suited for systems that typically include a high number of particles, as well as for comprehensively accounting for the intricate interactions among these particles. By iteratively alternating between Equation 2.4, which provides updated positions, and Equation 2.2, which calculates the forces acting on a specific system conformation, a molecular dynamics trajectory can be generated. This trajectory comprises consecutive frames that enable the observation of system dynamics. The Leap Frog algorithm [171] (Figure 2.5) was used for the various simulations conducted in this manuscript. The particle positions at a given time t are computed, while the velocities are determined at the time $t + \delta t$:

$$\begin{aligned} \mathbf{v}_i(t + \frac{1}{2}\delta t) &= \mathbf{v}_i(t - \frac{1}{2}\delta t) + \delta t \mathbf{a}_i(t) \\ \mathbf{r}_i(t + \delta t) &= \mathbf{r}_i(t) + \mathbf{v}_i(t + \frac{1}{2}\delta t) \delta t \end{aligned} \quad (2.5)$$

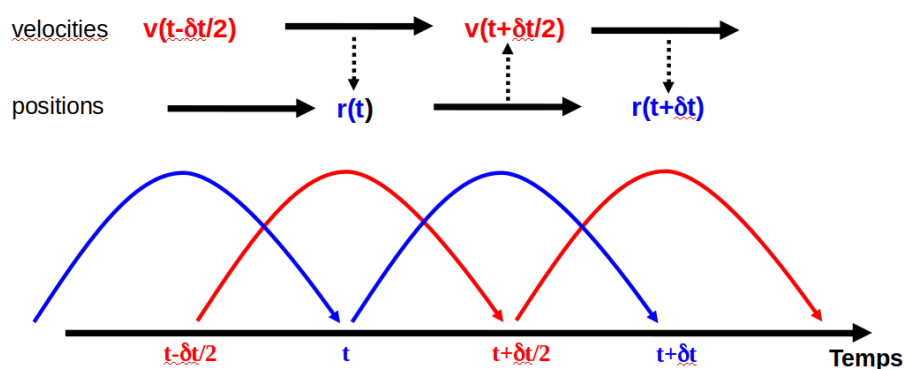


Figure 2.5: Leap Frog algorithm.

As a reminder, δt represents the time step utilized in the simulations. This parameter needs to be carefully adapted to the system and the force-field used, as it has to be slower than the most rapid motions within the specific system. In fact, the fastest movements in molecules are bond vibrations. However, in our all-atom systems the bonds involving hydrogen atoms were "frozen" to enable an augmentation of the time step δt and decrease the computational cost of the simulation, typically 2 fs. Furthermore, when utilizing the coarse-grained MARTINI force field, the δt can be increased even further (up to 20 fs) because we are not dealing with regular atoms but coarser beads.

2.1.4 Periodic Boundary Conditions

The molecules composing MD systems are conventionally placed within a simulation box (Figure 2.6B). However, molecules situated at the perimeter of the box cannot be treated as in contact with void, as this would lead to an artificial and implausible surface tension. In order to avoid this issue, Periodic Boundary

Conditions (PBCs) are established. The simulation box is duplicated across all spatial directions, as depicted in Figure 2.6A,C. Using this process, particles positioned at the box's periphery can exit the box through that border and immediately re-enter through the opposite border. There is now the illusion that molecules on one edge of the simulation box interact with molecules on the opposite edge, effectively eliminating edge effects and enabling the study of larger and more realistic systems. The utilization of PBCs necessitates the application of a cutoff, which must be smaller than the shortest half-length of the box. It is nonetheless very important to be careful about the size of the system, as it should not be too small, ensuring that a single large molecule (such as a protein) is incapable of interacting with itself.

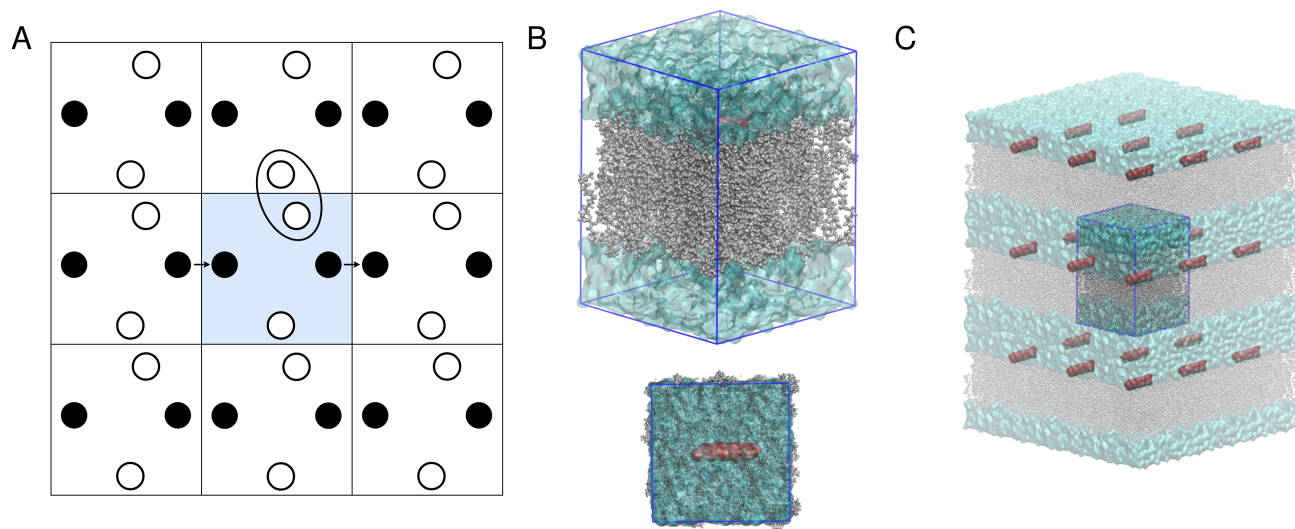


Figure 2.6: **Periodic Boundary Conditions (PBCs)**. (A) 2D Schema of the PBCs. The black particle is coming out of the box, and the two white particles interact with each other. (B) Simulation box, snapshot from the side of the box, and from the top of the box. The solvent is represented in cyan and in transparent surface representation. The lipids are in grey and in licorice representation. The protein is in red and in surface representation. The border of the box can be seen in blue. Atoms appear positioned beyond the confines of the box, as the molecules distributed across two borders were reconstructed to avoid being divided in half. (C) 3D representation of the PBCs. All the duplicated boxes can be seen around the simulation box, and shown transparent. The color scheme remains consistent with (B).

2.1.5 Energy of the system

In Molecular Mechanics (MM), and thus Molecular Dynamics (MD) systems, the different energies are fundamental quantities that characterize the interactions and dynamics of atoms and molecules. The total energy is defined as the sum of the kinetic energy and the potential energy (Equation 2.6). Kinetic energy originates from the motion of particles and depends on their mass and velocity. The equation is defined in Equation 2.7, where m_i as the mass of the particle i , v_i its speed (i.e. the magnitude of the velocity vector), and N the total number of particles. The potential energy is defined in the Force-field section 2.1.2 and in Equation 2.1.

$$E_{tot} = E_{kinetic} + E_{potential} \quad (2.6)$$

$$E_{kin} = \frac{1}{2} \sum_{i=1}^N m_i v_i^2 \quad (2.7)$$

2.1.6 Thermodynamic Ensembles

Thermostat

The movements of molecules is inherently linked to temperature. In fact, according to the theorem of equipartition of energy, the kinetic energy (E_{kin}) is directly associated with the temperature of the system. This underscores the connection between temperature and the velocities of the particles.

$$E_{kin} = \frac{1}{2} N_{df} k_B T \quad (2.8)$$

$$N_{df} = 3N - N_c$$

where N_{df} is the number of degrees of freedom, k_B the Boltzmann constant, T the absolute temperature, N the number of particles and N_c the number of constraints. There is as much degrees of freedom as there is Cartesian coordinates ($3 \times N$) from which is subtracted the number of constraints N_c in the system. A constraint refers to a degree of freedom that has been immobilized by assigning a predetermined value set by the modeler, such as constraining bond lengths or eliminating the overall movement of the system center of mass. For instance, in the CHARMM36 force field, all bonds involving hydrogen atoms are constrained. In this thesis, the LINCS algorithm [172] was employed for this purpose. Equation 2.8 depicts the relationship between the system energy and its temperature.

Since temperature and particle velocities are interconnected, temperature can be controlled by rescaling velocities, which is the purpose of a thermostat. Amplifying velocities corresponds to heating, while diminishing them corresponds to cooling. Within this project, two distinct thermostat algorithms have been utilized. The Berendsen thermostat [173] adjusts the temperature in each simulation step proportionally to the disparity between the current temperature and a reference temperature. Although it quickly converges to the desired temperature, it does not accurately reproduce genuine temperature fluctuations found in a canonical (NVT) ensemble. The second thermostat employed is v-rescale [174], which is slightly slower at reaching the target temperature compared to Berendsen. However, it incorporates an additional stochastic term in the equation of motion to ensure correct temperature fluctuations.

Barostat

In the systems presented in this manuscript, the pressure is fixed, with the assistance of a barostat. For a 3D system, the pressure is represented in the form of a tensor as seen in the Equation 2.9, where V is the volume of the system, \mathbf{v}_i is the velocity vector of particle i , \mathbf{r}_{ij} the distance vector between particles i and

j , \mathbf{F}_{ij} is the force acting on i due to j . The first term of the equation corresponds to the kinetic energy and the second to the virial (contribution due to cohesive forces between particles).

$$\mathbf{P} = \frac{1}{V} \left[\sum_{i=1}^N m_i \mathbf{v}_i \otimes \mathbf{v}_i + \sum_{i<j} \mathbf{r}_{ij} \otimes \mathbf{F}_{ij} \right] \quad (2.9)$$

The \otimes sign corresponds to the tensor product. Starting with two vectors in n dimensions, we generate a matrix with dimensions of $n \times n$. Hence, with the velocity vector \mathbf{v}_i of particle i which has 3 components (corresponding to dimensions x, y, z) we obtain :

$$\mathbf{v}_i \otimes \mathbf{v}_i = \begin{bmatrix} v_{ix}v_{ix} & v_{ix}v_{iy} & v_{ix}v_{iz} \\ v_{iy}v_{ix} & v_{iy}v_{iy} & v_{iy}v_{iz} \\ v_{iz}v_{ix} & v_{iz}v_{iy} & v_{iz}v_{iz} \end{bmatrix} \quad (2.10)$$

In Equation 2.9, there are two tensor products, one for the kinetic energy and one for the virial term. As a result, the pressure emerges as a 3x3 tensor, encompassing pressure values along all spatial directions:

$$\mathbf{P} = \begin{bmatrix} P_{xx} & P_{xy} & P_{xz} \\ P_{yx} & P_{yy} & P_{yz} \\ P_{zx} & P_{zy} & P_{zz} \end{bmatrix} \quad (2.11)$$

In most MD simulations, the off-diagonal values P_{xy} , P_{xz} , and P_{yz} are set to zero, otherwise the box deforms (it is no longer cubic). The diagonal elements represent the component according to each dimension. The mean of the diagonal terms represent the scalar pressure P of the system.

The pressure is regulated by modifying the volume and consequently adjusting the positions of the particles. When the volume adjustment is uniform across all three spatial directions, it is referred to isotropic coupling. Isotropic coupling is typically employed for simulating isotropic liquids like water. In this project, it was implemented for an all-atom system containing a peptide within a water box. Nevertheless, when dealing with a system containing a membrane, it becomes mandatory to treat the x and y directions separately from the z direction. This approach corresponds to semi-isotropic coupling, where adjustments are made to the x and y dimensions independently to the z dimension. In fact, for a membrane simulation, the semi-isotropic coupling ensures the imposition of zero surface tension, i.e. the area fluctuates around an equilibrium value. When volume scaling operates independently in all three spatial directions, the coupling becomes anisotropic. However, anisotropic coupling was not employed in this manuscript.

As for temperature, multiple algorithms can be used to control the pressure in a MD system. The Berendsen barostat [173] employs a similar principle to the Berendsen thermostat, adjusting the simulation box volume at each step. It rapidly reaches the target pressure but again exhibits incorrect fluctu-

ations expected in the isothermal/isobaric (NPT) ensemble. On the other hand, the Parrinello-Rahman barostat [175] introduces an extra term to the equation of motion. It takes more time to converge to the desired pressure compared to the Berendsen algorithm, yet it generates correct pressure fluctuations, thus maintaining the NPT ensemble.

2.1.7 Molecular Dynamics Protocol

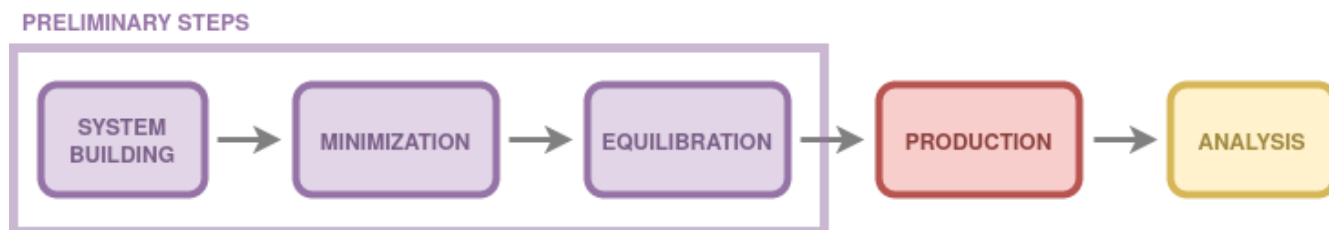


Figure 2.7: Scheme depicting the various stages within an MD Protocol.

System Construction

Before the initiation of an MD simulation, we have to deal with system preparation (as illustrated in Figure 2.7). The initial step involves constructing the system, often facilitated by tools included in the GROMACS software [176, 177] or the CHARMM-GUI web server [178]. The CHARMM-GUI web server was predominantly employed for constructing systems. The process of building the systems entails specifying the molecules to be included, ion concentrations, and the box dimensions. When dealing with a lipidic system, the box is automatically set to a rectangular shape, with its size contingent on the presence of proteins and the number of water molecules per lipid. Additionally, prior knowledge of the desired simulation temperature is crucial, ensuring compatibility with the molecules used and the chosen force field, as lipid systems can undergo gel-like transformations between a certain temperature.

Energy Minimization

After constructing the system and preparing all requisite files, relaxing the potential energy of the system is necessary to ensure a proper MD simulation. This minimization step is crucial to avoid high forces that could lead to algorithmic failure. Several algorithms exist for energy minimization, including steepest descent and conjugate gradient methods. Within this project, the Steepest Descent (SD) algorithm [179] was adopted.

This technique seeks the local minimum of the current conformation (as depicted in Figure 2.8) by utilizing the first derivative of the energy function. At each step of the process, the SD algorithm adjusts the structure to decrease potential energy by moving opposite to the gradient direction. To achieve this, it relies on the step length, called λ , which is often determined through a "line search" procedure [179]. The new conformation (b) must exhibit lower energy than both the preceding conformation (a) and the conformation obtained by increasing λ (c). When employing a line search, the molecular system

advances in consecutive orthogonal directions across the energy landscape (as depicted in Figure 2.8). Two parameters are essential to halt the minimization process. (i) The threshold for the maximum force (concerning each atoms of the system): once the maximum force is lower than the threshold value, the minimization is stopped. (ii) The maximum number of iterations for the algorithm : a maximum number of steps is defined and once attained, the minimization process is stopped. An example of energy minimization is shown in Figure 2.9, which shows the minimization of three water molecules.

SD serves as an efficient energy minimization technique for addressing unfavorable structures characterized by steric clashes, as it systematically reduces potential energy (Figure 2.8B). Nonetheless, it can encounter convergence issues, occasionally leading to oscillations around a minimum due to the orthogonal nature of consecutive directions. However, SD is generally suitable as a preliminary step before commencing an MD simulation because we just need to relax potential energy, not high convergence such as that needed for normal modes calculations.

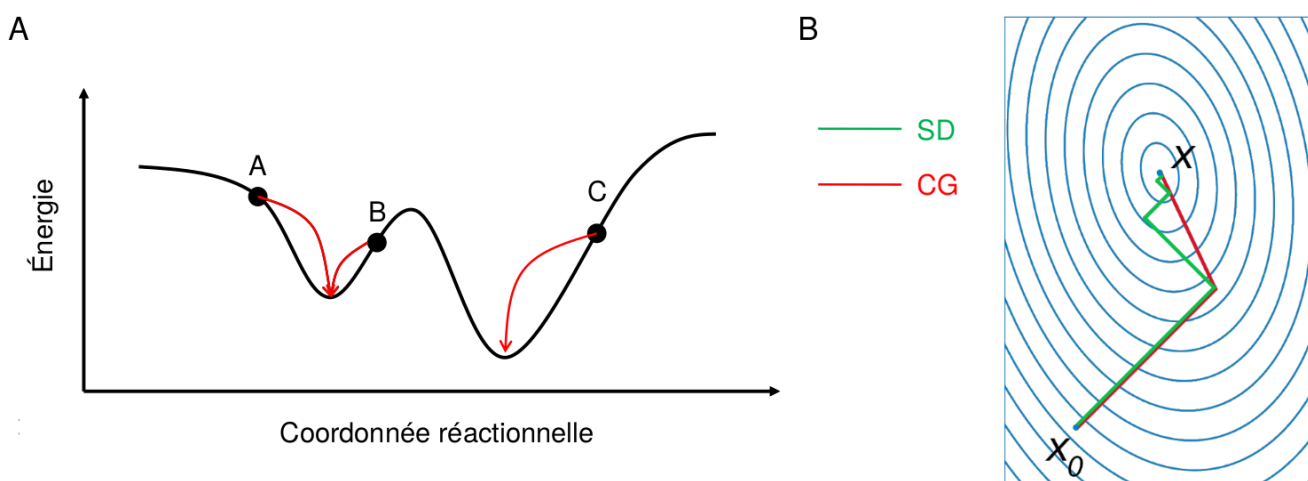


Figure 2.8: **Energy minimization main concepts.** (A) Example of a 2D energy landscape with one local minima and one global minimum. (B) Steepest descent (SD) and Conjugate gradient (CG, only for this figure) example.

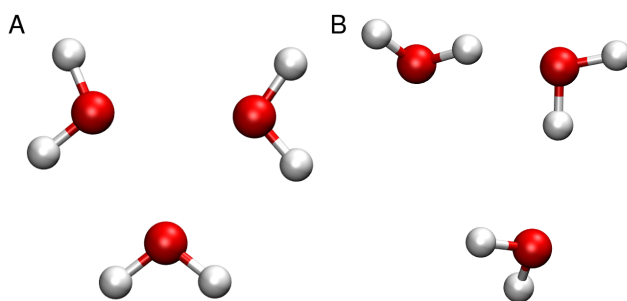


Figure 2.9: **Energy minimization of 3 water molecules.** (A) Three water molecules before minimization. (B) Three water molecules after minimization.

Equilibration Phase

Upon successful completion of energy minimization, the equilibration phase follows. During this phase, a short MD trajectory spanning a few nanoseconds is conducted to raise the system temperature to the desired one and permit molecules to adjust their conformations and relative positions more reliably. Temperature generation involves imparting random velocities to particles following the Maxwell-Boltzmann distribution. Position restraints can also be applied to the main solute molecule (e.g., proteins) to gently relax the solvent around or prevent large conformational changes. For instance, restraining the peptide/protein facilitates relaxation of water molecules around it. In instances where the equilibration phase comprises multiple steps, it's common to apply progressive reductions to the magnitude of position restraints. Equilibration can be initiated with an NVT (constant Number of particles, Volume, and Temperature) phase, followed by an NPT (constant Number of particles, Pressure, and Temperature) phase, although this sequence may vary. During this phase, the Berendsen thermostat and barostat are suitable, as they rapidly attain the desired temperature and pressure. Despite their tendency to produce less reliable fluctuations, this limitation is tolerable since the equilibration phase is not employed for producing results, just for preparing the system towards the next production phase.

Production Phase

The system generated through the preceding stages is now employed for the production step, which serves as the basis for subsequent analysis. This step is conducted under NPT conditions, utilizing the v-rescale thermostat and the Parrinello-Rahman barostat due to their capability to replicate accurate fluctuations. The initial frame of this trajectory is designated as the simulation's starting point, often referred to as "time 0". The first ns of the production are however often discarded for analysis, as the system is still equilibrating. The snapshots of molecules are taken with the visualisation softwares VMD [180].

2.2 Coarse-Grained Molecular Dynamics: two versions of the MARTINI force-fields

Molecular dynamics, as a powerful computational technique, can provide valuable insight in the investigation of intricate biological processes. Its application enables the exploration and analysis of various biological phenomena, thereby contributing to our understanding of complex biological systems. It is important to note that atomistic simulations are constrained to a limited number of molecules and sub-microsecond time scales, while cellular processes often span time scale ranging from nanoseconds to seconds, and involve numerous molecules interacting across various length scales. Consequently, many biologically significant events, such as vesicle fusion, lie beyond the capabilities of atomistic simulations. Coarse-grained (CG) molecular dynamics are a solution to this issue, as their simplistic representation of molecules allows us to model larger and longer timescale biomolecular systems, for a lowest computational cost, while providing realistic structural details. In this thesis, we extensively used this approach, we thus describe with more details in this section how CG MD works.

In our projects, we employed the MARTINI 2.2 (MARTINI2) [162] and MARTINI3.0 (MARTINI3) [164] force-fields for our coarse-grained simulations. The simulations with the MARTINI force fields were carried out using the GROMACS molecular dynamics software package [181, 176, 177], versions 2018 and 2022.

2.2.1 MARTINI2: The coarse-grained model tailored for proteins

The MARTINI force-fields (FF) are the most commonly employed CG force-field. These FFs were parametrized using a top-down approach with thermodynamic partitioning data as the main target [161, 162]. MARTINI uses a four-to-one mapping scheme, meaning that on average four heavy atoms and their associated hydrogens are matched into one CG bead.

The mapping for MARTINI2 is described for lipids and amino acids in Figure 2.10. The Martini model encompasses four primary classes of coarse-grained particles, labeled as C, N, P, and Q, representing nonpolar, moderately polar, polar, and charged chemical groups, respectively (see Figure 2.11B) [161]. Sublabels are employed within each class to further differentiate based on polarity levels or hydrogen donor/acceptor properties. In general, all beads are considered to be of the same size and are referred to as regular (R) beads (Figure 2.11A). However, special small (S) beads were introduced to accurately model ring-like compounds, where the standard four-to-one mapping scheme proves inadequate [161]. Furthermore, to replicate the correct stacking and hydrogen-bonding distances between nucleotides, even smaller tiny (T) beads were deemed necessary [182].

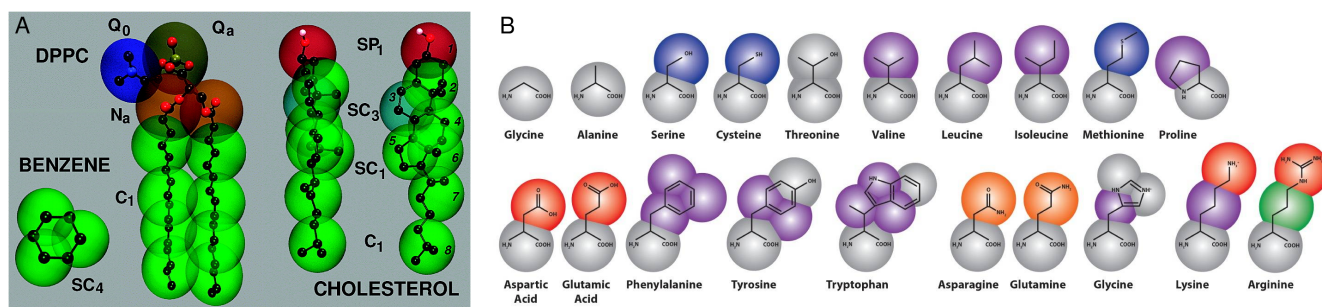


Figure 2.10: **MARTINI mapping.** (A) Mapping between the chemical structure and the coarse grained model for DPPC, cholesterol, and benzene. The coarse grained bead types which determine their relative hydrophilicity are indicated. The prefix “S” denotes a special class of CG sites introduced to model rings. Taken from [161]. (B) Coarse-grained representation of the Martini model extension to amino acids [162], colored by bead type (where purple is apolar, blue and green are intermediate, gray and orange are polar and red represents charged particles). Image taken from [183].

Each amino acid is assigned to a specific class that defines the characteristics of its side chain (Figures 2.10B and 2.11) [162]. Amino acids with apolar side chains, including Leu, Pro, Ile, Val, Cys, and Met, are represented as C-type particles. Polar uncharged amino acids like Thr, Ser, Asn, and Gln are denoted as P-type particles. Raphaëlle Versini Amino acids with small negatively charged side chains, such as Glu and Asp, are categorized as Q-type particles. Positively charged amino acids Arg and Lys are modeled

using a combination of a Q-type particle and an uncharged particle. Amino acids with bulkier ring-based side chains, namely His, Phe, Tyr, and Trp, are represented by three (His, Phe, Tyr) or four (Trp) beads of a special class of ring particles denoted as S. Glycine (Gly) and Alanine (Ala) residues are solely represented by the backbone particle. The type of the backbone particle depends on the protein secondary structure (see Table 2.1): when free in solution or forming a coil or bend, the backbone is strongly polar (P type). In contrast, as part of a helix or β strand, the presence of inter-backbone hydrogen bonds significantly reduces its polar character, leading to the N type. Proline (Pro) is less polar due to its limited hydrogen-donor capabilities.

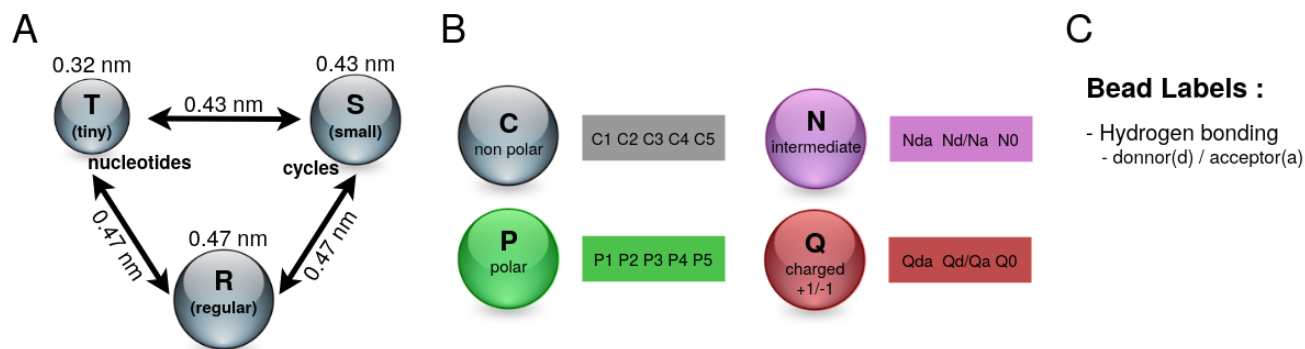


Figure 2.11: **Description of MARTINI2 particles.** (A) Bead size, and associated σ parameters. (B) Beads chemical types (18 different types). Grey is apolar particles, purple is intermediate, green is polar, and red is charged. (C) List of labels used in MARTINI2.

A

		Q					P					N					C				
sub		da	d	a	0	5	4	3	2	1	da	d	a	0	5	4	3	2	1		
Q	da	O	O	O	II	O	O	O	I	I	I	I	I	IV	V	VI	VII	IX	IX		
	d	O	I	O	II	O	O	O	I	I	I	III	I	IV	V	VI	VII	IX	IX		
	a	O	O	I	II	O	O	O	I	I	I	I	III	IV	V	VI	VII	IX	IX		
P	0	II	II	II	IV	I	O	I	II	III	III	III	III	IV	V	VI	VII	IX	IX		
	5	O	O	O	I	O	O	O	O	I	I	I	I	IV	V	VI	VI	VII	VIII		
	4	O	O	O	O	O	I	I	II	III	III	III	IV	V	VI	VI	VII	VIII			
N	3	O	O	O	I	O	I	I	II	II	II	II	II	IV	IV	V	V	VI	VII		
	2	I	I	I	II	O	II	II	II	II	II	II	II	IV	IV	V	VI	VI	VII		
	1	I	I	I	III	O	II	II	II	II	II	II	II	IV	IV	IV	IV	V	VI		
C	da	I	I	I	III	I	III	II	II	II	II	II	II	IV	IV	V	VI	VI	VI		
	d	I	III	I	III	I	III	II	II	II	II	III	II	IV	IV	V	VI	VI	VI		
	a	I	I	III	III	I	III	II	II	II	II	III	II	IV	IV	V	VI	VI	VI		
C	0	IV	IV	IV	IV	IV	IV	IV	III	III	IV	IV	IV	IV	IV	IV	IV	IV	V		
	5	V	V	V	V	V	V	IV	IV	IV	IV	IV	IV	IV	IV	IV	IV	IV	V		
	4	VI	VI	VI	VI	VI	VI	V	IV	IV	V	V	V	IV	IV	IV	IV	V			
	3	VII	VII	VII	VII	VI	VI	V	IV	VI	VI	VI	VI	IV	IV	IV	IV	IV			
	2	IX	IX	IX	IX	VII	VII	VI	VI	V	VI	VI	VI	V	V	V	IV	IV			
1	IX	IX	IX	IX	VIII	VIII	VII	VII	VI	VI	VI	VI	V	V	V	IV	IV				

B

	O	I	II	III	IV	V	VI	VII	VIII	IX
epsilon	5.6	5.0	4.5	4.0	3.5	3.1	2.7	2.3	2.0	2.0
sigma	0.47	0.47	0.47	0.47	0.47	0.47	0.47	0.47	0.47	0.62

super attractive \longrightarrow super repulsive

Table 2.1: **MARTINI2 Interaction Matrix.** (A) The level of interaction indicates the well depth in the LJ potential, described in (B). (B) σ and ϵ parameters for each levels described in (A). Taken from [161].

Non-bonded interactions within the Martini force field are determined by Lennard-Jones potentials for neutral beads, while charged beads also account for Coulombic interactions. The strength of these Lennard-Jones potentials, specifically their well depth, serves to differentiate between various levels of

bead polarity within the coarse-grained particles. Both bonded and non-bonded interactions are described by Equation 2.1. For the van der Waals interactions, which are modeled using Lennard-Jones potentials, the parameter ϵ takes on different values, ranging from $\epsilon_{ij} = 5.6$ kJ/mol for interactions involving strongly polar groups to $\epsilon_{ij} = 2.0$ kJ/mol for interactions between polar and apolar groups, effectively simulating the hydrophobic effect (refer to Table 2.1). The effective size of the particles is dictated by the LJ parameter σ , which remains constant at 0.47 nm for all regular particle types. However, for the specialized class of particles used to model ring-like molecules, slightly reduced parameters are employed to replicate ring-ring interactions, where $\sigma = 0.43$ nm, and ϵ_{ij} is scaled to 75% of the standard value (as illustrated in Figure 2.11). Furthermore, charged groups (designated as type Q) that carry a charge q interact via a Coulombic energy function, with a relative dielectric constant of $\epsilon_{rel} = 15$, reflecting explicit screening. To eliminate the generation of unwanted noise, the non-bonded potential energy functions are utilized in their shifted form, ensuring that both energy and force vanish at the cutoff distance $r_{cut} = 1.2$ nm. Specifically, the LJ potential is shifted from $r_{shift} = 0.9$ nm to r_{cut} , while the electrostatic potential is shifted from $r_{shift} = 0.0$ nm to r_{cut} . The shifting of the electrostatic potential in this manner effectively mimics the impact of distance-dependent screening. Notably, non-bonded interactions between nearest neighbors are excluded from these calculations.

2.2.2 MARTINI3: mitigating overaggregation issues from MARTINI2

While the MARTINI2 force field has proven to be valuable, it revealed certain shortcomings, with the main concern being its tendency to overestimate interactions between proteins and carbohydrates in solution, as well as proteins integrated into lipid membranes [184, 185, 186]. To address the issues, a rebalancing of the force-field was undertaken, which resulted to the development of MARTINI3 [164].

MARTINI2 presents four particle category (Figure 2.11B), but MARTINI3 had three other categories added (seven chemical bead types in total): polar (P), intermediate/non-polar (N), apolar (C), halo-compounds (X), monovalent ions (Q), divalent ions (D) and water (W) (Figure 2.12B) [164]. X, D, and W represent entirely new chemical types that were not present in the previous version. Except for W and D beads, each bead category includes subtypes differentiated by numbers, which indicate their relative polarity level, ranging from 1 (low polarity) to a maximum of 6 (high polarity). N and Q beads show the largest expansion. The inclusion of additional bead types is expected to provide a more precise representation of the chemical properties found in the original atomistic structure. The chemical bead types are categorized into distinct blocks, each having its own set of parameters (such as σ and ϵ). Specifically, P, N, C, and X beads belong to the organic block, while Q and D beads are associated with the ion block. Currently, W is the sole bead included in the solvent block.

Furthermore, three different particle sizes have been introduced for broader applicability in mapping molecules like amino acids: regular (R-bead, assumed default), small (S-bead, denoted with prefix S), and tiny (T-bead, denoted with prefix T) [164]. The bead sizes typically correspond to the mapping of different numbers of non-hydrogen atoms: regular ("R", with a 4-to-1-bead mapping, or simply 4-1),

small ("S", 3-1), and tiny ("T", 2-1).

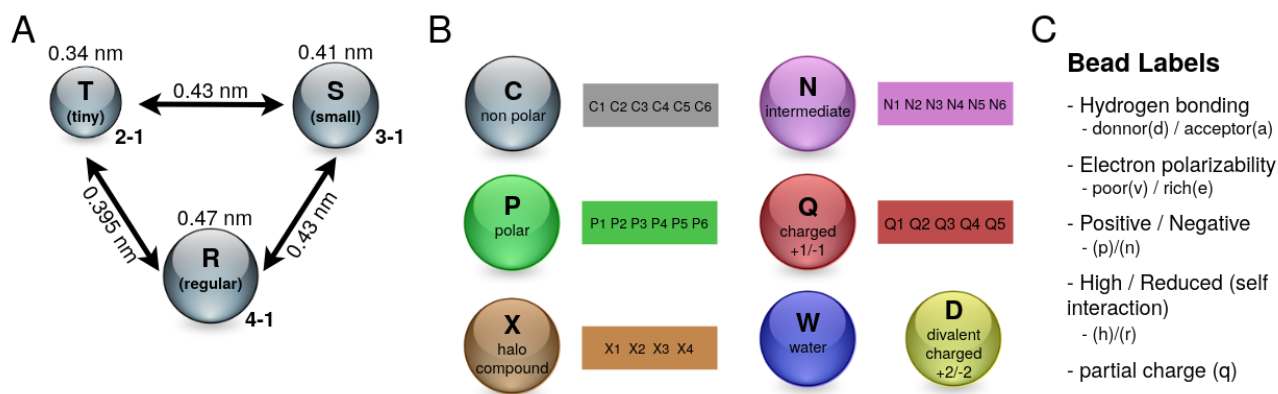


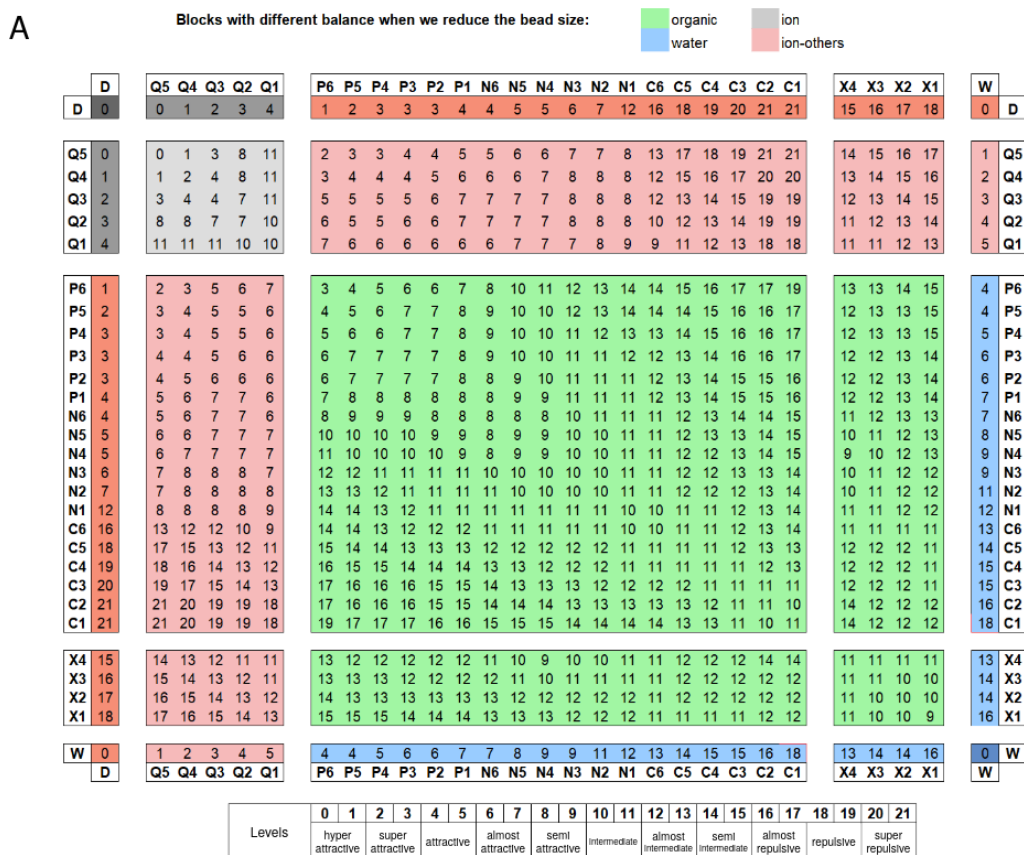
Figure 2.12: **Description of MARTINI3 particles.** (A) Bead size, and associated σ parameters. (B) Beads chemical types (18 different types). Grey is apolar particles, purple is intermediate, green is polar, red is charged, orange is halo-compounds, blue is water molecules and yellow is divalent ions. (C) List of labels used in MARTINI3.

Similar to Martini 2, Martini 3 employs a limited set of epsilon and sigma values (Table 2.2) [164]. These values are categorized into various tiers representing attractive, intermediate, and repulsive interactions. Notably, Martini 3 introduces a broader spectrum of defined levels, in order to facilitate a more gradual shift between distinct chemical bead types. Specifically, in the context of organic and ion-organic block interactions, Martini 3 introduces a total of 22 defined levels, in contrast to the 10 levels present in Martini 2 for these interactions. Additionally, Martini 3 assigns specific sets of levels to the W, D, and Q beads.

The final step in fine-tuning the interactions involves the incorporation of "labels" into particle definitions (Figure 2.12C) [164]. The concept of labels existed in previous versions but was initially limited to N and Q types, where it accounted for varying hydrogen bond capabilities among molecules with similar hydrophobicity levels. In Martini 3, the concept of labels has been expanded and can now be applied to all beads, leading to subtle changes in their behavior, reflected in their associated level within the interaction matrix.

Of these labels, three are chemically specific and are only applied to certain chemical types: hydrogen bonding, electron polarizability, positive/negative. Hydrogen bonding labels are denoted as "d" for hydrogen donors and "a" for hydrogen acceptors. These labels serve to reduce self-interactions between beads with the same hydrogen bond capability. For smaller-sized beads, they enhance interactions between "d" and "a" types. Electron polarizability label is represented by "v" for electron poor (vacancy) and "e" for electron richer, which, similar to hydrogen bond label, decreases self-interaction and increase "e-v" cross-interaction, in a size dependent way. Positive and negative labels (p/n) is related to charged particles. Interestingly, charged molecules can also exhibit hydrogen bonding capabilities, which depend on the sign of their charge. Typically, positive charges function as hydrogen donors, while negative

charges act as hydrogen acceptors. Cross-interactions between the three categories of labels are also defined.



B

Supplementary Table 2: Size and interaction levels for the organic block: $\sigma(O-O)$ and $\epsilon(O-O)$

level	R-R		R-S		S-S		R-T		S-T		T-T	
	σ	ϵ	σ	ϵ	σ	ϵ	σ	ϵ	σ	ϵ	σ	ϵ
0	0.470	5.790	0.430	5.510	0.410	5.130	0.395	5.270	0.365	4.860	0.340	4.300
1	0.470	5.490	0.430	5.210	0.410	4.840	0.395	4.870	0.365	4.510	0.340	4.020
2	0.470	5.240	0.430	4.920	0.410	4.550	0.395	4.540	0.365	4.220	0.340	3.750
3	0.470	4.990	0.430	4.680	0.410	4.290	0.395	4.230	0.365	3.930	0.340	3.470
4	0.470	4.730	0.430	4.400	0.410	4.040	0.395	3.910	0.365	3.640	0.340	3.220
5	0.470	4.480	0.430	4.170	0.410	3.820	0.395	3.670	0.365	3.370	0.340	2.990
6	0.470	4.250	0.430	3.970	0.410	3.550	0.395	3.430	0.365	3.100	0.340	2.740
7	0.470	4.060	0.430	3.770	0.410	3.310	0.395	3.190	0.365	2.830	0.340	2.500
8	0.470	3.880	0.430	3.590	0.410	3.070	0.395	2.940	0.365	2.570	0.340	2.280
9	0.470	3.690	0.430	3.380	0.410	2.840	0.395	2.700	0.365	2.340	0.340	2.020
10	0.470	3.520	0.430	3.160	0.410	2.600	0.395	2.500	0.365	2.110	0.340	1.770
11	0.470	3.390	0.430	2.920	0.410	2.350	0.395	2.310	0.365	1.910	0.340	1.510
12	0.470	3.240	0.430	2.770	0.410	2.200	0.395	2.110	0.365	1.750	0.340	1.230
13	0.470	3.070	0.430	2.530	0.410	2.040	0.395	1.850	0.366	1.600	0.352	1.050
14	0.470	2.960	0.430	2.320	0.410	1.910	0.395	1.670	0.378	1.450	0.366	0.935
15	0.470	2.790	0.430	2.160	0.410	1.750	0.398	1.450	0.394	1.290	0.385	0.855
16	0.470	2.620	0.430	1.930	0.414	1.560	0.399	1.180	0.404	1.130	0.411	0.801
17	0.470	2.440	0.430	1.730	0.418	1.400	0.401	0.983	0.409	1.080	0.424	0.776
18	0.485	2.240	0.443	1.480	0.421	1.250	0.404	0.830	0.423	0.981	0.438	0.731
19	0.520	2.120	0.473	1.280	0.453	1.150	0.465	0.703	0.484	0.890	0.505	0.680
20	0.570	2.000	0.514	1.110	0.496	1.050	0.511	0.659	0.537	0.808	0.561	0.630
21	0.620	1.960	0.552	1.010	0.535	0.986	0.524	0.629	0.588	0.763	0.599	0.620

Table 2.2: **MARTINI2 Interaction Matrix.** (A) Colors indicate blocks with different sets of interaction levels. The level of interaction indicates the well depth in the LJ potential, described in (B). (B) Example of the organic bloc set of σ and ϵ parameters for each levels described in (A). Taken from [164].

The remaining two labels, namely "self-interaction" and "partial charge," are more generic and can be applied to all beads within the organic block. This includes beads that may have already been modified with some of the chemically specific labels. The "self-interaction" labels categorize self-interactions as either higher "h" or reduced "r", but they are limited to certain chemical types. For P/N beads, they mimic minor differences in dipole moments, whereas for C/X beads, they could represent variations in dispersive interactions. Importantly, these labels do not affect interactions between P/N and C/X beads but only influence interactions within these two subgroups. Finally, partial charges were not widely used in the earlier non-polarizable versions of Martini, except for specific applications. However, in MARTINI3, partial charges can be incorporated using the "q" label. The "q" labels modify the Lennard-Jones (LJ) potential of the non-labeled beads in the organic block, assuming that these particles now possess a partial charge. This results in beads with "q" labels having increased interactions with themselves and their environment, particularly with W and Q beads.

2.3 Temperature-Replica Exchange Molecular Dynamics

A classical MD simulation runs for a defined duration at a consistent temperature. However, observing lengthy molecular processes or acquiring a substantial number of conformations can be intricate. Temperature-Replica Exchange Molecular Dynamics (T-REMD) [157] offers an advanced sampling technique. This approach involves simultaneously conducting numerous replicas, each simulated at varying temperatures. Typically, the lowest temperature corresponds to physiological conditions, while the upper temperature can be considerably elevated. For systems involving membranes, the upper temperature is often set around 400K, as this level maintains membrane integrity. To enhance sampling efficiency, a distinct random seed can be assigned to each replica. Throughout the simulation, GROMACS periodically attempts to exchange replicas between adjacent temperatures (i.e., those with consecutive temperatures) and evaluates whether the exchange should occur based on a predefined probability. A fundamental requirement for such an exchange is that the obtained ensemble of conformations at each temperature fulfils the Boltzmann distribution of conformations at equilibrium.

To ensure these requirements, the Metropolis criterion is imposed at each exchange (Equation 2.12). To simplify calculations, we introduce the concept of inverse temperatures, denoted as $\beta_i = \frac{1}{k_B T_i}$ and $\beta_j = \frac{1}{k_B T_j}$, where k_B is the Boltzmann's constant. The Metropolis criterion then reads:

$$p_{i \leftrightarrow j} = \min(1, e^{(\beta_i - \beta_j)(E_i - E_j)}) \quad (2.12)$$

where $p_{i \leftrightarrow j}$ defines the probability of exchanging the temperatures T_i and T_j between replicas i and j , E_i and E_j are the corresponding potential energies. When using the Metropolis criterion, T_i and T_j represent respectively the lower and higher temperature (hence, $T_j > T_i$). Applying the Metropolis criterion consists in selecting the minimum value between 1 and the term $e^{(\beta_i - \beta_j)(E_i - E_j)}$. When $E_i > E_j$, the resulting exponential term is always higher than 1. Hence, the chosen value is 1 and the exchange is auto-

matically accepted. Given that higher temperatures typically correspond to increased potential energies, the more common scenario is actually $E_i < E_j$, which leads to the exponential term falling between 0 and 1. As a result, the probability $p_{i \leftrightarrow j}$ is equivalent to this exponential term. This calculated probability is then compared to a random number drawn from a uniform distribution spanning between 0 and 1. If the random number is less than $p_{i \leftrightarrow j}$, the temperature exchange is accepted; otherwise, it is rejected. As the energy difference and/or temperature difference increases, $p_{i \leftrightarrow j}$ approaches 0, reducing the likelihood of accepting the exchange. It is evident that to enhance the likelihood of a successful exchange, significant overlap of the Gaussian energy distributions is necessary, as depicted in Figure 2.13.

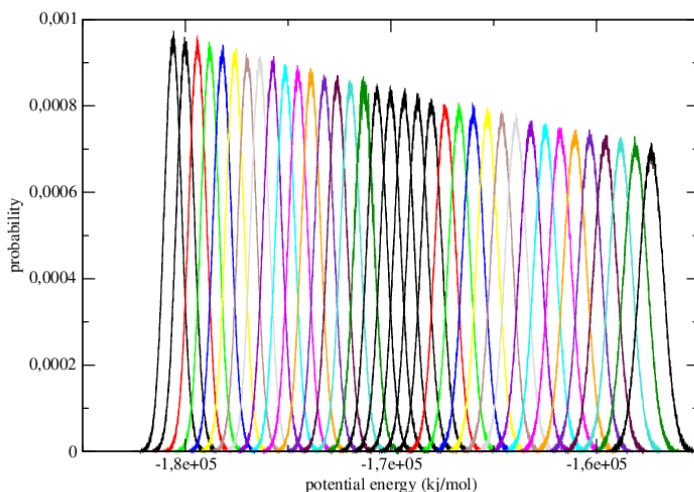


Figure 2.13: **Boltzmann distribution of the Potential Energy of each replica of an T-REMD simulation.**

The utilization of the Metropolis criterion as defined in equation 2.12 ensures the establishment of an appropriate equilibrium Boltzmann distribution. This is because it fulfils the fundamental principle of *detailed balance* [157]:

$$p_{i \leftrightarrow j} p(X) = p_{j \leftrightarrow i} p(Y) \quad (2.13)$$

where $p(X)$ is the probability of the system existing in state X , $p(Y)$ is the probability of the system existing in state Y . What are X and Y ? For instance, in a scenario involving replicas i and j , X is a vector containing the state of all replicas: $X = (i, j)$, prior to the execution of the exchange $i \leftrightarrow j$. On the other hand, $p(Y)$ signifies the probability of the system existing in state Y after the exchange $i \leftrightarrow j$ has been completed ($Y = (j, i)$). The concept of detailed balance essentially signifies that the likelihood of exchanging $i \leftrightarrow j$ from state X equals the likelihood of exchanging $j \leftrightarrow i$ from state Y .

Equation 2.12 is employed when simulating within the canonical ensemble (NVT). However, when

operating in the isothermal-isobaric ensemble (NPT), the consideration of pressure and volume of the replicas becomes necessary [187]. The probability of exchange acceptance then becomes:

$$p_{i \leftrightarrow j} = \min(1, e^{(\beta_i - \beta_j)(E_i - E_j) + (\beta_i P_i - \beta_j P_j)(V_i - V_j)}) \quad (2.14)$$

where P_i and P_j represent the pressure of replicas i and j respectively, while V_i and V_j denote the corresponding system volumes. In most cases, the contribution stemming from volume fluctuations has minimal impact on $p_{i \leftrightarrow j}$ particularly at low pressure settings [188].

Ultimately, upon the successful acceptance of an exchange, the velocities are rescaled to match with the new temperature. The overall concept of Replica Exchange Molecular Dynamics (REMD) is illustrated in Figure 2.14.

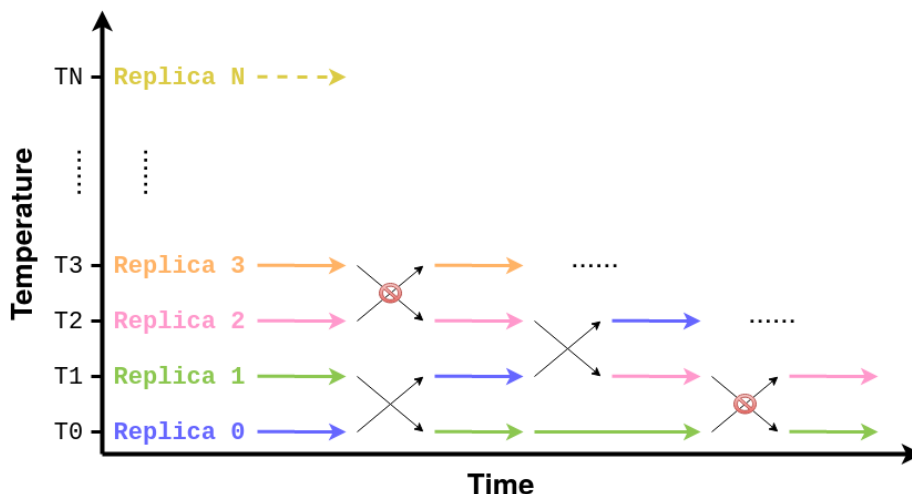


Figure 2.14: **Illustration of the T-REMD method.** A set of n replicas are simulated. At regular intervals, replica exchanges are attempted between neighboring temperatures, some of which are accepted, such as the exchange between replica 0 and replica 1, while others are rejected, like the exchange attempt between replica 3 and replica 4.

How does replica-exchange enhance sampling? Conducting simulations at various temperatures enables the system to explore diverse conformational ensembles while preserving a physically plausible distribution. Moreover, elevating the temperature imparts higher kinetic energy to the molecular system, facilitating its traversal across elevated free energy barriers more effectively than under physiological conditions (Figure 2.15A). As the energy landscapes changes when the temperature increases (Figure 2.15B), these free energy barriers can be further reduced, enhancing the efficiency of the process. As a result, enhanced sampling leads to the exploration of a larger conformational landscape. Furthermore, this method permits the acquisition of data at lower (ambient) temperatures and the stabilization of newly sampled conformations. However, a drawback of this technique lies in the fact that the system kinetics are altered by temperature changes, often making it challenging to extract accurate kinetic information.

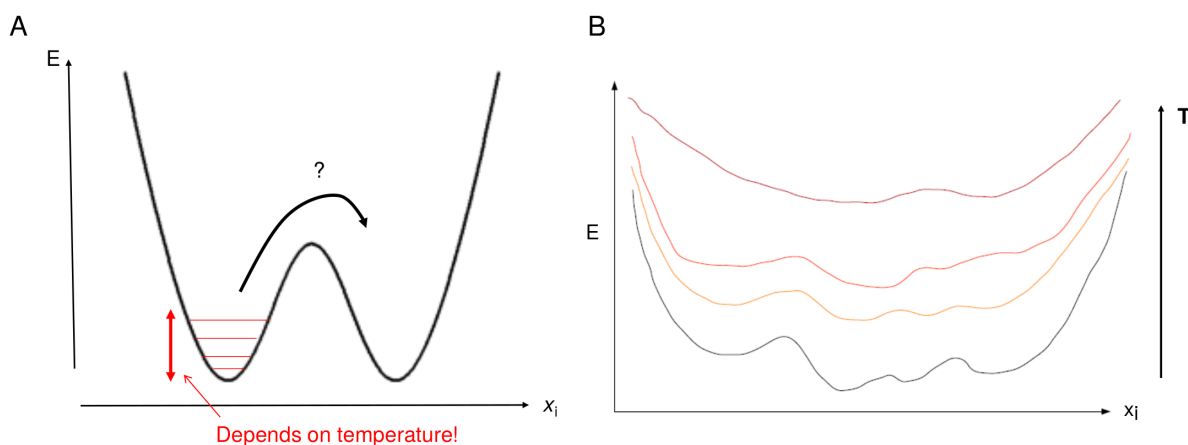


Figure 2.15: **Free energy landscapes and the effects of temperature.** (A) Illustration of the effect of temperature on the free energy barriers. Provided by Patrick Fuchs. (B) Illustration of the effect of temperature on the energy landscape. Taken from the REMD tutorials of Mark Abraham.

When preparing an REMD simulation, meticulous consideration must be given to selecting an appropriate total number of replicas. Striking the right balance is essential; having too many replicas should be avoided, while ensuring that the temperature intervals are sufficiently close for effective exchanges between replicas. The temperature ranges depends on the specific molecular system of interest. Patriksson and van der Spoel proposed a method for predicting these ranges [188]. They also offer a helpful web tool available at <http://virtualchemistry.org/remd-temperature-generator/>. To ascertain the replica temperatures, the initial step involves determining the extreme temperatures. For instance, in our projects, we opted for a range between 300 and 400 K. Moreover, factors such as the number of atoms, constraints (e.g., rigid bonds, rigid water molecules), and the mean acceptance probability of each exchange need to be considered. In this context, a standard value of 0.20, as commonly used in the literature [189], is employed. Utilizing this information, the web server predicts various temperatures by computing a Gaussian distribution of the potential energy, ensuring that there is an overlap between two consecutive temperatures. This overlap plays a crucial role in determining the final probability of exchange. Figure 2.13 provides an illustration of potential energy distributions following an REMD simulation we conducted.

When performing an REMD, the choice of the simulation length and the temperature range are critical. The simulation has to be long enough so that each replica shuttles between the lowest and highest temperatures several times. This depends on the choice of these temperatures. Certain REMD studies involving peptides in water have employed temperatures much higher than 400 K [190]. In this context, we selected 400 K as a compromise. This temperature is sufficiently elevated to augment conformational sampling, while not excessively high to maintain the bilayer structural integrity. Importantly, no position restraints were applied to the lipids. In literature, it has been demonstrated that temperatures exceeding 500 K led to the explosion of a DMPC bilayer [191]. In response, some researchers introduced restraints on lipids to prevent such explosion [191]. We chose not to employ these extreme measures. With the temperatures chosen, the bilayer remains stable, and during the time it takes for a replica at 400 K to

descend to the lowest temperature (which typically spans a few tens of nanoseconds), the bilayer has an opportunity to relax and more closely resemble a genuine bilayer at room temperature. In summary, selecting 400 K struck a favorable balance between intensified sampling and preserving the bilayer structural integrity. For our systems, we typically obtained between 30 and 40 replicas in the range 303-400K or 310-400K. Within a few hundreds of ns, each replica could visit the extreme temperatures several times.

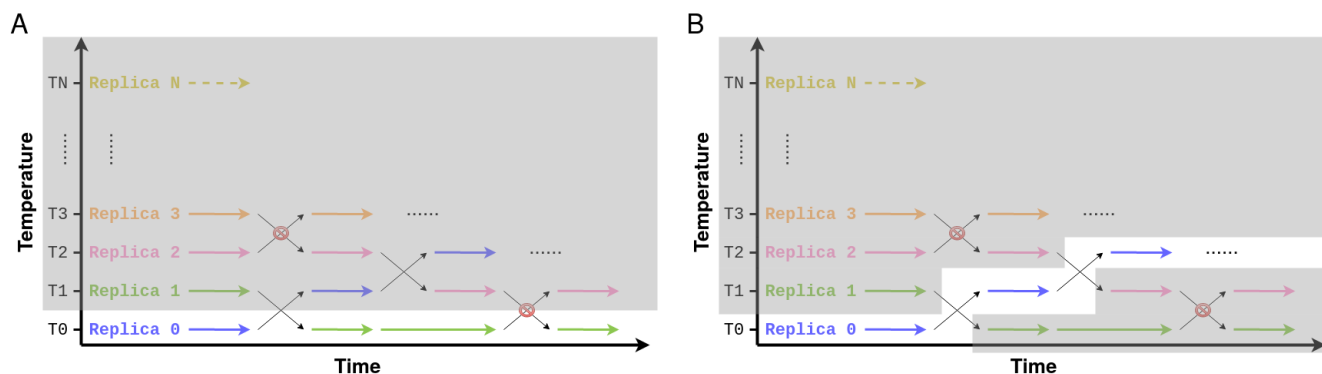


Figure 2.16: **Analysis of REMD.** (A) Ensemble of conformations at the lowest temperature. (B) Continuous replica, transitioning from one temperature to another.

REMD simulations can be analyzed in two ways. Either by temperature or by replica (Figure 2.16). The analysis by temperature is useful for computing averaged properties. It has to be reminded that the successive conformations at a given temperature do not represent a continuous trajectory, since there are frequent exchanges, even if GROMACS delivers these conformations with a time stamp. However, the detailed balance explained above warrants that all the conformations at a given temperature follows a Boltzmann distribution. Thus, we can safely compute averages and we can take advantage of the better sampling thanks to the visit of each replica to high temperatures. For example, if we simulate the folding of a peptide, we can measure the mean helix content at the bottom temperature. This will give more solid statistics compared to a regular MD at the same temperature. The other way of analyzing an REMD is per replica. This time, we follow one (or several) individual replica which diffuses in temperature space. Thus, this represents a continuous trajectory. In the peptide folding example, this would consist in monitoring the different conformations of the peptide between an unfolded to the folded state. This allows to understand the mechanism, for example folding from N- to C- or vice-versa.

2.4 Advancing molecular modeling: Revolutionizing protein structure prediction with AlphaFold

Predicting the three-dimensional structure of proteins has been a pivotal and persistent challenge. In fact, as proteins are central to biological processes, their structure are necessary to provide insights into their functions and mechanism within cells, as well as into the designs of targeted therapies. Modeling proteins using bioinformatics tools is valuable as experimental methods can be time-consuming, expensive,

and/or technically challenging. Prediction methods provide a faster and cost-effective means to predict 3D structures, which can be applied to all proteins, albeit with varying accuracy. AlphaFold [158] and RoseTTaFold [159] are two tools that revolutionized the landscape of structural biology and are considered as largely reliable. In this work, we were able to use AlphaFold.

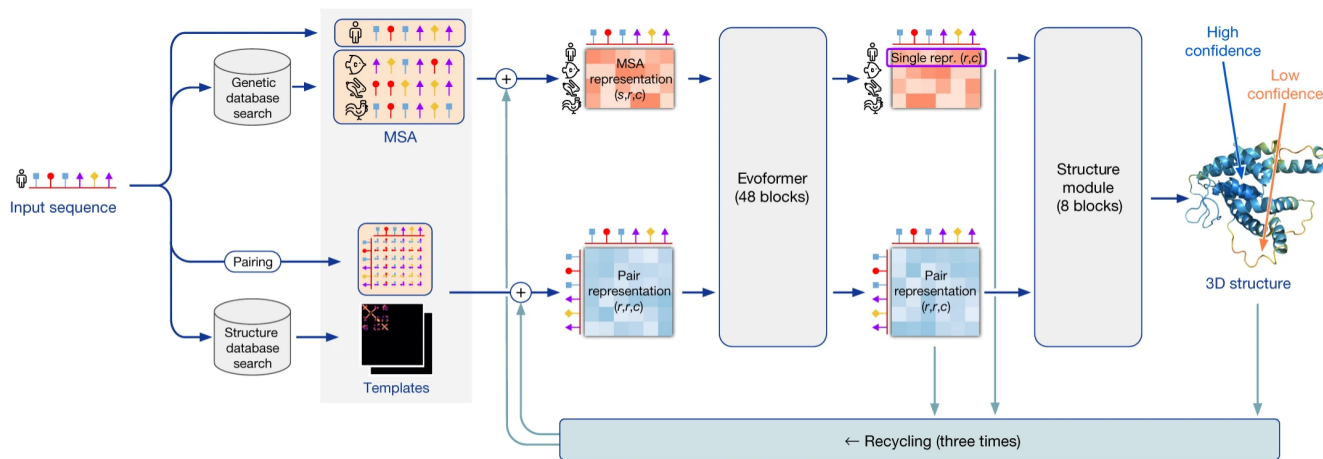


Figure 2.17: **AlphaFold model architecture.** Arrows show the information flow among the various components described in this paper. Array shapes are shown in parentheses with s the number of sequences ; r the number of residues ; c the number of channels.

AlphaFold demonstrates a new architecture (described in Figure 2.17) using both amino acid sequence and multiple sequence alignments (MSAs) to predict the 3D coordinates of all heavy atoms for a given protein [158]. The sequence is given in a fasta file, and the MSAs are built using JackHMMER [192] and HHblits [193]. The MSA can also be provided by the user, in an A3M format. The MSA produced are then used to retrieve templates (a maximum of 4 are used). A pair representation matrix of size $r \times r$ (r , the number of residues) is then built using the sequence and the template provided. These various information are fed to the neural network, which comprises two main stages. (i) The network input processing involves iterative layers of a novel neural network block known as Evoformer. This produces two arrays: one of dimensions $s \times r$ (s , the number of sequences) representing the processed MSA, and the other of dimensions $r \times r$. (ii) Subsequently, the structure module processes the two arrays produced, outputting an explicit 3D structure. This section of the network include breaking the chain structure to allow simultaneous local refinement of all parts of the structure, as well as a novel equivariant transformer, which empowers the network to implicitly infer information about the unrepresented side-chain atoms.

Iterative refinement is applied at the end of the structure module as well as throughout the whole network: the outputs are fed to either the same module (Evoformer module outputs) or the previous module (Structure module outputs). The iterative refinement using the whole network is termed recycling. Each residues of the model is then assigned a value of predicted local-distance difference test (pLDDT), which predicts the C- α local-distance difference test accuracy of the corresponding prediction. The lower this value is, the less confidence the model has in the position of the residue.

CHAPTER 3

MOLECULAR DYNAMICS BASED PREDICTION OF FZO1 TRANSMEMBRANE DOMAINS STRUCTURE

The pages that follow present the initial draft of the article stemming from the principal project undertaken during this Ph.D endeavor. The central focus of this project was a meticulous examination of the transmembrane (TM) domain of Fzo1, a critical protein in mitochondrial fusion. To comprehensively understand this essential domain, we employed a sophisticated multiscale analysis approach, combining MARTINI simulations for a massive conformational sampling and all-atom Temperature Replica Exchange Molecular Dynamics (T-REMD) for detailed, high-resolution refinement and test of robustness. Furthermore, experiments were carried out by our ANR collaborators Laetitia Cavellini and Michael Cohen. This combined methodology allowed us to gain intricate structural knowledge about the TM domain of Fzo1, providing a foundation for unraveling its functional intricacies and contributions to mitochondrial dynamics. The aim was to not only unravel the structural aspects but also to shed light on how this domain potentially influences the fusion process. Through this concerted effort, we sought to bridge the gap between structural understanding and functional implications, forming a solid basis for further explorations into the dynamics of mitochondrial fusion.

All simulations and their analyzes were performed by the Ph.D. student. The experimental work was completed by our collaborator Mickael Cohen and his team.

3.1 Introduction

Mitochondria form a complex network inside the cells, undergoing continuous fusion and fission events. These processes shape mitochondrial dynamics and are essential for the maintenance, function, distribution and inheritance of mitochondria. The morphology of the latter therefore respond to the ever-changing physiological changes of the cell [3].

Mitofusins are large GTPase transmembrane proteins involved in the tethering to and fusion of mitochondrial outer membranes (OM) [91]. The mitofusins Mfn1 and Mfn2 are found in mammals [97, 98]. Fzo1 (*Fuzzy Onion 1*) is the only mitofusin homolog in *Saccharomyces cerevisiae* [94]. The structure of Mfn1 was partially solved, but without its transmembrane domain [194, 195], and no solved structures are available for either Mfn2 or Fzo1. Mitochondrial inner membrane fusion and crista organisation are mediated by human OPA1 (*Optic Atrophy 1*) [196] and yeast Mgm1 (*Mitochondrial Genome Maintenance 1*) [197].

Mitochondrial fusion dysfunction can cause neurodegenerative diseases such as Parkinson's, Alzheimer's, and Huntington's [117, 118] as well as cancer [123, 126]. A number of studies have linked Mfn1 and Mfn2 to various cancers, including breast cancer [127], liver cancer [128], lung cancer [129], cervical cancer [130], and colon cancer [131]. They showed that their dysregulated expression was associated with increased cell proliferation, invasion, and resistance to chemotherapy. Regulation of mitofusin activity has been shown in preclinical studies to reduce cancer cell growth and spread. In addition, research has shown that mutations in Mfn2 trigger the development and progression of muscular dystrophies such as Charcot-Marie-Tooth type 2A, the most common form of axonal CMT disease [119, 120]. The precise mechanism by which mitofusins contribute to cancer or neurodegenerative disease, as well as the exact molecular fusion mechanism mediated by mitofusins, require further structural investigation.

From other membrane fusion machines such as the SNARE proteins, we know that anchoring in the membrane, transmembrane domain amino-acid composition, and dynamic properties are crucial elements that determine the interplay between the main players of the fusion process at different stages [198, 199, 200, 201]. With the help of a membrane-embedded structural model of Fzo1, such properties, the fusion itself as well as its intermediate stages could be studied by computational approaches, in particular molecular dynamics simulations. To this end, we are striving to build a complete structural model of Fzo1, including in particular the fusion-related transmembrane domains, for which we have very limited data.

Fzo1 has two heptad repeat domains (HRs) with coiled-coils on its N-terminal side: HRN (only in yeast) and HR1 flanking a GTPase domain. A third heptad repeat domain HR2 is located at the C-terminus [94, 202]. Some models of Fzo1 are based on the mitofusin-related bacterial dynamin-like protein (BDLP) [65, 68]. BDLP is involved in membrane remodelling and exists in two conformational states, a closed, compact version that transitions to an open, extended structure upon GTP binding. The latter structure can therefore bind lipid bilayers and results in self-accelerating polymerization leading to

a coated lipid bilayer and strong curvature. However, BDLP has no transmembrane part, whereas Fzo1 is embedded in the mitochondrial OM via two transmembrane segments exposing N- and C-terminal parts to the cytosol and a loop to the intermembrane space [99]. The two transmembrane segments are putative α -helices called TM1 and TM2 [1].

We previously constructed an initial model of Fzo1 based on the closed compact conformation of BDLP, which was experimentally validated by mutation studies [1]. The opened extended structure of BDLP was used to create a second model [2, 133]. In the absence of a BDLP transmembrane template, the structure of TM1 and TM2 of Fzo1 was predicted using an *ab initio* method, namely the PREDDIMER [156] web server. Here we attempt a more comprehensive investigation of the possible membrane associations of the two helices to form a dimer using coarse-grained molecular dynamics simulations. Indeed a new version of the popular Martini force field, solved a bias favoring protein/protein association in membranes [164]. This new force field, Martini 3, therefore paved the way to more realistic studies of membrane protein associations[203]. In the case of Fzo1, the TM domain presents a particular challenge, as there is a basic conserved lysine residue in the middle of TM1. In addition to dimerization itself, we are also investigating the extent to which the protonation state of this residue may affect dimer stability, membrane incorporation, and destabilization. Lysine protonation may be functionally relevant, as the literature has hypothesized specific roles for individual transmembrane domains in fusion and, in particular, charge-related effects. Specifically for the SNARE system, Lindau *et al.* postulated a mechanism in which the formation of fusion pores is triggered by the movement of the charged C-terminus of the transmembrane helix syb2 within the membrane [198].

Through extensive molecular simulations across coarse-grained and atomistic scales, we arrive at an improved model of the Fzo1 transmembrane domain that reveals new insights into the dimerization interface, key regulatory residues, and their potential influences on mitochondrial fusion.

3.2 Materials and Methods

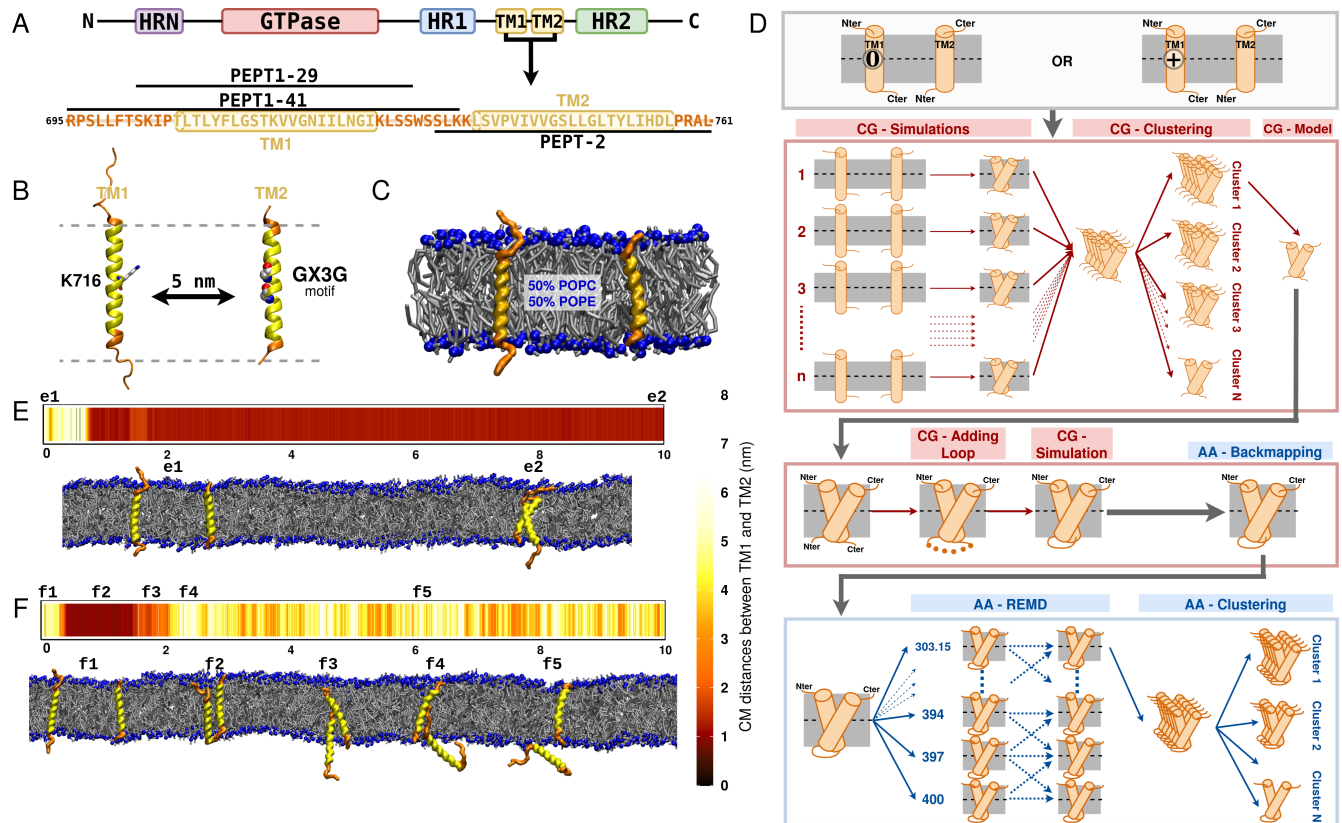


Figure 3.1: **Protocol.** (A) Sequence definition of the peptides PEPT1-29, PEPT1-41 and PEPT2. The TM domains are represented in yellow and the flanking residues are in orange. This color code is maintained for the snapshots in B,C,E,F. (B) Images of the all atom structures of the peptides PEPT1-41 and PEPT2. (C) Snapshot of the coarse-grained system. In blue are the phosphate groups, in silver are the lipids POPC and POPE. (D) A detailed scheme of the protocol. (E) Center of mass distances throughout the simulation, with snapshots of the beginning and end point. (F) Center of mass distances throughout the simulation, for a replica with TM1 expelled from the membrane. Snapshots throughout the simulations.

The transmembrane (TM) domain of Fzo1 contains two TM α -helices (called TM1 and TM2) connected by a loop, plus some flanking residues on the N-terminal part of TM1 and C-terminal part of TM2. In addition, TM1 possesses a lysine residue (Lys716) at its exact center, thus located in the middle of the membrane. It therefore questions its protonation state knowing that the local pKa of lysine may go below 7.0 in very apolar environments [204, 205, 206].

The computational protocol used in this study consisted in two main parts. The first part used coarse-grained (CG) simulations for sampling the TM1/TM2 contacts and selecting the best possible TM1/TM2 dimer. Two CG force-fields (Martini 2 and Martini 3) were tested as well as the two protonation states of Lys716 (neutral or positively charged). In the second part, the best CG dimer was chosen, the loop between TM1 and TM2 added, the structure backmapped to an all-atom (AA) representation, followed by AA simulations to refine the whole Fzo1 TM domain. Everything is summarized in Figure 3.1. Below,

we explain the details of each part. The GROMACS 2018.5 program was used to perform all molecular dynamics (MD) simulations [177].

3.2.1 Coarse-Grained conformational sampling

Peptide Definition

The *S. cerevisiae* Fzo1 sequence and domains were obtained from the UniProtKB database (Universal Protein Resource Knowledgebase [207], entry: P38297). The secondary structures of the protein were predicted using PSIPRED 4.0 [208, 209]. The positions of the transmembrane helices of Fzo1 were determined using TMHMM2.0 [210, 211]. Some peptides were defined (PEPT1 or PEPT2) which contained either TM1 or TM2 respectively, plus various flanking residues: one from Arg695 to Lys735 called PEPT1-41 (of 41 residues length), an other from Ser702 to Ser730 called PEPT1-29 (of 29 residues length), and a last one from Ser733 to Leu761 called PEPT2 (of 29 residues length). PEPT1-29 and PEPT2 were used with Martini 2, whereas PEPT1-41 and PEPT2 were used with Martini 3. All sequences are shown in Figure 1A. The peptide 3D-structures were built using Basic Builder 1.0.2 on the Moby server (<https://moby.le.rpbs.univ-paris-diderot.fr>) [212]. The residues from Thr706 to Ile726 (TM1) and from Leu737 to Leu57 (TM2) were defined as a perfect α -helix and the flanking residues were defined as coil. This step gave a first all-atom 3D structure for each peptide, which was then used as an input to Martini / CHARMM-GUI tools (next section).

Box setup

When we started the work, Martini 2 was the main CG Martini force field and Martini 3 was in its beta version. However, Martini 3 force field came out during the course of this work [164]. We thus decided to test the two versions of the force-field Martini 2 or Martini 3. We also tested the two possible charge-states of Lys716 (positively charged or neutral), resulting in a total of four systems.

The Martini 2 systems were built using the CHARMM-GUI Membrane builder [178, 213, 163] with the Martini 2 coarse-grained (CG) force field [161, 162]. The two peptides were separately embedded in a mixed lipid bilayer of 50 palmitoyl-oleoyl-phosphatidylcholine (POPC) and 50 palmitoyl-oleoyl-phosphatidylethanolamine (POPE) (these two lipids are the most abundant in mitochondrion OM). Thus we had one box with PEPT1 (PEPT1-29 or PEPT1-41) and another one with PEPT2. About 40 water molecules per lipid were used as solvent for both PEPT1-29 and PEPT2, and about 50 water molecules per lipids were placed in the system of PEPT1-41. To the solvent were added 0.15M of NaCl for each system. The two systems were then assembled, in order to have the two peptides embedded in the same membrane at a distance of about 5.2 nm. In order to obtain a neutral Lys716 system, we replaced in the ITP file the Qd charged bead by a P1 neutral and polar bead.

Since the mapping between Martini 3 and Martini 2 is different, we could not convert the topologies directly. Instead, the Martini 3 systems were built from atomistic models of the peptides (using the same coordinates than for Martini 2) using the martinize2.py workflow module (see <https://github.com/>

marrink-lab/vermouth-martinize). These Martini 3 structures of the peptides were then placed in lieu of the peptides structures in the Martini 2 system. In order to obtain a neutral Lys716 system, we replaced in the ITP file the SQ4p charged bead by a SN6d neutral and polar bead. As the mapping of the lipids did not change between the two versions of the force-field, we were able to use the membranes produced with Martini 2.

Simulation parameters

For all systems, we followed the protocol of CHARMM-GUI which consisted in two energy minimizations of 5000 steps, followed by an equilibration of 5 simulations within the NPT ensemble. The velocity-rescaling thermostat [174] at 303.15 K and the Berendsen barostat at 1 bar [173] were applied for a sequence of 5 simulations of 1 ns, 1 ns, 1 ns, 0.75 ns and 1 ns (with a timestep of 0.002 ps, 0.005 ps, 0.01 ps, 0.015 ps, 0.020 ps respectively). From the equilibrated system, a last step of 1 ns equilibration (time step 0.020 ps) with the same thermostat and barostat parameters was then used to redefine the velocities of the system (with a fixed seed). A production run of 10 μ s followed, at 303.15 K using the velocity-rescaling thermostat [174] (lipid, water and proteins coupled separately) and 1 bar using the Parrinello-Rahman barostat [175] (compressibility of $3.0 \times 10^{-4} \text{bar}^{-1}$). Pressure coupling was applied semi-isotropically. These final two steps were repeated multiple times, the seed being changed for each preceding equilibration step. A time step of 0.020 ps was used with the leapfrog integrator. Lennard-Jones interactions were cutoff at 1.1 nm. Bond lengths were constrained using the LINCS algorithm [214]. The reaction-field method [215] was used for evaluating electrostatic interactions, with a Coulomb distance cutoff of 1.1 nm, a relative dielectric constant of 15. The neighbor list was updated every 20 steps.

Clustering and model extraction

We ran as many simulations as necessary in order to obtain 25 trajectories ending in successful dimerization for each condition (two Martini versions and two protonation states). The unsuccessful trajectories were discarded. The successful ones were submitted to a conformational based clustering. The first 2 μ s of the productions were systematically ignored. All simulations were then concatenated (using 161 frames per simulation representing 8 μ s) resulting in a total of 4025 frames. This concatenated trajectory was used as input to the *gmx cluster* program of GROMACS. The GROMOS method [181] was used. Briefly, one first computes the pairwise RMSD matrix of TM1 and TM2 (RMSD of all pairs of conformations, considering backbone beads only) and then group conformations in different clusters. Within each cluster, any pair of conformations presents an RMSD below a cutoff that has to be chosen. This non-supervised method (the number of clusters is not fixed and is a result of the clustering) maximizes the size of the clusters. The cutoff was set to 0.3 nm in order to get 5 to 6 clusters totalizing 80 to 90 % of all conformations.

Trajectory analysis

The crossing angle between the TM domains calculation was calculated as described by Chothia *et al.* [216] using an in-house script. Only the backbone beads of TM1 and TM2 were considered.

Contacts between TM1 and TM2 were studied using the python library MDAnalysis [217, 218]. The minimum distance between each residues was then plotted using the R library ggplot2 [219].

A principal component analysis (PCA) of the cartesian coordinates was carried out using the programs *gmx covar* and *gmx ana eig* of the GROMACS package. It was done on a combined trajectory of the dimerized structures of the 4 systems using the backbone beads of TM1 and TM2. The results are presented in terms of free energy projection against the two first principal components (PC1 and PC2) using a grid:

$$\Delta G(i, j) = -RT \ln p_{ij}$$

where i and j are indices of the grid points, p_{ij} the probability of finding a conformation in grid point (i, j) and $\Delta G(i, j)$ the relative free energy of that grid point. The lowest free energy was set to 0 kJmol^{-1} . 150 grid points were used for PC1 and PC2.

Lipid packing defects are small apolar areas of the membrane which are accessible to water. They were quantified using PackMem [52, 145]. A protrusion event is defined as one of the carbon atom of a tail bulging into the polar layer (or a backbone bead of a lipid tail), extending 0.1 nm above (or below depending on the leaflet) its phosphorus atom [146, 147]. Protrusions were identified using an in-house script. Both analyses were performed separately for each leaflet.

3.2.2 All-Atom refinement of the model

The CHARMM36m force field for proteins [220] and CHARMM36 for lipids [170] were used for the remaining all-atom simulation described in this section.

System building and equilibration

Prior to all-atom simulations, the loop between TM1 and TM2 was reconstructed and sampled using CG simulations. We used position-restraints on TM1 and TM2 in order to keep the contacts predicted in the previous phase. The details of this step can be found in the Supplementary Material (section 3.6). Briefly, the best loop conformation was chosen based on conformational clustering.

The whole TM domain including the loop was then backmapped using the CHARMM-GUI backmapping tool [221]. We reduced the box size in order to have 100 lipids located around the TM domains, as well as 40 water molecules per lipids and 0.15M of NaCl. In total, the system consisted in 26144 atoms.

The preceding step introduced a layer of vacuum on the box edges. Using 8 minimizations of 5000 steps, we progressively shrunk the box size to get rid of this vacuum layer and recover periodic boundary conditions. The system was then submitted to a sequence of 6 equilibrations of 125 ps, 125 ps, 2 ns, 2 ns, 2 ns, and 2 ns (with a timestep of 0.001 ps, 0.001 ps, 0.001 ps, 0.002 ps, 0.002 ps, 0.002 ps respectively) in which we progressively released the position-restraints on the protein. The first two equilibrations were performed within the NVT ensemble, with the Berendsen thermostat, and the follow-

ing simulations were performed within the NPT ensemble, with the Berendsen thermostat and barostat. The temperature was maintained at 303.15 K and the pressure at 1 bar. Pressure was applied semi-isotropically. Electrostatic interactions were calculated with the particle-mesh-Ewald (PME) method [166, 167], with a real-space cutoff of 1 nm. Van der Waals interactions were computed using a Lennard-Jones force-switching function over 10 to 12 Å. Bond lengths were constrained using the LINCS algorithm [214]. Water molecules were kept rigid with the SETTLE algorithm [222].

Temperature replica-exchange molecular dynamics

In order to explore efficiently the conformational landscape of the TM domain, we used temperature replica-exchange molecular dynamics (T-REMD)[157]. The replica temperatures were predicted using the webserver <https://virtualchemistry.org/remd-temperature-generator/> [188] by setting the exchange probability to 0.2 and the temperature range between 303.15 and 399.83 K. The upper limit of nearly 400 K was chosen so that conformational sampling of the protein was more efficient, but the membrane stayed intact (if heated too much, it can explode). In total, we obtained 38 replica.

Each replica was equilibrated at the chosen temperature for 1 ns (time step 0.002 ps) using the Berendsen thermostat and barostat (at 1 bar) with different starting velocities. The production run of 500 ns followed with the velocity-rescaling thermostat [174] (lipid, water and proteins coupled separately) and the Parrinello-Rahman barostat at 1 bar [175] (compressibility of $4.5 \times 10^{-5} \text{bar}^{-1}$). Exchanges between neighboring replicas were attempted every 10 ps. The other settings were identical to those described in the previous section.

Trajectory analysis

All the analyses were performed either based on individual replica that diffuse in temperature, or on the conformations of the bottom temperature (303.15 K). On the latter, crossing-angles (using helical $C\alpha$ atoms only), conformational clustering (using a cutoff of 0.2 nm and a distance between the TM1 and TM2 center of mass below 2 nm) and contact-maps were calculated using the same programs as for the CG simulations. The cutoff of 0.2 nm used for the clustering was chosen so that each cluster roughly coincided with the group of points obtained in the PCA analysis below.

A PCA was carried out on a trajectory combining the REMD structures used for the clustering and the Martini 3 neutral Lys716 structures. To do this, the all-atom conformations were converted to a CG representation, and concatenated to the Martini 3 structures for the covariance matrix calculation. Only the backbone beads of TM1 and TM2 were considered.

A conformational clustering was performed on the $C\alpha$ atoms of TM1 and TM2 using the same algorithm and tool as for CG simulations (cutoff of 0.2 nm). The central structure of the first and third clusters were then extracted. We selected these two structures because of their positioning within the deepest energy wells identified by the previous PCA.

Hydrogen bonds were calculated using *gmx hbond* from GROMACS 2018.5. Contacts within a dis-

tance cut-off of 3.5 Å and up to 30 degree off-axis angle were considered.

3.2.3 AlphaFold2 predictions

To predict the structures of Fzo1, we used Alphafold version 2.2 [158, 223], and Colabfold 1.3.0 [224], both monomer and multimer versions. The provided sequences of Fzo1 (from residues 491 to 813, total length of 323 residues, Uniprot: P38297) and Ugo1 (Uniprot: Q03327) were taken from uniprot [207].

Plasmids, yeast strains and growth conditions.

Mutations on K716 (plasmids MC430, MC437, MC587 and MC589, Table1) were generated by PCR using QuikChange Lightning Site-Directed Mutagenesis Kit (Agilent Technologies 210518, Santa Clara, California, USA). The QuikChange Primer Design Program is available online at <https://www.agilent.com/store/primerDesignProgram.jsp> and was used to design mutagenic primers based on the Fzo1 sequence. Standard methods were used for growth, transformation and genetic manipulation of *S. cerevisiae*. Minimal synthetic media [Difco yeast nitrogen base 291940 (Voigt Global Distribution, Inc., Lawrence, Kansas, USA), and drop-out solution] supplemented with 2% dextrose (SD) or 2% glycerol (SG) were prepared as previously described in Sherman et al, J. Methods in Yeast Genetics (1986)[225]. All experiments were performed with the fzo1D shuffle strain MCY571 where mitochondrial fusion efficiency is maintained by the pRS416-FZO1 shuffle plasmid carrying a copy of the Fzo1 wild-type gene and the URA3 selection marker. This strain was transformed with the pRS314 FZO1 plasmids described in Table 1 carrying the TRP1 selection marker and resulting transformants were plated on SD selective media lacking uracil and tryptophan. Colonies were isolated on SD selective media and replica-plated on 5'-fluoroorotic acid (5'-FOA) plates to cure the strains from the FZO1 shuffling plasmid.

Spot assays.

Cultures grown overnight in SD selective media lacking tryptophan were pelleted, resuspended at OD₆₀₀=1 and serially diluted (1:10) four times in water. Five microliters of the dilutions were spotted onto SD and SG selective plates and grown for 2 days at 23 °C, 30 °C or 37 °C.

Protein extracts and immunoblotting.

Cells grown in SD selective media lacking tryptophan were collected during the exponential growth phase (OD₆₀₀ = 0.7–1). Total protein extracts were prepared using the NaOH/trichloroacetic acid (TCA) lysis technique[226]. Proteins were separated on 8% SDS-PAGE gels and transferred to nitrocellulose membranes (Amersham Protran 0,45 µm 10600002; GE Healthcare, Little Chalfont, United Kingdom). The primary antibodies used for immunoblotting were monoclonal anti-Pgk1 (Abcam ab113687, Cambridge, United Kingdom) and polyclonal anti-Fzo1 (generated by Covalab, Bron, France). Primary antibodies were detected using horseradish peroxidase-conjugated secondary anti-mouse or anti-rabbit antibodies (HRP, Sigma-Aldrich 12-348 and A5278, Saint-Louis, Missouri, USA), followed by incubation

with a Clarity Western ECL Substrate (Bio-Rad 1705060, Hercules, California, USA). Images of the immunoblots were acquired using a Gel Doc™ XR+ (Bio-Rad) and analysed using the Image Lab 3.0.1 software (Bio-Rad).

Table 3.1: **Plasmids used in this study.**

Name (Collection number)	Description	Reference
pRS314 (MC219)	CEN, TRP1, Amp	[227]
pRS314-FZO1 (MC250)	CEN, FZO1 promoter-FZO1, TRP1, Amp	[228]
pRS314-FZO1-K716R (MC430)	CEN, FZO1 promoter-FZO1-K716R, TRP1, Amp	This study
pRS314-FZO1-K716S (MC437)	CEN, FZO1 promoter-FZO1-K716S, TRP1, Amp	This study
pRS314-FZO1-K716V (MC587)	CEN, FZO1 promoter-FZO1- K716V, TRP1, Amp	This study
pRS314-FZO1-K716I (MC589)	CEN, FZO1 promoter-FZO1- K716I, TRP1, Amp	This study

Table 3.2: **Saccharomyces cerevisiae strains used in this study.**

Name	Genotype	Reference
FZO1 (MCY571)	MAT α ura3-1 trp1-1 leu2-3,112 his3-11,15 can1-100 fzo1 Δ ::LEU2 pRS416-FZO1	[1]
fzo1 Δ (MCY620)	MAT α ura3-1 trp1-1 leu2-3,112 his3-11,15 can1-100 fzo1 Δ ::LEU2 pRS314	This study
FZO1 (MCY1261)	MAT α ura3-1 trp1-1 leu2-3,112 his3-11,15 can1-100 fzo1 Δ ::LEU2 pRS314-FZO1	This study
FZO1-K716R (MCY1402)	MAT α ura3-1 trp1-1 leu2-3,112 his3-11,15 can1-100 fzo1 Δ ::LEU2 pRS314-FZO1-K716R	This study
FZO1-K716S (MCY1425)	MAT α ura3-1 trp1-1 leu2-3,112 his3-11,15 can1-100 fzo1 Δ ::LEU2 pRS314-FZO1-K716S	This study
FZO1-K716V (MCY2258)	MAT α ura3-1 trp1-1 leu2-3,112 his3-11,15 can1-100 fzo1 Δ ::LEU2 pRS314-FZO1-K716V	This study
FZO1-K716I (MCY2259)	MAT α ura3-1 trp1-1 leu2-3,112 his3-11,15 can1-100 fzo1 Δ ::LEU2 pRS314-FZO1-K716I	This study

3.3 Results

3.3.1 The association of transmembrane helices is reproducible with two coarse-grained force fields

Our aim was to predict the structure of the transmembrane domain of Fzo1 in a 1:1 POPC-POPE bilayer. This lipid composition was chosen considering the two most abundant phospholipids in the outer mitochondrial membrane and was the same as in our previous study [1]. To evaluate the possible associations between the two helices TM1 and TM2 in coarse-grained (CG) simulations, the domain was cut into two parts and some peptides were defined containing either TM1 or TM2: PEPT1-29, PEPT1-41, and PEPT2. Each sequence contains also some flanking residues on both the N- and C-terminal sides (see Figure 3.1A). In the simulations performed with the Martini 2 force field, PEPT1-29 and PEPT2

were used. However, in the simulations performed with the Martini 3 force field, this short version of the TM1-containing peptide, PEPT1-29, was observed to exit the membrane, preventing dimerization events. Inspired by a recent study of Martini 3 dimerization of TM-helices [203], we replaced the short sequence with the longer PEPT1-41 variant, which contains additional flanking residues at both the N- and C-termini, effectively reducing the number of ejections. The longer TM1 sequence allowed us to generate 25 successful dimerizations (for each protonation state of Lys716) for subsequent analyses. Because the simulations with Martini 2 and Martini 3 produced quite similar results in terms of dimer associations, and because Martini 3 addresses a number of shortcomings of Martini 2, such as exaggerated protein-protein aggregation, we decided to present only the Martini 3-based results in the remaining sections of this article. The corresponding Martini 2 results can be found in supplementary Figure S3.4.

3.3.2 Protonation of Lys716 interferes with the formation of a stable TM1-TM2 dimer

The simulations were started with a distance between the two peptides of about 5.2 nm. Most of the time, spontaneous and irreversible dimerization was observed (Figure 3.1 e1-e2 and f1-f2), but sometimes the peptide containing TM1 was ejected from the membrane (Figure 3.1 f3-f4-f5). All ejections occurred on the intermembrane side, which corresponds to the lower leaflet in our simulations. When dimerization occurred, we observed that the distance between the two peptides stabilized at 1.5 nm. This event generally occurred within the first 2 μ s in each replicate (supplementary Figure S3.1A). In the Martini 2 simulations, dimerization was irreversible in all runs (supplementary Figure S3.1A). In contrast, in a considerable number of Martini 3 simulations, TM1 ejection occurred, which affected the dimerization process. We therefore had to run up to 63 simulations with Martini 3 to obtain the targeted set of 25 trajectories that ended with a stable dimer (supplementary Figure S3.1A and S3.1B). For charged Lys716, we observed almost 5 times more ejections (38 ejections versus 25 dimerizations) than for the neutral version (8 ejections versus 25 dimerizations) (see supplementary Figure S3.1). The lower propensity for dimerization observed with Martini 3 when Lys716 is charged underscores the greater compatibility of a neutral form for self-association within the hydrophobic environment of the membrane.

3.3.3 Protonation of Lys716 acts as a switch for remodeling the TM1-TM2 interface

Next, we analyzed the TM1-TM2 contacts that resulted from the CG simulations after dimerization. To identify the most important dimer conformations from the two sets of 25 trajectories, we clustered the dimers using the GROMOS method [181]. This clustering was based on the pairwise RMSD matrix of the backbone beads of each pair of dimerized TM domain conformations. In the Martini 3 simulations with a neutral Lys716, clustering resulted in 5 clusters representing 96% of the conformations, with the first 3 clusters corresponding to 91.4% of the structures. However, when Lys716 was charged, we found that the first cluster was smaller, while the others were larger. Also, the total number of clusters was

larger with charged Lys716. This is an indication of a greater conformational diversity. The same trend was observed in the Martini 2 simulations (Table 3.3, Supplementary Figure S3.4).

Table 3.3: **Cluster populations from the CG Martini simulations.** Shown is the fraction of the 5 first clusters, the sum of these 5 fractions and the total number of clusters.

FF version	charged state of Lys716	cluster 1 (%)	cluster 2 (%)	cluster 3 (%)	cluster 4 (%)	cluster 5 (%)	total (%)	total number of clusters
Martini 3	neutral	55.7	21.6	14.1	3.4	1.9	96.7	16
Martini 3	charged	34.1	26.7	19.3	6.7	2.3	89.1	25
Martini 2	neutral	60.0	13.9	10.0	7.4	3.0	94.3	13
Martini 2	charged	31.9	25.7	20.6	10.1	4.3	92.6	17

The interactions between the two TM helices can be observed conveniently by plotting the position of the center of mass of TM1 relative to TM2. All structures used for the clustering analysis were fitted to the backbone beads of TM2, and the positions of the center of mass of TM1 were then plotted in Figure 3.2A,B. This plot shows the position of TM1 around TM2, which is fixed in the center. Overall, this analysis reveals that the charge state of Lys716 controls the TM1-TM2 association. For charged Lys716, TM1 contacts TM2 on the left and top (Figure 3.2B), whereas for neutral Lys716, TM1 contacts TM2 on the right and top (Figure 3.2A). TM-TM contacts are therefore completely different depending on the charge state of Lys716.

3.3.4 The TM domain energy landscape quantifies Lys716-mediated dimer destabilization

A principal component analysis (PCA) was performed on the dimerized structures from the 4 sets of simulations. Figure 3.2C shows the projection of each conformation onto the first two principal components, in terms of free energy, for neutral Lys716 with Martini 3. For charged Lys716 (as well as for Martini 2 simulations), the PCA plots are shown in supplementary Figure S3.4. For neutral Lys716, there is one main free energy well (Figure 3.2C), whereas there are several shallow wells when it is charged (supplementary Figure S3.4). This observation is consistent with the clustering results (Table 3.3). The charged residue promotes the exploration of a greater variety of conformations. We compared these results with dimers previously obtained in Ref. [1] predicted with PREDDIMER [156]. It can be observed that none of the PREDDIMER predictions match the first 5 clusters or the deepest wells (Figure 3.2A, 3.2B, 3.2C).

For the neutral Lys716 system, the deepest free energy well (Figure 3.2C) coincides exactly with the center of the first (largest) cluster (Figure 3.2A). Therefore, we decided to choose this latter structure as our best CG model. We extracted it for further analyses and conformational sampling at the all-atom level (see below). This best model shows a compact structure characterized by a crossing angle of -137.4° (Figure 3.2C) and it is a left-handed antiparallel dimer. The GX₃G motif contained in TM2 is involved in the interaction with TM1 (Figure 3.2C), consistent with the literature [229]. However, this motif is

usually observed in right-handed dimers [230, 231, 232], which is not the preferred arrangement here.

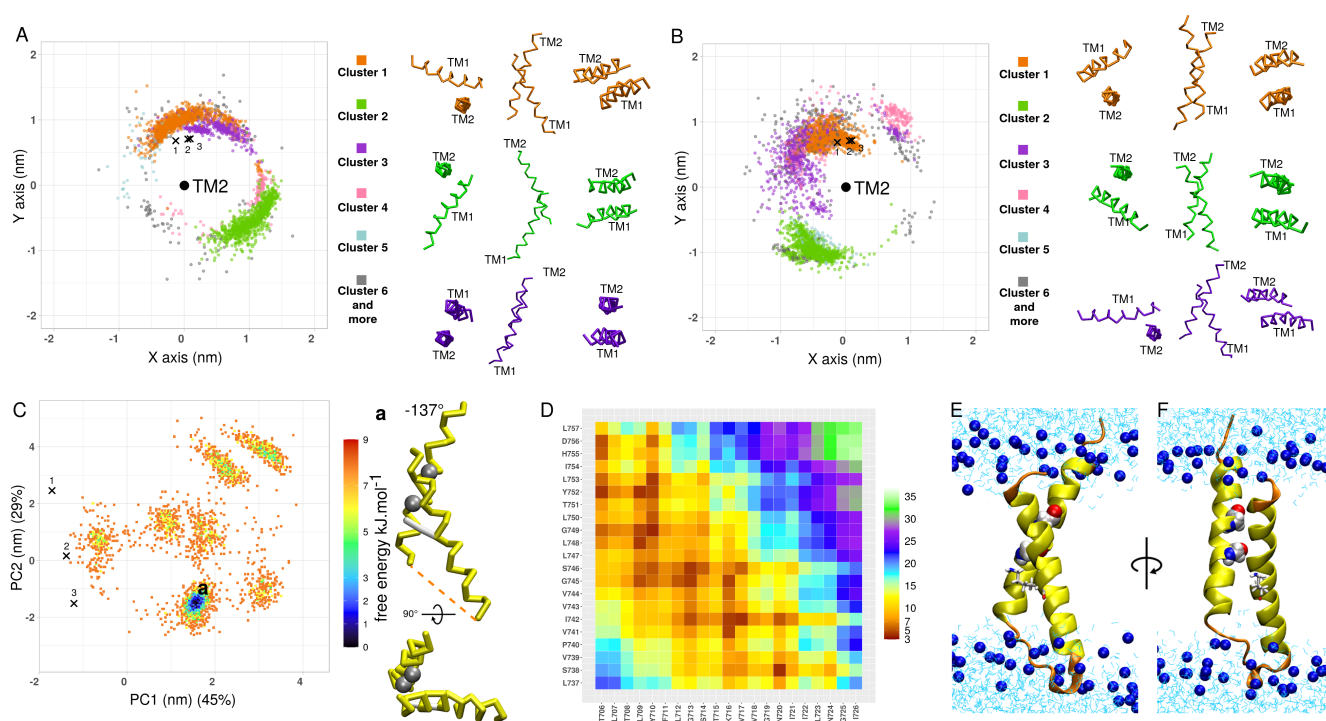


Figure 3.2: TM1-TM2 contacts determined using Martini 3 and best model extraction. (A,B) Positions of the center of mass of TM1 around the center of mass of TM2 (midpoint) for neutral (A) and charged (B) Lys716. The coloring of TM1 positions is based on the cluster to which the structure belongs to. Shown on the right side of each plot are the central structures of the first three clusters, colored similarly. (C) Free energy projection on the first two principal of a PCA analysis (neutral Lys716 system). This PCA was performed on a concatenated trajectory containing all CG simulations (Martini 2 and 3, neutral and charged Lys716). On the plot, only the CG data are shown. The crosses 1, 2 and 3 correspond to the 3 dimers obtained with PREDDIMER in ref. [1]. Shown on the right are two snapshots of the best model (labeled "a" and corresponding to the center of cluster 1 in panel A and to the deepest free energy well), together with its crossing angle. The glycines of the GX₃G motif are shown in van der Waals representation. Lys716 is shown in stick representation. (D) Contact map of the best model. (E,F) Best model back-mapped to an all-atom representation with the loop between TM1 and TM2 added. The protein is shown in a cartoon representation. TM1 and TM2 are shown in yellow and the flanking residues (with the loop) are shown in orange. Lys716 is shown in stick representation, and the GX₃G motifs are shown in van der Waals representation. The phosphorus atoms of the lipids POPC and POPE are shown as blue spheres, and the water molecules are shown as cyan sticks. The loop was added according to the procedure described in the supplementary material.

To have a better idea of the contacts, Figure 3.2D shows a contact-map of this best CG structure, and Figure 3.2E and 3.2F shows a back-mapping of it to an all-atom representation. The part of each helix involved in the interaction ranges from T706 to N720 for TM1 and S738 to L753 for TM2. The N-terminal part of TM1 interacts mainly with the C-terminal part of TM2 (Figure 3.2B).

3.3.5 Charged Lys716 destabilizes the membrane

The presence of a Lys residue in the middle of a TM helix raises the question of its putative role in the fusion process. Here, we performed CG simulations of the dimerization of TM1 and TM2 (as well as some flanking residues) with charged or neutral Lys716, allowing us to assess the effects of the dimers on the surrounding membrane environment. Thus, we analyzed two parameters associated with the onset of hemifusion, the fusion of the outer layers of each membrane: (i) lipid packing defects, which quantify the hydrophobic membrane surface in contact with the solvent [52, 145] and (ii) lipid tail protrusions, defined as the appearance of a carbon atom (or a coarse-grained bead belonging to a lipid tail) protruding above the level of the phosphate group [146, 147]. When such a protrusion occurs, the hydrophobic lipid tail is assumed to be in contact with the solvent. Thus, both parameters indicate the probability that the hydrophobic tails are exposed to the solvent, which is a prerequisite for hemifusion [233, 234, 235].

For lipid packing defects, the π constant provides information on the occurrence and size of such defects, with a higher value indicating more frequent and larger defects. Interestingly, the π constants are higher when the TM domains are present compared with pure membranes (supplementary Figure S3.2A). The constant for charged Lys716 is slightly higher, which suggests more packing defects, than that for neutral Lys716. The effect is however too modest to draw a definitive conclusion for this parameter. As for the protrusions, the presence of the protein favors their occurrence (Supplementary Figures S3.2B), which is consistent with the analysis of packing defects. In addition, an increased occurrence of protrusion events is observed when Lys716 is charged, indicating a destabilizing effect of the charge on the membrane. In summary, the route to hemifusion is favored not only by the presence of the TM domain, but the charge state of Lys716 also matters.

3.3.6 Replica exchange MD provides a refined atomistic model and verifies stable TM assembly

To fine-tune a model of the whole TM domain, we performed all-atom simulations (AA) using an enhanced sampling technique, temperature replica-exchange molecular dynamics (T-REMD). As a starting structure, we chose the best dimer of the Martini 3 simulations obtained with neutral Lys716, as described above and in Figure 3.2. The missing loop was added and sampled as described in the supplementary methods. Finally, the system was back-mapped to an AA representation (see Figure 3.2E and 3.2F) and used as the initial structure for a T-REMD simulation of 500 ns. In total, 38 replica were simulated ranging from 303.15 K to 400 K. This REMD protocol allowed us to test the robustness of the model by exposing it to high temperatures while maintaining a physical Boltzmann distribution at each temperature.

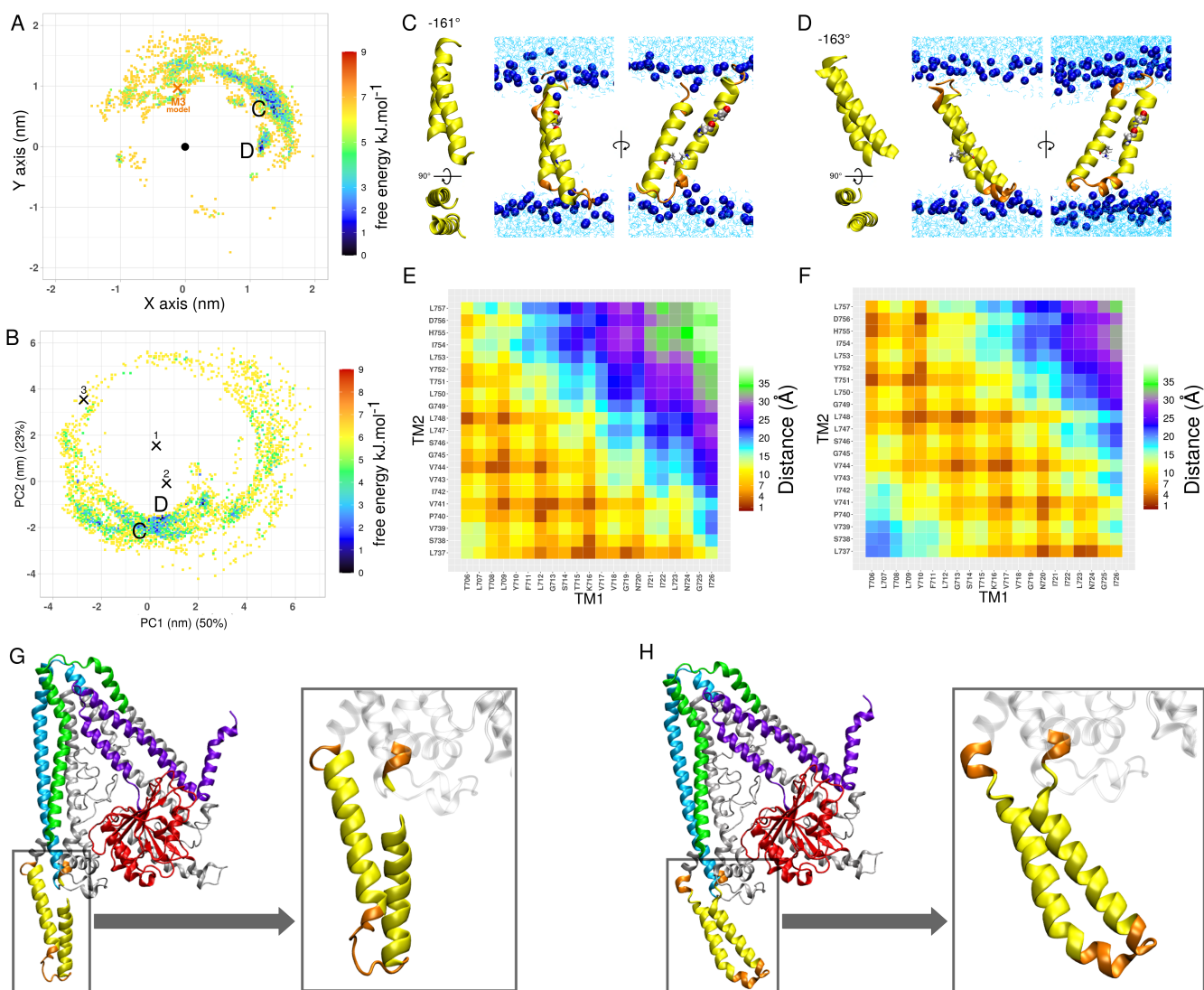


Figure 3.3: TM domain prediction based on REMD simulations. (A) Positions of the center of mass of TM1 around the center of mass of TM2 (center point) colored as function of the free energy. The orange cross is the best CG model obtained with Martini 3 (in Figure 2) used as a starting point of the REMD. (B) Free energy projection on the first two principal components of a PCA analysis. This PCA was performed on a concatenated trajectory containing Martini 3 (neutral K716) and all-atom (bottom temperature) conformations. On the plot, only the all-atom data are shown. The crosses 1, 2 and 3 correspond to the 3 dimers obtained with PREDDIMER in ref. [1]. The structures selected for both (A, B) have a TM1-TM2 COM-COM (center-of-mass) distance of less than 2 nm. (C,D) Center structure of the first and third cluster respectively, for a cutoff of 0.2 nm. These clusters roughly correspond to the 2 main free energy wells (bluest parts) seen in (A,B) and labeled C and D. The TM domains and the flanking residues are in cartoon representation. TM1 and TM2 are in yellow, and the flanking residues (with the loop) are in orange. The glycines of the GX₃G motif are shown in van der Waals representation. The Lys716 is shown in stick representation. (E,F) Contact map of the models (C,D) respectively. (G,H) Addition of respectively (C) and (D) to the model of Fzo1 built by De Vecchis *et al.* in 2017 [1]. TM1 and TM2 are seen in yellow, the other residues used for the REMD are seen in orange, HRN is in purple, HR1 in blue, HR2 in green and the domain GTPase is in red. The residues that do not belong to a specific domain are in light grey. The second image is the TM portion, zoomed in. The residues before Ser702 and after Lys761 are represented in transparent gray.

We first analyzed the behavior of each replica as it propagated through temperature space. Of the 38 replicas, 19 showed persistent interactions between the two TM helices (center of mass / center of mass distance below 2 nm) throughout the simulation, 12 showed TM dissociations, while 7 showed TM dissociations and re-associations (Supplementary Figure S3.5A). Importantly, the C α RMSD of TM1 and TM2 showed minimal structural changes for each replica when the two TM regions maintained their interaction during the simulation (Supplementary Figure S3.5B), indicating stability and robustness of the original structure.

Next, we focused on the ensemble of structures at the lowest temperature (303.15 K) (Figure 3.3). In total, 79.2 % of the conformations presented stable TM1 / TM2 contacts. In addition, all conformations showed stability of their secondary structures in the two TM helices, even those which displayed dissociation (Supplementary Figure S3.6). Figure 3.3A shows the position of TM1 around TM2 fixed at the center, similar to Figure 3.2A for CG simulations, in terms of free energy. The conformations of the bottom temperature quickly left the area of the starting structure (represented by a cross), and populated mainly the right side of TM2, as well as its upper side but in a less pronounced way. The Martini 3 simulations had captured the right and upper parts overall, but not the exact upper right region found here.

In the following, we consider only the conformations with TM1 / TM2 in contact. From this ensemble of structures, we extracted the two best models of the entire TM domain from the two wells with the lowest free energy, as shown in Figure 3.3A-F. The two wells are labeled C and D in panels 3.3A and 3.3B, whose structures are shown in panels 3.3C and 3.3D. In both models C and D, TM1 touches TM2 in the lower part (the most likely contacts in Figure 3.3E-F are below the diagonal of the contact map), especially in model C. Both models C and D were then compared with the overall Fzo1 model that we proposed in 2017 [1] to check which model fits better (Figure 3.3G-H). As can be seen, model D (Figure 3.3D/H) fits better with the overall model of Fzo1 because the TM domain can be connected to the rest of the model at both the N- and C-terminal sides. We therefore selected model D as our best all-atom model. However, it is important to keep in mind that the TM contacts have a certain degree of flexibility, so that the alternative conformation C cannot be completely excluded.

We also analysed the promiscuous stabilizing interactions between TM1 and TM2 (Figure 3.3E-F). While we observed a similar set of residues involved in the interactions in TM1, there is a clear shift in the interactions involving TM2 (Figure 3.3). Instead of Gly745 and Gly749 of the GX₃G motif, residues Val741 and Leu748 were the most involved in the interactions. We also found that among the structures located within the energy wells (Figure 3.3), Thr706, Leu709, Gly713, Lys716 from TM1 and Leu737, Val741, Val744, Leu748 from TM2 were the most promiscuous residues.

In terms of hydrogen bonds, we found some between the side chains of Lys716 and Ser738 with 8% of persistence. However, the latter residue frequently formed hydrogen bonds with the side chain of the TM1 residue Asn720 (12% of persistence) as well as with the residues of the loop from Lys726 to Lys735

(both side chains and backbone with 7% of persistence) and most frequently with the solvent (21% of persistence).

3.3.7 Experiments show that the polar residue 716 is crucial for mitochondrial respiration in yeast

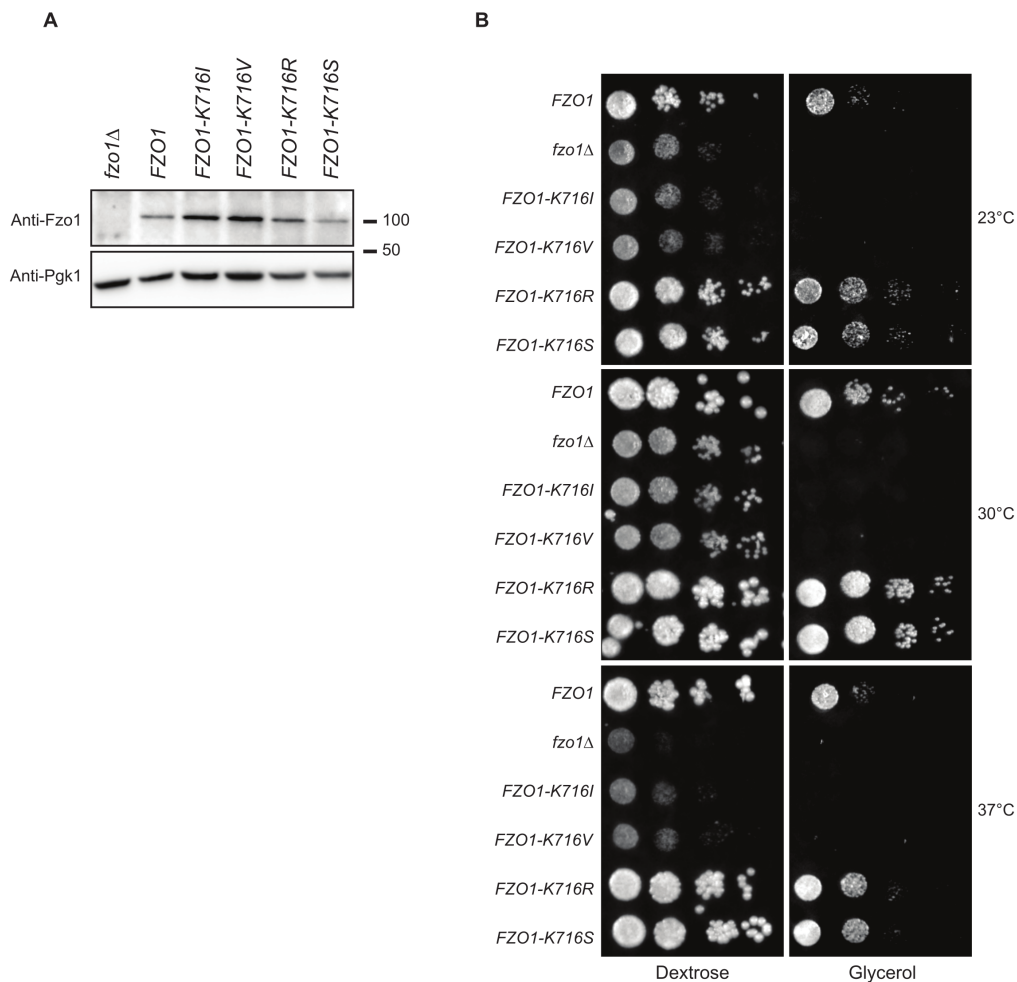


Figure 3.4: **The polarity of K716 is essential for Fzo1 function.** (A) Anti-Fzo1 and anti-Pgk1 immunoblots of total protein extracts prepared from, *fzo1Δ* shuffle strains transformed with an empty plasmid or plasmids expressing FZO1 WT or mutated in K716. (B) Dextrose and glycerol growth spot assay with strains used in (A).

We sought to obtain experimental confirmation of our theoretic observations on residue K716. We reasoned that mutating this Lysine into apolar residues (I or V) should impact mitochondrial fusion efficiency while mutation into polar (S) or charged (R) residues should have no effect. To test this prediction, we took advantage of the established link between mitochondrial fusion efficiency and respiratory growth of *Saccharomyces cerevisiae*. Depending on the carbon source provided in their media, yeast cells grow

through either fermentation or respiration. Dextrose is a fermentative carbon source that inhibits respiration whereas Glycerol is a fully respiratory carbon entry [236, 237]. Consequently, since mitochondrial fusion is essential for respiration, its inhibition abolishes yeast growth in Glycerol-containing media [94]. WT, *fzo1Δ* and cells expressing distinct versions of Fzo1 mutated in K716 as the sole source of Fzo1 (Fig. 4a) were thus subjected to serial dilutions growth assays on Dextrose or Glycerol-containing media at 23, 30 or 37°C (Fig. 4b). All mutants were expressed at levels comparable to WT Fzo1 (Fig. 4A). However, respiratory growth of FZO1 K716I and FZO1 K716V cells was abolished at all temperatures, similar to *fzo1Δ* cells. In contrast, respiratory growth of FZO1 K716S and FZO1 K716R cells was not affected, similar to WT cells. These results indicate that mutation of Lys716 to an apolar residue (K716I or K716V) impairs respiration likely because of an inhibition of mitochondrial fusion. Moreover, mutation of Lys716 to an Arg (K716R), the main alternative in Mammalian mitofusins, or Mutation of Lys716 to a polar residue (K716S) has no effect on respiration. In this context, the positive charge of Arg or Lys does not seem to be mandatory, but the residue polarity of Lys, Arg or Ser at position 716 would be essential for mitochondrial fusion.

3.4 Discussion

Our extensive simulations provide new insights into the structure and dynamics of the transmembrane domain of Fzo1. Comparison with previous predictions reveals important differences, while independent validation suggests that the refined model accurately reproduces the folding of the TM domain. In this discussion, we first examine the robustness of the predicted TM1-TM2 interface in different simulation methods. Comparison of coarse-grained and all-atom approaches shows the robustness of the main TM domain contacts. Next, we explain how our extensive multiscale simulations have led to a new structural model that significantly improves on previous computational predictions for the Fzo1 TM domain. We analyze the areas where our model deviates and discuss on the possible reasons for the increased accuracy. An independent prediction of the Fzo1-Ugo1 complex from AlphaFold2 is used to externally validate our new TM domain fold. We examine the remarkable agreement between these completely different approaches. We then discuss the functional implications of our refined structure, including how specific residues may be actively involved in the membrane fusion process. Our model sheds light on how the properties of the TM domain may facilitate the hemifusion and full fusion stages. Finally, we compare the results with other studies of dimerization, which give a consistent picture of such processes when examined with coarse-grained MD simulations.

3.4.1 The TM1-TM2 interface is robust across force fields and levels of representation

To investigate the possible association of TM1 and TM2, we generated twenty-five 10 μ s coarse-grained (CG) MD trajectories showing dimerization. Although the TM1-TM2 biological construct is connected by a loop in the intermembrane space, we intentionally cut the TM domain into two peptides so that

dimerization was freely driven by TM1-TM2 contacts within the membrane. This assembly approach can be considered equivalent to docking, but confined within an explicit membrane environment. Because we used the CG Martini force fields [161, 162, 164] with smoother energy surfaces than a fully atomistic model, we were able to benefit from accelerated kinetics and thus efficiently sample the different modes of interaction of the two TM helices. As a result, we obtained robust statistics on TM1-TM2 contacts.

Our protocol was first tested with the Martini 2 force field (supplementary Figure S3.4). During the progress of this work the Martini 3 force field was released, which encouraged us to use it as well. Interestingly, the Martini 2 simulations yielded a very similar dimerization pattern compared to Martini 3, albeit with a stronger association, which is a known artefact of Martini 2 [164]. Conformational clustering showed the same trends for both force fields, i.e., the charged Lys716 system has a larger number of clusters, and the first cluster of the simulations with neutral Lys716 accounts for more than 50% of the sampled structures. Experimentally, some ^2H experiments were performed on a TM helix containing a Lys in its center [205]. A charged Lys was leading to a multistate behavior in terms of peptide orientation in the membrane (tilt and azimuthal rotation), whereas a neutral Lys gave a single orientation. In our CG simulations we have two TM helices dimerized, but we find the same kind of behavior since we get a single free energy well for neutral Lys716, and multiple shallow ones for the charged version.

When the model was subjected to all-atom simulations (AA) using an enhanced sampling method (T-REMD), we observed a slight shift in the most frequent interactions between the two TM helices. Lamprakidis *et al.* showed that Martini 3 does not always favor the experimentally solved interface of interactions between TM domains [238] and recommended that a refinement procedure be used. Nevertheless, the interfaces of the interactions involving TM1 are overall the same in the Martini 3 and CHARMM36 refinements. The change to a detailed AA representation affected mainly the interactions involving TM2, while in the overall model, the interface of the interactions and the crossing angle were only slightly affected.

3.4.2 How can we interpret TM1 expulsion from the membrane with Martini 3?

Next to experiments of biophysics or cellular biology, CG simulations with Martini 2 or 3 have been widely used to predict TM-TM helix dimerization (or higher order oligomerization), for example in recent refs [239, 240, 241, 242]. Both force field versions are able to predict TM-TM interfaces, but Martini 2 has a tendency to overaggregate TM segments. Considerable efforts have thus been put in the development of Martini 3 to solve this issue [164]. This new version was recently tested on many known TM-TM dimers with success [203], but the authors highlighted the ability of Martini 3 to sample alternative conformations as well as the importance of flanking residues (around TM helices). Subsequent studies found the possible ejection of TM helices with Martini 3 [242, 243], ending adsorbed on the membrane in a horizontal orientation. To avoid this, some solutions were proposed such as adding position restraints or rescaling protein-water van der Waals interactions [244]. In summary, Martini 3

is still in a testing phase by the scientific community. We are learning progressively how it behaves and how to interpret its outcomes by testing it on several different systems. In our case, we tested the rescaling procedure [244], but still observed TM1 ejections (data not shown).

In this context, how can we interpret the ejections of TM1 observed in our simulations with Martini 3? On one hand, this is unexpected since we are dealing with a TM helix. ^2H NMR experiments have confirmed that a single TM helix containing a Lys in its center assumes a transmembrane topology regardless of the charge state [205]. On the other hand, we have to consider that there are 3 consecutive polar residues STK in the middle of TM1. Moreover, Lys 716 may be charged depending on the conditions. In the context of the full protein, which bears the HR1 cytoplasmic domain on its N-terminal side, these ejections are probably not realistic. But due to the simplified description of coarse-grained vs all-atom representation (fixed secondary structure, etc.), due to the absence of the cytoplasmic domains, this is how Martini 3 is warning us that something is going on with TM1: it is not an ideal helix for a hydrophobic environment like the center of a membrane. Yet, we demonstrated that TM1 destabilizes the membrane. If Lys716, were to be charged, this would be even more pronounced. This is interesting, because in the context of membrane fusion, a TM helix able to destabilize the membrane is clearly an asset, such as in SNARE proteins [154, 199]. We discuss this aspect further 2 sections below. Last, as stated by Sahoo *et al.*, we observed that the flanking residues matter, since the longer PEPT1-41 underwent less ejections than the shorter PEPT1-29 [203]. We also observed that charged Lys716 was ending in far more ejections than neutral Lys716. The ratio of ejections may thus be seen as a proxy towards the likeliness to perturb the membrane.

3.4.3 Extensive multiscale simulations yield a new structural model of the Fzo1 TM domain improving over previous predictions

The TM domain model refined with our multiscale protocol shows significant deviations from the 2017 prediction [1]. The soluble part of the previous model could be validated by experimental mutation studies, while the TM1-TM2 contacts of the transmembrane part were based on an *ab initio* prediction by the PREDDIMER method [156] that could not be experimentally assessed at that time. Of the three PREDDIMER models created, the highest scoring conformation was selected, a right-handed antiparallel dimer characterized by a crossing angle of 119.7° . In contrast, the model created here with Martini 3 is a left-handed antiparallel dimer with a crossing angle of -137.4° , and the model refined with REMD has an angle of -161.4° . In addition, the Martini 3 model shows involvement of the GX_3G motif, while the refined model no longer shows interaction of these residues with TM1. This motif could thereby be free for other contacts such as homodimerization, or with another partner in the membrane. In addition, TM1 shows no matching interactions with the residues observed with PREDDIMER. T715 is most closely associated with the GX_3G motif in the PREDDIMER model, whereas in the new model it is not T715 but L709, Y710, and G713, among others.

3.4.4 An independent Fzo1-Ugo1 complex prediction matches the novel TM domain fold

The field of structure prediction has been revolutionized recently by the success of AlphaFold2 (AF2) [158, 223]. Other systems have appeared like ESMfold [245], and it has been shown that comparing those tools could help solve structures [246]. These observations prompted us to use AF2 and ESMFold to independently predict the structure of the TM domain of Fzo1.

Using AF2, we first predicted the TM domain of Fzo1 alone, then a whole Fzo1 monomer and a homodimer of Fzo1. All these predictions led to the two TM helices unstructured, with a low pLDDT (Predicted Local Distance Difference Test), which is the confidence value per residue (Supplementary Figure S3.8). This observations seems to echo the difficulty to predict membrane-inserted protein segments with AF2.

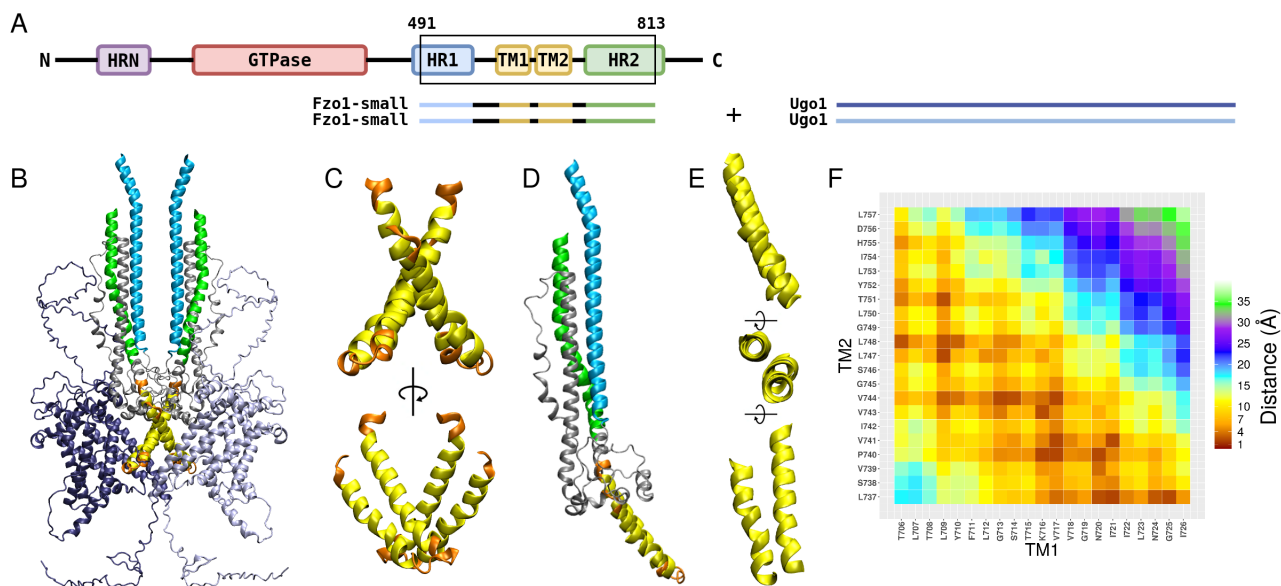


Figure 3.5: **AlphaFold2 prediction of Fzo1 in interaction with Ugo1.** (A) Scheme of the protocol. (B,C,D,E) The four proteins are in cartoon representation. In dark blue and light blue are the models of Ugo1. TM1 and TM2 are seen in yellow, the other residues used for the REMD are seen in orange, HR1 in blue and HR2 in green. The residues that do not belong to a specific domain are in light grey. (B) The overall result of AlphaFold. (C) Zoom on the TM domains of the Fzo1-small dimers. (D) One Fzo1-small monomer. (E) Zoom on TM1 and TM2 of Fzo1-small monomer. (F) Contact map of TM1 and TM2.

In yeast, Fzo1 has an important biological partner in the outer membrane named Ugo1 [108] which is involved in mitochondrial fusion [109, 247]. Interestingly, when two Fzo1 monomers and two Ugo1 monomers were subjected to AF2, we observed that the two TM helices were correctly predicted to interact with each other (Figure 3.5). Strikingly, compared to our best model from the REMD simulations (Figure 3.3D), the two structures are very close: the RMSD (on backbone C α atoms of TM1 and TM2

only) is as low as 0.27 nm, the promiscuous residues are very similar, and the crossing angles are close (-159° for AF2, -163° for our model) (Figure 3.5). Moreover, the AF2 model shows that the TM domain of each Fzo1 monomer interacts with each other around the TM helices (mainly TM2-TM2 contacts). This result is interesting because it suggests that Fzo1-Fzo1 dimerization may also involve contacts between the two TM domains. As the GX3G motif does not actually interact with TM1, these TM2 residues could be involved with the other monomer, even if we find closer interactions with other residues.

In summary, the overall agreement between our strategy and an artificial-intelligence-based method reinforces the pertinence of our physics-based model.

3.4.5 Could Fzo1 TM domain play an active role in membrane fusion?

The fusion process starts with the two membranes getting close to one another. The approach is followed by the formation of a stalk intermediate resulting from the mixing of the outer bilayer leaflets. Then a hemifused state follows prior to the final fused state. Outer leaflet mixing is possible when the hydrophobic areas are in contact with one another [49].

Recent experimental studies have shown the importance of lipid conformations in the initiation of the outer leaflets mixing. The ability of lipids to splay, i.e. expose a part of their hydrophobic tail towards the solvent also known as protrusion, was shown to trigger membrane fusion [248]. It was also shown that lipid packing defects, small hydrophobic areas exposed to the solvent, were qualitatively correlated to the nucleation rate of fusion [235]. Protrusions and packing defects are logically directly correlated on lipid composition and membrane curvature [52, 249, 145, 147]. These two parameters are thus critical in the initiation of membrane fusion.

Regarding membrane fusion mediated by proteins, it is now well established that their TM domains play a pivotal role [250]. In the well-studied case of SNARE proteins, the unique presence of a single TM helix in each leaflet catalyses outer leaflet mixing [154]. The TM helix sequence matters since some mutants induce less protrusions than the wild type [199]. In addition, the lipids are more perturbed near the TM helix than far away. Another well known example is the influenza fusion peptide [234]. Again, the TM sequence is decisive for the generation of protrusions around it (leading to membrane fusion), while some mutants are less efficient. A recent experimental study on model TM helices has also shown that the amount of lipid splay (i.e. protrusion) was directly correlated with membrane fusion [248]. Also there it was sequence dependent, a poly LV16 being more efficient than a poly L16 TM peptide. Similar to these examples, our results suggest also a destabilization of the membrane promoted by the presence of the Fzo1 TM domain.

We discuss now the possible role of Lys716 in membrane fusion. First, this lysine is well conserved in fungi (Figure S3.8). In mammals, an arginine is rather found at this position. In organisms that have a full TM domain (not a paddle which only partially binds the membrane like in bacterial BDLP), it is interesting to note that evolution have conserved a basic residue in the middle of TM1, which raises

questions about its role. Our experiments showed that mitochondrial respiration is disabled when Lys716 is mutated to an apolar residue (Leu or Val), but mutation to an Arg or Ser has no effect on respiration. Amino-acid polarity is thus required, but having a basic one is not mandatory. These data are in line with the membrane destabilization hypothesis, since a polar residue will anyway perturb the membrane (recall there are also two other polar residues next to Lys716). However, these findings do not preclude the possibility of Lys716 positive charge to play a role. The experiments of Gleason *et al.* evaluated the pKa of a Lys in the middle of a TM helix to be around 6.2 at 50 °C [205]. Correcting for temperature, the pKa was then estimated to be ~ 6.5 at 37 °C and ~ 6.8 at 25 °C. Given an acidic pH in yeast cytoplasm [251], these values would suggest that Lys716 could be, at least partially, protonated.

The role of positively charged residues is not new in the context of membrane fusion. In the case of the SNARE fusion machinery, Lindau *et al.* examined the transmembrane domains in detail and hypothesized that well-placed charges could significantly assist membrane deformation and destructuring, thereby initiating the fusion process. In particular, they investigated the role of charged residues at the end of a Syb2 TM domain construct when pulled into the membrane [198]. It has further been suggested that charged motifs play an important role for fusion to occur, such as shown by the bilayer destabilization by a conserved membrane-embedded motif at the juxtamembrane region of the vesicle-anchored v-SNARE comprising for fusion to occur, membrane bilayers must be destabilized by a conserved membrane-embedded motif located at the juxtamembrane region of the vesicle-anchored v-SNARE comprising several basic residues [252]. In TM1 of Fzo1, the Lys is in the middle of the TM helix, not flanking it, but it does not exclude that a similar mechanism may be operating. Overall, these observations echo the idea of a protonation-state induced switch of Lys716 to assist membrane fusion. Such a switch could increase membrane destabilization when the cell needs to fuse its mitochondria. The lack of effect when the Lys is mutated in a polar, but not titratable, residue is however arguing against this effect being decisive. It is therefore tempting to speculate that the ability to protonate could be associated with some other function of Fzo1, besides mitochondrial fusion.

3.5 Conclusion

We have constructed an improved model of the TM domain of mitofusins using both coarse-grained and all-atom molecular dynamics. This model has been further confirmed using the deep-learning tool AlphaFold2. This model has revealed the role of Lys716 that is found in the middle of the membrane. The importance of this residue is confirmed by its evolutionary conservation and the effect of its mutations on mitochondrial fusion. Further studies will therefore be needed to explore the exact role of this residue in mitochondrial fusion but could also target other functions associated with mitofusins.

3.6 Supplementary Material

Coarse-grained loop conformational sampling

System Building

The center of the first cluster obtained through Martini 3 simulations with a neutral Lys716 was selected for the following simulations. The lipids and solvent of the corresponding frame were also extracted. This dimer conformation was used as a starting point for the addition of the missing residues between PEPT1-41 and PEPT2 (containing respectively TM1 and TM2).

In order to add the missing residues between TM1 and TM2, a structure of the loop was built using Basic Builder 1.0.2 on the MobyLe server (<https://mobyLe.rpbs.univ-paris-diderot.fr>) [212]. This structure was then converted to coarse-grained (CG) representation using the martinize2.py workflow module of the Martini 3 force field. As a first step, the residues at the end of the loop were used to align the structures of the dimer with the structure of the loop. Coordinates of residues Lys727 to Lys736 of the dimers were then removed and replaced by the coordinates of the structure available. Residues Arg695 to Thr701 included were also removed.

Simulation parameters

The GROMACS 2018.5 program was used to perform all MD simulations [177]. This system was then subjected to two energy minimization phase of 5000 and 10000 steps. Position restraints of $100000 \text{ kJ.mol}^{-1}.\text{nm}^{-2}$ were used for the TM1 and TM2 residues. Subsequently, all simulations were performed within the NPT ensemble. The velocity-rescaling thermostat [174] at 303.5K and the Berendsen barostat at 1bar [173] was applied for 500 ps of equilibration, with a time step of 0.01 ps. The position restraints for the TM1 and TM2 residues were lowered at $20000 \text{ kJ.mol}^{-1}.\text{nm}^{-2}$. A production run of 5 μs followed at 303.5K using the velocity-rescaling thermostat [174] (lipid, water and proteins coupled separately) and at 1 bar using the Parrinello-Rahman barostat [175] (compressibility of 3.0×10^{-4} bar). Pressure coupling was applied semi-isotropically. The position restraints for the same residues were fixed at $1000 \text{ kJ.mol}^{-1}.\text{nm}^{-2}$. A time step of 0.01 ps was used with the leapfrog integrator. Lennard-Jones interactions were cutoff at 1.1 nm. Bond lengths were constrained using the LINCS algorithm [214]. The reaction-field method [215] was used for evaluating electrostatic interactions, with a Coulomb distance cutoff of 1.1 nm, a relative dielectric constant of 15. The neighbor list was updated every 20 steps.

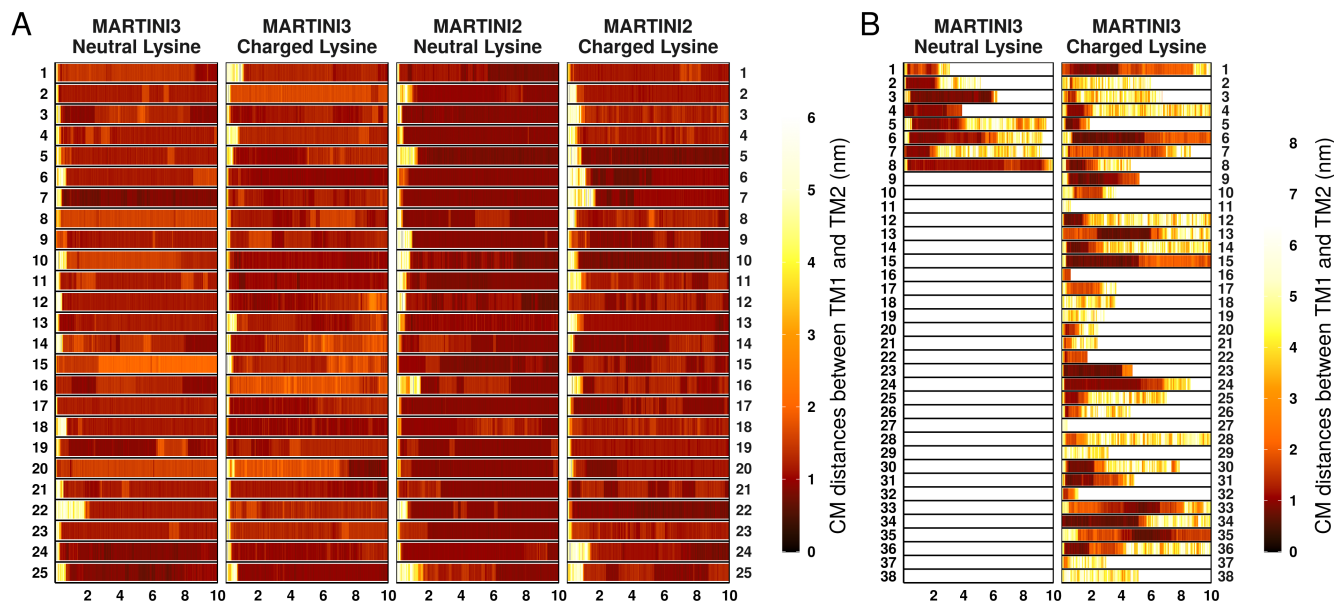
At the end of this stage, we thus have a coarse-grained system with TM1 and TM2 connected by the loop and embedded in the bilayer surrounded by solvent and ions.

Clustering

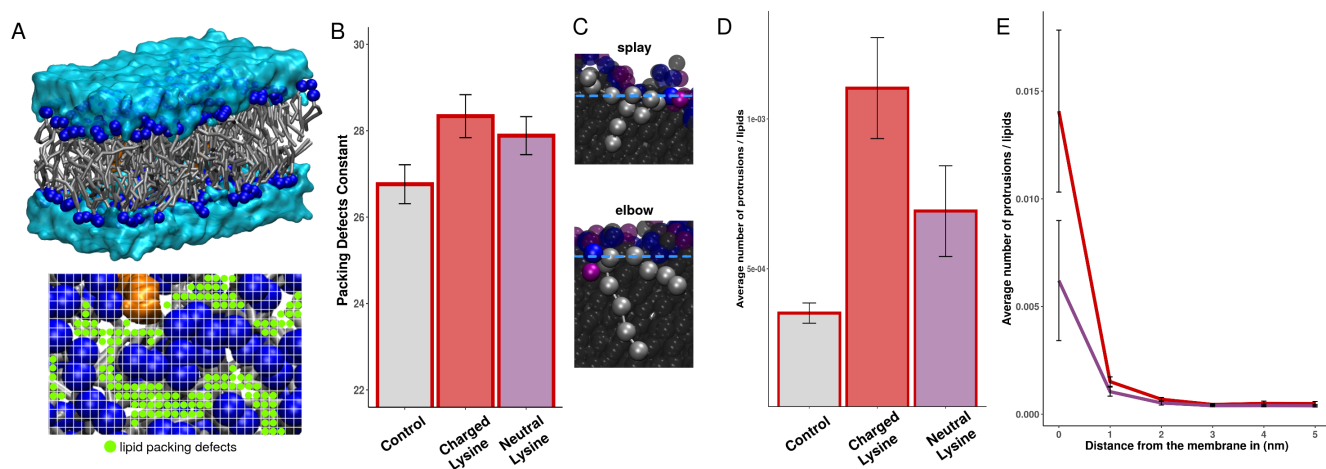
The loop was submitted to a conformation based clustering. The first 200 ns of the production were ignored, resulting in a total of 9601 frames. The frames underwent a clustering with the GROMOS method [181] using a cutoff of 0.2 nm (in order to obtain around 5 clusters representing 80-90 % of all

conformations). The center conformation of the first cluster was then selected for the next step.

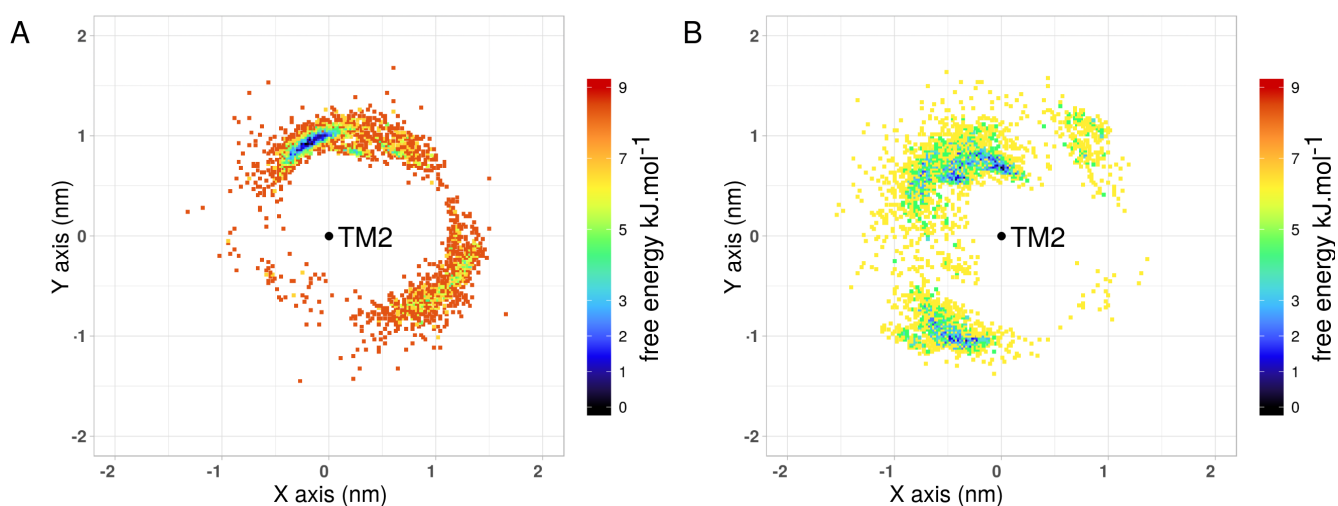
3.7 Supplementary Results



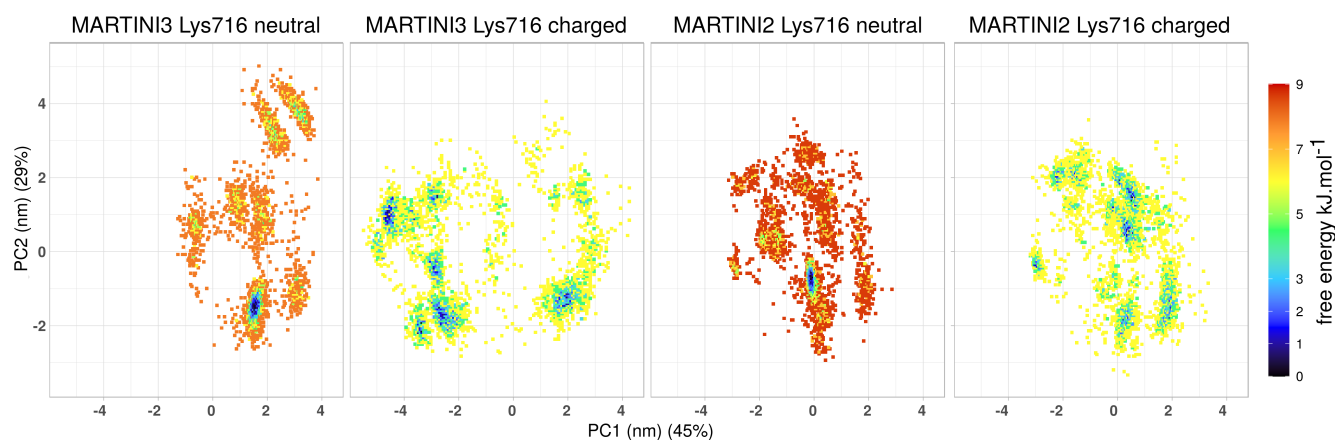
Supplementary Figure S3.1: **Distance between the center of mass of the two TM domains, as a function of time.** (A) Results for Martini 2 and Martini 3 systems. For all trajectories, TM1 and TM2 have dimerized after 2 μ s. (B) Results for Martini 3 simulations for which TM1 was expelled from the membrane. There are way more TM1 expulsions for the charged lysine than for the neutral one.



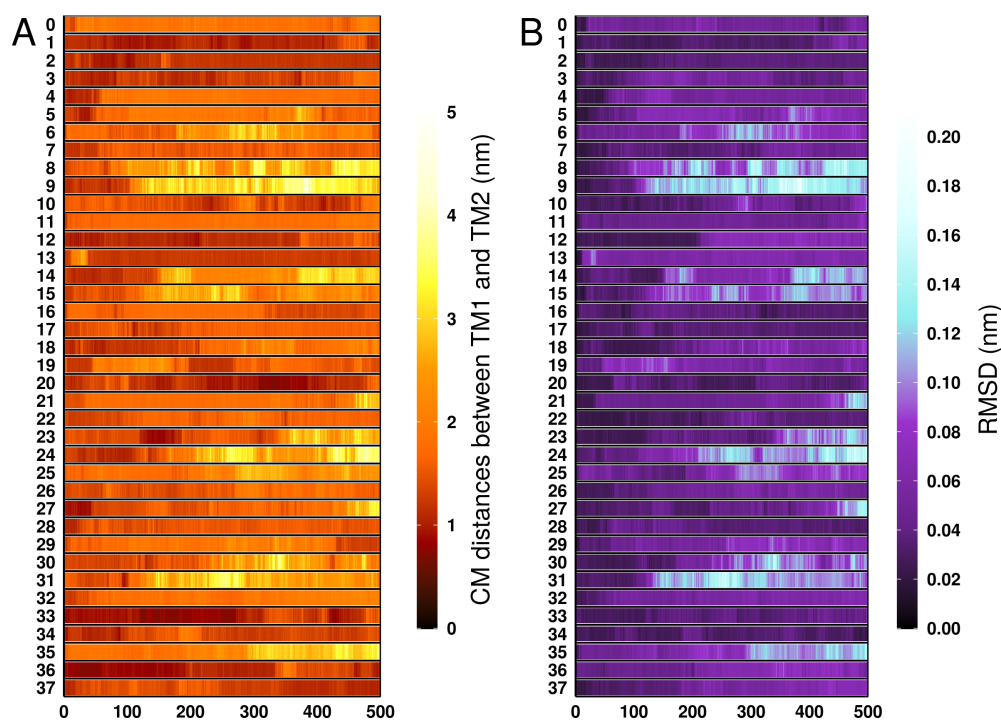
Supplementary Figure S3.2: **Effect of the TM domain on lipid properties relevant for fusion.** (A) Illustration of lipid packing defects between polar heads. (top) Scheme of a bilayer. Polar heads are represented in dark blue spheres, aliphatic tails in gray sticks, water in light blue surface. (bottom) Top view of the bilayer with the grid. Blue spheres are the lipid polar heads, the orange surface is the TM peptide (not considered in the analysis), the green dots are elementary defects. A packing defect is defined as a merge of contiguous elementary defects. It represents a spot where polar heads are not well packed against each other, leaving some apolar area exposed to water. (B) Packing defect π constants in units of \AA^2 for the Martini 3 simulations. (C) Definition of a protrusion event. (top) Definition of a lipid “splay” which typically occurs when the terminal beads of a lipid tail (gray spheres) goes above the phosphate bead (dashed blue line). (bottom) Definition of a lipid “elbow” which occurs when the first beads of the aliphatic tail (C1 and/or C2) goes above the phosphate group (dashed blue line). (D) Average number of protrusions per lipid. (E) Average number of protrusions per lipid as a function of the distance from the TM domain.



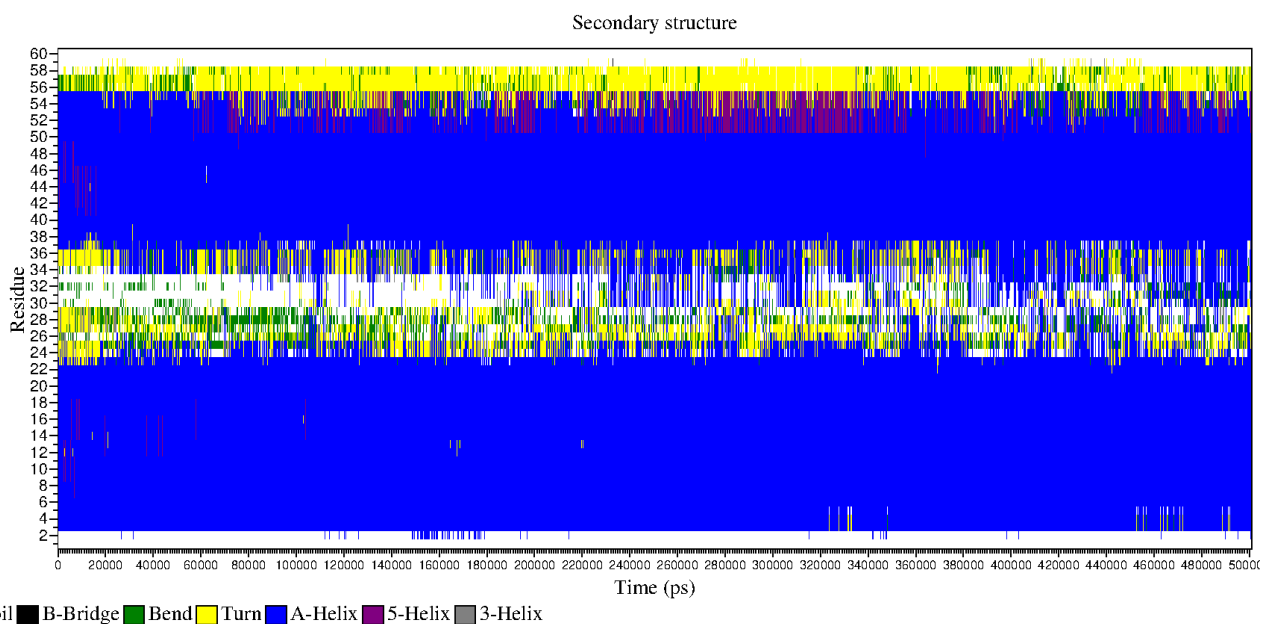
Supplementary Figure S3.3: **Position of TM1 relative to TM2 colored as a function of the free energy.** (A) Neutral Lys716. (B) Charged Lys716. This plot is obtained by aligning all conformation on TM2 backbone beads (center point), so that we can observe how TM1 is placed around TM2. Each plot is colored as a function of the free energy. For neutral Lys716, there is one main deep well, whereas there are many shallow wells for charged Lys716.



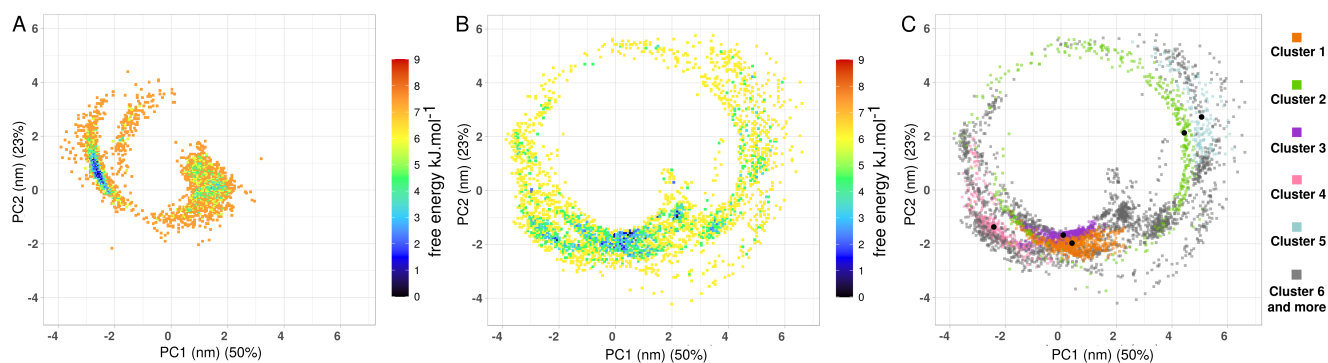
Supplementary Figure S3.4: **PCA colored as a function of the free energy for the MARTINI simulations.** The PCA was performed on all concatenated trajectories, but only one condition is shown in each plot, so that the 4 conditions are comparable. For neutral Lys716, there is one main deep well, whereas there are many shallow wells for charged Lys716.



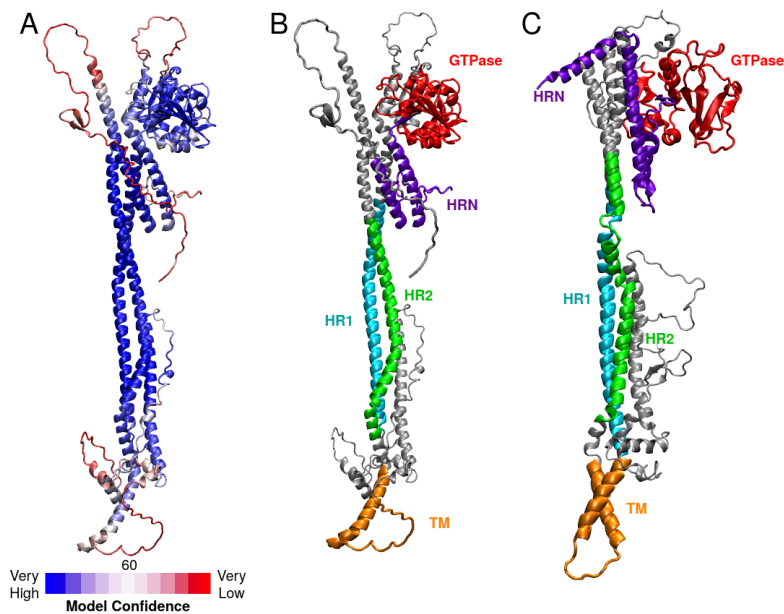
Supplementary Figure S3.5: **Conformations of the TM domain during the REMD simulations.** (A) Distance between the center of mass of TM1 and TM2 as a function of time for for all replicas. (B) RMSD of TM1 and TM2 (considering C_{α} only) with respect to the starting structure as a function of time. For both panels, we follow each replica which diffuse in temperature space (thus the trajectories are continuous). The bands becoming yellow in panel A and light blue in panel B undergo TM1-TM2 dissociation, those remaining dark indicate intact TM1-TM2 contacts.



Supplementary Figure S3.6: **Supplementary results of the REMD.** Here is shown the ensemble of structures at 303.15 K (thus this does not represent a continuous trajectory). Both TM1 and TM2 remain α -helical.

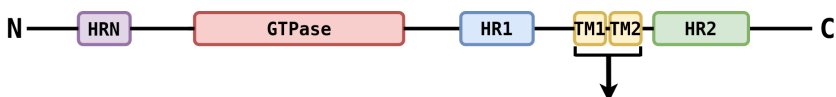


Supplementary Figure S3.7: **Comparison of the PCA between AA and CG simulations.** (A) Martini 3 Lys716 neutral structures colored as function of free energy. (B) REMD structures colored as function of free energy. (C) REMD structures colored as a function of the cluster number to which they belong to. The PCA analysis was performed on a concatenated trajectory between AA REMD simulations and Martini 3 (neutral Lys716) simulations, so that they can be compared. However, in panel A or B, only the Martini 3 or AA simulations are shown respectively. Note that panel B is identical to panel B of Figure 3.3. The way the PCA was done illustrate how the AA simulations (panel B) transition to a new region from the starting structure obtained with Martini 3 (panel A).

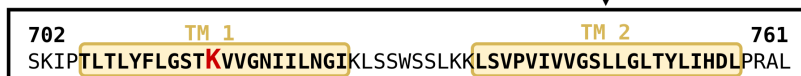


Supplementary Figure S3.8: **Fzo1 model predicted with AlphaFold2.** (A) Model colored as a function of pLDDT (predicted local distance difference test, i.e. the confidence score of AlphaFold2). (B) Model colored as a function of Fzo1 domains (TM in orange, HR1 in cyan, HR2 in green, HRN in purple, GTPase in red, the rest in gray). (C) Model built in 2017 [?] for comparison purposes. In each panel, the model is shown in cartoon representation. The AlphaFold2 model shows a large portion of the TM domain predicted as unfolded with a low pLDDT. Compared to the model of 2017, the AlphaFold2 model presents a new placement of the HRN domain, the absence of a hinge in the heptad-repeat domains HR1 and HR2, and a different orientation of the GTPase domain.

Fzo1 *Saccharomyces cerevisiae*



Fzo1 *Saccharomyces cerevisiae*



Fzo1 *Eremothecium gossypii*
 FZ01-like *Saccharomyces eubayanus*
 FZ01 *Candida glabrata*
 FZ01 *Hanseniaspora osmophila*
 FZ01 *Zygosaccharomyces parvulus*
 FZ01p *Saccharomyces boulardii*
 Fzo1 *Kluyveromyces lactis*
 Fzo1 *Saccharomyces paradoxus*
 mitofusin *Kazachstania barnettii*
 mitofusin *Kazachstania exigua*
 mitofusin *Kazachstania unispora*
 mitofusin *Kluyveromyces marxianus*
 mitofusin *Saccharomyces pastorianus*
 mitofusin *Zygosaccharomyces mellis*
 related to FZ01 *Saccharomyces ludwigii*
 related to FZ01 *Zygosaccharomyces bailii*
 similar to FZ01 *Kazachstania saulgeensis*

SRIPALAVYSYGGV**K**LVTNLLLYGTRFFSWQSLRK**I**STSLLLVGSALGAAYIISDLPRAL
 SKIP**T**LLTYFLG**S**T**K**VVGN**I**ILNGIKLSSWSSLK**K**LSVPVIVVGSLLGLTYLIHDLPRAL
 SRIPALAVYSYGGV**K**LVTNLLLYGTRFFSWQSLRK**I**STSLLLVGSALGAAYIISDLPRAL
 SKIP**T**LLTYFLG**S**T**K**VVGN**I**ILNGIKLSSWSSLK**K**LSVPVIVVGSLLGLTYLIHDLPRAL
 SRLPTMAIYSVGG**S**KLMSN**I**AYNGLRRLTSVNSL**K**KIASPL**L**ILASLLG**V**AYLIHDLPRAL
 SKIP**S**LLV**S**LG**G**A**K**LIVNVLMYGA**S**LFWSAM**K**NI**G**STV**V**LIGGS**L**G**C**AYLIHDLPRAL
 SKIP**T**LAVYSFGG**A**R**V**LRGVV**I**HGVQFFSWGAI**K**R**I**GG**S**V**L**FVGSLLSLAYLVHDLPRAL
 SKIP**T**LLTYFLG**S**T**K**VVGN**I**ILNGIKLSSWSSLK**K**LSVPVIVVGSLLGLTYLIHDLPRAL
 SKIP**T**LLV**S**FGG**S****K**MITN**I**VLHGS**R**FFS**L**ESL**K**KLSG**S**L**V**LLGGV**L**GIAYLIHDLPRAL
 SKIP**T**LLTYFLG**S**T**K**VVGN**I**ILNGIKLSSWSSLK**K**LSVPVAVVGSLLGLTYLIHDLPRAL
 SKLPALAIYSFGG**S****K**IAT**T**VIFN**G**LSAFSWK**S**L**G**Q**I**AG**S**V**V**IAG**S**LLGMAYI**V**YDIPRAL
 SKLPALAIYSFGG**S****K**IIT**T**IIFN**G**ISSF**S**L**S**L**G**Q**I**T**G**S**I**VAFGSLLG**V**AYLIYDIPRAL
 SKLP**T**LAIYSFGG**S****Q**I**V**K**T**ILW**N**GV**Q**T**S**IK**T**L**G**K**I**AG**S**T**V**VIG**C**LLG**V**S**Y**LIYDIPRAL
 SKIP**T**LLV**S**FGG**S****T**M**L**K**N**AL**I**NG**S**M**F**FS**L**R**S**L**K**K**P**S**G**LL**I**V**G**S**F**L**G**IAYLIHDLPRAL
 SKIP**T**LLTYFLG**S**T**K**VVGN**I**ILNGIKLSSWSSLK**K**LSVPVIVVGSLLGLTYLIHDLPRAL
 SKIP**T**LAVYSFGG**A****K**L**R**NA**I**IQ**G**VQFFSW**S**T**I**K**K**I**S**G**S**LL**M**V**G**T**L**LG**V**TYLVHDLPRAL
 SKIP**T**LFMYSFGG**A****K**I**L**T**N**I**F**MY**G**T**Q**IF**S**L**Q**A**L**K**N**I**G**G**S**LL**I**L**G**S**C**L**S**AAYLVHDLPRAL
 SKIP**T**LAVYSFGG**A****R**V**L**RGVV**I**HGVQFFSWGAI**K**R**I**GG**S**V**L**FVGSLLSLAYLVHDLPRAL
 SKLPALAIYSFGG**S****K**I**V**T**T**VIFN**G**LSAFSWK**S**L**G**Q**I**AG**S**V**V**FAG**S**LLGMAYI**I**YDIPRAL

Mfn1 *Homo sapiens* MITL**V**TGLAS**L**T**S**R**T**SM**G**I**I**V**G**GV**I**W**K**T**I**GW**K**LL**S**V**S**L**T**MY**G**AL**Y**LY**E**R**L**SW
 Mfn1 *Bos taurus* M**V**T**L**I**T**LAS**L**T**S**R**T**SM**G**I**I**V**G**GV**I**W**K**T**V**GW**K**L**I**S**V**S**L**S**M**Y**G**AL**Y**LY**E**R**L**TW
 Mfn1 *Canis lupus familiaris* M**V**T**L**I**T**LAS**L**T**S**R**T**SM**G**I**I**V**G**GV**I**W**K**T**V**GW**K**L**I**S**V**S**L**S**M**Y**G**AL**Y**LY**E**R**L**TW
 Mfn1 *Gallus gallus* M**V**PL**V**MS**L**AS**L**T**S**R**T**SM**S**I**I**V**G**GV**I**W**K**T**V**GW**K**L**I**S**L**S**L**S**M**Y**G**LL**Y**LY**E**R**L**TW
 Mfn1 *Mus musculus* M**I**T**L**I**T**LAS**L**T**S**R**T**SM**G**I**I**V**G**GV**I**W**K**T**V**GW**K**L**I**S**V**T**L**S**M**Y**G**AL**Y**LY**E**R**L**TW
 Mfn1 *Rattus norvegicus* M**I**T**L**I**T**LAS**L**T**S**R**T**SM**G**I**I**V**G**GV**I**W**K**T**V**GW**K**L**I**S**V**T**L**S**M**Y**G**AL**Y**LY**E**R**L**TW
 Mfn1 *Xenopus tropicalis* M**L**S**V**M**S**GLAS**L**T**S**R**G**S**M**S**V**I**V**G**G**V**I**W**R**T**V**GW**R**L**I**S**G**M**L**AY**G**LL**Y**LY**E**R**L**TW
 Mfn1 *Macaca mulatta* M**I**T**L**V**T**GLAS**L**T**S**R**T**SM**G**I**I**V**G**GV**I**W**K**T**I**GW**K**L**I**S**V**L**T**MY**G**AL**Y**LY**E**R**L**SW
 mfn1b *Danio rerio* M**L**T**M**V**N**N**L**AS**V**T**S**R**T**SM**S**V**I**V**G**GV**V**W**R**T**V**GW**R**L**I**AL**S**M**S**MY**G**LL**Y**LY**E**R**L**TW

Agap *Anopheles gambiae* V**I**S**K**V**A**I**A**S**I**G**S**Q**G**T**L**G**L**-**V**V**A**G**L**M**L****K**T**I**G**R**V**V**I**V**G**A**G**V**I**G**S**V**LY**E**R**L**S
 MFN2 *Bos taurus* V**S**M**V**T**G**LAS**L**T**S**R**T**SM**G**I**L**V**V**G**G**V**V**W**K**A**V**G**W**R**L**I**A**L**S**L**G**LY**G**LL**V**Y**E**R**L**T
 MFN2 *Canis lupus familiaris* V**S**M**V**T**G**LAS**L**T**S**R**T**SM**G**I**L**V**V**G**G**V**V**W**K**A**V**G**W**R**L**I**A**L**S**F**G**LY**G**LL**V**Y**E**R**L**T
 MFN2 *Gallus gallus* V**S**M**V**T**G**LAS**L**T**S**R**T**SM**G**I**I**V**V**G**G**V**V**W**K**A**V**G**W**R**L**I**A**L**S**F**G**LY**G**LL**V**Y**E**R**L**T
 MFN2 *Homo sapiens* V**S**M**V**T**G**LAS**L**T**S**R**T**SM**G**I**L**V**V**G**G**V**V**W**K**A**V**G**W**R**L**I**A**L**S**F**G**LY**G**LL**V**Y**E**R**L**T
 MFN2 *Macaca mulatta* V**S**M**V**T**G**LAS**L**T**S**R**T**SM**G**I**L**V**V**G**G**V**V**W**K**A**V**G**W**R**L**I**A**L**S**F**G**LY**G**LL**V**Y**E**R**L**T
 MFN2 *Pan troglodytes* V**S**M**V**T**G**LAS**L**T**S**R**T**SM**G**I**L**V**V**G**G**V**V**W**K**A**V**G**W**R**L**I**A**L**S**F**G**LY**G**LL**V**Y**E**R**L**T
 Marf *Drosophila melanogaster* L**I**S**R**F**A**V**S**S**I**G**S**Q**G**T**V**G**L**V**V**A**G**V**M**L**K**T**I**G**R**V**L**V**G**V**G**A**L**Y**G**C**I**Y**L**Y**E**R**L**S
 Mfn2 *Mus musculus* V**S**M**V**T**G**LAS**L**T**S**R**T**SM**G**I**L**V**V**G**G**V**V**W**K**A**V**G**W**R**L**I**A**L**S**F**G**LY**G**LL**V**Y**E**R**L**T
 Mfn2 *Rattus norvegicus* V**S**M**V**T**G**LAS**L**T**S**R**T**SM**G**I**L**V**V**G**G**V**V**W**K**A**V**G**W**R**L**I**A**L**S**F**G**LY**G**LL**V**Y**E**R**L**T
 fzo-1 *Caenorhabditis elegans* T**Q**M**V**L**T**S**A**A**F**L**A**NG**S**L**G**V**L**V**V**G**G**I**V**Y**K**A**V**G**W**R**V**I**A**V**G**G**A**A**Y**A**G**L**Y**A**W**E**R**M**R**
 mfn2 *Danio rerio* V**S**M**V**T**G**LAS**L**T**S**R**T**SM**G**I**I**V**V**G**G**V**I**W**K**A**V**G**W**R**L**I**A**L**S**V**G**LY**G**LL**V**Y**E**R**L**T
 mfn2 *Xenopus tropicalis* V**S**M**V**T**G**LAS**L**T**S**R**T**SM**G**I**L**V**V**G**G**V**V**W**K**A**V**G**W**R**L**I**A**L**S**F**G**LY**G**LL**V**Y**E**R**L**T

Supplementary Figure S3.9: **TM domain sequence alignments from eucaryotic mitofusins.** Each predicted TM helix is represented as a yellow rectangle. The basic residue in TM1 is highlighted in red. For most yeast species, a lysine is found, whereas an arginine is found in mammals.

CHAPTER 4

**A CASE BY CASE STUDY OF THE
PROTEIN-MEMBRANE INTERACTIONS OF
MARTINI2 AND MARTINI3 FORCE-FIELDS**

4.1 Introduction

Molecular dynamics (MD) simulations provide a unique opportunity to investigate biological processes with exceptional spatial and temporal precision, surpassing the limitations of experimental approaches [253]. Indeed, despite the computational time and cost, simulations offer the ability to capture atomic-level details and explore dynamic processes occurring at very short timescales, thus providing valuable insights into molecular behavior. Simulations can also sample diverse conformations and configurations, contributing to a more comprehensive understanding of biological systems. Moreover, certain biological states or conformations might be difficult to access experimentally due to kinetic barriers or limited experimental conditions. Here, MD simulations prove to be particularly advantageous, as they can overcome these limitations and reveal elusive states that are otherwise challenging to observe. Additionally, MD simulations furnish detailed information on molecular interactions, energetics, and spatial arrangements. These insights are often difficult to obtain through experiments alone, underscoring the unique value of simulations in enhancing our comprehension of intricate molecular phenomena. To enable these simulations, biomolecular force field parameters have been developed extensively, encompassing diverse molecules such as inorganic ligands, small organic compounds, proteins, lipids, and nucleic acids. These force fields are carefully tuned and validated based on thermodynamic measurements and structural features of individual components, such as soluble proteins or lipid bilayers.

Nonetheless, numerous pertinent biological processes encompass significantly larger biomolecular assemblies or unfold over extended periods, requiring simulations that span considerable timeframes and use considerable computational power. As seen before in the previous chapters (Material and Methods Chp. 2, Fzo1 TM study Chp. 3), the computational complexity of these challenges can be reduced by grouping atoms into single particles referred to as "beads". These coarse-grained (CG) models vary in resolution, encompassing representations that involve one or a few beads per amino acid up to a single bead per hundreds or thousands of DNA bases. The Martini model stands as one of the most widely adopted coarse-grained (CG) models in biomolecular simulation, owed to its user-friendly building block approach. Utilizing a four-to-one mapping scheme, the Martini model aggregates an average of four heavy atoms and their associated hydrogens into a single CG bead [161, 162, 163] (a more detailed description of the force-field can be found in Material and Methods Chp. 2, Figure 2.10).

The primary motivation for employing CG models is the accelerated sampling they offer. This speedup can be attributed to four key factors [254] (Figure 4.1). (i) The first one is a reduced number of particles to compute (less degrees of freedom) and a decreased number of neighbors to take into account. The reduction factor varies from 3 to over 10, as certain models can map multiple water molecules into a single CG particle. The Martini model traditionally consider 1 water particle to be equivalent to 4 water molecules. (ii) The second reason is that only short-range interactions are computed (with a cut-off at 1 nm). Costly Particle Mesh Ewald (PME) methods are unnecessary as the short-range potentials effectively capture the electrostatic interactions. (iii) The third factor is an other consequence of low

number of degrees of freedom (DOFs). Due to the smoothing of the potential energy surface resulting from reduced DOFs, there is less friction, leading to a phase space that is more highly sampled within the same simulation time. (iv) Lastly, the overall smoother energy surface allows for the utilization of larger integration time steps, typically in the range of tens of femtoseconds, as opposed to the 1-4 femtoseconds used in all-atom MD simulations.

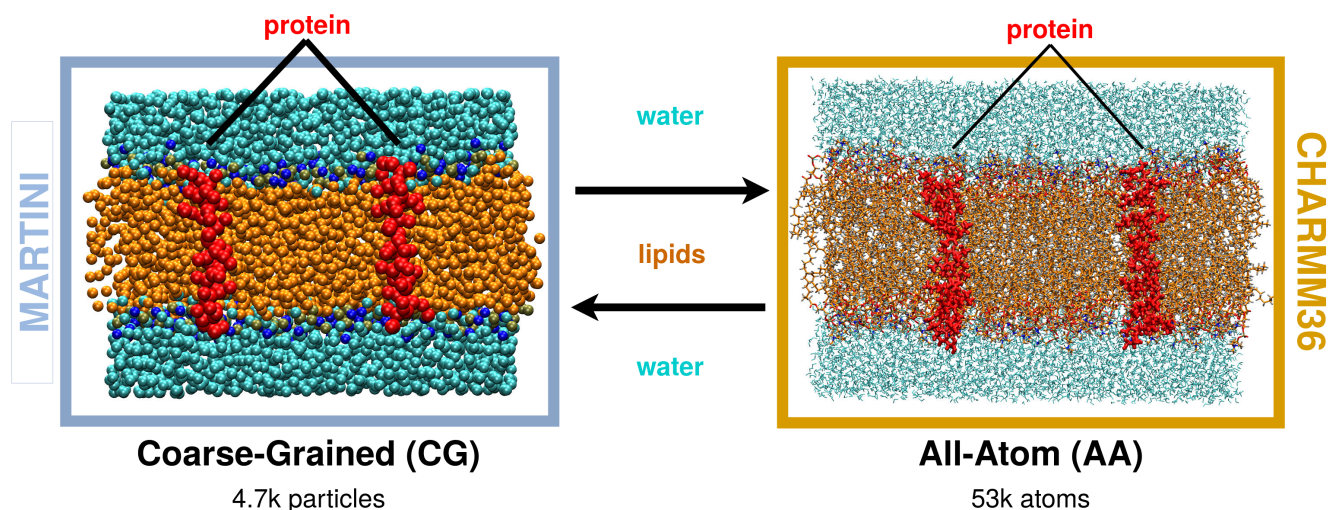


Figure 4.1: **Comparison of a Coarse-Grained system with its All-Atom version.** The CG system is shown in van der Waals representation. The all-atom system is shown in licorice representation. Water particles (CG) and water molecules (all-atom) are represented in cyan. Lipids are represented in orange. The phosphate group particle (CG) and phosphate atom (all-atom) is represented in blue. The protein is represented in red.

However, the precision of MD outcomes relies on the quality of the employed force field, and there could be constraints in accurately representing specific molecular interactions. The Martini force-field, more precisely the Martini2.2 version, has been criticized for a number of shortcomings, such as overestimation of aggregation of molecules. This phenomenon has been observed not only for proteins and carbohydrates in solution but also for proteins embedded in membranes [184, 185, 186]. In fact, the Martini 2 force field tends to overestimate the dimerization free energy for membrane proteins [185, 164], resulting in instantaneous, nonselective, and irreversible binding [185] (Table 4.1, Figure 4.2). This can lead to the formation of unrealistic protein oligomers or superaggregates. This adds further complexity to the interpretation of simulation data concerning dimerization interfaces. When the binding between two proteins is excessively strong and rapid due to the force field’s characteristics, the dimerization interface predicted by coarse-grained simulations may be inaccurate. Moreover, the lateral association of embedded amphipathic helices was also investigated, revealing that the Martini2.2 force field underestimates the repulsive free energy between the two amphipathic helices to a significant extent [255].

	EphA1	ErbB1
Experimental	-15.4 ± 0.5	-10.5 ± 0.4
Standard Martini2.2	-29.9 ± 1.0	-39.5 ± 1.0

Table 4.1: **EphA1 and ErbB1 TM domain dimerization free energy ΔG_{DIM} (in kJ/mol)**. Values taken from [185].

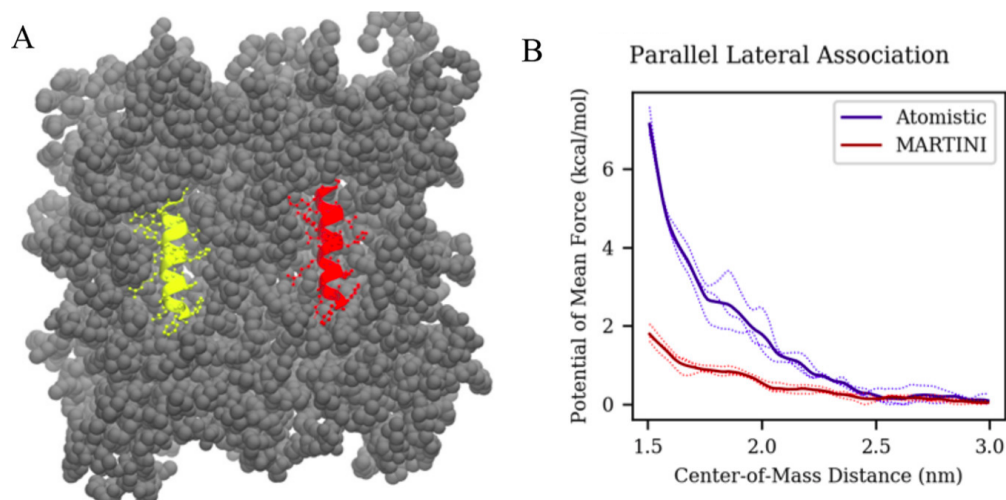


Figure 4.2: **Lateral association of embedded amphipathic helices.** (A) Snapshot of amphipathic HO helices (red and yellow) embedded in DOPC bilayer (gray) with a center-of-mass distance of 3.0 nm and (B) potential of mean force as a function of center of mass distance between the two embedded helices for the atomistic (blue) and MARTINI 2.0 (red) models. Sampling error bars are shown on each curve. Taken from [255].

To alleviate the problems listed above, all nonbonded interaction terms of the Martini model were rebalanced, and new beads were added in the version Martini3 (see Material and Methods chp. 2, Figures 2.11 and 2.12) [164]. Moreover, with the availability of the beta version of Martini3, numerous studies on this version became quickly accessible around the time the paper was published. As time has passed, an increasing amount of data has been accumulated in the literature concerning Martini3 simulations. To begin with, the updated version of the force field demonstrated improvements in packing and protein-protein interactions (see Figure 4.3) [164]. Addressing the issue of hyper hydrophobicity resulted in noticeable enhancements in predicting protein-membrane interfaces as well [256]. However, even though it was shown to reproduce experimental trends for amphipathic helix, the relative binding free energies were shown to be generally lower than those calculated from atomistic simulations [257]. Furthermore, transmembrane (TM) domains have been shown to not integrate membranes or micelles as expected when simulated with Martini3 [244]. This study showed that scaling down protein-water interactions improved the TM domains insertion and interaction with the membrane. Ironically, Martini 3 simulations of intrinsically disordered proteins (IDPs) exhibit overly compact conformational ensembles, leading to limited agreement with small-angle X-ray scattering (SAXS) and paramagnetic relaxation enhancement

(PRE) experiments [258]. Increasing the strength of protein-water interactions by 10% showed that more expanded ensembles are observed, which better align with experimental data [259].

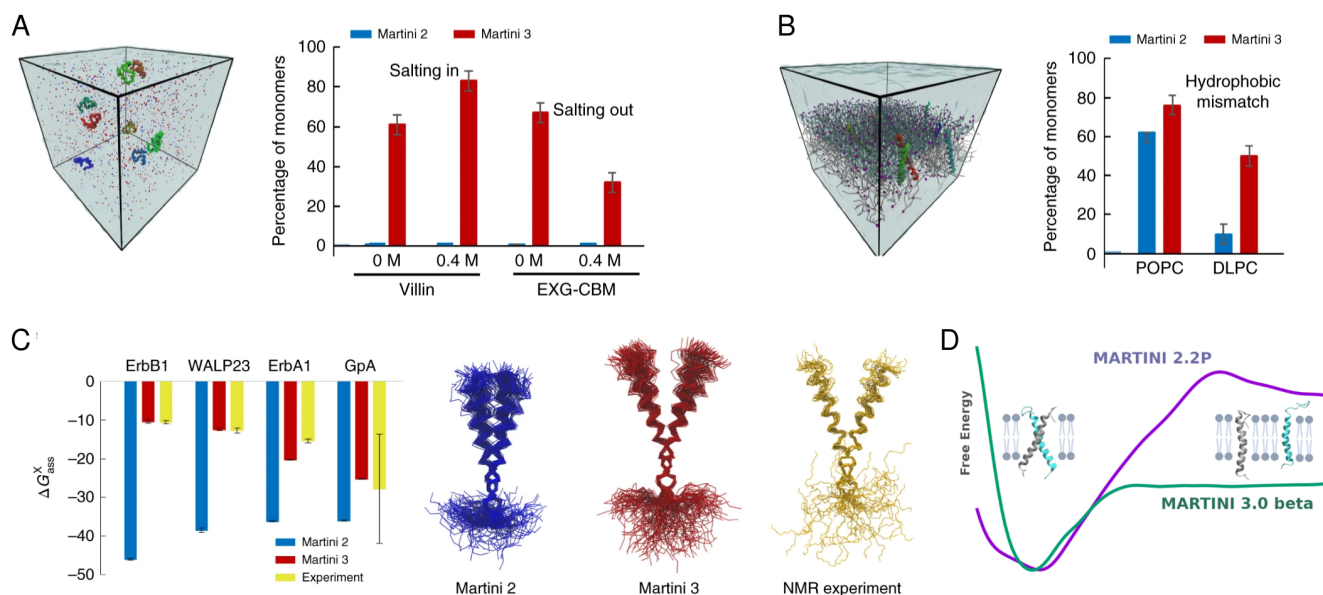


Figure 4.3: **Improving packing and reducing protein stickiness.** (A) Aggregation levels of the soluble proteins villin headpiece and the modified EXG-CBM in different salt concentrations. (B) Aggregation levels of polyleucine helices in POPC and 1,2-dilauroyl-sn-glycero-3-phosphocholine (DLPC) bilayers. Errors in the average monomer percentage of (A) and (B) are estimated by block averaging. (C) Dimerization of transmembrane helices. The left panel shows a comparison between experimental and calculated values for the mole fraction standard Gibbs free energy of dimerization (ΔG_{ass}^X) of the following transmembrane protein domains: ErbB1, EphA1, WALP23 and GpA. (A), (B) and (C) are taken from [164]. (D) Free energy evaluation for the dimerization of EphA1. Taken from [238].

To compare the performance of Martini 2 and Martini 3 force fields, we have employed various membrane systems involving amphipathic helices and transmembrane domains. Firstly, membrane only systems were simulated and analyzed in order to compare the membrane behavior between the two force fields. Next, we performed molecular dynamics simulations on peptides interacting with the membrane, including penetratin, a well-studied cell-penetrating peptide with known experimental data [260], and the amphipathic helix of Mfn1, which was identified in this study [135]. By examining the peptide-membrane interactions, we aim to assess the force fields' accuracy in reproducing experimental observations and characterizing the peptides behavior in different environments.

Through this comparative study, we aim to discern any improvements or discrepancies introduced by Martini 3 compared to Martini 2 in representing peptide behavior and interactions. This investigation will provide insights into the strengths and limitations of the Martini force-fields, facilitating the informed selection of the most suitable force field for specific peptide systems and membrane-related studies.

4.2 Materials and Methods

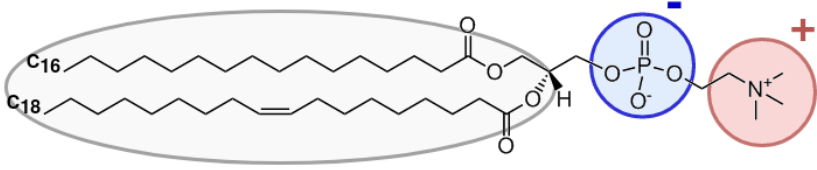
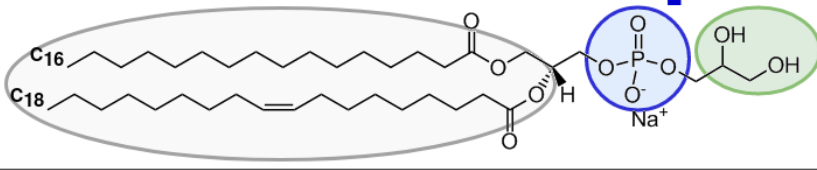
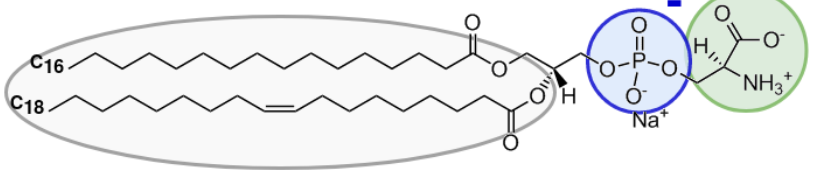
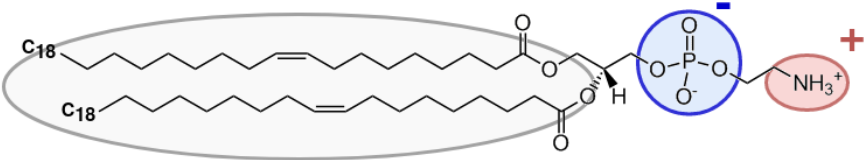
name	stick representation	charge
POPC		0
POPG		-1
POPS		-1
DOPE		0

Figure 4.4: **Stick representation of the lipids used in this chapter.** POPC stands for Palmitoyl-Oleoyl-Phosphatidyl-Choline, DOPE stands for DiOleoyl-Phosphatidyl-Ethanolamine, POPS Palmitoyl-Oleoyl-PhosphatidylSerine, POPG stands for Palmitoyl-Oleoyl-Phospho-Glycerol. In fact, the first two letters of the lipids refer to the carbon tails : 16:0 is Palmitic acid (P), 18:1 is Oleic acid (O). POPG and DOPE phospholipids are neutral. POPG and POPS phospholipids are anionic. DOPE has a smaller hydrophilic head, and has thus a conic shape. The negative phosphate group is represented in a blue circle. The neutral head, rendering the phospholipid charged, are in green. The positively charged heads, neutralizing the phospholipid, are in red.

System type	Lipidic composition	Ratio	Simulation time (μ S)	Force-Field
Membrane only systems	POPC	100	10	MARTINI 2 and 3
	POPG	100	10	
	POPS	100	10	
	POPG:POPS	50:50	10	
	POPC:DOPE	70:30	10	
Penetratin in membrane	POPC	100	10	MARTINI 2 and 3
	POPG	100	10	
	POPS	100	10	
Mfn1-AH in solvent	POPG:POPS	50:50	10	MARTINI 2 and 3
	POPC	100	10	
Mfn1-AH in membrane	POPC:DOPE	70:30	10	MARTINI 3
	POPC:DOPE	30:70	10	
	POPS	100	10	
Mfn1-AH in membrane	POPC	100	10	MARTINI3 scaled
	POPC:DOPE	70:30	10	
Fzo1-TM1	POPC:POPE	50:50	10	MARTINI3 (normal and scaled)

Table 4.2: **Summary table of the simulation systems.** POPC stands for Palmitoyl-Oleoyl-Phosphatidyl-Choline, DOPE stands for DiOleoyl-Phosphatidyl-Ethanolamine, POPS Palmitoyl-Oleoyl-PhosphatidylSerine, POPG stands for Palmitoyl-Oleoyl-Phospho-Glycerol.

4.2.1 Software details

All MD simulations were performed using the GROMACS (v 2018x) [176, 177] package, with the Martini2.2 (MARTINI2) [161, 162] and Martini3 (MARTINI3)[164] versions of the force-fields.

4.2.2 Systems setup

Various membrane systems were analyzed and are listed in Table 4.2, and the different lipids used in these systems are describe in Figure 4.4.

Membrane systems

The MARTINI2 systems were built using the CHARMM-GUI Membrane builder [178, 213, 163] with the MARTINI2 coarse-grained (CG) force field [161, 162]. As the mapping of the lipids does not change between the two version of the force-fields, the same systems were used with the new version of the force-field [164]. The phospholipidic composition of the various systems is described in Table 4.2. Furthermore, about 40 molecules per lipids were used as solvent, to which was added 0.15 M NaCl.

Amphipathic helix systems

The penetratin and Mfn1 amphipathic helix (Mfn1-AH) peptides were built using Basic Builder 1.0.2 on the Mobylye server (<https://mobylye.rpbs.univ-paris-diderot.fr>) [212]. The sequences used

were: RQIKIWFQNRRMKWKK for the penetratin (N-ter neutral and C-ter charged) and DVKKKIKEV-TEEVANKVS for Mfn1-AH (both termini kept charged, in accordance to the experimental data). The alignments between the sequences and their associated predicted secondary structures (α -helix) were submitted in order to build a 3D structure of the peptides.

The MARTINI2 systems were built using the CHARMM-GUI Membrane builder [178, 213, 161, 162, 163] with the MARTINI2 coarse-grained (CG) force field [161, 162]. In the systems with penetratin or Mfn1-AH embedded in the membrane, about 40 molecules per lipids were used as solvent. In the systems with Mfn1-AH in water, about 65 molecules per lipids were used as solvent. To the solvent were added 0.15M of NaCl for each system.

As the mapping of the lipids did not change between the two versions of the force-field, we were able to use the membranes produced in MARTINI2 for our MARTINI3 systems. Atomistic models of the peptides were converted to the MARTINI3 CG representation using the martinize2.py workflow module of the MARTINI3 force field (see <https://github.com/marrink-lab/vermouth-martinize>). These MARTINI3 structures of the peptides were then placed in lieu of the peptides structures in the MARTINI2 system.

Fzo1-TM1 system

The systems involving the transmembrane domain TM1 of Fzo1 (Fzo1-TM1) were built in the same manner. The sequence used is SKIPTLTLYFLGSTKVVGNIILNGIKLSS and was provided to Basic Builder 1.0.2 on the Mobylye server (<https://mobylye.rpbs.univ-paris-diderot.fr>) [212]. All residues were defined as helical except the first and last two, defined as coiled.

MARTINI2 system [161, 162] were built with the CHARMM-GUI Membrane builder [178, 213, 161, 162, 163]. The peptide was placed in the center of the box, the main axis of the helix being parallel to the normal of the membrane. From this system was built the MARTINI3 system, with the MARTINI3 structure of the peptide being built from the all-atom structure, and then replacing the MARTINI2 structure in the box. About 40 molecules per lipids were used as solvent to which was added 0.15M of NaCl.

4.2.3 Scaling of water beads non-bonded interactions in MARTINI3

Two simulations were ran with 10% scaled down non-bonded interactions. Hence, a uniform scaling factor $\alpha = 0.9$ was applied on energy well depths ϵ_{ij} of the Lennard-Jones potentials of all pairs involving water beads, as described in Cabezudo et al. (2023) [244] :

$$\epsilon_{ij}^{new} = \alpha \epsilon_{ij} \quad (4.1)$$

4.2.4 Simulation parameters

For membrane-only and amphipathic helix system, we followed the protocol of CHARMM-GUI which consisted in two energy minimizations of 5000 steps, followed by an equilibration of 5 simulations within

the NPT ensemble. The velocity-rescaling thermostat [174], at 295 K for the penetratin and 310 K for the Mfn1-AH (in accordance with the experimental data [260] and [135] respectively), and the Berendsen barostat at 1 bar [173] were applied for a sequence of 5 simulations of 1 ns, 1 ns, 1 ns, 0.75 ns and 1 ns (with a timestep of 0.002 ps, 0.005 ps, 0.01 ps, 0.015 ps, 0.020 ps respectively). A production run of 10 μ s followed, at 295 K for the penetratin and 310 K for the Mfn1-AH using the velocity-rescaling thermostat [174] (lipid, water and proteins coupled separately) and 1 bar using the Parrinello-Rahman barostat [175] (compressibility of $3.0 \times 10^{-4} \text{bar}^{-1}$). Pressure coupling was applied semi-isotropically. A time step of 0.020 ps was used with the leapfrog integrator. Lennard-Jones interactions were cutoff at 1.1 nm. Bond lengths were constrained using the LINCS algorithm [214]. The reaction-field method [215] was used for evaluating electrostatic interactions, with a Coulomb distance cutoff of 1.1 nm, a relative dielectric constant of 15. The neighbor list was updated every 20 steps.

4.2.5 Analysis details

Helix wheels

The helix wheels were built using the HELIQUEST webserver [261]. Both sequences of the penetratin (RQIKIWFQNRRMKWKK) and Mfn1-AH (DVKKKIKEVTEEVANKVS) were submitted, and the "full window" option was used, in order to have all the residues of sequences on one helix wheel. We then adapted the colors of the amino acids in the sequence based on their physico-chemical properties: in green are represented charged residues, polar residues are in pink, hydrophobic residues are in yellow.

Membrane thickness, position of the peptide, and partition plots

These analysis of the positions of the peptide and its residues were carried out using GROMACS (v 2018x) [176, 177], with the command *gmx traj*. The positions on the z -axis of the center of mass of the protein was determined using the backbone beads only. The positions on the z -axis of the center of mass of each residues of the penetratin was determined using the side chain beads only. The positions of the peptide or the residues with respect to the bilayer center were then calculated using the R library *ggplot2* [219]. The position of the center of mass of the peptide was studied throughout all simulations. The positions of the residues side chains were determined only when the peptide was found to bind the membrane.

To assess the membrane thickness, we initially divided the 10 μ s interval into five segments (excluding the initial 0.05 μ s). For each segment, we computed the density along the z -axis for both the membrane and the solvent separately. The command "gmx density" of the GROMACS package was used. Using the density data, it becomes feasible to compute the membrane thickness (using an in-house R script). This is achieved by determining the distance between the two points where the densities of the solvent and the membrane are equal.

Packing Defects

Lipid packing defects between the lipid polar heads are small apolar areas of the membrane which are accessible to the solvent. They are useful proxy to understand the binding of amphipathic helices [52, 249] or for predicting the fusogenicity of a lipid composition [235].

Packing defects were quantified using the PackMem software [52, 145]. The principle is illustrated in Figure 4.5. The software uses a grid of 1 \AA^2 granularity. For each grid point, it evaluates if the atom accessible vertically below the grid point is hydrophobic (from the aliphatic tails in yellow). If so, the grid point is considered as an elementary defect (red dot). Using a connected component algorithm, the red dots are merged into a packing defect on which it is possible to calculate its area. 3 types of defects are considered, deep ones (below the glycerol level), shallow ones (above the glycerol), or "all" corresponds to deep + shallow. In this work, we only used the "all" category, which is the relevant one for studying fusion [235]. In panel C of Figure 4.5, we can see an example of 3 defects ("all" category). Then statistics are collected on all the packing defects observed in a molecular dynamics trajectory (each leaflet is considered separately). The corresponding distribution is fitted to a monoexponential decay:

$$p(A) = be^{-A/\pi}$$

where A is the area of a given packing defect, $p(A)$ is the probability of finding a packing defect of area A , π is the packing defect constant, and b is the pre-exponential factor (not used here). The packing defect constant π thus reports on the quantity and size of packing defects. It is in unit \AA^2 . The larger, the more probable and the larger (in terms of area) the packing defects for a given lipid composition. An example is given in 4.5 on four lipid compositions and two force fields.

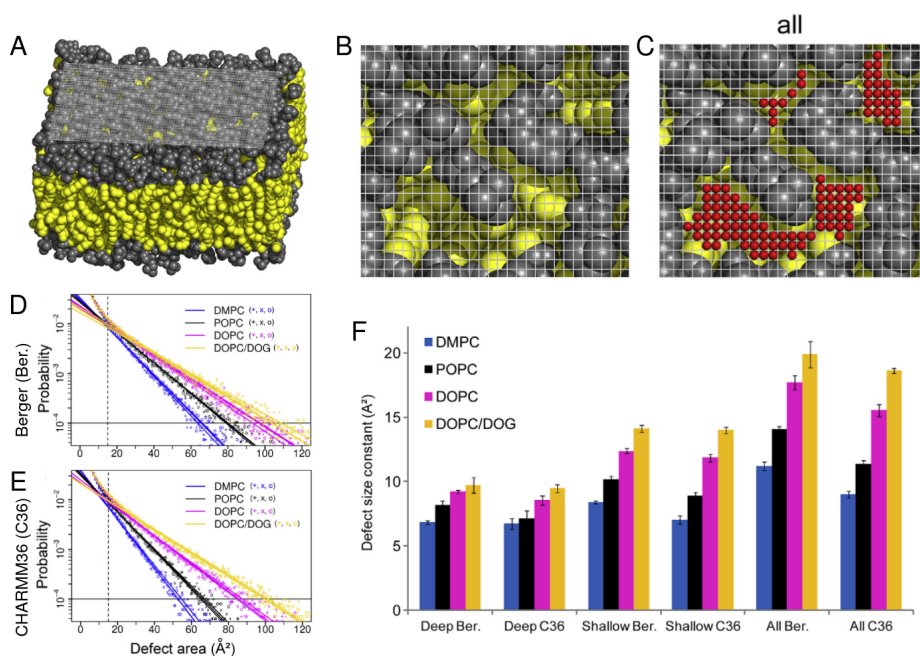


Figure 4.5: **Quantification of lipid packing defects.** (A) Scheme of the bilayer and the grid. Polar heads are in gray, aliphatic tails in yellow. (B) Top view with the grid. (C) Illustration of the quantification of 3 packing defects. Each red dot represents 1 Å². (D) and (E) Exponential fits for a few simulations (4 lipid compositions and two force fields, CHARMM36 and Berger). (F) Barplot of packing defect constants for "deep", "shallow" and "all" defects.

When the peptide is observed binding to the membrane, the first ns of simulations without the peptide embedded in the membrane are discarded for the various analysis. In this case, the packmem analysis take into account the peptide for packing defects calculations. In situations where the peptide does not bind to the membrane, only the membrane is analyzed (in the case of packmem), and the entire simulation is assessed, with the initial 50 ns discarded.

Area per Lipids and Protrusion events

The area per lipids is calculated using the fatslim software [262]. This value is obtained by initially computing local Voronoi cells for each lipid and subsequently calculating the area of each cell.

A protrusion event is defined as one of the carbon atom of a tail bulging into the polar layer (or a backbone bead of a lipid tail), extending 0.025 nm above (or below depending on the leaflet) its phosphorus atom [147, 146]. Protrusions were identified using an in-house script.

4.3 The penetratin has a more realistic behavior in MARTINI3 simulations

To investigate the positioning of the penetratin in various membrane composition, we initially positioned the helix within the membrane, at the level of phosphate groups (Figure 4.6A). First, the protein's dis-

tance from the bilayer center over time was calculated and depicted in Figure 4.1C. Additionally, the distribution of this distance was graphed in Figure 4.1D. Instances in which the minimum distance was approximately 2 nm were identified as membrane-bound states, aligning with the general position of the upper layer's phosphate groups within the membrane.

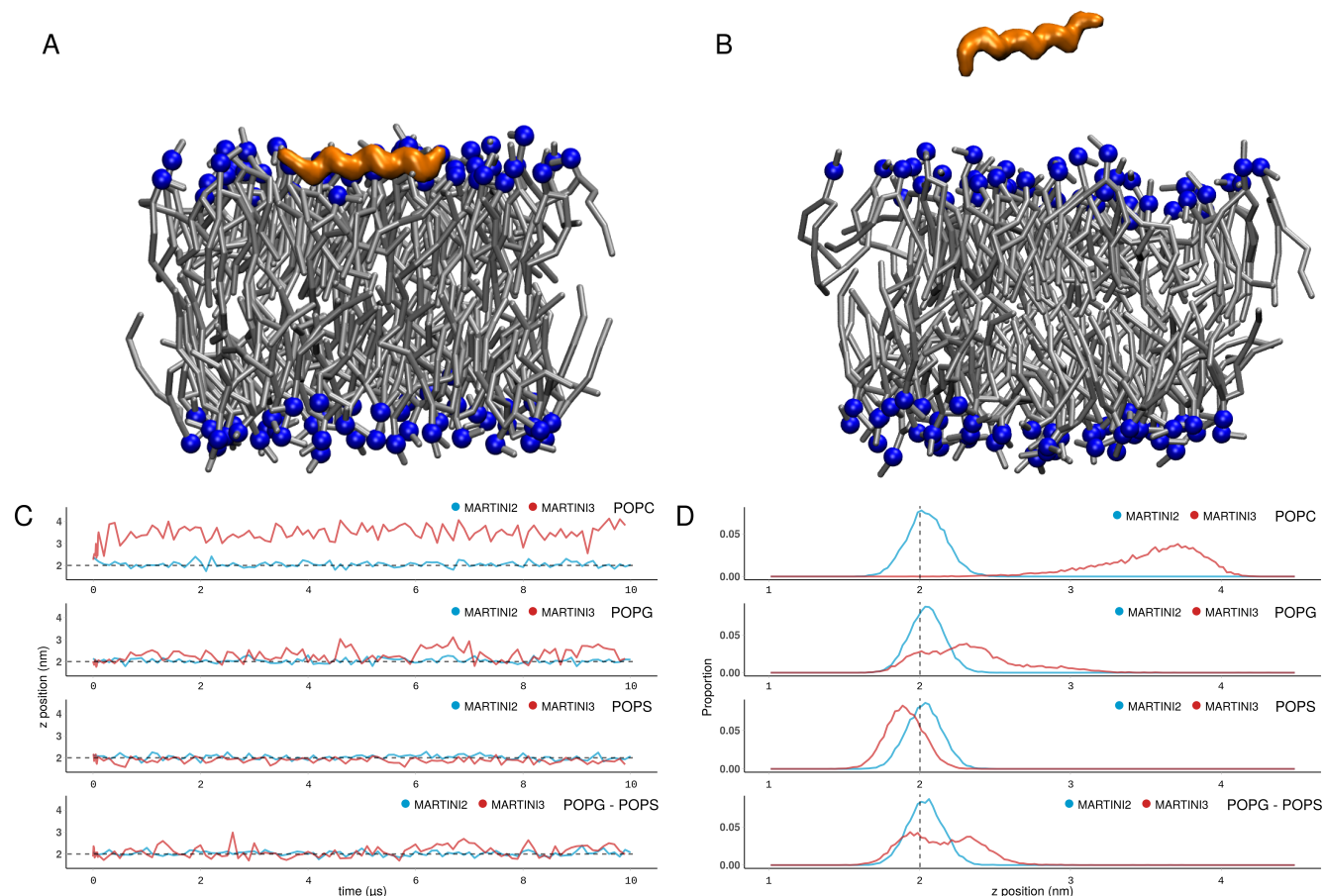


Figure 4.6: Characterization of penetratin membrane binding. (A) Initial state of the penetratin placed in a POPG membrane. This state corresponds to the bind state of the penetratin with the membrane. The membrane is shown in grey and stick representation, the phosphate groups in blue and van der Waals representation, and the protein in orange and surface representation. The water and ions were omitted for clarity. (B) Unbound state of the protein, with a POPC membrane. (C) Distance from the bilayer center over time. In blue, the MARTINI2 systems; in red, the MARTINI3 systems. The dashed dark line represent the position of the upper layer phosphate group. (D) Probability density distribution of the same distances.

These analyses reveal distinct behaviors of the penetratin as a function of membrane composition between the two versions of the MARTINI force field. Specifically, while MARTINI2 simulations consistently exhibit a highly stable bound state across all membranes, MARTINI3 simulations indicate that the stability of the bound state varies with membrane composition. Notably, the POPS environment demonstrates the highest stability, while the POPC bilayer displays the lowest, the penetratin being unbound from the membrane throughout the MARTINI3 simulation. The POPG membrane simulation showed

dissociation events of the protein from the membrane, rapidly succeeded by a new binding event. Hence, within a POPG-POPS membrane, the penetratin is less deeply embedded, all while remaining within the vicinity of the membrane. Notably, it is interesting to observe that, despite relatively consistent distributions of bound distances across different membrane types in MARTINI2, there are differences in the binding state within MARTINI3 simulations for POPG and POPS membranes. Specifically, in a POPS membrane, the protein appears to be embedded more profoundly, even if POPS lipids only constitute a portion of the entire membrane.

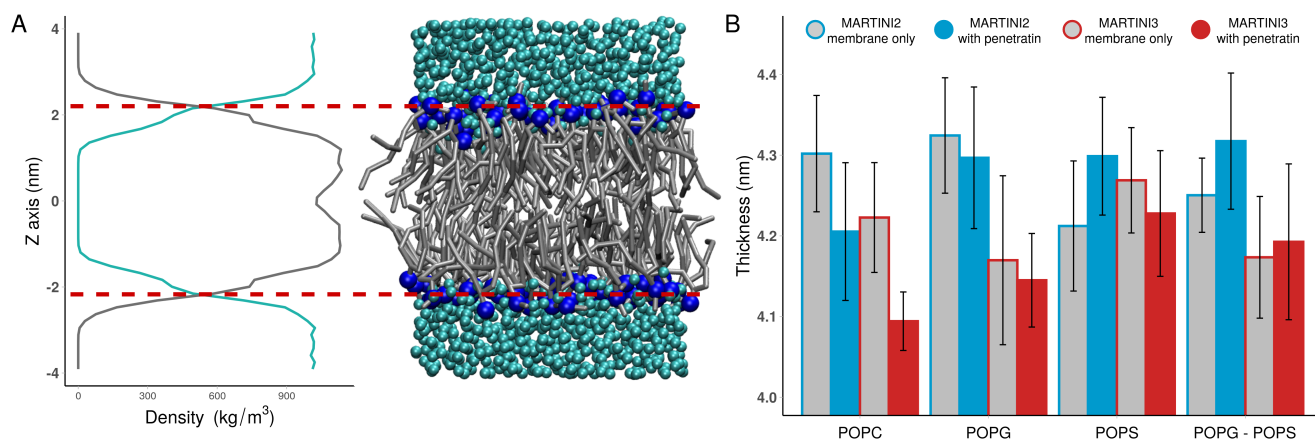


Figure 4.7: Membrane thickness analysis of the penetratin. (A) Density profile of a POPC membrane only MARTINI3 system. The density of water is represented in cyan, the density of the membrane is represented in grey. On the right of the plot is shown the snapshot of the POPC membrane system. The water beads are in cyan and van der Waals representation. The POPC molecules are in grey and licorice representation. The phosphate groups (PO₄ beads) of the POPC molecules are shown in blue and van der Waals representation. The membrane thickness is computed by calculating the distance between the two crossovers of water and membrane densities (red dashed lines). (B) Barplot representation of the membrane thickness values. Errors were calculated by dividing the simulation in XXX blocks and computing the standard deviation of the mean of each block. The membrane only system are filled with grey. The MARTINI2 systems are in light blue, the MARTINI3 systems are in red.

Furthermore, we analysed various membrane parameters in order to investigate the impact of the protein on the membrane as well as to conduct a comparative assessment of the two versions of the MARTINI force fields. Our examination first focused on the membrane thickness (Figure 4.7A). MARTINI3 membranes seem to exhibit a reduced thickness compared to MARTINI2 membranes. This inclination is confirmed by the area per lipid analysis (APL) (see Figure 4.8A). A lower value indicates a more compact membrane, as it signifies that each lipid occupies less space. Except for POPC, the APL demonstrates an increase upon employing MARTINI3 simulations, showing that MARTINI2 simulations consistently have a more compact membrane. Additionally, it is evident that the inclusion of penetratin leads to an increase in APL, hence, indicating that the peptide increases the fluidity of the membrane. Regarding the POPC system within MARTINI3 simulations, an interesting observation is that the distribution of the APL remains rather unchanged, with or without penetratin. This can be attributed to the fact that the

penetratin interactions with the membrane are limited throughout the simulation. Moreover, it is worth noting that APL values exhibit greater consistency for the POPC membrane, even with the application of the two force field versions. Overall, these analyses show that both versions of MARTINI give similar results with zwitterionic POPC but different ones when some anionic POPG or POPS are present.

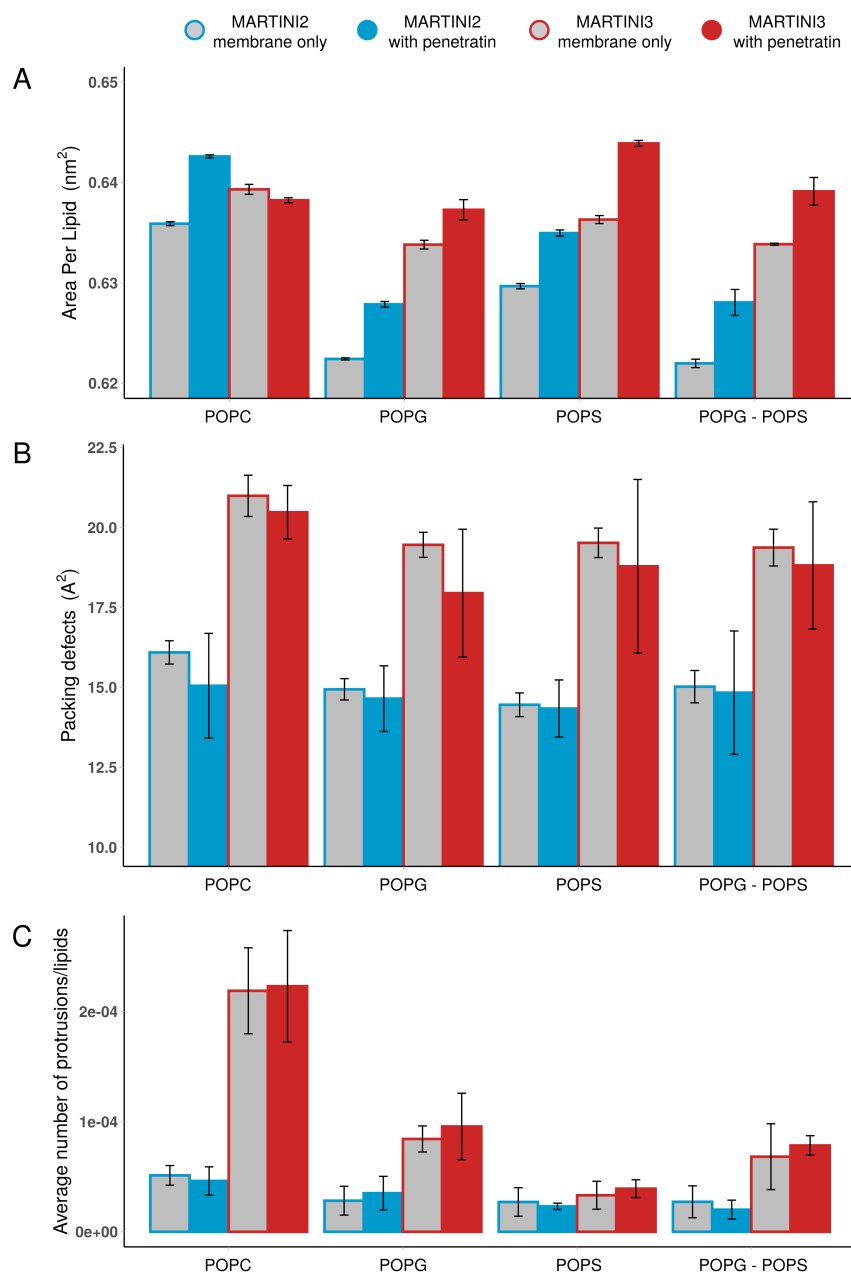


Figure 4.8: **Membrane analysis of penetratin systems.** Color scheme can be seen at the top of the plots. The membrane only systems are filled with grey. The MARTINI2 systems are in light blue, the MARTINI3 systems are in red. (A) Area per lipid of the different Penetratin systems. The values are given in nm². (B) Packing defects in Å². (C) Average number of protrusions per lipids.

Additional membrane analyses were conducted, including the assessment of packing defects [145] and protrusion events [147] (Figure 4.7B,C). Yet, these analyses did not reveal substantial differences

when comparing systems with or without the peptide. It is logical with POPC since penetratin is bound to the membrane, for the other compositions this is a result. Given the large error bars for packing defects, it would be interesting to carry out the analysis per leaflet (w/wo peptide). Importantly, these values exhibit a systematic increase in MARTINI3 systems compared to MARTINI2, aligning coherently with the findings from the membrane thickness and APL. It is worth highlighting that the POPC membranes exhibit the highest occurrence of protrusion events, in agreement with the packing defect tendencies.



Figure 4.9: **Distribution of the residues of the penetratin in the membrane.** (A), (B) Boxplot of the position on the z -axis of the residues side chains, of respectively MARTINI2 and MARTINI3 systems. Only the frames of our simulations showing the penetratin embedded in the membrane were used. Hence, there is not the POPC membrane system in (B). The dashed dark line represent the position of the upper layer phosphate groups. (C) Helix wheel of the penetratin, colored as function of the properties of the residues. Hydrophobic residues are colored in yellow, hydrophilic residues are colored in pink, and charged residues are colored in green. The dashed dark line represent the position of the upper layer phosphate groups. Snapshots of the helix embedded in the membrane are presented, of the MARTINI3 POPS membrane system. The residues are colored according to (C) and the phosphate groups of the phospholipids are in blue van der Waals representation.

Figure 4.9A,B shows the positioning of penetratin residues within the membrane. As the penetratin is not embedded in the POPC membrane in the MARTINI3 simulation, this simulation was not used for Figure 4.9B. A common aspect across all systems was the alignment of a similar helical face embedded within the membrane (Figure 4.9C). The non-polar residues, particularly Ile3, Trp6, Phe7, and Trp14, are frequently positioned beneath the phosphate groups. Additionally, in MARTINI3 simulations, the polar residue Gln2 is commonly observed beneath the phosphate groups. Furthermore, the charged residues

Arg1, Lys4, Arg10, Arg11, and Lys15 occupy the same level as the phosphate groups, along with the polar residue Glu2. Interestingly, MARTINI3 simulations can exhibit a more profound peptide integration into the membrane compared to MARTINI2, except for the C-terminal residues, whose positions fluctuate in and out of the membrane when the membrane contains POPG. In fact, the POPS membrane simulation demonstrated the deepest burial of residues, which corroborates what has been observed in Figure 4.6D. However in the MARTINI3 POPG and POPG-POPS membrane systems we can observe that the C-terminal fluctuates more along the z -axis compared to POPS. This observation suggests that the stability of C-terminal residues is compromised when POPG is present in the membrane.

4.4 The behavior of Mfn1-AH exhibits distinct dissimilarities between MARTINI2 and MARTINI3.

As a second project, we wanted to investigate the binding capability of Mfn1-AH in two membrane environments: a full POPC membrane, and a POPC:DOPE membrane with a ratio of 70:30. These ratios were chosen with David Taresté our collaborator on the study of Mfn1-AH. The helix was initially positioned outside of the membrane, in the solvent. The distribution of the distance of the protein to the bilayer center was plotted in Figure 4.10B. The two force fields yield contrasting outcomes, with MARTINI2 showing protein binding to the membrane, while MARTINI3 does not exhibit such binding (Figure 4.10A,B). Hence, the MARTINI3 system does not manifest any discernible impact of the peptide on the APL (Figure 4.10C), as it remains similar across both membrane-only and membrane-peptide systems. In contrast, MARTINI2 simulations with the peptide show increased APL values in comparison to membrane-only system.

Regarding pure lipids, MARTINI2 shows a decrease of APL, and conversely an increase of thickness (Table 4.3), ongoing from POPC to POPC-DOPE. This is expected, since the conical shape of DOPE (small polar head) results in its partitioning slightly below POPC leading to a thickening of the membrane. This is the exact same effect as when adding diacylglycerol (DAG) to a membrane made of PC lipids [52, 263]. Interestingly, MARTINI3 shows the opposite trend (increase of APL and thinning of the membrane) thus failing at predicting the right behaviour upon DOPE addition to POPC.

Lipidic composition	MARTINI2 membrane only	MARTINI3 membrane only	MARTINI2 with Mfn1-AH	MARTINI3 with Mfn1-AH
POPC	4.17 ± 0.06	4.14 ± 0.17	4.17 ± 0.07	4.11 ± 0.07
POPC-DOPE	4.24 ± 0.05	3.98 ± 0.09	4.00 ± 0.06	4.07 ± 0.09

Table 4.3: **Summary table of the membrane thickness for the Mfn1-AH systems.** The membrane thickness of the POPC membrane systems is different than in the previous section, as the temperature has increased (310K for Mfn1-AH and 295K for penetratine).

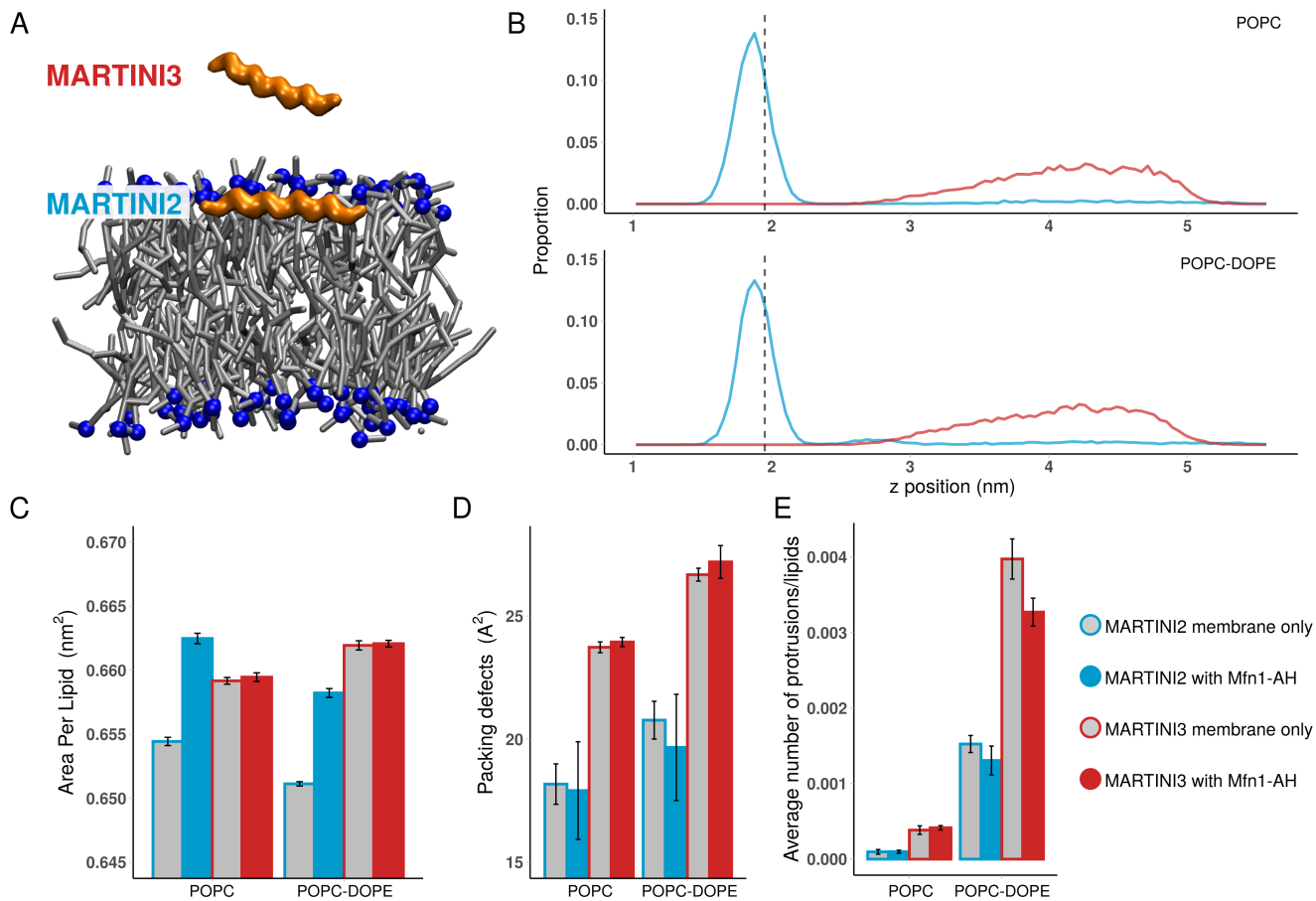


Figure 4.10: Membrane analysis of the Mfn1-AH simulations. (A) Snapshot of the POPC-DOPE membrane-peptide MARTINI2 and MARTINI3 systems. The POPC molecules are in grey and licorice representation. The phosphate groups (PO4 beads) of the POPC molecules are shown in blue and van der Waals representation. The peptide is represented in orange. Only one peptide is present in each MARTINI systems, but the two distinct results are shown here on the same membrane. In MARTINI3 systems the protein is located in the solvent throughout the simulation, with limited membrane-peptide interactions. In contrast, the MARTINI2 simulations show the peptide consistently embedded in the membrane for the entire simulations. (B) Probability density distribution of the distance of the peptide from the bilayer center over time. In blue, the MARTINI2 systems; in red, the MARTINI3 systems. The dashed dark line represent the position of the upper layer phosphate group. (C) Area per lipids of the different Mfn1-AH systems. The values are given in nm². (D) Packing defects barplot, comprising both shallow and deep defects. The values are given in Å². As the membrane-peptide MARTINI2 systems exhibit the peptide being embedded, the analysis considered the peptide as a polar group concealing the hydrophobic regions of the membrane. Conversely, for the MARTINI3 systems, the analysis excluded the peptide. (E) Average number of protrusions per lipid barplot. (C),(D),(E) Color scheme can be seen at the right of the plots.

Variations are observed with other parameters, such as packing defects and protrusion events (Figure 4.10C,D). First of all, these parameters are shown to increase in all systems with the DOPE phospholipid in the membrane. Moreover, the MARTINI3 systems exhibit larger values compared to those of the MARTINI2 systems. Consistently with the APL, the membrane-peptide and membrane-only systems

show very similar values in the MARTINI3 systems (which is consistent given that the peptide does not bind), but surprisingly in MARTINI2 systems as well. These analysis show very little disturbances of the membrane integrity caused by the peptide. Last, MARTINI3 predicts systematically more packing defects and protrusions than MARTINI2.

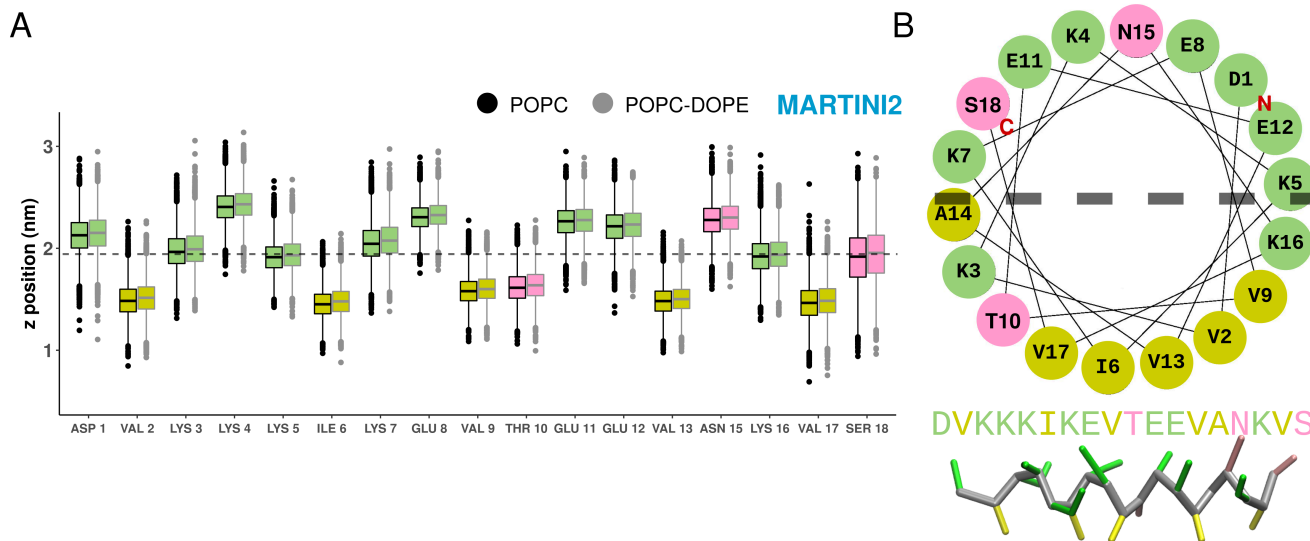


Figure 4.11: **Distribution of the residues of Mfn1-AH in the membrane for the MARTINI2 membrane-peptide systems.** (A) Boxplot of the position on the z -axis of the residues side chains, of the MARTINI2 systems. Only the frames of our simulations showing the penetratin embedded in the membrane were used. Ala14 is not shown, as in MARTINI2 there is no side chains for this residue. The dashed dark line represent the position of the upper layer phosphate group. (B) Helix wheel of the penetratin, colored as function of the properties of the residues. Hydrophobic residues are colored in yellow, hydrophilic residues are colored in pink, and charged residues are colored in blue. The dashed dark line represent the position of the upper layer phosphate groups. On the bottom is shown a snapshot of the peptide embedded in the membrane.

Finally, the positions of the residues of the peptide in the membrane is analysed in Figure 4.11A for the MARTINI2 simulations. As anticipated, the hydrophobic residues Val2, Ile6, Val9, Val13, and Val17 demonstrate the deepest integration into the membrane. Charged residues Lys3, Lys5, Lys7, and Lys16 align with the phosphate groups, suggesting potential interactions between these residues and the phosphate beads.

The MARTINI3 simulations of Mfn1-AH reveal an absence of interactions with the membrane. Interestingly, this lack of membrane-peptide interactions persists even under conditions of heightened packing defects with the POPC:DOPE membrane. To explore the interaction potential of MARTINI3 and ascertain whether these interactions remain intact upon peptide integration into the membrane, we opted to conduct simulations where the peptide initiates from the same plane as the upper leaflet's phosphate groups (similar to the initial state of the penetratin systems, described in Figure 4.6A). We also opted to assess two other membrane compositions: one with an elevated proportion of DOPE and another with the

anionic phospholipid POPS. Increasing the DOPE content allow us to evaluate Mfn1-AH responsiveness to packing defects (Figure 4.12A), while the inclusion of the anionic phospholipid POPS will enable us to examine the peptide sensitivity to a charged membrane.

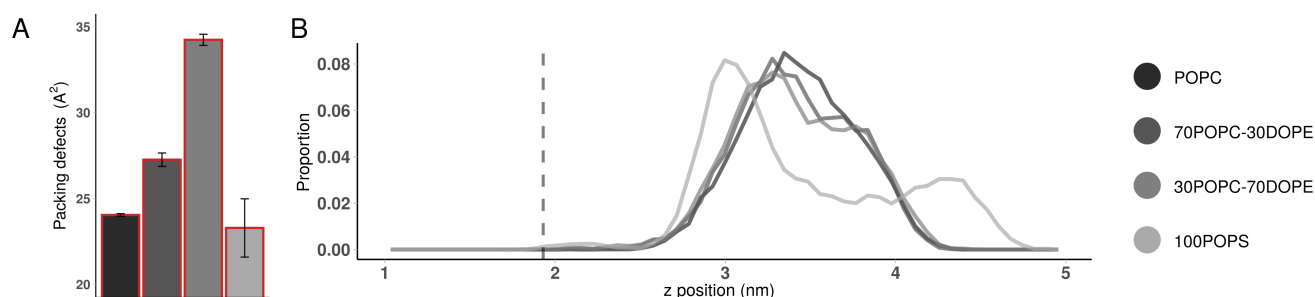


Figure 4.12: **Study of the driving force in membrane-Mfn1-AH interactions.** (A) Packing defects of the new membrane-peptide systems. (B) Probability density distribution of the distance of Mfn1-AH from the bilayer center. The dashed dark line represent the position of the upper layer phosphate groups. Because of the presence of ions, the POPS system has more solvent particles (water + ions) so the box is thicker in the z -axis.

The distribution of the distance of the peptide to the center of the bilayer is seen in Figure 4.12B. All of the simulations show very early Mfn1-AH exiting the membrane and remains unbound for the duration of the simulation. However, slight variations can be observed, as the membranes composed of DOPE show a subtle shift of their highest peak towards the centre of the membrane. This shift is nevertheless minor when compared to the peptide distribution in a POPS membrane system. In fact, in the POPS system, the peptide is frequently situated closest to the membrane compared to the other systems. In this particular system, the peptide can also reach higher positions along the z -axis. In POPS we thus observe a two-state system: membrane bound or diffusing in solvent.

Overall, none of the composition studied here leads to a real Mfn1-AH binding to the membrane with MARTINI3. Negative PS shows only a slight adsorption. In contrast, MARTINI2 predicts Mfn1-AH binding to POPC and POPC-DOPE.

4.5 Discussion

4.5.1 Martini3 membranes exhibit a reduced level of compactness in membranes

Through the preceding findings, distinct membrane behaviors in the two force fields were discerned by analyzing various parameters, encompassing membrane thickness, area per lipid (APL), packing defects, and protrusions. Both membrane thickness and APL serve as metrics for gauging the membrane compactness. The identification of packing defects and protrusions are surface properties. They refers to the defects within a membrane, which exposes its hydrophobic regions to the solvent. They are key parameters for the binding of amphipathic helices. They are also key in the initiation of hemifusion (see previous and next chapters).

These analyses highlights several aspects. Notably, MARTINI3 membranes exhibit reduced thickness in the penetratin associated simulations (except in POPC where no binding occurs), and the phospholipids constituting the membrane adopt a comparatively less tightly packed arrangement. It would be nevertheless worthwhile to run replica simulations of the systems presented here, in order to build more confidence in the results shown.

This observed shift suggests that the MARTINI3 correction addressing the previously observed hydrophobicity overestimation in the MARTINI2 system [184, 255] has also an effect on the properties of membranes. The change of APL and thickness upon DOPE addition to POPC is correct with MARTINI2 but not MARTINI3. However, the two versions of the force-field show a consensus in the effects of the conical lipid DOPE on the packing defects (Figure 4.10D,E).

4.5.2 The MARTINI3 simulations of the penetratin shows good agreement with experimental data

Penetratin belongs to the category of cell-penetrating peptides (CPPs), a group of cationic peptides endowed with the capacity to permeate cell membranes [260]. These peptides employ two primary mechanisms for cell entry: endocytosis and direct translocation across the plasma membrane. The penetratin translocation abilities were assessed in a prior study of Gehan et al. 2020 [260]. Notably, translocation was absent in membranes composed solely of pure POPC or when POPC constituted one of the leaflets in asymmetric membranes, as well as in cases where POPC dominated the membrane composition. In our work, the results from the POPC membrane-peptide MARTINI2 simulation contrast with these findings, revealing continuous interactions between penetratin and the POPC membrane throughout the simulation duration. However, the MARTINI3 system portrays a distinct pattern, with minimal interactions observed between penetratin and the POPC membrane. This aligns more closely with the results reported in ref [260].

Furthermore, the later study [260] found that POPG or POPS on the proximal leaflet leads to fluo-penetratin accumulation on bilayers, as well as POPG is essential for penetratin translocation. In addition, both POPG or POPS on the opposing leaflet can facilitate penetratin translocation. These findings show how negatively charged lipids are center for the penetratin to penetrate cell. Notably, the MARTINI3 simulation involving POPG/POPS membrane-peptide interactions exhibited robust binding between the membrane and the peptide. However, the most pronounced interactions were observed within the POPS membrane, despite pure POPS membranes showing fewer translocation events and weaker adhesion to POPS leaflets when tested experimentally [260]. These results demonstrated MARTINI3 improved capability, compared to MARTINI2, in faithfully reproducing the importance of the negative membrane charges. Nevertheless, we found penetratin less deeply buried in POPG than in POPS, although it translocates in POPG but in POPS.

4.5.3 Insufficient role of Packing Defects in driving membrane binding of amphipathic helices: Insights from Mfn1-AH

In this portion of our study, we examined the membrane binding capacity of the amphipathic helix situated within the HR1 domain of Mfn1, unveiled in the study by Daste et al. (2018) [135]. The latter study showed the HR1 domain capacity to bind membranes as well as to induce membrane fusion, which strongly suggests membrane-destabilizing effect in the domain. Given the domain's inherent membrane-interacting capability, it was entirely anticipated that our simulations would depict the peptide engaging with the membranes. Furthermore, an enhanced propensity for binding to a DOPE-containing membrane was expected due to the potential facilitation of hydrophobic membrane-peptide interactions, attributed to induced membrane defects. While binding is observed in the MARTINI2 simulations, the MARTINI3 simulations revealed a lack of observable interactions between Mfn1-AH and each membrane type (as depicted in Figures 4.10 and 4.12). Nevertheless, there were indications of closer interactions with anionic lipids, despite the absence of embedding. This discrepancy raises intriguing questions about the specific mechanisms governing peptide-membrane interactions in MARTINI3 simulations.

In the context of MARTINI3, the existence of membrane defects alone does not appear to suffice for the facilitation of membrane binding by Mfn1-AH. Arriving at a definitive conclusion regarding whether (i) the peptide has inherently a lack of sensitivity for packing defects and affinity for membrane binding, or whether (ii) a potential flaw exists within the MARTINI3 force-field, is a complex matter. Intriguingly, interactions are increased when the lipids are anionic, which imply that Mfn1-AH binding mechanism would necessitate more than packing defects in the membrane. In fact, the existence of positive charges in Mfn1-AH suggest a compatibility with the anionic lipids constituting the mitochondrial outer membrane (mainly phosphatidylinositols, see Table 1.1). The predominant force behind membrane-peptide interactions in MARTINI3 appears to stem from electrostatic interactions, rather than hydrophobic interactions. However, it is important to note that Srinivasan et. al [256] showed good agreements with experimental data for the mastoparan and Amphipathic Lipid Packing Sensor (ALPS) motifs, and even showed overestimation of the interactions in some instances.

Considering the surprising results showing TM1 of Fzo1 (referred later as Fzo1-TM1) coming out of the membrane (Chapter 3), we can reasonably doubt the results showed here with MARTINI3, and more specifically the results obtained for the amphipathic helix Mfn1-AH. The helix could be sensitive to packing defects and in the event that MARTINI3 underestimate hydrophobic interactions of helices, the sensitivity of the helix for hydrophobic defects would be underestimated. In the preceding Chapter, it was suggested that the surprising result of Fzo1-TM1 exiting the membrane was an illustration of the instability in the membrane conferred by Fzo1-TM1. As the helix results in more instability (i.e. hydrophobic defects) with a charged Lys716, it is more often expelled from the membrane. Since Mfn1-AH is expelled by the membrane, we could wonder if it is the instability provided by the helix that drives the peptide out of the membrane (Figure 4.12). However, as the peptide comes out of the membrane

within the first ns of the simulation, it was not possible to assess the actual effect of the peptide on the membrane in MARTINI3 simulations. Other simulations with position restraints could answer this question.

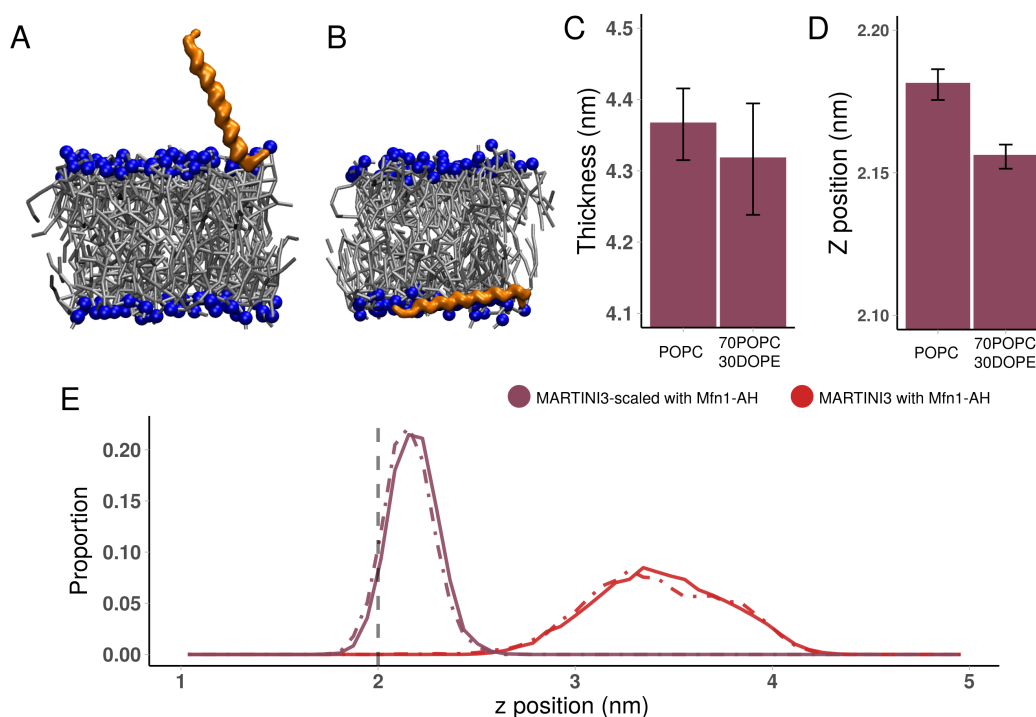


Figure 4.13: **MARTINI3 scaled results.** (A) Snapshots of the MARTINI3 (normal) simulations of Fzo1-TM1 in a POPC-POPE membrane. The POPC molecules are in grey and licorice representation. The phosphate groups (PO4 beads) of the POPC molecules are shown in blue and van der Waals representation. The peptide is represented in orange. (B) Snapshots of the MARTINI3 rescaled simulations of Fzo1-TM1 in a POPC-POPE membrane. (C) Thickness of the membranes of the Mfn1-AH systems in nm. (D) Mean position of the peptide on the z -axis in nm. (E) Probability density distribution of the distance of Mfn1-AH from the bilayer center. The dashed dark line represent the position of the upper layer phosphate groups.

In fact, Cabezudo et al. (2023) [244] observed that MARTINI3 simulations failed to show insertion of TM helix dimer into phospholipic micelles or bilayers, only production TM-water interactions. To solve the issue, the study proposed to reduce the protein-water interactions by introducing a small uniform scaling factor of the Lennard-Jones interactions in MARTINI3. The insertion issues were solved with this method, suggesting that the original version of MARTINI3 overestimate the hydrophilic properties of proteins able to interact with membranes. We were able to test a version of the MARTINI3 rescaling with a Master 1 student, Hanene Samia Hameur, who implemented the scaling of Lennard-Jones interactions involving water molecules. This scaling was used to produce simulations of TM1 in a 50-50 POPC-POPE membrane as well as Mfn1-AH in both 100 POPC and 70-30 POPC-DOPE membranes. The results are shown in Figure 4.13. In the simulations involving Mfn1-AH, the peptide consistently interacts with both membranes over the course of the simulation (Figure 4.13D,E). The membranes show an increased

thickness (Figure 4.13C) in comparison to the results showed in Table 4.3. However, in the case of Fzo1-TM1, the helix remains expelled from the membrane (Figure 4.13A,B). The key distinction from the initial MARTINI3 version is that the peptide still engages interactions with the lipid heads, resembling an amphipathic helix. Given the TM1 results, and the unexpected effect on membrane thickness (Figure 4.13C), we have reservations regarding the scaling of interactions to be a sound solution to the issue of TM helices expulsions with the MARTINI3 force-field. Indeed, the proliferation of such methods is likely to result in an extensive array of customized versions of the MARTINI force-field, rendering them less universally applicable. Moreover, these modifications could yield unforeseen effects on other parameters or molecules, necessitating thorough benchmark testing and rigorous comparisons to experimental data for validation. It would be perhaps interesting to look into some of the changes made between the two versions of the MARTINI force-field. One of the main changes in the later version of the force-field is the withdrawal of a specific backbone defined for α -helix and β -strands. In contrast to MARTINI2, where the backbone particles were designated as neutral beads, MARTINI3 now characterizes the helix backbone as polar beads. This alteration theoretically promotes hydrophilic interactions with our helices rather than the anticipated hydrophobic interactions. After some discussion with some MARTINI developers, we are aware they are working on a new version which could address this issue of TM expulsion.

CHAPTER 5

COMPUTATIONAL INVESTIGATION OF THE INSERTION OF AN MFN1-HR1 DOMAIN AMPHIPATHIC HELIX

5.1 Introduction

As described in the Introduction (Chapter 1.4), mitofusins are key molecular players of the outer mitochondrial membrane fusion. However, the underlying mechanisms of the fusion remains unknown. While the domain composition of the mitofusins have been thoroughly described [99, 96, 1, 133], the role of each domains in the fusion process is still debated. In fact, Huang et al. (2017) [134] suggested that the C-terminal section of mitofusins binds to and destabilizes the lipid bilayer by means of an amphipathic helix in HR2. HR1 was proposed to target the membrane as well. Furthermore, Daste and colleagues (2018) [135] have shown that isolated HR1 and HR2 domains of Mfn1 mediate membrane docking *in vitro*. Furthermore, in this study, the HR1 domain induced membrane fusion, and it was postulated that an identified amphipathic helix (AH) conferred membrane-binding capacity to the domain. This helix will be referred as Mfn1-AH. From these findings, the HR1 domain was proposed to induce OM fusion through the perturbation of the membrane, while the HR2 domain was suggested to participate in membrane tethering through trans-dimerization. These hypothesis were described in more detail in section 1.4.

Amphipathic helices (AHs) are protein sequences known to fold into an α -helical structure when interacting with a polar/non-polar interface. Typically short in length (< 25 residues), these sequences remain unfolded in an aqueous environment. The helix formed presents two faces with opposite chemical features: a hydrophobic face and a polar face. When the AH folds in contact with the surface of a bilayer-bound organelle or a lipid droplet inside the cell, the hydrophobic side of the AH faces the lipids. The affinity of the AH for the membrane will depend on the AH sequence, as well as the physico-chemical membrane properties such as the degree of curvature, the charge of the lipid heads, or the hydrophobic defects. Additionally, research has shown that numerous AHs not only serve as anchors to the membrane but also have diverse functions due to their prolonged interaction with membrane interfaces [264, 265].

In fact, Mfn1-AH has been suggested to confer membrane binding capacity to the domain HR1, as well as being involved in membrane fusion (Figure 5.1) [135]. In Figure 5.1A is shown the circular dichroism spectra of HR1 and HR2 to characterize their secondary structure in presence, or absence, of liposomes. The mean residue molar ellipticity of HR1 at 208 and 222 nm shows an increase in the absolute values when in the presence of liposomes, showing an increase of α -helical content in HR1, as depicted in the right panel as well. These findings suggest a folding of the amphipathic helix of HR1 into the liposome membrane. Furthermore, Figure 5.1B shows the inability of the Mfn1- Δ AH mutant to recover the typical tubular mitochondrial morphology in Mfn1 KO cells. These results, in addition to the inability of an AH deleted HR1 fragment to induce liposome fusion or docking, suggest that the docking and fusion ability of HR1 is due to its interactions with the membrane facilitated by the AH [135].

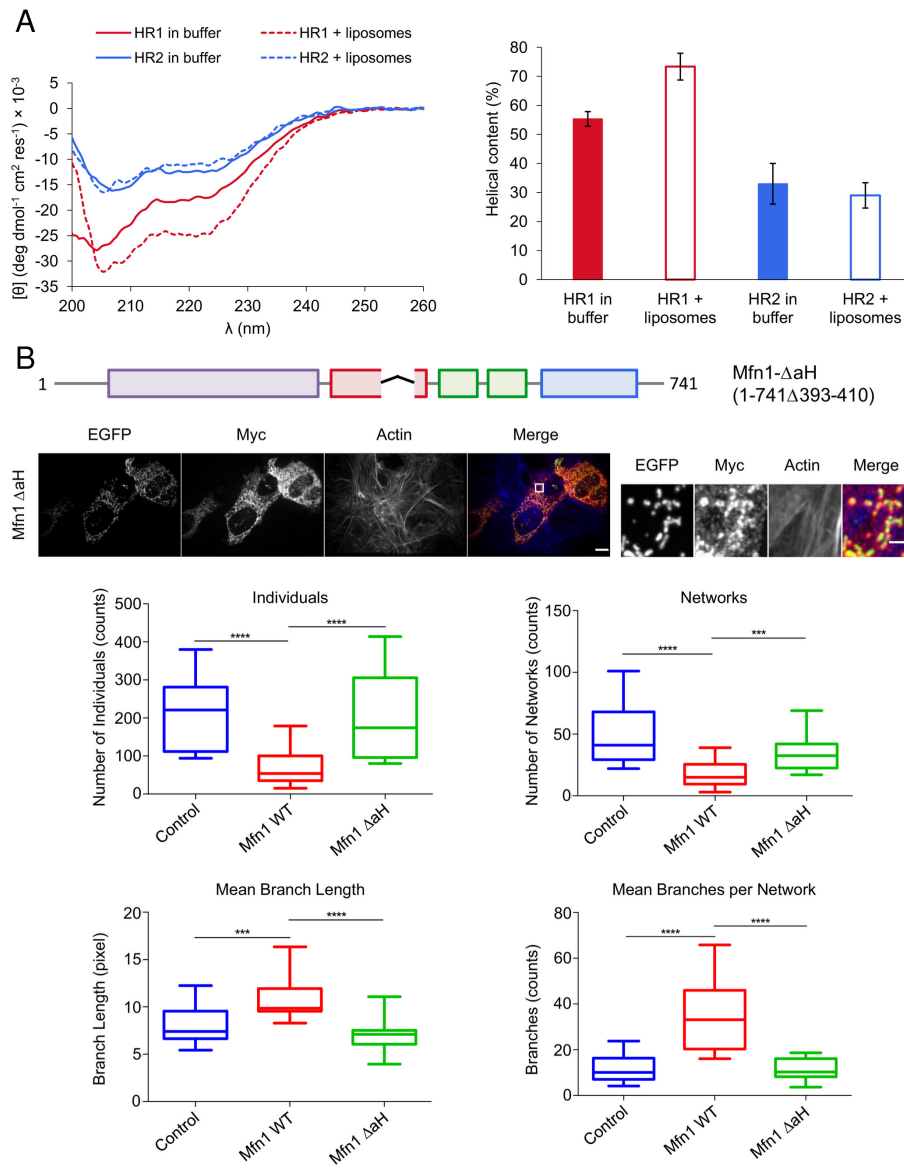


Figure 5.1: Experimental investigation of the interaction between Mfn1-AH and lipid bilayer structure. (A) Left, circular dichroism spectra of the HR1 and HR2 domains of Mfn1 in the absence or presence of maleimide-containing liposomes. The circular dichroism spectra of HR1 and HR2 were recorded after 30 min of incubation at 37°C with or without POPC liposomes. Right, helical content of HR1 and HR2 in the absence or presence of liposomes. (B) Top, Domain architecture of Mfn1: N-terminal GT-Pase domain in purple; two heptad repeat domains HR1 in red and HR2 in blue; transmembrane (TM) region in green. Middle, Mfn1 KO MEFs were co-transfected with a plasmid expressing mtEGFP and a plasmid expressing Mfn1-Myc lacking the conserved amphipathic helix of HR1 (Mfn1- Δ AH). The right panels show magnified views of the boxed area in the left panels. Expression of Mfn1- Δ AH in Mfn1 KO MEFs could not rescue filamentous mitochondrial morphology. The scale bar is 10 μm for the left panels and 2 μm for the right panels. Bottom, mitochondrial morphologies were classified as either individuals (structures with no junction, which can be puncta or rods) or networks (structures with at least one junction and three branches). The mean length of rods and network branches, and the mean number of branches per network were calculated and plotted as boxplots. Mfn1 KO MEFs were transfected with a plasmid expressing mtEGFP alone (control) or in combination with a plasmid expressing Mfn1-Myc full length (Mfn1 WT). Taken from [135].

An amphipathic helix sequence is characterized by hydrophobic amino-acids regularly distributed every $N + 3$ and/or $N + 4$ positions with polar residues in between. These sequences can be recognized by representing the relative position of each residues in the α -helix, as first described by Schiffer et. al in 1967 [266], as a so-called helix wheel. This can be achieved using the Heliquest webserver [261]. Furthermore, the amphipathicity of the helix can be quantified by calculating the helical hydrophobic moment μ_H [267]. A high μ_H value signify high amphipathicity, indicating a clear separation of polar and non-polar residues on opposite sides of the helix. The helical wheel of Mfn1-AH is shown in Figure 5.2C and the AH is characterized by a high hydrophobic moment μ_M of 0.508 (when the value is superior to 0.3, the peptide is often considered as AH).

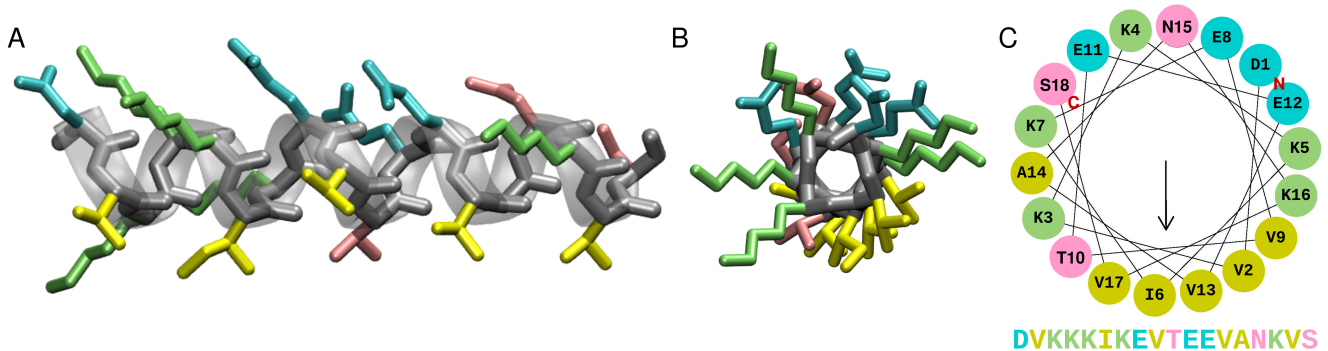


Figure 5.2: **Description of Mfn1's amphipathic helix properties.** (A) Side view of Mfn1-AH. (B) Front view of Mfn1-AH. (C) Helical Wheel of Mfn1-AH. The peptide is characterized by a sequence composed of 33% apolar residues and a hydrophobic moment $\mu_M = 0.508$. For all three sections of this figure, the residues are colored as followed : green for basic residues, cyan for acidic residues, yellow for apolar, and pink for apolar. The backbone is colored in grey.

The general mechanism of AH membrane binding can be summarized by three steps : attraction, adsorption and folding [268]. These steps are described in Figure 5.3. The first attraction step corresponds to the peptide approaching the membrane. In the case where the peptide comprises charged residues, this step is mainly driven by electrostatic interactions, given that the peptide will initially interact with the exposed polar heads of the phospholipids. On the other hand, if the peptide or the membrane lacks charged residues, the hydrophobic defects of the membrane will drive the interactions. In the second step, the adsorption, the peptide is now parallel to the surface of the membrane, adopting an unfolded and extended conformation along the membrane. The residues are not fully inserted yet. The final step involves the peptide folding into an α -helix, a process that occurs simultaneously with the partitioning of the peptide into the membrane. The position of the residues first involved in the insertion depends on the sequence of the peptide. The apolar residues will partition within the hydrophobic aliphatic chains of the membrane, while the polar and/or charged residues will partition within the polar heads / solvent. This partitioning will drive the folding and more globally the binding to the membrane. Throughout this phase and upon its conclusion, the peptide remains in a parallel orientation to the membrane.

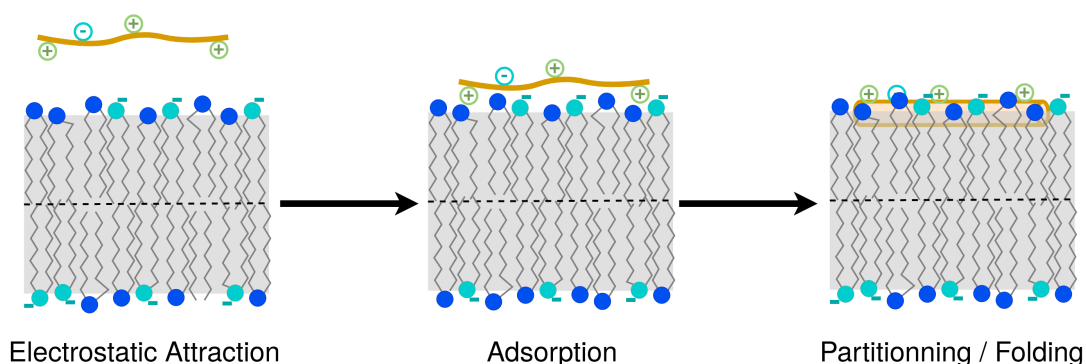


Figure 5.3: **Phases of amphipathic helix / membrane interaction.** Adapted from [268].

In this study, we delve into the molecular dynamics of the amphipathic helix Mfn1-AH. This peptide is assumed to promote fusion by inducing membrane destabilization. By employing advanced molecular dynamics simulations, we aim to unravel the intricate details of how this amphipathic helix interacts with lipid membranes, exploring its potential involvement in the fusion process. Our goal is to highlight the effect of the peptide on the membrane, but also to get insights into the binding event of Mfn1-AH.

At the same time, our colleague from the ANR David Taresté is performing *in vitro* experiments on the same systems: i) fusion experiments using fluorescence dequenching on liposomes w/wo Mfn1-AH, ii) CD experiments to evaluate the helix content upon binding to liposomes. Thus, the choice of the systems presented here (lipids, peptide, P/L ratio, ions, temperature, etc.) was done in partnership with David Taresté.

5.2 Materials and Methods

The various systems analyzed in this Chapter are listed in Table 5.1. The building of each systems, as well as the simulation parameters of each force-field are described below.

Simulation type	System (ratio)	Lipid Quantity	Replica	T (K)	Time (ns)
normal MD	POPC (100)	100 / 256	1	310	300 / 400
normal MD	POPC:DOPE (70:30)	100 / 256	1	310	300 / 400
normal MD	AH-POPC (1-100)	100 / 256	1	310	300 / 400
normal MD	AH-POPC:DOPE (1-70:30)	100 / 256 / 512	1	310	300 / 400 / 400
normal MD	AH-POPC (1-100)	100	1	400	300
normal MD	AH-POPC:DOPE (1-70:30)	100	1	400	300
T-REMD	AH in water (1)	0	26	310-400	500
T-REMD	AHh-POPC:DOPE (1-70:30)	100	35	310-400	500
T-REMD	AHu-POPC:DOPE (1-70:30)	100	35	310-400	1000

Table 5.1: **Summary table of the simulation systems.** POPC stands for Palmitoyl-Oleoyl-Phosphatidyl-Choline, DOPE stands for DiOleoyl-Phosphatidyl-Ethanolamine. T stands for temperature. AHh represents AH in helix structure, AHu represents AH in an unfolded structure. The first 4 lines show multiple options of membrane size per system composition.

5.2.1 Preliminary 300 ns simulations

Systems Setup

The Mfn1 amphipathic helix (Mfn1-AH) peptide was built using Basic Builder 1.0.2 on the MobyLe server (<https://mobyLe.rpbs.univ-paris-diderot.fr>) [212]. The sequence used was DVKKKIKEV-TEEVANKVS (both termini kept charged). The alignment between the sequence and its associated predicted secondary structures (α -helix) was submitted in order to build a 3D structure of the peptide.

The systems were built using the CHARMM-GUI Membrane builder [178] with the CHARMM36m force field [170, 220]. Two phospholipid composition were used: 100 POPC (50 per leaflet) and 70:30 POPC:DOPE (35:15 POPC:DOPE per leaflet). For each membrane composition, two systems were built: one with Mfn1-AH and one without. Furthermore, about 40 water molecules per lipid were used as solvent, to which was added 0.15 KCl.

Simulation Parameters

The following simulations were ran with the GROMACS software (v2022x) [176, 177].

For membrane-only and amphipathic helix system, we followed the protocol of CHARMM-GUI which consisted in an energy minimization step of 5000 steps with the steepest descent algorithm, followed by an equilibration of 6 simulations within the NPT ensemble. The first two equilibration steps of 125 ps were done in an NVT ensemble, with the Berendsen thermostat [173] and a timestep 0.001 ps. The next equilibration steps were ran in an NPT ensemble, with the Berendsen thermostat [173] and the Berendsen barostat at 1 bar [173]. A sequence of 4 simulations of 125 ps, 500 ps, 500 ps and 500 ns were ran with a timestep of 0.001 ps, 0.002 ps, 0.002 ps and 0.002 ps respectively. The temperature used for the equilibration as well as the production steps is 310 K for membrane only systems and either 310K or 400K for the AH-membrane systems.

A production run of 300 ns followed, using the velocity-rescaling thermostat [174] (lipid, water and proteins coupled separately) and 1 bar using the Parrinello-Rahman barostat [175] (compressibility of $4.5 \times 10^{-5} \text{bar}^{-1}$). Electrostatic interactions were calculated with the particle-mesh-Ewald (PME) method [166, 167], with a real-space cutoff of 1 nm. Water molecules were kept rigid with the SETTLE algorithm [222]. Pressure coupling was applied semi-isotropically. Bond lengths were constrained using the LINCS algorithm [214]. A time step of 0.002 ps was used with the leapfrog integrator. Electrostatic interactions were calculated with the particle-mesh-Ewald (PME) method [166, 167], with a real-space cutoff of 1 nm. Van der Waals interactions were computed using a Lennard-Jones force-switching function over 1.0 to 1.2 nm and were cutoff at 1.2 nm. Water molecules were kept rigid with the SETTLE algorithm [222]. The neighbor list was updated every 20 steps.

5.2.2 Membrane analysis simulations

Additional simulations were ran, specifically to understand the effect of the peptide on the membrane. The setup steps and simulation parameters are exactly identical to the previous preliminary simulations (see Section 5.2.1), but the membrane size is increased for each systems. 256 are used: one membrane with 256 POPC (128 per leaflet) and one membrane with 180:76 POPC:DOPE (90:38 POPC:DOPE per leaflet). For each membrane composition, like previously, we proceeded to built 2 systems: one with Mfn1-AH and one without.

One additional simulation was ran for the MfnA-AH and 70:30 POPC:DOPE ratio, with an increased membrane size of 512 lipids. The simulation setup and parameters are described in Section 5.2.1.

5.2.3 Computational strategy for studying Mfn1-AH / membrane interaction further

In order to study the interaction between Mfn1-AH and the membrane more in depth, we used, like in the previous chapter, an enhanced sampling method: Temperature Replica Exchange Molecular Dynamics (T-REMD). This technique allows to address more complicated problems such as peptide insertion in the membrane and its folding. The strategy we used is resumed in Figure 5.4. First, we did a T-REMD of Mfn1-AH in water (REMD water) which allowed us to assess the structure of the peptide in solution, and generate a representative (unfolded) conformation. Second, we carried out a T-REMD of Mfn1-AH already folded in alpha-helix and inserted in the membrane (REMD helix) to verify its stability. Last, we performed a long T-REMD starting with the unfolded peptide in water and followed its insertion and possible folding within the membrane / water interface (REMD folding). All these T-REMD simulations were performed with the GROMACS software (v2018) [176, 177] together with the CHARMM36m force field [170, 220]. Unless otherwise stated, all parameters are identical to the simulations described in the previous section.

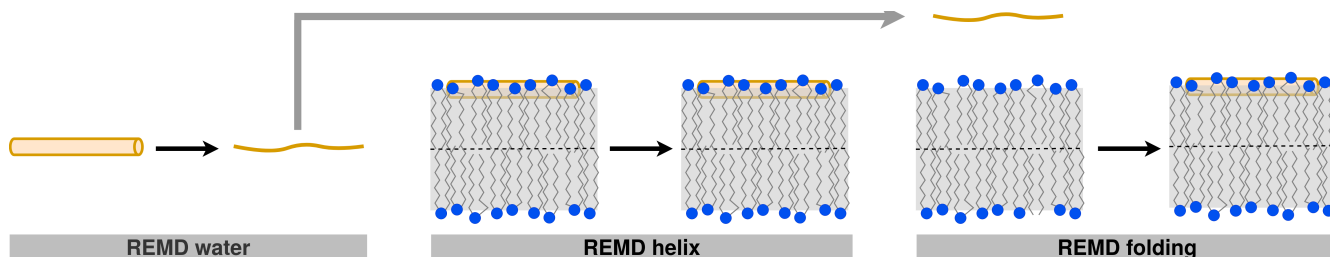


Figure 5.4: Schematic description of all three REMD carried out for this project.

5.2.4 T-REMD of Mfn1-AH in water (REMD-water)

Systems setup and equilibration

The peptide, in its α -helix conformation, was placed within a dodecahedron-shaped water box. The box is composed of 2857 water molecules (TIP3), to which was added enough ions to neutralize the system,

as well as 0.15 KCl.

A first minimization step of 5000 steps is conducted, using the steepest descent algorithm. The system was then submitted to one equilibration step of 125 ps within the NVT ensemble and with a timestep 0.001 ps. The Berendsen thermostat was used, at 310K. The other settings were similar to the classical simulations presented in the previous section.

REMD parameters

In order to efficiently explore the conformational landscape of the AH in water, we used temperature replica-exchange molecular dynamics (T-REMD)[157]. The replica temperatures were predicted using the webserver <https://virtualchemistry.org/remd-temperature-generator/> [188] by setting the exchange probability to 0.2 and the temperature range between 310K and 402.76 K. The upper limit of nearly 400 K was chosen to stay consistent with the REMD parameters of the membrane systems. In total, we obtained 26 replica.

Each replica was equilibrated at the chosen temperature for 1 ns (time step 0.002 ps) using the Berendsen thermostat and barostat (at 1 bar) with different starting velocities. The production run of 500 ns followed with the velocity-rescaling thermostat [174] (lipid, water and proteins coupled separately) and the Parrinello-Rahman barostat at 1 bar [175] (compressibility of $4.5 \times 10^{-5} \text{bar}^{-1}$). Exchanges between neighboring replicas were attempted every 10 ps. The other settings were identical to those described in the previous section.

Extraction of a representative unfolded conformation

The conformations at 310K were used for this analysis. For this selection we removed the first 100 ns of the trajectory, as the initial α -helix structure was still retained. The updated smaller simulation was then used as input to the *gmx cluster* program of GROMACS. The non-supervised GROMOS method [181] was used, with a cutoff set to 0.45 nm. The center structure of the first cluster was used for the following steps.

5.2.5 T-REMD of Mfn1-AH with membrane (REMD-helix and REMD-folding)

Two T-REMD were run (Figure 5.4): a first with the AH adopting a folded conformation binding the membrane (REMD-helix), a second with the AH in an unfolded conformation in the solvent (REMD-folding), without interactions with the membrane. The two systems have the exact same molecular composition.

Systems setup and equilibration

A first system with the peptide folded and binding to the membrane was built using CHARMM-GUI Membrane builder [178]. The same system composition previously described was used (in Section 5.2.1), except one type of membrane was used, the 70:30 ratio of POPC:DOPE. The second system starting with

an unfolded AH was first built using a POPC:DOPE membrane only system. This system was submitted to a steepest descent minimization of 5000 steps. The minimization was followed by a sequence of 6 equilibrations of 125 ps, 125 ps, 125 ps, 500 ps, 500 ps, and 500 ps (with a timestep of 0.001 ps, 0.001 ps, 0.001 ps, 0.001 ps, 0.002 ps, 0.002 ps respectively) in which we progressively released the position-restraints on the protein. The first two equilibrations were performed within the NVT ensemble, with the Berendsen thermostat, and the following simulations were performed within the NPT ensemble, with the Berendsen thermostat and barostat.

The second system starting with an unfolded AH was first built using a POPC:DOPE membrane-only system. This system was submitted to a steepest descent minimization of 5000 steps. The minimization was followed by a sequence of 6 equilibrations of 125 ps, 125 ps, 125 ps, 500 ps, 500 ps, and 500 ps (with a timestep of 0.001 ps, 0.001 ps, 0.001 ps, 0.001 ps, 0.002 ps, 0.002 ps respectively) in which we progressively released the position-restraints on the protein. The first two equilibrations were performed within the NVT ensemble, with the Berendsen thermostat, and the following simulations were performed within the NPT ensemble, with the Berendsen thermostat and barostat. The temperature was maintained at 303.15 K and the pressure at 1 bar. Pressure was applied semi-isotropically. The most representative conformation of the AH in water, previously extracted from the REMD simulation in a water box (cluster 1 center structure, described previously in section 5.2.4), was then placed in the solvent of the system. We proceeded to multiple steepest descent minimizations (a total of 19), in order to remove all the clashes present in the system from the addition of the peptide. The system was subjected to a last equilibration step, of 500 ps and a timestep of 0.002 ps. This step was performed within the NPT ensemble, with the Berendsen thermostat (310K) and barostat (1 bar).

Simulation Parameters

The replica temperatures of both systems were predicted using the webserver <https://virtualchemistry.org/remd-temperature-generator/> [188] by setting the exchange probability to 0.2 and the temperature range between 310K and 400.54K. In total, we obtained 35 replica.

Each replica was equilibrated at the chosen temperature for 1 ns (time step 0.002 ps) using the Berendsen thermostat and barostat (at 1 bar) with different starting velocities. The production run of 500 ns followed with the velocity-rescaling thermostat [174] (lipid, water and proteins coupled separately) and the Parrinello-Rahman barostat at 1 bar [175] (compressibility of $4.5 \times 10^{-5} \text{bar}^{-1}$). Exchanges between neighboring replicas were attempted every 10 ps. The other settings were identical to those described in the previous section.

5.2.6 Analysis

Helix

The helix wheels were generated using the HELIQUEST webserver [261]. Mfn1-AH sequence (DVKKKIKEV-TEEVANKVS) was submitted, and the "full window" option was used, in order to have all the residues

of sequences on one helix wheel. We then adapted the colors of the amino acids in the sequence based on their physico-chemical properties: in green are represented positively charged residues, negatively charged residues are in cyan, polar residues are in pink, hydrophobic residues are in yellow.

The helicity of the peptide was calculated using the GROMACS tools *gmx helicity* and *gmx dssp*.

Membrane thickness, order parameter, position of the peptide, and partition plots

The analysis of the positions of the peptide and its residues were carried out using the GROMACS tool *gmx traj*. The positions on the z -axis of the center of mass of the protein was determined using the backbone beads only. The positions on the z -axis of the center of mass of each residues of the peptide was determined using the side chain beads only. The positions of the peptide or the residues with respect to the bilayer center were then calculated using the R library *ggplot2* [219]. The position of the center of mass of the peptide was studied throughout all simulations. The positions of the residues side chains were determined only when the peptide was found to bind the membrane.

The order parameter was calculated using the GROMACS tool *gmx order*. The computation characterizes the motion of the C-H bond vector using the following equation:

$$S_{CH} = \frac{1}{2} \langle 3 \cos^2(\theta) - 1 \rangle \quad (5.1)$$

where $\langle \dots \rangle$ means ensemble averaging (over all lipids and frames for a given C-H bond vector), θ is the angle between the C-H bond vector and the bilayer normal (z -axis). Of note, we represent $-S_{CH}$ in each plot as is usually done for the order parameter of lipid tails in literature. In this chapter, $-S_{CH}$ will be referred interchangeably to order parameter or simply S_{CH} . For each C-H, since we average over many orientations, the order parameter usually varies between 0 (fully disordered, all possible C-H orientations) to 0.5 (fully ordered, very restrained C-H orientation(s)).

To assess the membrane thickness, we initially divided the 300 ns interval into three segments (excluding the initial 10 ns). For each segment, we computed the density along the z -axis for both the membrane and the solvent separately. The command *gmx density* of the GROMACS package was used. Using the density data, it becomes feasible to compute the membrane thickness (using an in-house R script). This is achieved by determining the two crossovers between membrane and solvent densities, and measuring the distance between them.

Area per Lipid, Packing Defects and Protrusion events

The area per lipid is calculated using the FATSLiM software [262]. This value is obtained by initially computing local Voronoi cells for each lipid and subsequently calculating the area of each cell. When Mfn1-AH is in the system, the calculation was performed individually for each leaflet and averaged across the various lipids composing the membrane.

Lipid packing defects are small apolar areas of the membrane which are accessible to water (Figure

1.25). They are not only important for the binding of peptides or proteins rich in hydrophobic residues (such as amphipathic helices) [249, 52], but also for the nucleation of hemifusion [269]. Packing defects were quantified using the Packmem software [52, 145]. The principle of this analysis is described in section 4.2.5. Briefly, Packmem quantifies each packing defect using a grid, and collects statistics over a trajectory. The corresponding distribution is fit to an exponential decay, which gives the packing defect constant in units of nm^2 . The higher this constant, the more numerous and the larger the packing defects. For the leaflets with peptide, we considered it analogous to membrane polar heads so that PackMem ignored it and did not consider it as a large defect. When Mfn1-AH is in the system, the calculation was performed individually for each leaflet.

A protrusion event is defined as one of the carbon atom of a tail bulging into the polar layer (or a backbone bead of a lipid tail), extending 0.1 nm above (or below depending on the leaflet) its phosphorus atom [147, 146], as shown in Figure 1.25. Protrusions were identified using an in-house script. When Mfn1-AH is in the system, the calculation was performed individually for each leaflet.

5.3 Mfn1-AH leads to thinning of the membrane

As an initial investigation, our objective was to assess the impact of the amphipathic helix (AH) on the membrane. Simulations of 300 ns and at a temperature of 310 K were performed. The helix was initially positioned in the membrane, at the same level as the phosphate groups of the phospholipids. The parameters used to measure the influence of the AH on the membrane environment are identical to those presented in Chapters 3 and 4 : (i) membrane thickness, (ii) area per lipid, (iii) order parameter, (iv) protrusions, and (v) packing defects. These analyses can be seen in Figures 5.5, 5.6 and 5.7. These observables are suitable for quantifying the potential disturbance in the membranes induced by the peptide. In the AH-membrane systems, some analyses were done separately per layer (Figure 5.7A,B): (i) the upper layer containing the peptide and (ii) the lower layer, which remained peptide-free throughout the simulation. The pure lipid systems have one and only value for each parameter, as there is no distinction between the two layers.

First, we examined the membrane thickness and area per lipid (APL) in Figure 5.7. We start with pure membranes. Addition of DOPE to POPC decreases the mean APL which is expected since DOPE has a smaller polar head, and thus a lower APL, than POPC. This has the effect of increasing the thickness, POPC:DOPE membrane is thicker than pure POPC. This effect has been already observed in simulations composed of DOPC in which the small headed phospholipid diacylglycerol (DAG) is added [52, 263]. In fact, DOPE which has a smaller polar head partitions slightly below POPC, which expulses the POPC towards the exterior and thus thickens the membrane. For both compositions POPC and POPC:DOPE, the thickness decreases when the peptide is embedded in the membrane, whereas the APL increases. This is perfectly consistent, Mfn1-AH induces thinning of the membrane which leads to its lateral expansion. We then examine the APL on the POPC:DOPE simulations with Mfn1-AH. We were expecting to have a lower APL in the leaflet with the peptide compared to that without. This is not the case, since both leaflets

give nearly equal APL. This result was somewhat of a surprise and we are still investigating a possible explanation. We have been suspecting the software FATS LiM [262] since some artefacts were observed on the APL calculations (inconsistent spikes, described in Figure S5.1). However, the next analysis on the order parameter may tell that this equal area is relevant.

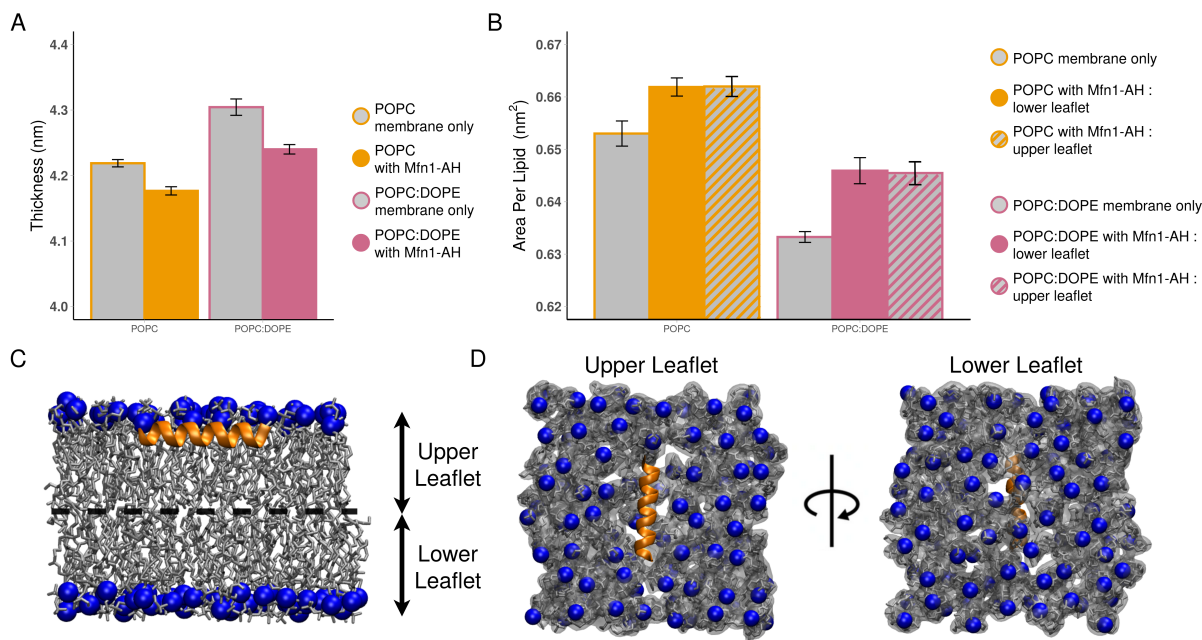


Figure 5.5: Mfn1-AH effect on the membrane global properties. (A) Membrane thickness in nm. (B) Area per lipid in nm². For a better readability on the POPC:DOPE system, each bar represents a mean value on POPC and DOPE. (C) Snapshot of the starting frame of a simulation containing Mfn1-AH. The upper layer contains the helix. (D) Snapshots of the (i) upper layer and (ii) lower layer. For both (C) and (D) the POPC molecules are in grey and licorice representation (in D is shown in transparent the surface of the lipids). The phosphates of the POPC molecules are shown in blue and van der Waals representation. The protein is shown in ribbons and orange.

Next, we examined the order parameter S_{CH} which informs on the mobility of lipid tails (Figure 5.6). The closer to 0, the more disordered the tails, the closer to 0.5 the more ordered. This analysis is complementary to membrane thickness and APL, but this time at the level of individual C-H bonds. The first striking result is the decrease of S_{CH} upon peptide addition for both lipid compositions. This is perfectly in line with the thickness and APL. A lower order parameter means that the tails occupy more space, which leads to a lateral expansion and a thinning of the membrane. We can also see that the order parameter of POPC in presence of DOPE is higher than that in pure POPC. This is expected since we observed membrane thickening (and decrease of APL) upon DOPE addition. Again, a similar effect has been observed upon DAG addition in DOPC [52]. Regarding the leaflets w/wo peptide, we hardly see a difference in terms of order parameter. This result is again surprising, since we could have thought that the peptide could influence it. Yet we saw that the APL is also equal between both leaflets. At this point, we could question how the peptide would fit in a membrane with the same APL and tail order

parameters? To answer this question, that would be interesting to calculate the order parameter of the polar heads, since the APL is largely influenced by the internal mobility of both polar heads and aliphatic tails.

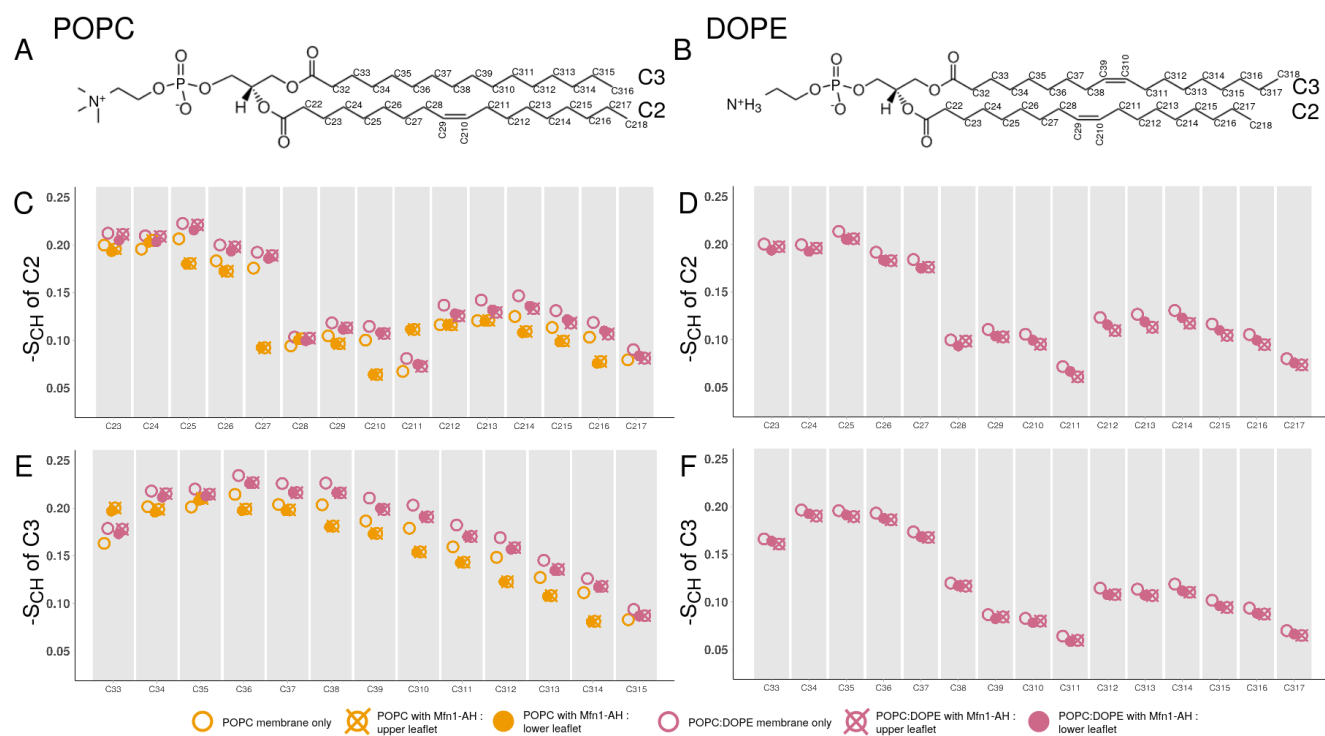


Figure 5.6: **The impact of Mfn1-AH on the order parameter of the lipid tails.** (A) Chemical structure of POPC lipids. (B) Chemical structure of DOPE lipids. (C) Order parameter of *sn*1 carbon tail for POPC. (D) Order parameter of *sn*1 tail for DOPE. (E) Order parameter of *sn*2 tail for POPC. (F) Order parameter of *sn*2 tail for DOPE.

So far, the different observables we have examined were classical analyses reporting on the structure and dynamics of a membrane. Here, we want to go further and analyze the surface properties of the membrane since they are directly connected to the binding of a peptide and more importantly to the initiation of hemifusion. These properties are lipid tail protrusions and polar head packing defects. Figure 5.7A reports on the average number of protrusions per lipid and Figure 5.7B on the packing defect constant π .

We start with the simulations on pure lipids. The number of protrusions reduces upon DOPE addition. This is expected since DOPE thickens the membrane by partitioning below POPC, which reduces the APL, thus impairing the capacity of the aliphatic tails to protrude. For packing defects, the values are slightly upper for POPC:DOPE compared to POPC, but within the error bars. In literature, it was shown that POPE addition to POPC (or DOPE addition to DOPC) increases the packing defect constant [263, 235]. Thus we believe the trend we observe is relevant and more sampling would confirm this. The explanation comes from the shape of DOPE, which is conical due to its small polar head compared to POPC. This directly creates packing defects between polar heads, since PE impairs the (more) efficient

packing of cylindrical POPC between them. Overall, protrusions and packing defects are in essence different phenomenons. Even if they both promote hemifusion, they have different origins and can have different behavior when we compare two lipid compositions.

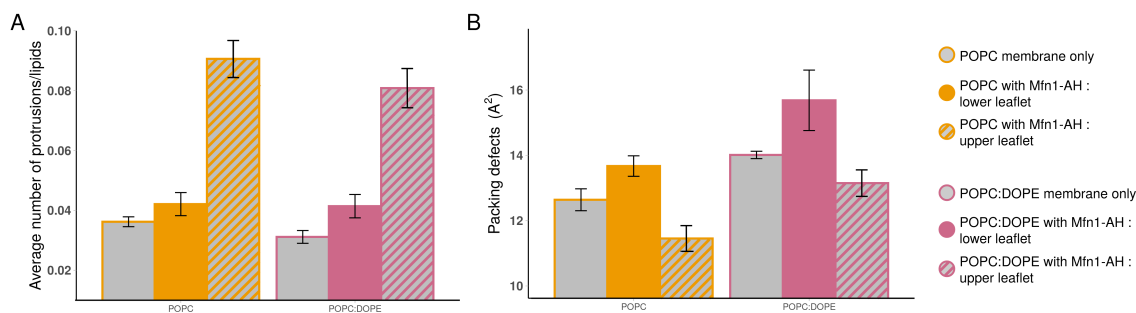


Figure 5.7: **The impact of Mfn1-AH on the membrane surface properties.** (A) Average number of protrusions per lipids. (B) Barplot of the packing defect constants π in \AA^2 .

We now examine what happens to protrusions when the peptide is added. They spectacularly increase in the leaflet with peptide for both lipid compositions. This result is very interesting, since this means that the binding of Mfn1-AH would promote hemifusion. It is in line with what was proposed by the study of Daste *et al.* [135]. For the lower (peptide free) leaflet, the value is equal or slightly greater than that for pure lipids, but definitely lower than the leaflet with peptide. Even if interesting fusion-wise, the difference of protrusion between both leaflets (whatever the lipid composition) is a bit counter-intuitive. Especially, we would have expected more protrusions in the lower leaflet, since it does not contain the peptide volume which is present in the upper leaflet, yet both leaflets have the same APL. At this stage, we have not found a convincing explanation to these observations, but we are actively searching.

Last, we examine packing defects. For both lipid compositions, the packing defect constant increases in the lower leaflet compared to pure lipids. It is expected, since it follows the increase of APL. Each lipid takes laterally more space, which means the polar heads are less packed against each other. For the upper leaflet (with peptide), we find a puzzling result. For both lipid compositions, the packing defect constant decreases compared to the other leaflet and pure lipids. We already mentioned that protrusions and packing defects are different phenomenons, however this decrease contradicts what we found with the protrusions. This would mean Mfn1-AH does not promote hemifusion, and contradicts the study of Daste *et al.* [135]. It also contradicts the increase of APL. How an increased APL would not lead to an increase of packing defects? Currently, we are suspecting a problem with Packmem and how we managed the presence of the peptide. We do not consider this result of packing defects on the leaflet with peptide relevant.

5.4 Mfn1-AH is more structured and stable in a DOPE membrane

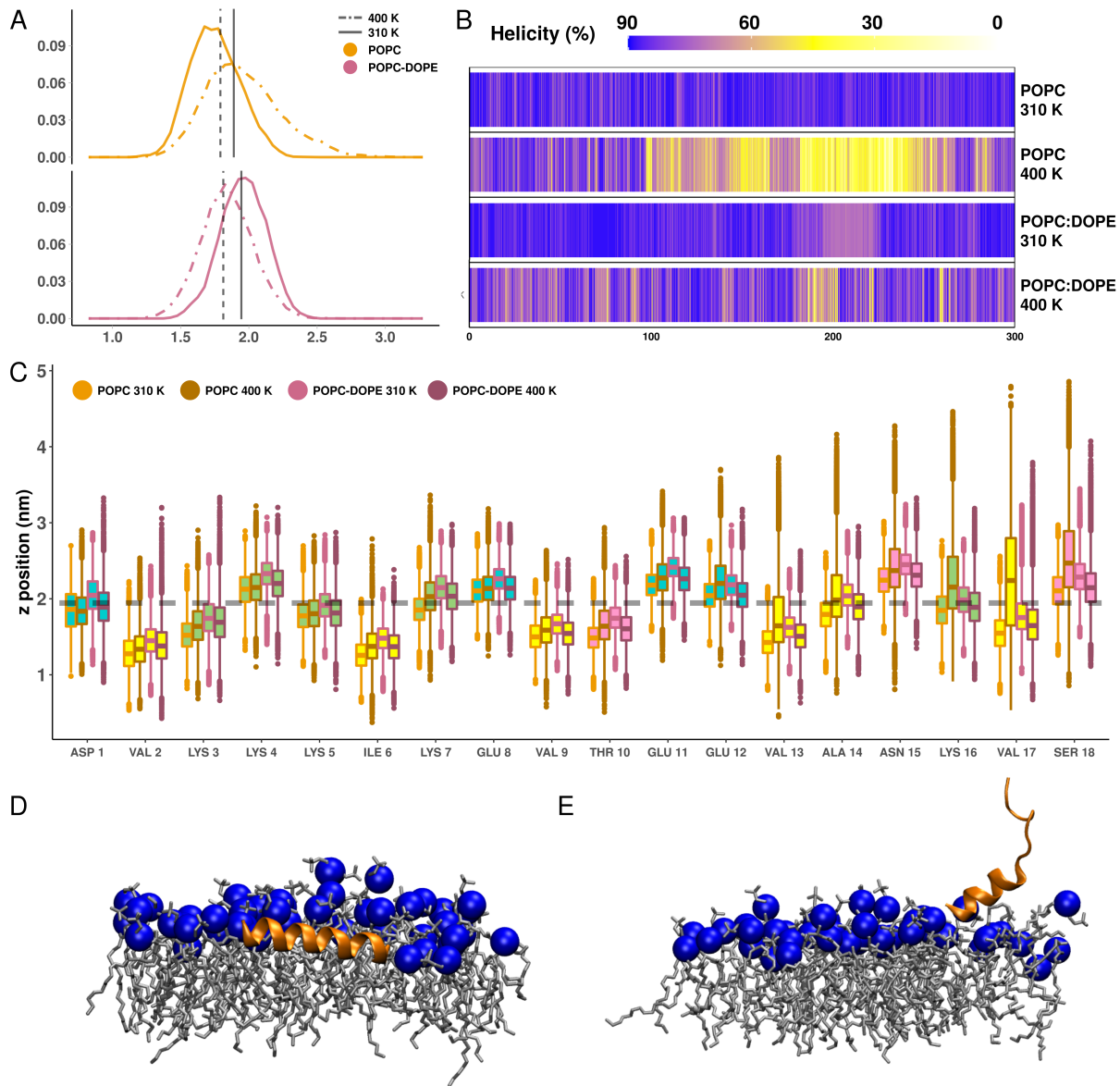


Figure 5.8: **Mfn1-AH stability in POPC and POPC:DOPE membranes.** (A) Density distribution of the position of Mfn1-AH to the membrane. The vertical lines represent the phosphate groups mean position. (B) Evolution of the helicity content as a function of time. (C) Distribution of Mfn1-AH residues in the membrane. Hydrophobic residues are colored in yellow, hydrophilic residues are colored in pink, positively charged residues are colored in green and negatively charged residues are colored in cyan. The dashed dark line represent the position of the upper layer phosphate groups. (D) Snapshot of Mfn1-AH embedded in a POPC:DOPE membrane. (E) Snapshot of Mfn1-AH embedded in a POPC membrane. For both (D) and (E) the POPC molecules are in grey and licorice representation. The phosphates of the POPC molecules are shown in blue and van der Waals representation. The protein is shown in ribbons and orange.

One of the objectives of these initial simulations was to compare the incorporation of Mfn1-AH in POPC and POPC:DOPE membranes. For this goal, we ran replica simulations at 400K, as the structural stability / instability of the peptide is more evident at such a temperature. In fact, while the peptide seems to be more embedded in the POPC membrane than in the POPC:DOPE membrane, this tendency is reversed in the simulations at 400K (Figure 5.8A) suggesting that Mfn1-AH is more likely to exit a POPC membrane than a POPC:DOPE membrane. This is confirmed by the secondary structure analysis in Figure 5.8B. The helicity is shown to be lower in the POPC membrane at 400K, while the secondary structure of the peptide is more stable in the POPC:DOPE at the same temperature. The partitioning analysis depicted in Figure 5.8C indicates that the C-terminal segment of the helix is less embedded in the membrane. The lowest stability in terms of secondary structure is located at the C-terminal end of the peptide, which can be observed in Figure 5.8E. As expected, apolar residues are deeply embedded in the membrane (as well as the polar residue Thr10), and the lysines are located around the same levels as the phosphates, probably stabilized by electrostatic interactions.

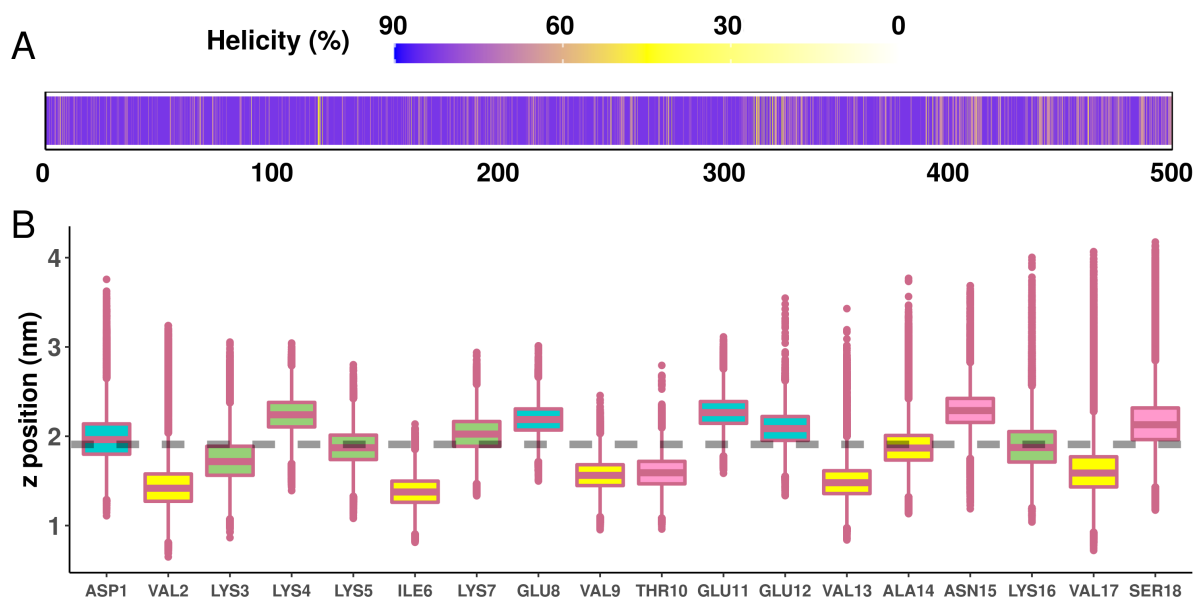


Figure 5.9: **REMD-helix : Ensemble of Mfn1-AH conformations at 310K.** (A) Evolution of the helix content as a function of time. (B) Distribution of Mfn1-AH residues in the membrane. Hydrophobic residues are colored in yellow, hydrophilic residues are colored in pink, positively charged residues are colored in green and negatively charged residues are colored in cyan. The dashed dark line represent the position of the upper layer phosphate groups.

Considering these results, we decided to proceed on studying the dynamics of the helix in a POPC:DOPE membrane. Initially, we conducted a T-REMD simulation with Mfn1-AH adopting a helical structure and being embedded within the membrane (REMD-helix). With REMD-helix, we were able to further analyse the stability of the peptide embedded in the membrane. We first analysed the ensemble of conformations at 310K, which according to the REMD protocol follows a Boltzmann distribution. We recall

that the successive conformations do not represent a continuous trajectory (see Figure 2.16). In this ensemble at 310 K, the secondary structure of Mfn1-AH remains highly helical as described in Figure 5.9A. In fact, 74% of the frames have about or more than 80% of the peptide structured, and 99% of the simulation show the 50% or more of the peptide structure in α -helix. The position of the sampled residue exhibits a strong resemblance to the previous simple MD simulations, suggesting a consistent behavior and a robustness of the predicted AH-membrane interactions.

Moreover, we had a closer look at the different replicas of the simulation (Figure S5.2). This time, we analyze individual replica which diffuse in temperature space (see Figure 2.16). 34 out of 35 replicas demonstrate that the peptide remains firmly embedded within the membrane (Figure S5.2A). Furthermore, the secondary structures remain stable throughout the 34 simulations (Figure S5.2B). Indeed, 33 out of 35 replica show at least 50% of the peptide structured in α -helix for about 95% of the simulation time, and 25% replica show at least 70% of the peptide structures for about 89% of the trajectory.

5.5 Structural dynamics of Mfn1-AH: Unfolding, Insertion, and Folding processes in water and membrane environments

Our aim was to investigate the dynamics of the peptide within a membrane environment. To achieve this, we decided to study the protein as it is positioned in the solvent, enabling us to observe both the insertion and folding processes. Therefore, we initially focused on sampling AH conformations in water using an REMD approach (REMD-water). An unfolded structure could then be extracted and placed in the solvent of a membrane POPC-DOPE system.

5.5.1 Unfolding process of Mfn1-AH in water

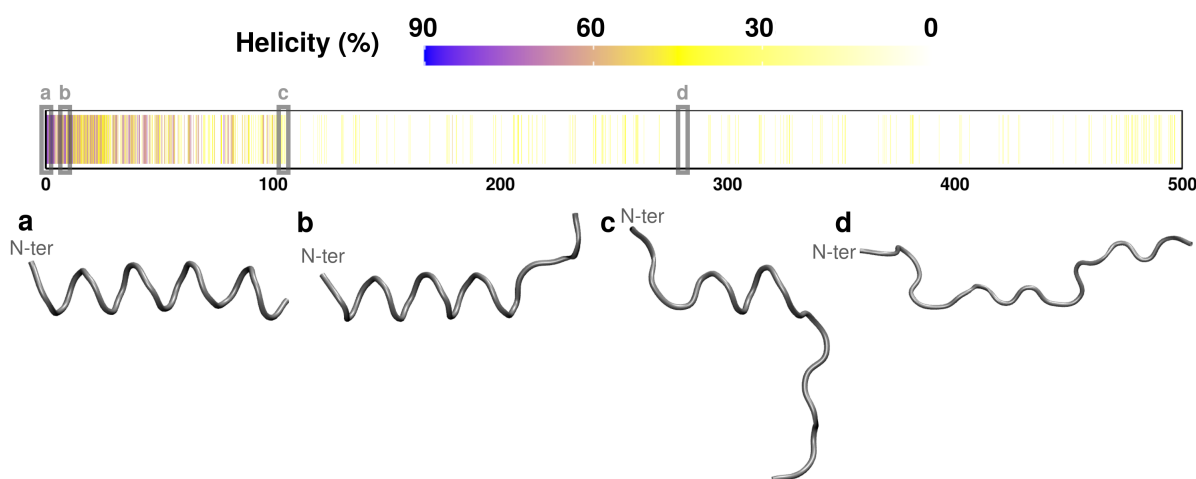


Figure 5.10: **REMD-water: Evolution of the helicity content as a function of time.** The ensemble of conformation at 310 K was studied. The completely unfolded structure was used as the starting structure of Mfn1-AH in REMD-folding.

The conformations used for model extraction corresponds to those at 310K. We observe that the helix content decreases at the beginning of the simulation (Figure 5.10) and highly fluctuates between 0 and 20%. In the last 400ns of the simulation, the helix content stabilizes at a mean of 2.5 %, and the peptide is most often in a fully coiled structure.

Hence, the last 400 ns were used to select a representative structure, with the clustering method GROMOS. The cutoff used, 0.45 nm, revealed 5 groups representing 77% of the structures used. The first cluster represent 37% of the structures. The center structure of the first cluster can be seen in Figure 5.10d. This conformation was used as the starting structure of the REMD-folding.

5.5.2 The insertion process of Mfn1-AH in a POPC:DOPE bilayer

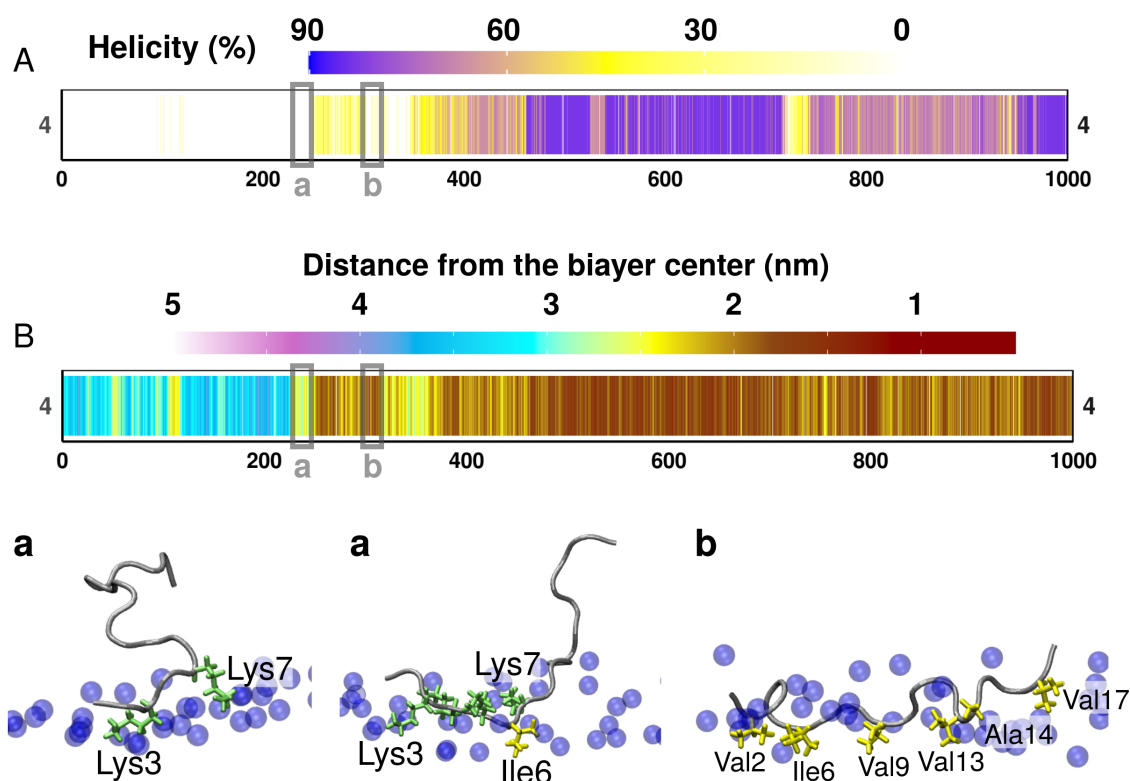


Figure 5.11: **REMD-folding: Study of replica 4.** (A) Evolution of the helix content as a function of time. (B) Evolution of the distance of the peptide to the center of the bilayer. On the bottom, snapshots showing the first stages of interactions between the peptide and the membrane.

One of the goals of this project is to study the insertion and folding process of the helix. Hence we first sampled the most probable conformation of the peptide in the solvent, which was then placed in a POPC:DOPE membrane only system. In the REMD-folding, it was observed that only one of the replicas consistently interacted with the membrane upon binding (Figure S5.3A). Indeed, at 310K, Mfn1-AH was observed to interact with the membrane for only 9% of the time in the replica. Nevertheless, upon analyzing the distribution of distances for each residue in the membrane across all replicas (Figure

S5.3D), it became evident that hydrophobic residues Ile6, Val2 and Val9 are predominantly engaged in interactions with the membrane. The lysine residues in the beginning of the sequence show low distance with the bilayer center throughout the simulations as well. As a consequence, we can observe Asp1 and Glu8 at a low distance as well. It could be argued that residues Lys3, Lys4 and Lys5 foster the hydrophobic interactions between the peptide and the membrane, through their interactions with the phospholipids heads, and more specifically the phosphate groups.

The replica in which binding and folding was observed is number 4 (Figure S5.3A,B). The binding process of replica 4 was further studied in Figures 5.11 and S5.3C. In accordance with the previous description of the peptide interactions with the membrane (see previous section), we first observe the peptide interacting through the lysines which will favor the deeper hydrophobic interactions involving the apolar residues. Mfn1-AH is then able to fully bind the membrane, first in an unstructured manner (Figure 5.11A,B). It is important to highlight that the peptide can adopt a partial α -helical structure before a complete embedding within the membrane. Nevertheless, a complete structuration of Mfn1-AH outside the membrane was not observed in our study. Indeed, outside of the membrane, the peptide remains predominantly unfolded.

5.5.3 The folding process of Mfn1-AH in a POPC:DOPE bilayer

Very few replicas showed Mfn1-AH folding into an α -helix (Figure S5.3B). Moreover, the folding of the helix was not consistently synchronized with its interaction with the membrane. In fact, among the conformations showing 30% or more of helicity, 65% of them have a distance from the bilayer of 2.5 nm or less. However, 95 % of the structure with an helicity above 70% are within 2.5 nm of the bilayer center, which suggest that binding to the membrane is necessary to obtain a fully folded AH.

As described previously in Figure 5.11, we observe the complete folding of the peptide in replica 4, shown in Figure 5.13. As described in the previous section, the folding was preceded by interactions between a mostly unfolded peptide, and the membrane. In fact the folding first starts at 300 ns, and proceeds for about 100 ns. In replica 4, the embedding of HA is primarily initiated by the residue Ile6. While some folding was noted in the C-terminal section outside of the membrane, complete folding of the peptide occurs once the N-terminal section is fully embedded and folded. The N-terminal section of the protein is in fact the most stable section of the protein, as can be seen in Figure 5.12.

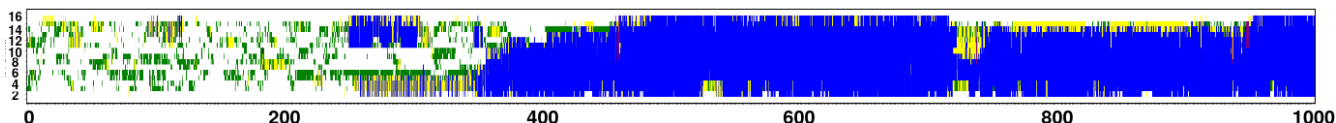


Figure 5.12: REMD-folding: Secondary structure evolution of replica 4.

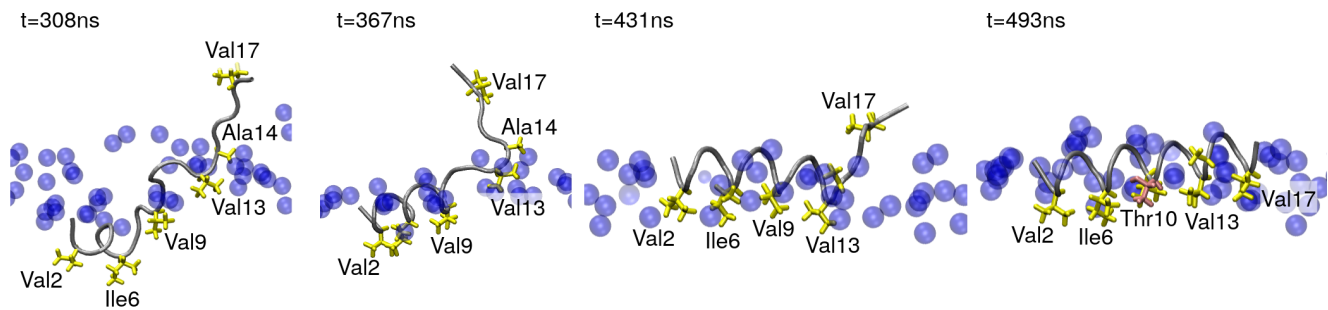


Figure 5.13: **REMD-folding: Folding process of Mfn1-AH.**

5.6 Discussion

5.6.1 Can Mfn1-AH fold into the membrane on its own ?

The various simulations ran in this chapter showed first and foremost that the POPC:DOPE membrane is an environment in which Mfn1-AH is more stable. In fact the secondary structure was the most stable in the POPC:DOPE membrane at high temperature (Figure 5.8B). The embedding of the protein varies the least as well (Figure 5.8C). This could be explained by the conical shape of PE lipids, which could be more accommodating to the peptide. Furthermore, the position of the Lysines at the same level as the phosphate groups can participate in initiating or maintaining of the AH-membrane contacts.

However, the REMD-folding showed most of the replica not interacting with the membrane. What could drive the embedding of Mfn1-AH in a membrane? Indeed, the OM comprises some anionic lipids (phosphatidylinositides and cardiolipins), potentially promoting interactions between the membrane and the peptide, given the positively charged nature of the N-ter portion of the residues in Mfn1-AH. Moreover, the diameter of the liposomes used in the 2018 study was smaller than 100 nm, meaning that HR1 requires some level of curvature (i.e. packing defects), to bind the membrane. Our systems might not accurately reproduce the packing defects necessary for the folding of Mfn1-AH. In addition, the unfolded structure of the helix could participate in reducing the peptide-membrane interactions. In fact, in the context of the full protein Mfn1, this peptide is most likely to harbor an α -helix structure. Furthermore, Daste et. al 2018 [135] showed HR1 domain to be partially folded without any lipids (Figure 5.1A). Hence, an α -helix starting structure could participate in the docking of the helix. Finally, Daste and collaborators [135] have also showed that HR1 could not dock any membrane and induce membrane fusion if the domain was not chemically linked to the membrane. In that sense, the REMD-folding results are in accordance to what was experimentally shown. It is worth noting that in the context of the whole protein Mfn1, HR1 will be anchored to the membrane through the TM domain.

While our simulations did display only one spontaneous folding, the simulations with the peptide already embedded in the membrane demonstrated a robust and sustained interaction observed between the peptide and the membrane, as indicated by the REMD-helix. Based on these findings, it can be inferred

that the helix plays a crucial role in maintaining the interactions between HR1 and the membrane.

5.6.2 Has Mfn1-AH fusion inducing properties?

In agreement with what Daste and collaborators [135] expected, our simulations showed more protrusions in the leaflet with peptide. Moreover, the peptide did affect the membrane thickness, area per lipid, and the order parameter, which increased in the layer containing Mfn1-AH. These events were in fact hypothesized to favor fusion events and initiate the stalk phase [147, 146]. It is nonetheless complicated to draw any conclusions on the fusion properties of the peptide alone with the simulations ran for this projects. It could be interesting to proceed to study the effects of the peptide in a two membrane systems, and observe the stalk or fusion events. Furthermore, other simulations could be performed with peptides inducing fusion, such as influenza fusion peptide [146], in order to compare the results obtained in our systems.

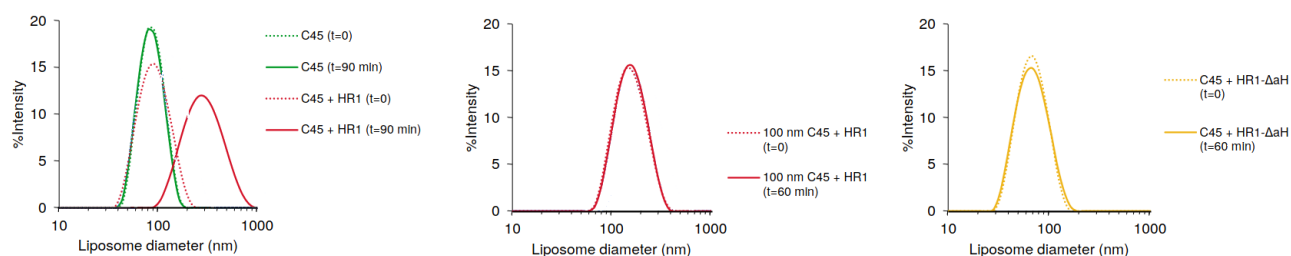


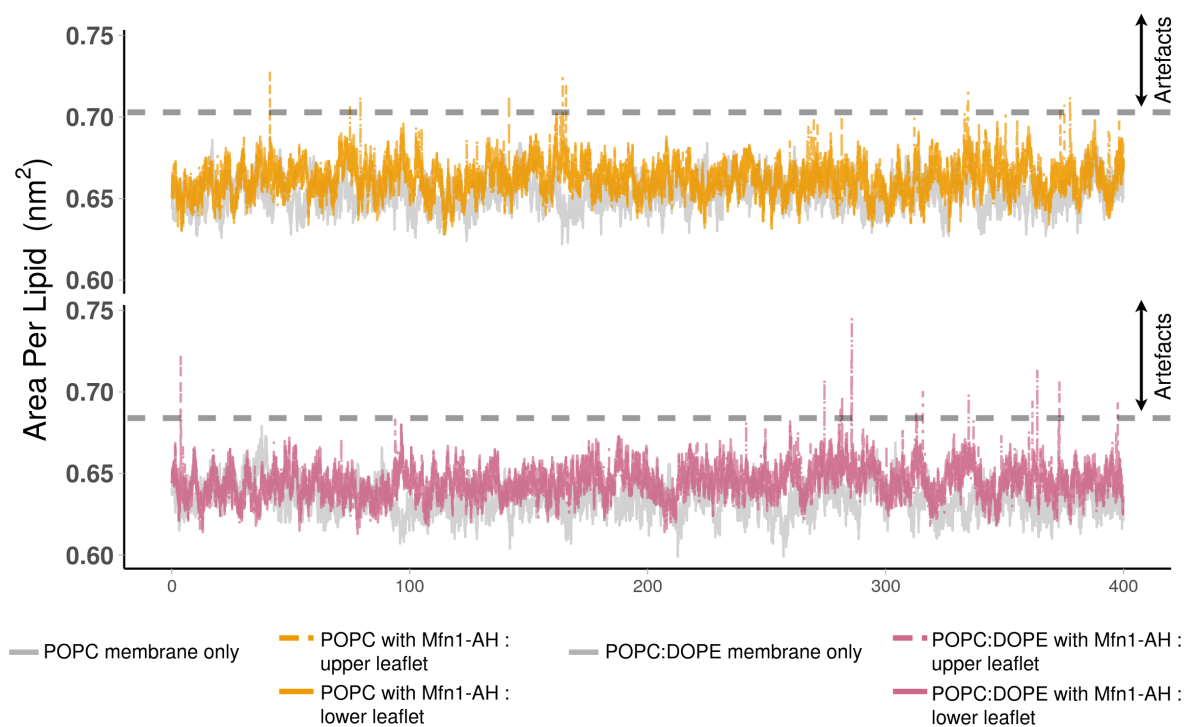
Figure 5.14: **Liposome-liposome docking and fusion by HR1 of Mfn1 probed by Dynamic Light Scattering (DLS).** (Left), the size (diameter) of liposomes, composed of mainly POPC (92%) and prepared by extrusion, was measured by DLS before and after 90 min of incubation at 37°C with the HR1 or HR2 domain of Mfn1. (Middle) Size distribution of 100 nm POPC:C45(95:5) liposomes prepared by extrusion before and after 1 hour of incubation at 37degC with HR1 or HR2. (Right) size distribution of POPC:C45(95:5) liposomes before and after 1 hour of incubation at 37°C with the amphipathic helix deleted HR1 mutant, HR1- Δ AH. Taken from [135].

The 2018 study [135] studied the docking and fusion process in presence of HR1 (red) or HR1- Δ AH, an amphipathic helix deleted HR1 mutant, both showed in Figure 5.14. When the incubation starts with small size liposomes (lower than 100 nm), their size increase after 1 hour, which indicates docking and fusion events in the system. However, when HR1 is placed with larger liposomes, no size changes are observed after an hour, indicating the absence of docking and fusion in the system. This underlines the necessity of high membrane curvature for HR1 to dock and then induce fusion. As a matter of fact our membrane composition used in the REMD-folding might not have reproduce the curvature and/or packing defects necessary to induce the peptide's docking to the membrane. Finally, HR1- Δ AH systems did not show any increase of liposomes size, showing that without the AH, HR1 cannot mediate liposome docking. This latter result is in fact in agreement with the *in vivo* experiment showed in Figure 5.1B.

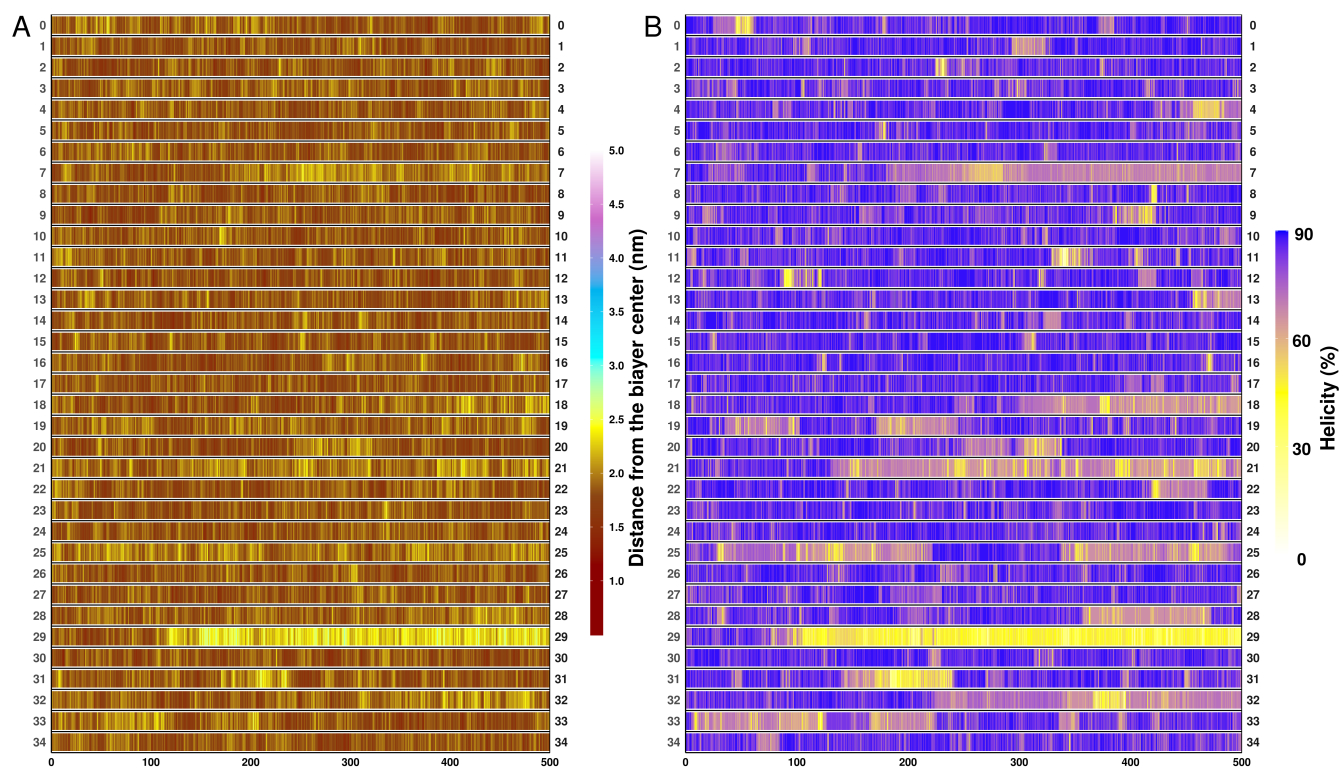
In light of our most recent findings, we are inclined to propose a hypothesis: the peptide functions in anchoring the Mfn1 domain within the membrane. The data suggests that establishing a stable connection

between Mfn1/HR1 and the membrane could be one of the functions of the amphipathic helix, which would result in facilitating HR1 induced fusion. Further investigations and in-depth analyses will be essential to substantiate this hypothesis and unveil the precise mechanisms at play. Our collaborator David Taresté is currently doing experiments on Mfn1-AH in interaction with liposomes (fusion and CD). Comparing the outcome of these experiments with our simulations will be particularly interesting.

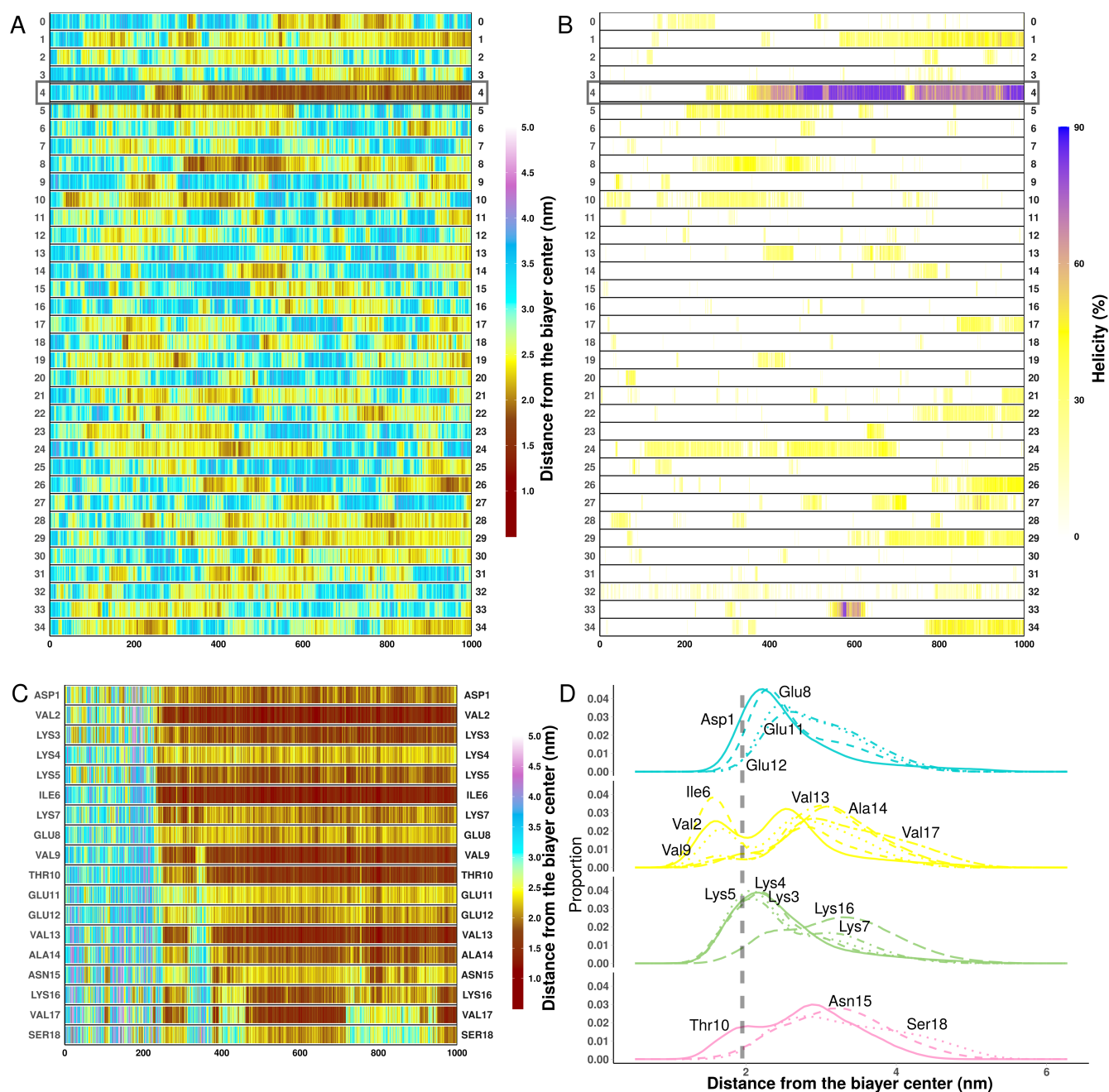
5.7 Appendix



Supplementary Figure S5.1: **Area per lipid as a function of time during classical simulations at 310K.** Above the dashed line, we consider the values as artefact as they rapidly spike to very high points within only a few nanoseconds. The cause of this anomaly remains unresolved.



Supplementary Figure S5.2: **REMD-helix : Analysis per replica.** The 35 ensemble of conformations at each temperature were rearranged to obtain 35 continuous trajectories per replica which can be analysed. (A) Evolution of the distance of Mfn1-AH from the bilayer center as a function of time. The closer the peptide from the bilayer center, the darker the color. (B) α -helix content for all the replica of the REMD starting with the helix embedded in the membrane.



Supplementary Figure S5.3: **REMD-folding : Analysis per replica.** The 35 ensemble of conformations at each temperature were rearranged to obtain 35 continuous trajectories per replica which can be analysed. (A) Evolution of the distance of Mfn1-AH from the bilayer center as a function of time. The closer the peptide is from the bilayer center, the darker the color is. (B) α -helix content for all the replica of the REMD starting with helix embedded in membrane. (C) Evolution of the distance of the residues of Mfn1-AH from the bilayer center as a function of time. (D) Distribution of the positions of individual residues across all replicas. The dashed line represents the position of the phosphates.

CHAPTER 6

EXPLORING THE MITOFUSIN CONFORMATIONAL LANDSCAPE WITH ALPHAFOLD

6.1 Introduction

Throughout this Ph.D, we were able to study specific domains of two mitofusins, Fzo1 and Mfn1. However, we studied the structures produced by AlphaFold (AF) [158] as well. This tool is recognized as largely reliable and effective method for protein structure prediction [158, 159]. This method was tested on mitofusins, and did not show completely satisfactory results. Here, we are studying the different results and limitations of the AlphaFold method.

6.2 Materials and methods

To predict the structures of mitofusins, we used Alphafold versions 2.2 and 2.3.1 [158, 223], and Colabfold 1.3.0 [224], both monomer and multimer versions. The various predictions are described in Table 6.1.

	Protein(s) (Sequence)	MSA
Monomers of solute carriers	Ugo1[1-502]	AF
	SLC25A46[1-418]	AF
Monomers of mitofusins	Fzo1[1-855]	AF
	Fzo1[1-855]	Custom
	Mfn1[1-741]	AF
	Mfn2[1-757]	AF
Oligomers of mitofusins	2×Fzo1[1-855]	AF
	2×Mfn1[1-741]	AF
	2×Mfn2[1-757]	AF
	Mfn1[1-741] + Mfn2[1-757]	AF
Oligomers with fusion partners	2×Fzo1[60-855] + 2×Ugo1[100-502]	AF
	2×Mfn1[1-741] + 2×SLC25A46[1-418]	AF
	2×Mfn2[1-757] + 2×SLC25A46[1-418]	AF
	Mfn1[1-741] + Mfn2[1-757] + 2×SLC25A46[1-418]	AF

Table 6.1: **Summary table of the models produced with AlphaFold.** AF stands for AlphaFold. The provided sequences were taken from uniprot [207] for Fzo1 (P38297), Mfn1 (Q8IWA4), Mfn2 (O95140), Ugo1 (Q03327) and SLC25A46 (Q96AG3).

Each structure underwent a verification process to detect any clashes. Following this, two minimization steps of 5000 steps were conducted using GROMACS version 2022.x versions. We then proceeded to initiate the complex refinement pipeline using HADDOCK3 [270] (see github <https://github.com/haddock/haddock3/>). The models produced by the refinement stage were ranked according to the HADDOCK score, and the best scored model was selected for analysis.

Custom Multiple Sequence Alignment. 47 sequences of mitofusins were found using PSI-BLASTP version 2.13.0 [271, 272] and residues 702-760 of Fzo1 sequence (Uniprot: P38297). The sequences obtained are listed in Supplementary Table S6.1 and the MSA of the TM domains are shown in Supplementary Figure S6.1. The full sequence of the mitofusins were then aligned using the T-coffee alignment

procedure [273, 274]. This alignment was then provided to Alphafold in A3M format for the prediction of the Fzo1 monomer.

Contact Analysis. The lowest distances between all residues pairs was measured using all the atoms of the structures.

6.3 AlphaFold provides a new type of cis-dimerization conformation involving the coiled-coil domains in the interactions

6.3.1 AlphaFold exclusively produces mitofusins structures in an open conformation, unsuitable with membrane tethering mechanism

The results of AF (default usage) on Mitofusins monomers can be observed in Figures 6.1 and 6.2. First, we can observe that the structures predicted for these three molecules are all in an open conformation (Figures 6.1A and 6.2A,E). Supplementary Figure S6.2 presents on the left of each panel, the structure colored as a function of the pLDDT, and on the right, as a function of the domains. Each structure presents low pLDDT values in the TM domains, and both Mfn2 and Fzo1 have low values in the N-ter section of the structure. In Fzo1, the N-ter section of the protein (before the HRN domain) are in fact predicted as intrinsically disordered by AF. In addition, Fzo1 TM domain and N-ter section are predicted as mainly disordered, in direct contradiction with the PSIPRED secondary structure predictions (for Fzo1, described in Section 3). For both Mfn1 and Mfn2, although the helicity content is higher, AF does not find a two helices conformation for any of the models (Figure 6.2D and H). Half of TM1 is in fact folded as α -helix for both Mfn1 and Mfn2. It is interesting to note that the helix starts at the conserved Arginine residue (observed in Supplementary Figure S3.9 and annotated on D and H panels of Figure 6.2).

The Fzo1 structure proposed by AF displays a very different structural organization than the models proposed in 2017 [1] and 2019 [2]. Both Fzo1 original models (closed and open conformation) are shown and detailed in Figure 1.22 and Section 1.4.3. First and foremost, the TM section exhibits significant differences, notably because AF fails to generate the anticipated helical structures. The TM section of this first model has been disputed in Section 3. The HRN domain is the second main difference with the first model, as it is organized differently : the domain is now placed underneath the GTPase domain, instead of on its left. In fact, the HRN domain is placed similarly to the N-termini helices observed in both Mfn1 and Mfn2 (Figure 6.2 and see Figure 1.1 of Section 1.4.3).

Finally, the hydrophobic residues of HR1 and HR2 domains are distributed differently in the AF than what was predicted in 2017 [1]. These domains organized in a coiled coil conformation are structured in one continuous block in the AF models, instead of the two sections of helices, based on BDLP [65, 68] (see Section 1.3.2 and Figures 1.14 and 1.16). Furthermore, while the hydrophobic spine of HR2 was constructed solvent exposed, here the two heptad repeat domains, as well as the residues from 570 to 605, are involved in more typical HR interaction pattern (Figure 6.1C). Similar interactions are observed

in Mfn1 and Mfn2 models. A third helix is involved in the hydrophobic coiled-coil interactions as well (Figure 6.2C and G). Finally, the hydrophobic spine of the amphipathic helix of Mfn1 HR1 domain (described in 2018 [135]) is facing the coiled-coil instead of the solvent. This implies that the amphipathic helix is not readily disposed to interact with the membrane, contrary to what was suggested by the 2018 study [135].

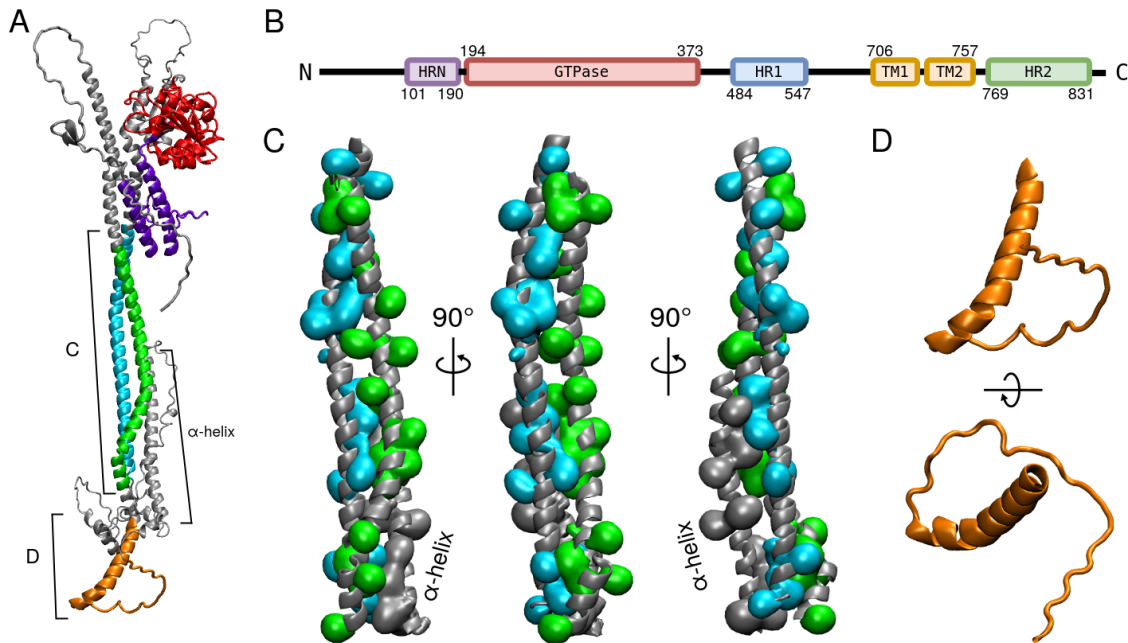


Figure 6.1: AlphaFold model of Fzo1. (A) Monomeric model of Fzo1 produced by AF. The domains are colored as function of the domains defined in (B). The unassigned sections of the protein are colored in grey. (B) Schematic representation showing the domain organization of the mitofusins Fzo1. GTPase domain in red; HR1/2, heptad repeat 1/2 in blue/green; HRN in purple; TM, transmembrane region (including the loop in between TM1 and TM2) in orange. Boundaries of each element are indicated by residue numbers. (C) Zoom in on HR1 and HR2 domains. The surface of hydrophobic residues of both domains are represented in cyan for HR1 and green for HR2. On the right panel, a third helix (residues 570 to 605) is represented in grey, as it is involved in hydrophobic interactions. (D) Zoom in on the TM domain.

The absence of a loop in the center of the mitofusins HR1/2 coiled-coil implies strong conformational rearrangement in order to fit the hypothesized mechanisms described in Section 1.4.3 and Figures 1.23 and 1.24. In fact, to fit these proposed mechanisms (specifically presented in Figures 1.23B and 1.24B), the helix bundles of the mitofusins models would have to locally break and unfold into a loop. However, as these fusion models have not yet been validated by experimental data, new mechanisms could arise from the analysis of the models produced by AF, and more specifically from the analysis of multimers of mitofusins.

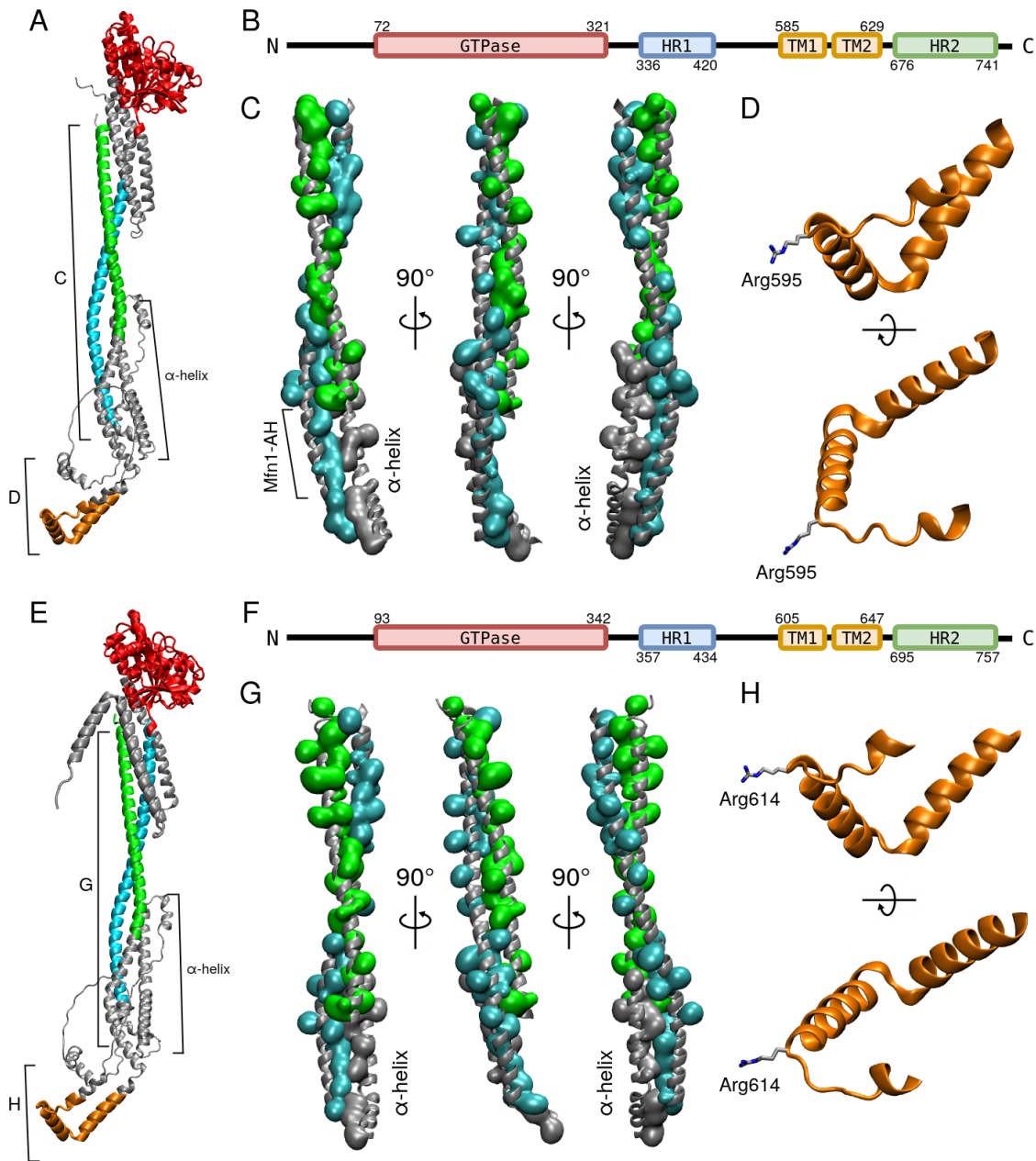


Figure 6.2: AlphaFold model of human mitofusins Mfn1 and Mfn2. (A) Monomeric model of Mfn1 produced by AF. The domains are colored as function of (B). The unassigned sections of the protein are colored in grey. (B) Schematic representation showing the domain organization of the mitofusin Fzo1. GTPase domain in red; HR1/2, heptad repeat 1/2 in blue/green; HRN in purple; TM, transmembrane region in orange. Borders of each element are indicated by residue numbers. (C) Zoom in on HR1 and HR2 domains. The surface of hydrophobic residues of both domains are represented in cyan for HR1 and green for HR2. On the right panel a third helix (residues 445 to 485) is represented in grey, as it is involved in hydrophobic interactions. (D) Zoom in on the TM domain. (E) Monomeric model of Mfn2 produced by AF. The domains are colored as function of (F). The unassigned sections of the protein are colored in grey. (F) Same as (B). (G) Same as (C). The third grey helix are residues ranging from 470 to 503. (H) Zoom in on the TM domain.

As the experimentally solved structures of mitofusins and homologue BDLP show homo-dimerization

through the GTPase domain, we decided to investigate the dimers generated by AF (Figure 6.3). First and foremost, Fzo1 dimers were produced and again showed very different results from the Fzo1 open cis-dimer previously modeled (see Figure 1.22). While the model retains the open conformation previously described, the type of dimerization is very different to the BDLP homologue (see Figure 1.15). In fact, the model shows a cross-type of dimerization, involving the GTPase domain as well as residues of the HRN and HR2 domains in the interactions (Figure 6.3A, B and C). In contrast, the dimer produced in 2019 [2] only involved the GTPase domain, similarly to what has been established for BDLP [68]. Precise interactions between monomers of Fzo1 are described in the Supplementary Table S6.2A. In fact, it can be observed that the dimeric structure seems to be maintained through salt bridges, observed in the HRN, GTPase, and HR2 domains. Indeed, polar and charged residues able to form salt bridges and hydrogen bonds are observed in close proximity.

In comparison, the human mitofusins seem to present models compatible with a first step of membrane tethering. In fact, the Mfn1 homodimer, as well as the Mfn1-Mfn2 dimer, show a trans-dimer type of interactions, with two mitofusins that would be placed on different membranes. On the other hand, the Mfn2 homodimer, as well as an other model of the Mfn1-Mfn2 dimer, show what appears to be cis-dimers. In the case of the Mfn2 homodimer, we have obtained a BDLP type of interactions, mainly involving the GTPase domain in interactions between monomers, while the Mfn1-Mfn2 model presents a cross type of cis-dimerization. Surprisingly, AF was able to produce a diversity of models in the case of Mfn1 and Mfn2 heterodimer. Furthermore, one of this model involves interactions between the coiled coil helices, similarly to the prediction of Fzo1 dimer. Similarly to the Fzo1 dimer previously described, salt bridges between the human mitofusins are observed, mostly involving the GTPase domain (Supplementary Table S6.2B). In the cross-like cis-dimer of Mfn1-Mfn2, proximity between residues able to form hydrogen bonds is described as well, involving the HR2 domain of the mitofusins with residues located between HR1 and TM domains.

These models of dimers can be sorted into two categories: trans-dimers (two monomers on opposite membranes) and cis-dimer (two monomers on the same membrane). Trans-dimers may inspire novel concepts for the fusion mechanisms of mitofusins. However, as expected from members of the dynamin superfamily, important conformational changes are required to facilitate the outer mitochondrial membrane fusion (see Section 1.3). While the rupture of coiled-coil structures might be conceivable and consistent with previously proposed mechanisms, these structures could also undergo bending without necessitating helical breakage, bringing the two opposing membranes closer together and possibly interacting with the membrane, upon reorganization of the HR domain hydrophobic spines. Furthermore, these new cross-type of cis-dimerization could be induced by interactions of the GTPase domain, which will help finalize membrane tethering. The first trans-membrane interactions could first involve the GTPase domain only, followed by these HR domains interactions (HRN and HR2 for yeast Fzo1, and HR2 for human Mfn1/2), similar to inter-protein coiled-coil interactions observed in SNARE [199]. The dimers observed in Figures 6.3A and G would be post-fusion complexes.

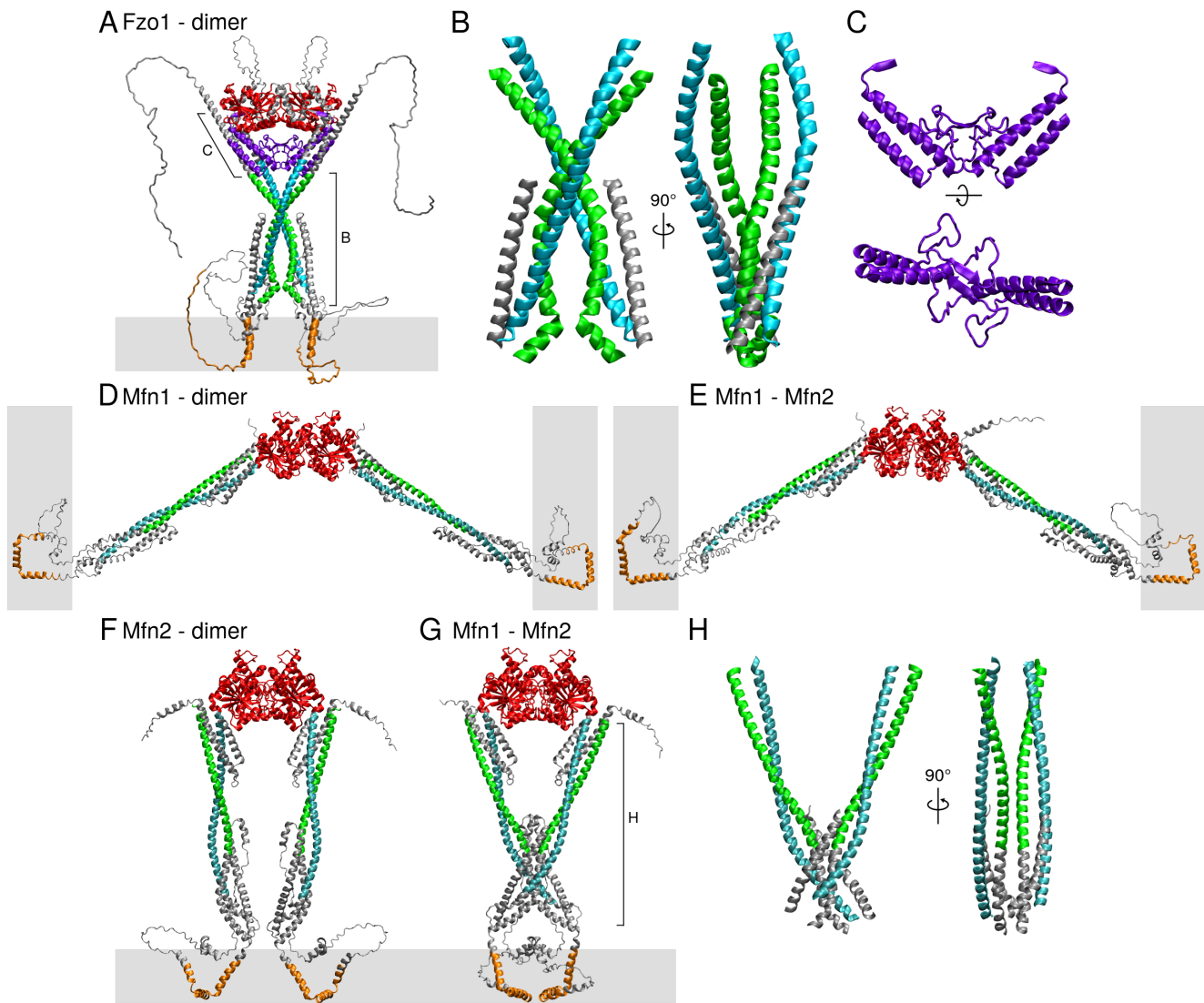


Figure 6.3: **AF dimeric models of human and yeast mitofusins.** (A) Dimer model of Fzo1 produced by AF. The domains are colored as function of domains, defined in Figure 6.1B. The unassigned sections of the proteins are colored in grey. (B) Zoom in on HR1 (cyan) and HR2 (green) domains, as well as residues 570 to 605 (grey). (C) Zoom in the HRN domains. (D), (E), (F) and (G) AF models of respectively Mfn1 homodimer, Mfn1-Mfn2 heterodimer (version 1), Mfn2 homodimer and Mfn1-Mfn2 heterodimer (version 2). The domains are colored as function of domains, defined in Figures 6.2B and F. The unassigned sections of the proteins are colored in grey. (H) Zoom in on the model of Mfn1-Mfn2 version 2: HR1 (cyan) and HR2 (green) domains, as well as residues 445 to 485 for Mfn1 and residues 470 to 503 for Mfn2 (grey).

6.3.2 The AF models are validated by the available experimental data

In the previous implementation of the model [1, 2] various salt-bridges and hydrophobic interactions were underlined and validated experimentally, using swap mutations[1]. These salt bridges are shown described in Figure 6.4D. A first salt-bridge was found involving the Lys464 residue, a target for post-translational modification by ubiquitin in Fzo1 [142], and Asp335. Single point mutations mutations

D335K and K464D induced a total inhibition of respiratory growth, while the swap mutation D335K-K464D partially but significantly corrected the defect. Similarly, K200-D313 and D523-H780 salt-bridges were found although the H780D mutant did not show respiratory inhibition [1]. Figure 6.4D underlines that salt bridges D335K-K464D and K200-D313 predicted in 2017 were found in the AF model (and validated in the experimental structure, result not shown), while D523-H780 residues are found to be quite far apart in the AF model. However, D523-H780 salt-bridge could be reasonably questioned, as one of the two single point mutant does not show respiratory inhibition. Hydrophobic contacts were hypothesized as well in the 2017 study [1]. L501-L504-L802 and T490-L819 were observed to be in close contact, however they are farther apart in the AF model.

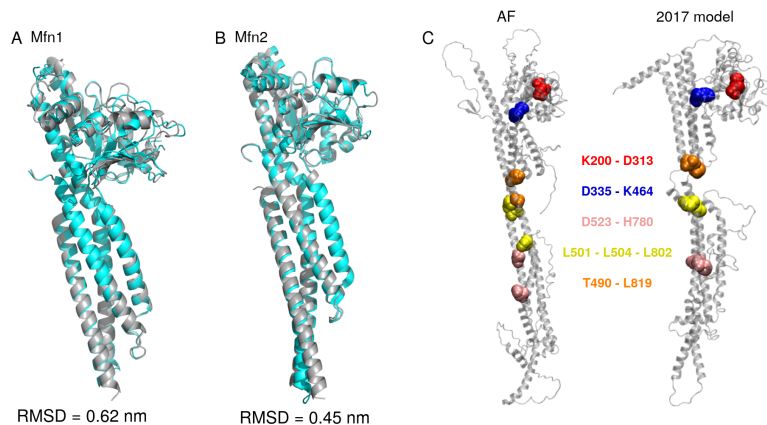


Figure 6.4: Experimental structures aligned with the AlphaFold models. In all panels the AlphaFold model is in grey, the experimental structure is in cyan. (A) AlphaFold prediction of Mfn1 aligned with Mfn1 structure PDB: 5GOF. (B) AlphaFold prediction of Mfn2 aligned with Mfn2 structure PDB: 6JFK. (C) Left, model obtained using AF. Right, model obtained using homology modeling [1, 2]. Residues in contact described in the 2017 model are shown in van der Waals representation and color-coded according to their respective groups of residues.

These experimental data show a first partial validation of the AF model, it however does not allow us discriminate between it and the 2017 model [1]. For the human mitofusins, partially solved structures are available (see Section 1.4.3 and Figure 1.1). The alignment of these AF models with experimental structures are shown in Figure 6.4 A and B. Each couple of structures (AF and experimental structures) present very low RMSD with each other (Figure 6.4). It is indeed expected for both Mfn1 and Mfn2 as these structures are present in the PDB, on which AF was trained. However, the unpublished Fzo1 dimer produced by our collaborator Philippe Meyer (using the methodology developed by Mirabello et al. [275]) showed strong agreement with the AF structure (results not shown), validating the position of the HRN domain produced by AF. In fact, the structures presented an RMSD of 0.36 nm with the AF structure (for each monomer). Furthermore, the position of each monomer short coiled-coil conformation in the experimental structure seemed to agree with the cross-like cis-dimerization observed in the AF models. Hence the dimerization scenario does present strong differences with the BDLP homologue. However, considering that the two proteins exhibit only 43% similarity [1], the structural disparities

observed between them could be attributed to their differences in sequence.

6.3.3 New models involving fusion partners Ugo1 shed new light on cross-type cis-dimer

Ugo1 is a modified mitochondrial solute carrier embedded in the outer mitochondrial membrane showed to be required for outer mitochondrial membrane fusion. Indeed, Sesaki et al., 2001 [108] demonstrated that mutants lacking Ugo1 exhibit numerous small mitochondrial fragments, contrasting with the few long tubular-shaped mitochondria observed in wild-type cells. The human orthologue to Ugo1 would be the member of the mitochondrial solute carrier family SLC25A46 [138, 276]. SLC25A46 has been showed to participate in both upregulation [277] and downregulation [278, 138] of mitochondrial fusion. Hence, the role of the protein is argued to be associated with an overall regulation of mitochondrial dynamics. Neither of Ugo1 and SLC25A46 have an identified substrate, despite their apparent belonging to the solute carrier family [277, 276].

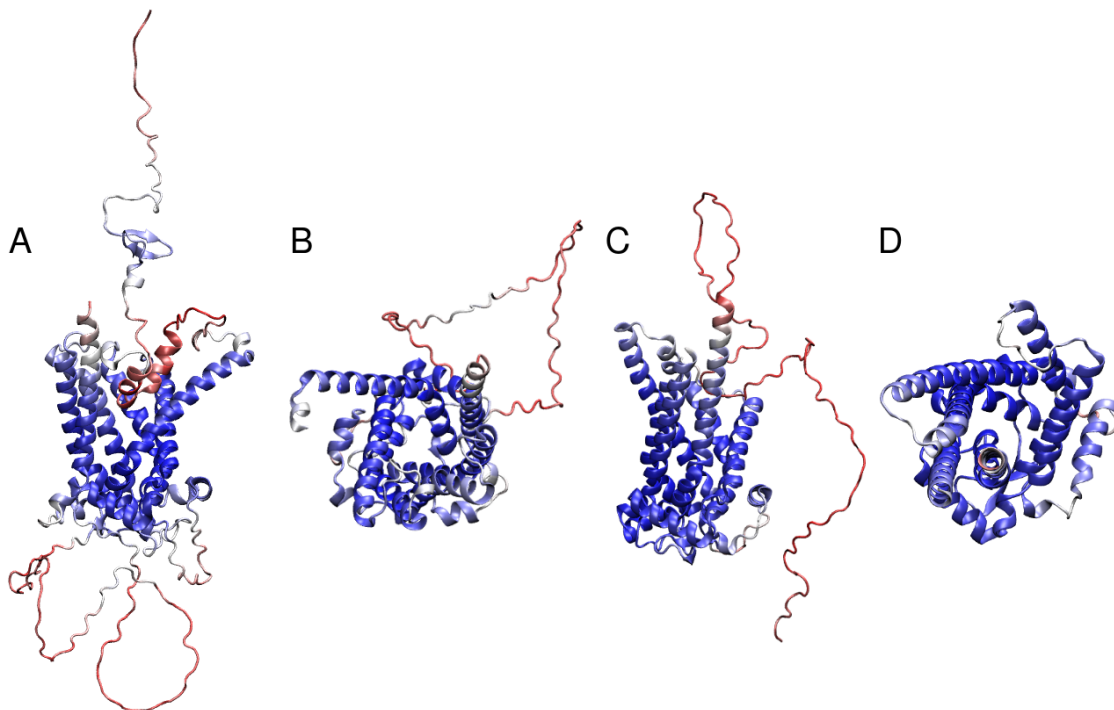


Figure 6.5: **AF structure prediction of mitofusins fusion regulators.** (A) Modified mitochondrial solute carrier Ugo1. (B) Top view of Ugo1. Residues 1 to 100 were removed from the visualization, as they were predicted intrinsically disordered. (C) Mitochondrial solute carrier SLC25A46. (D) Top view of SLC25A46. Residues 1 to 90 were removed from the visualization, as they were predicted intrinsically disordered.

The AF structure prediction of these two proteins is shown in Figure 6.5. It can be observed that AF predicts a typical solute carrier structure, similar to what was described by Kunji and collaborators in 2020 [279]. The top perspective of the proteins depicted in Figure 6.5B and D reveal the channels formed

by the proteins, suggesting the potential passage of a substrate. However they both show an extended N-terminal intrinsically disordered section, which is atypical for mitochondrial metabolite carriers [280]. Ugo1 has an additional extended intrinsically disordered domain in the middle of the sequence (residues 143 to 227). Ugo1 NH₂ terminus has been showed to face the cytosol while its COOH terminus faced the intermembrane space [108]. The experimental description of the SLC26A46 termini localization has not been reported in literature yet. That being said, the interactions between the proteins involved in mitochondrial dynamics, such as mitofusins, and those solute carriers has been previously described [108, 109, 110, 280, 279, 276, 277]. Consequently, we decided to study the oligomers of mitofusins and these mitochondrial solute carriers.

Tetramers involving two mitofusins and two solute carriers yielded the most interesting results and are showed in Figure 6.6. Interestingly, the presence of these solute carriers impacts the predicted structures of the associated mitofusins. First and foremost, both Ugo1 and SLC25A46 are localized on the same level as the TM domains on the mitofusins involved (showed in Figure 6.6A, D, E, H). Consequently, the structure of the TM domain of mitofusins is the most impacted. In the absence of solute carriers, the transmembrane (TM) domain of mitofusins appears to be unfolded and/or less compact. However, with the presence of Ugo1/SLC25A46, a more compact conformation of the domain is evident (Figure 6.6B, F, G and I). In Fzo1, although a structure of two TM helices separated by a loop is not observed, an α -helix secondary structure is present throughout the TM domain. Notably, a kink is located on the Lys716 of Fzo1 TM1, which can be observed as well in TM1 of Mfn1 and Mfn2 (models of Figure 6.6E and H) on respectively Arg595 and Arg614. Nonetheless, the model of Figure 6.6D (2 Mfn1 with 2 SLC25A46) seems to lean toward a more continuous structure of TM1. None of the models presented here show interactions between TM1 and TM2 of the mitofusins.

Secondly, the other impact of the solute carriers on the structure of mitofusins is the type of dimerization between the mitofusins. In fact the Mfn1 and Mfn2 homodimers (Figure 6.6D and E) now present a cross-type of dimerization, which was not observed in the previous section (Figure 6.3). However, AF produced diversity in the conformation of these tetramers. While they all showed an intersection in the HR coiled-coil, certain models had their GTPase domains dissociated (as observed in the (2)Mfn2-(2)SLC25A46 tetramer, Figure 6.6E). This dissociation has also been noted in other models of (2)Mfn1-(2)SLC25A46 (results not shown here). Furthermore, diversity of conformation was also observed in the positioning of SLC25A46, as it seemed to have troubles in positioning the protein in the plane of the membrane (the various conformations of each tetramers are not shown here). Nevertheless, when combining Mfn1 and Mfn2 with two SLC25A46, we consistently obtain a GTPase dimerization and the two solute carrier aligned with the membrane plane and the two Mfn1 and Mfn2 TM domains.

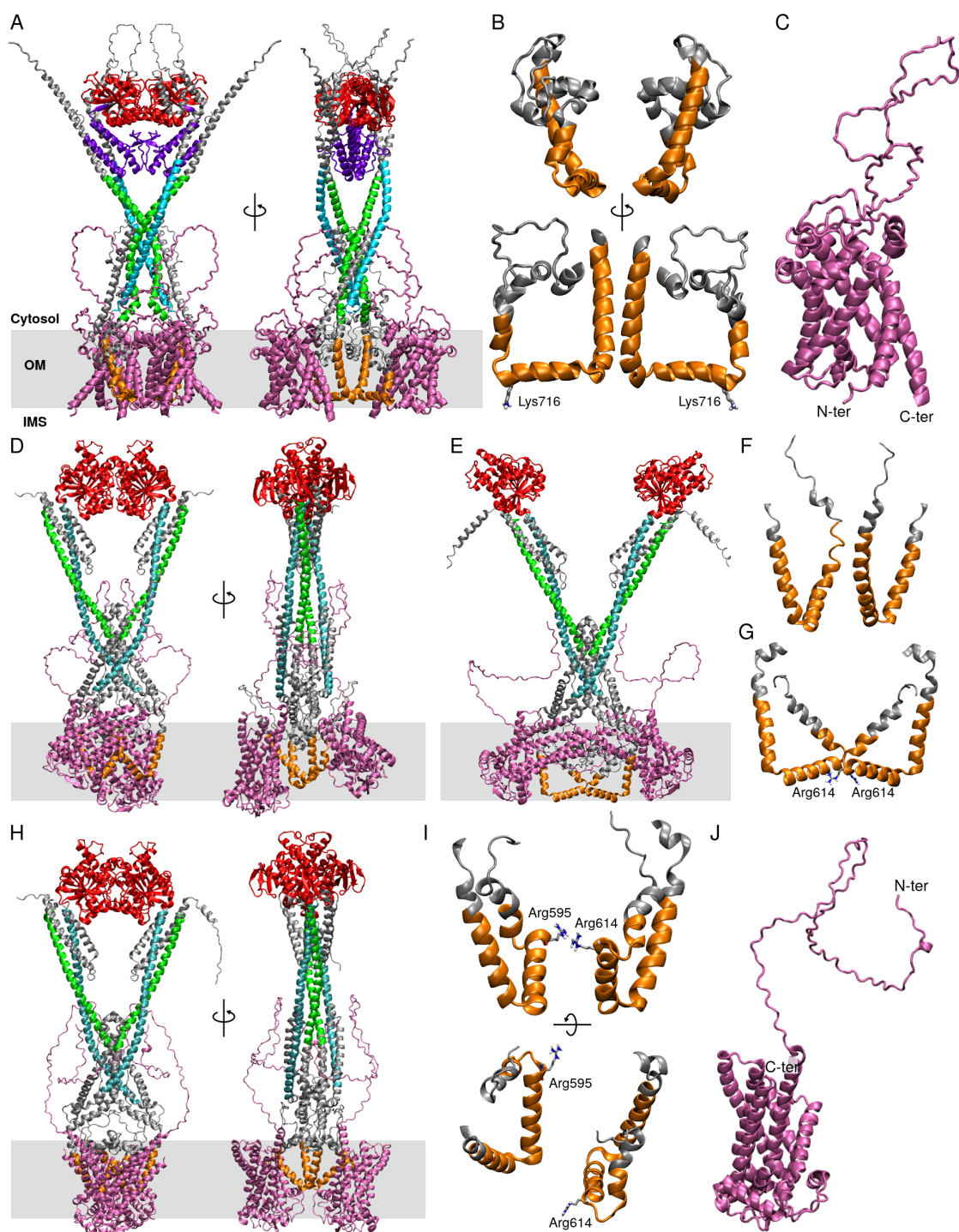


Figure 6.6: AF tetrameric models of mitofusins and solute carriers Ugo1/SLC25A46. (A) Tetradimeric model of two yeast mitofusins Fzo1 (without the first 60 intrinsically disordered residues) and two Ugo1 (without the first 100 intrinsically disordered residues). Fzo1 is colored as a function of its domains, defined in Figure 6.1B. The unassigned sections of the proteins are colored in grey. The two Ugo1 monomers are represented in magenta. The membrane position is represented with a grey stripe. (B) Zoom on the model in (A) showing the conformation of two Fzo1 TM domain. Flanking residues to the TM domain are shown in grey. (C) Zoom on the model in (A) showing the conformation of Ugo1. (D) Tetrameric model of two yeast mitofusins Mfn1 and two SLC25A46. Mfn1 is colored as a function of its domains, defined in Figure 6.2B. The unassigned sections of the proteins are colored in grey. The two SLC25A46 monomers are represented in magenta. (E) Same as (C) but with Mfn2 instead of Mfn1. The residues of the two Mfn2 are colored as a function of Mfn2 domains defined in Figure 6.2F. (F) Zoom on the TM domains of Mfn1 monomers in (D). (G) Zoom on the TM domains of Mfn2 monomer in (E). (H) Tetrameric model containing Mfn1, Mfn2 and two SLC25A46. The coloring of each monomers is conform with the previous panels. (I) Zoom on the mitofusins TM domain. (J) Zoom on one of the SLC25A46 monomers.

Finally, it can be noticed that Ugo1 N-termini (corresponding to the residue 101 of Ugo1 sequence) is in fact located on the intermembrane space(IMS), which is unexpected, as the opposite was described by Sesaki and collaborators in 2001 [108]. However, we are lacking the first 100 amino acid in our model, as they are intrinsically disordered. Furthermore, the C-term is in fact on the IMS side which is coherent with the experimental data [108]. The second extended intrinsically disordered domain of the protein is located on the cytosol side of the membrane, and seem to interact with the HR domains. Similarly, the N-termini disordered section of SLC25A46 is interacting with the human mitofusins coiled sections. In fact, some of the closest contacts between the mitofusins and their solute carriers involve the intrinsically disordered sections of those solute carriers (described in Supplementary Table S6.3). It can be noted that the position of Ugo1 in interaction with Fzo1 seems to be the reverse of the position of SLC25A46 in interaction with Mfn1/2. No significant changes were observed in the nearest contacts (within 2Å) between mitofusin monomers.

6.4 A specific MSA provides additional insights into TM domain interactions and structure prediction

In this last section, we decided to investigate more Fzo1 TM domain through AF predictions. In fact, AF models present strong limitations in modeling the mitofusins, as first and foremost, the two TM helices of mitofusins are predicted as fully or partially unstructured in the absence of Ugo1. However, even in the presence of the solute carrier, TM1 and TM2 are not interacting with one another, contrary to our expectations and predictions (see Section 3). In fact, residues located within the plane of the membrane (Figure 6.6B) exceed the range of residues defined as transmembrane by Fritz and collaborators in 2001 [99].

Hence, we decided to test two protocols: first a custom MSA, and second a prediction involving Ugo1 and Fzo1 without its GTPase domain. The second protocol is presented in Section 3, and in Figure 6.7 is presented the other set of models produced using an MSA composed of 48 sequences of fungal species (see Supplementary Table S6.1). This MSA is particularly well aligned on the TM domain of Fzo1 (Supplementary figure S6.1). In this figure can be observed one of the conformations produced: two helices in the TM domain are shown corresponding to TM1 and TM2, evidently interacting with one another. It can be noted that the TM domain produced show a diversity of conformations (Figure 6.7A). However, the residues involved in interactions are similar to ones described previously in Section 3 and Figures 3.3 and 3.5. These interaction are shown for the second ranked model in Figure 6.7, however all conformations show similar sections of the helices involved. It is interesting to note that the dimer obtained with this custom MSA proposed a cross-type cis-dimer without interactions in the GTPase domain (result not shown), similar to the previous predictions in Figure 6.5E.

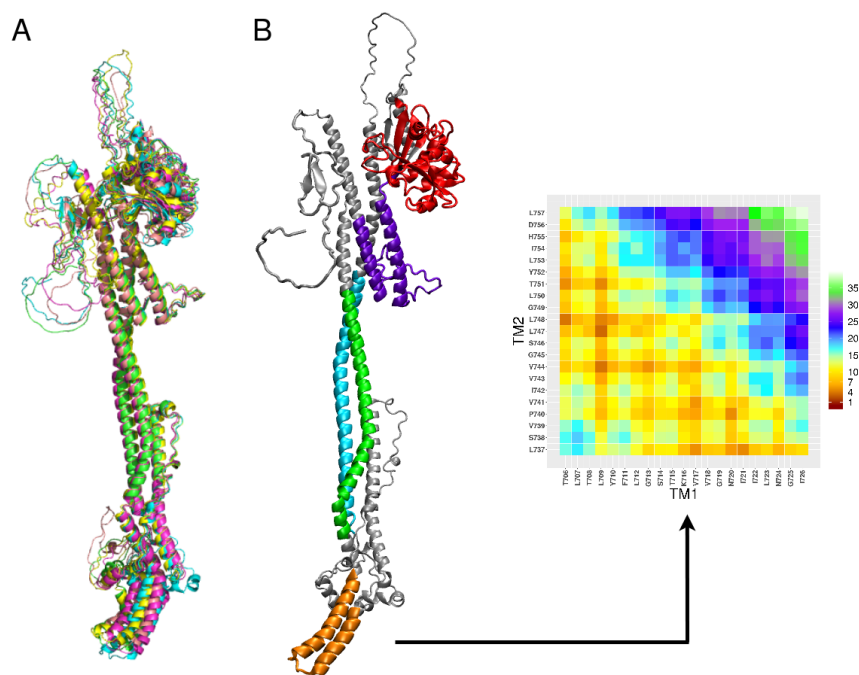


Figure 6.7: **Models produced with AF provided with a custom MSA.** (A) Superposition of 5 models produced by AF. (B) Left, 2nd ranked model colored as a function of domains, previously described in Figure 6.1. Right, contact map between TM1 and TM2.

Two conclusions can be drawn from these observations. First, when AF is given a more specific alignment, it converges (i) onto a two helices type of TM domain (with interactions between the two helices), and (ii) with our TM domain model. In fact, removing the GTPase domain most probably allowed AF to find sequences for the MSA better aligned with the TM domain, similar to our custom MSA. However, it is important to note that the results of the prediction is drastically different without Ugo1 in the system and the TM domain is partially intrinsically disordered (similar to the full Fzo1 dimer predictions, results not shown). These results underline that a variation of conformations can be obtained with AF, when parameters are adapted to the specific case studied. Nevertheless, as observed previously, all conformations are open. These observations underline that conformational diversity can be observed in local domains of mitofusins, but large-scale conformational transition can be more complicated to obtain.

6.5 Conclusion

In this Chapter, we extensively studied the modelization of mitofusins through the use of AlphaFold. Monomers, dimers and tetramers involving fusion partners Ugo1/SLC25A46 were produced and analysed. While AF is rarely able to provide conformational diversity for one given model, we obtained variations of structures by changing the mitofusins environment.

Each model produced showed mitofusins in an open conformation, and an absence of hinges in coiled structures, in opposition to the bacterial homologue BDLP [65, 68]. Moreover, the dimers and tetramers

displayed unique interactions among mitofusins, implicating the HR domains and resulting in a cross-type cis-dimerization, which contrasts with the homologous BDLP. This might be attributed to the relatively low similarity (about 43% [1]) between BDLP and mitofusins, leading to structural differences. However, it's worth noting that the low-resolution structure of the open conformation of BDLP could also play a role. Given the advancements in electron microscopy (EM), there is potential to revisit and improve the structure. Interestingly, the tetramers involving the mitochondrial solute carriers SLC25A36 (humans) showed that these inter-protein HR interactions are possible between any combination of mitofusins.

Nevertheless, the models produced by AF necessitate important conformational changes in order to fully drive OM fusion. This implies that AF produces only a fraction of the conformations that these proteins can adopt. This issue could be attributed to the lack of structural information related to mitofusins in the PDB.

6.6 Appendix

Species	Gene ID	NCBI Accession Number	Alignment Length	Identity (%)
<i>Saccharomyces paradoxus</i>	54628961		855	93.450
<i>Saccharomyces kudriavzevii</i>	80922466		855	88.070
<i>Saccharomyces uvarum</i>		WBF12004.1	855	85.965
<i>Saccharomyces eubayanus</i>	28930342		855	86.082
<i>Saccharomyces pastorianus</i>		QID84352.1	855	85.848
<i>Saccharomyces arboricola</i>		EJS44778.1	855	86.901
<i>Saccharomyces mikatae</i>	80916627		855	89.123
<i>Torulaspora delbrueckii</i>	11502587		854	55.504
<i>Naumovozya dairenensis</i>	11496578		867	55.017
<i>Naumovozya castelli</i>	11525200		860	55.116
<i>Zygosaccharomyces rouxii</i>	8205611		863	53.187
<i>Torulaspora globosa</i>	59323954		843	53.737
<i>Zygotorulaspora mrakii</i>	59238749		845	55.621
<i>Zygosaccharomyces mellis</i>		GCF01234.1	842	53.800
<i>Zygosaccharomyces parabailii</i>		AQZ09951.1	837	55.197
<i>Kazachstania saulgeensis</i>		SMN19588.1	894	50.783
<i>Nakaseomyces glabratus</i>	2891667		861	52.149
<i>Kazachstania barnettii</i>	64856637		892	51.345
<i>Kazachstania africana</i>	13883486		863	52.028
<i>Eremothecium cymbalariae</i>	11471225		830	52.892
<i>Kazachstania exigua</i>		KAG0667837.1	866	50.924
<i>Lachancea lanzarotensis</i>	34685323		861	50.290
<i>Ashbya aceris</i>		AGO10664.1	840	51.190
<i>Lachancea dasiensis</i>		SCU84805.1	841	51.011
<i>Zygosaccharomyces bailii</i>		SJM85540.1	781	55.698
<i>Eremothecium gossypii</i>	4619254		842	50.950
<i>Lachancea thermotolerans</i>	8292224		837	51.135
<i>Lachancea nothofagi</i>		SCU94789.1	839	51.013
<i>Kazachstania unispora</i>		KAG0656311.1	917	48.637
<i>Lachancea sp. 'fantastica'</i>		SCU87952.1	837	50.060
<i>Kazachstania naganishii</i>	34523668		853	50.645
<i>Lachancea meyersii</i>		SCV03020.1	837	51.732
<i>Lachancea quebecensis</i>		CUS23951.1	837	50.179
<i>Lachancea fermentati</i>		SCW03635.1	847	51.712
<i>Eremothecium sincaudum</i>	28724097		779	51.220
<i>Kluyveromyces dobzhanskii</i>		CDO95175.1	791	51.327
<i>Kluyveromyces lactis</i>	2894339		786	50.382
<i>Kluyveromyces marxianus</i>	34714445		790	50.759
<i>Tetrapisispora phaffii</i>	11532272		824	49.029
<i>Tetrapisispora blattae</i>	14497819		896	42.299
<i>Saccharomycodes</i>	70107361		793	43.253
<i>Hanseniaspora osmophila</i>		OEJ83133.1	805	40.870
<i>Hanseniaspora valbyensis</i>		OBA27200.1	676	35.947
<i>Hanseniaspora opuntiae</i>		OEJ81218.1	760	33.684
<i>Hanseniaspora guilliermondii</i>		SGZ40984.1	760	33.289
<i>Hanseniaspora uvarum</i>		OEJ90379.1	743	32.840

Supplementary Table S6.1: **Summary table of the sequences selected for a custom alignment.** When Gene ID could not be retrieved, the NCBI Accession Number was written instead. Identity stands for amino acid identity. The percentage of identity with the mitofosin Fzo1 of *Saccharomyces Cerevisiae* is written in the last column.

Saccharomyces cerevisiae	SKIPTLTLTYFLGSTKVVGNIIINGIKLSSWSSLKLLSVPVIVVGSLLGLTYLIHDLPRAL
Saccharomyces paradoxus	SKIPTLTLTYFLGSTKVVGNIIINGIKLSSWSSLKLLSVPVAVVGSLLGLTYLIHDLPRAL
Saccharomyces kudriavzevii	SKVPTLTLTYFLGSTKVVGNIIINGIKLSSWSSLKLLSIPVIVVGSLLGITYLIHDLPRAL
Saccharomyces uvarum	SKIPTLALTYFLGSTKIVGNIVLHGIKLSSWNSLKKLSVPIIVVGSLLGITYLIHDLPRAL
Saccharomyces eubayanus	SKIPTLTLTYFLGSTKVVGNIVLNGIKLSSWNSLKKLSVPIIVVGSLLGITYLIHDLPRAL
Saccharomyces pastorianus	SKIPTLTLTYFLGSTKVVGNIVLNGIKLSSWNSLKKLSVPIIVVGSLLGITYLIHDLPRAL
Saccharomyces arboricola	SKIPTLTLTYFLGSTKIVAGSIILNGIKLTSWNSLKKLSIPVIVVGSLLGITYLIHDLPRAL
Saccharomyces mikatae	SKIPTLTLTYFLGSTKVVGNIIINGIKLSSWSSLKLLSVPVIVVGSLLGITYLIHDLPRAL
Torulaspora delbrueckii	SKLPTLALYSFSGSVKVLRDVVLHGVQFSWHTFKRVSGSLLLLGGLLGAVYLIHDLPRAL
Naumovozyma dairenensis	SKVPALVVYSFGGAKIVGNLIINGITTFSWRTLGVVSGSILVITSLLGVAYFIHDLPRAL
Naumovozyma castellii	SKLPTLALYSFGGARLAGTVIINGLSTFSWKSGLGSLAII LCSLLGAAYFINDLPRAL
Zygosaccharomyces rouxii	SKIPTLAVYSVGGAKLMRNVIQGVQFFSWSTIKRISGSLLVIGTVLGAAYLVHDLPRAL
Torulaspora globosa	SKVPTLAVYSFSGSVKILRNVLQGFQFFSWNTIRRVSGSLLVLGGLLCAAYLIHDLPRAL
Zygotorulaspora mrakii	SKIPTLAVYSVGGANVMKMMVHGFQFFSWQTIKRISGSLLLIGGLLVGAYLVHDLPRAL
Zygosaccharomyces mellis	SKIPTLAVYSLGGAKLLRNIIQGVQFFSWSTIKRISGSLLMVGTLLGVTVLHDLPRAL
Zygosaccharomyces parabaillii	SKIPTLAVYSFGGARVLRGVVIHGVOFFSWGAIKRIGGSVLFVGSLLSLAYLVHDLPRAL
Kazachstania saulgeensis	SKLPALAIYSFGGSKIVTTVIFNGLSAFWSKSLGQIAGSVVFAGSLLGMAYIIVYDIPRAL
Nakaseomyces glabratus	SRLPTMAIYSVGGSKLMSNIAYNGLRLTSVNSLKKIASPLLIASLLGVAYLIHDLPRAL
Kazachstania barnettii	SKLPALAIYSFSGGSKIATTVIFNGLSAFWSKSLGQIAGSVVIAAGSLLGMAYIIVYDIPRAL
Kazachstania africana	SNLPFAIYSFGGSKIIISNVIIINGISSISAKSLELLSGYLLLVGGCLLSVSYLIHDLPRAL
Eremothecium cymbalariae	SKIPTLAIYSYGGVKNVNFLLYGRFFFTWQSFKKLSTSFVLIGSVLGIAYLISDLPRAL
Kazachstania exigua	SKLPALAIYSLGGSKIITTIIFNGLISSFSLKSLGQITGSIVAFGSLLGVAYLIYDIPRAL
Lachancea lanzarotensis	SKIPALAVYSWGGTRVFTTILFYGSRFFSWQAVSRLSSSALLIGSVMGIAYLVHDLPRAL
Ashbya aceric	SRIPALALYSYGGVIVTNILLYGRFFFSWQSLRKLSTSLLLVGSALGAAYIVSDLPRAL
Lachancea dasiensis	SKIPALAVYSWGGTRVLTAMIHGSRFFSWQAFSRIISTSIILVSSVLGVSYLHDLPRAL
Zygosaccharomyces baillii	SKIPTLAVYSFGGARVLRGVVIHGVOFFSWGAIKRIGGSVLFVGSLLSLAYLVHDLPRAL
Eremothecium gossypii	SRIPALAVYSYGGVKNVNFLLYGRFFFSWQSLRKLSTSLLLVGSALGAAYIISDLPRAL
Lachancea thermotolerans	SRIPALAVYSWGGARVLSNIVLYGSRFFFTWQSI TRASSSVLLVGTVLGAAYLIHDLPRAL
Lachancea nothofagi	SKIPALAVYSWGGARVITTVFYGSRFFSWQALRRISSSLLLVGSILGTAYLIHDLPRAL
Kazachstania unispora	SKLPTLAIYSFGGSKIVKTLWNGVQTFSIKTLGKIAGSTVVIIGCLLVGVSYLIVYDIPRAL
Lachancea sp. 'fantastica'	SKIPALAVYSWGGTRVFTTILVYGSKFFSWHAFSRLSSSVLVLGSLVGIAYLVHDLPRAL
Kazachstania naganishii	SKLPALAIYSLGGVRLVSTMVNLGLTFSVRTLARVSGSVLLLGSLLVGVSYLIVYDIPRAL
Lachancea meyersii	SKIPALAVYSWGGTRVFTTIVLMYGSRFFSWHSLTRLSSSVLLLVGSVMGIAYLIHDLPRAL
Lachancea quebecensis	SRIPALAVYSWGGARVLSNIIYGSRRFFTWQSI TRASSSVLLVGTVLGAAYLIHDLPRAL
Lachancea fermentati	SRIPTLAVYSWGGAKFLTNIAIYGTKFFSWQSLRRMSTSIILIGSILGIAYLIHDLPRAL
Eremothecium sinecaudum	SKIPALAVYSYGGVKNVNFLLYGRFFFTWQSIKRLSTSVLLIGSVLGVAYLISDLPRAL
Kluyveromyces dobzhanskii	SKIPTLLVYSFSGGSKMITNVIHGSKFFSFESLKKLSGSLALLGGVLGVAYLIHDLPRAL
Kluyveromyces lactis	SKIPTLLVYSFSGGSKMITNIVLHGSRFFSLESKLLSGSLVLLGGVLGIAYLIHDLPRAL
Kluyveromyces marxianus	SKIPTLLVYSFSGGSKMITNIVLHGSRFFSLESKLLSGSLVLLGGVLGIAYLIHDLPRAL
Tetrapisispora saffhii	SGLPALAVYSVGSVKVIGSVLNLQFFSWNSFKSMIIPFTASCLFLGTTYLIHDLHRAL
Tetrapisispora blattae	SKIPAMAVYSVGGAKALESILFNKIKFFSWDIIKHSIGPIFLTASVLAAYLIQDISRAV
Saccharomycodes	SKIPTLFMYSFGGAKILTNIIFYGTQIFSLQALKNIIGGSLLLIGSCLSAAYLVHDLPRAL
Hanseniaspora osmophila	SKIPSLLVYSLGGAKLIVNVLMYGASLFSWSAMKNIGSTVVLIGGSLGCAYLINDLPRAL
Hanseniaspora valbyensis	SRIPTLALYSLGGSKIINLMVYGSMLTWSITNIATTLATSGCLVGAYLINDLPRAL
Hanseniaspora opuntiae	SRIPTLALYSLGGSKIIISNIFYGSSFLSWSIINLTSTLAATGGCLVGAYLVXDLPRAL
Hanseniaspora guilliermondii	SRIPTLALYSLGGSRIIISNIFYGSSFLSWSIINLTSTLAATGGCLVGAYLISDLPRAL
Hanseniaspora uvarum	SRIPTLALYSLGGSKIIISNIFYGSSFLSWSIIVNLTSTLAATGGCLVGAYLISDLPRAL

Supplementary Figure S6.1: **TM domain alignment of the mitofusins used for the custom MSA.** Here is the TM domain alignment of the custom MSA. Each predicted TM helix is represented as an orange rectangle.

A			B		
Fzo1 - M1	Fzo1 - M2	Distance	Mfn1 - M1	Mfn2 - M2	Distance
LYS141	LYS141	1.863	SER85	GLU230	1.746
LYS141	ASP143	1.659	ILE105	GLU266	1.822
ASP143	ASN139	1.955	HIS107	GLU266	1.687
ASP143	LYS141	1.631	HIS144	GLU272	1.686
LYS163	ASN155	1.990	ALA145	GLN276	1.868
ASN197	GLU344	1.758	HIS147	GLU272	1.918
ASP216	ARG380	1.852	ASP183	GLN235	1.763
GLN217	ARG376	1.904	ASP183	THR236	1.643
ASN318	LEU349	1.902	THR186	GLN235	1.844
GLU344	ASN197	1.909	GLU209	SER106	1.705
ASN345	ASN345	1.836	GLU209	ARG259	1.751
LEU349	ASN318	1.895	THR211	THR105	1.909
LYS352	MET319	1.730	ASN214	ASP204	1.744
LYS374	GLN217	1.867	THR215	ASP204	1.717
ARG380	ASP216	1.591	ARG238	GLU230	1.685
ASP523	ARG795	1.600	GLU245	ILE126	1.774
ASP523	ARG799	1.590	GLN255	ALA166	1.975
GLU527	ARG795	1.643	ARG259	GLN169	1.982
ARG799	ASP523	1.603	ILE496	GLN701	1.841
ARG803	GLU806	1.663	ASP502	HIS686	1.860
ARG803	ASP810	1.599	ASP502	GLN690	1.814
GLU806	ARG803	1.785	SER504	ASN683	1.844
ASP810	ARG803	1.646	SER660	LEU528	1.937
			THR661	TYR679	1.900
			ASN664	ASN525	1.954
			GLN671	SER523	1.804
			GLN682	MET515	1.834

Supplementary Table S6.2: **Distances in Å between the closest residues of mitofusins monomers in mitofusins dimers.** (A) Residues at a distance lower than 2Å of the Fzo1 homodimer AF model. (B) Residues at a distance lower than 2Å of the Mfn1-Mfn2 heterodimer AF model. Lines colored in grey represent the salt bridges.

A - (2)Fzo1-(2)Ugo1

Fzo1	Ugo1	Distance
VAL615	PRO189	2.100
ARG617	PHE187	1.916
ARG617	GLU191	1.592
LYS624	GLU182	1.776
LYS624	GLU183	2.888
ARG625	GLU182	1.583
LYS631	ASP165	1.908
ARG632	ILE162	2.060
ARG632	ARG164	2.922
LEU637	ASP238	1.823
ILE639	ASN234	1.844
LYS736	LYS501	2.883
THR520	GLU184	1.935

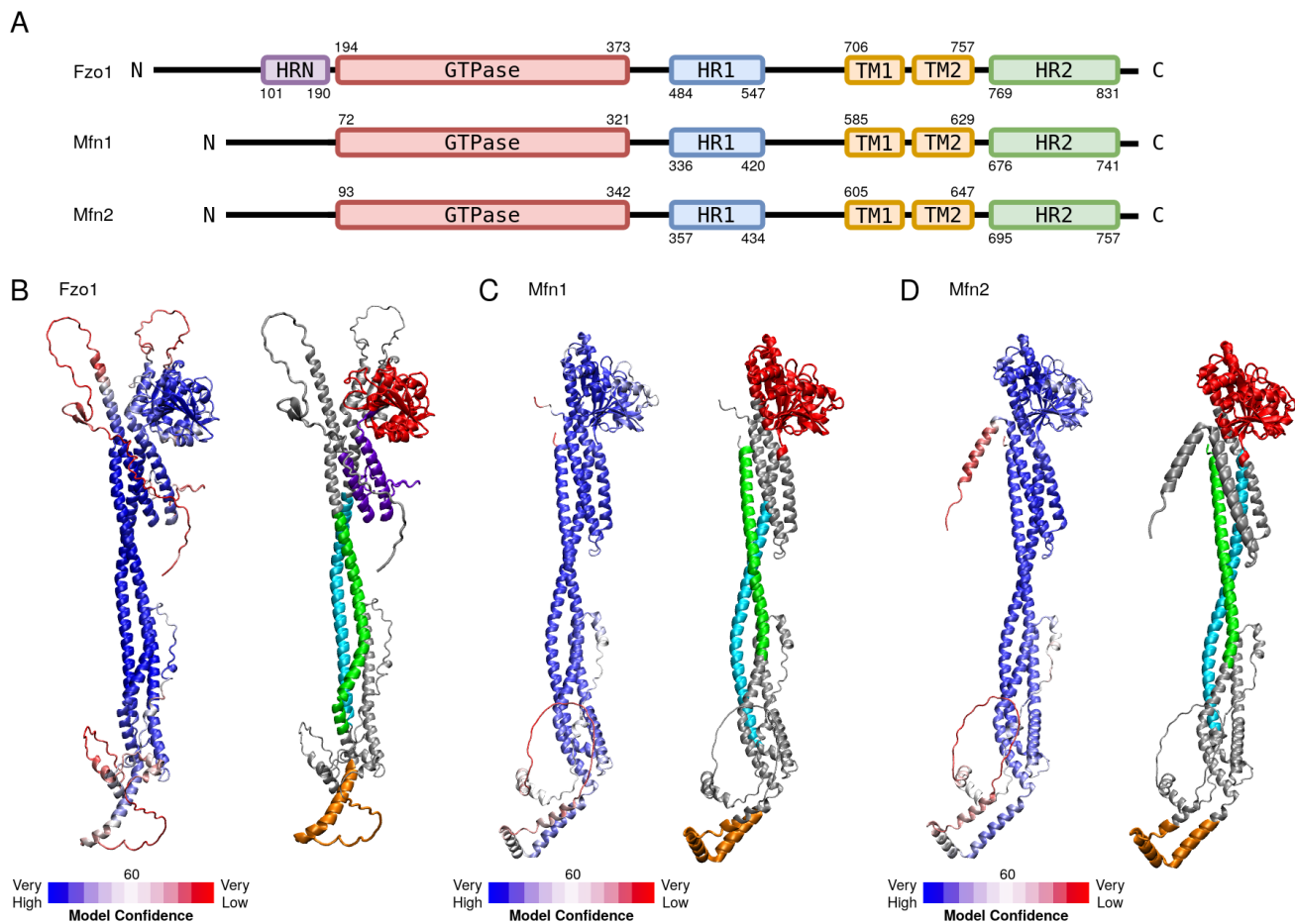
B - Mfn1-Mfn2-(2)SLC25A45

Mfn1	SLC25A46	Distance
LYS608	GLY235	1.784
ARG455	ARG15	2.917
ARG594	GLU177	1.559
GLU579	GLN96	1.727
LYS608	GLY235	1.784
PHE553	GLU182	2.002
ARG594	LYS206	2.073
GLU578	GLN96	2.256
GLU579	GLN92	2.552
THR592	GLU316	2.737
ILE552	GLU182	2.835
ILE582	ARG99	2.969
THR592	GLN283	2.990

C - Mfn1-Mfn2-(2)SLC25A45

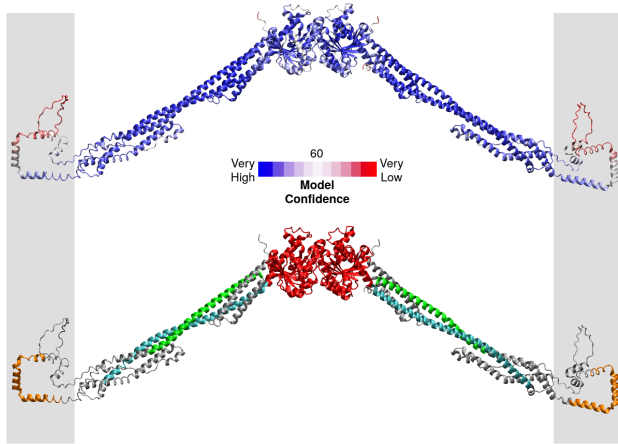
Mfn2	SLC25A46	Distance
ARG613	GLU189	1.646
ARG613	GLU177	1.801
GLU598	ARG99	1.946
VAL601	ARG99	2.564
ARG519	ARG5	1.696
ARG476	ARG15	1.782

Supplementary Table S6.3: **Distances in Å between monomers of the tetramers.** (A) Residues at a distance lower than 3Å for Fzo1-Ugo1 in the (2)Fzo1-(2)Ugo1 tetramer AF model. (B) Residues at a distance lower than 3Å for Mfn1-(2)SLC25A46 of the Mfn1-Mfn2-(2)SLC25A46 tetramer AF model. (C) Residues at a distance lower than 3Å for Mfn2-(2)SLC25A46 of the Mfn1-Mfn2-(2)SLC25A46 tetramer AF model. Lines colored in grey represent the salt bridges.

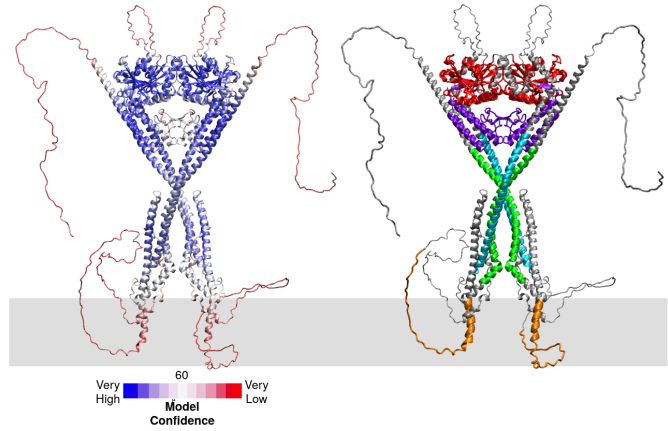


Supplementary Figure S6.2: **AlphaFold monomeric models of mitofusins.** (A) Schematic representation showing the domains organization of mitofusins. GTPase domain in red; HR1/2, heptad repeat 1/2 in blue/green; HRN in purple; TM, transmembrane region in orange. Borders of each element are indicated by residue numbers. (B) Left, Fzo1 AlphaFold model colored as a function of pLDDT score. Right, Identical model colored as a function of the domains. (C) Left, Mfn1 AlphaFold model colored as a function of pLDDT score. Right, Identical model colored as a function of the domains. (D) Left, Mfn2 AlphaFold model colored as a function of pLDDT score. Right, Identical model colored as a function of the domains.

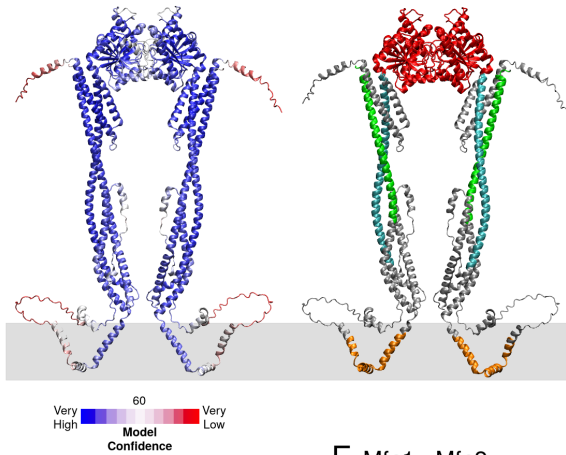
A Mfn1 - dimer



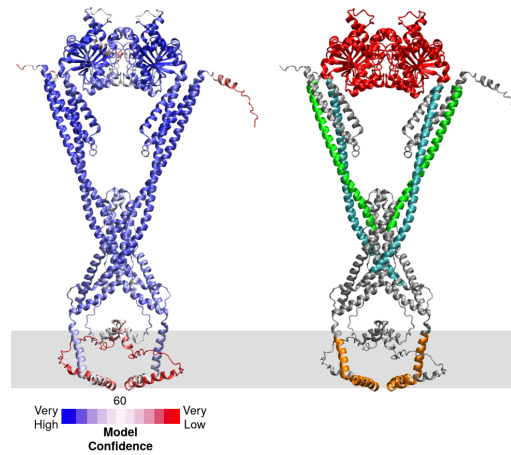
B Fzo1 - dimer



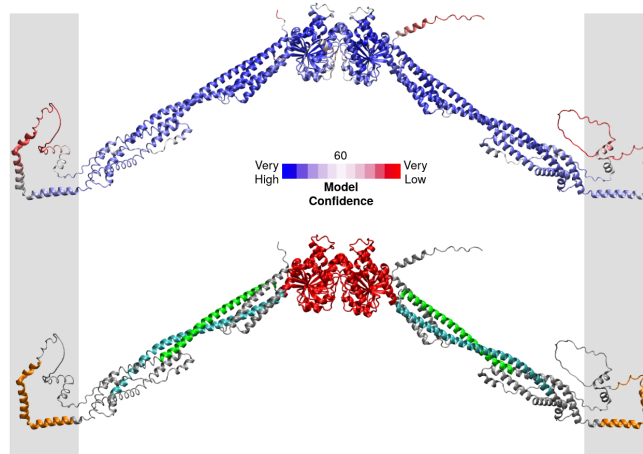
C Mfn2 - dimer



D Mfn1 - Mfn2



E Mfn1 - Mfn2



Supplementary Figure S6.3: **AlphaFold oligomeric models of mitofusins.** (A) Left, AF model of Mfn1 homodimer colored as a function of pLDDT score. Right, identical model colored as a function of the domains. (B) Left, AF model of Fzo1 homodimer colored as a function of pLDDT score. Right, identical model colored as a function of the domains. (C) Left, AF model of Mfn2 homodimer colored as a function of pLDDT score. Right, identical model colored as a function of the domains. (D) Left, AF model of Mfn1 and Mfn2 cis-dimer colored as a function of pLDDT score. Right, identical model colored as a function of the domains. (E) Left, AF model of Mfn1 and Mfn2 trans-dimer colored as a function of pLDDT score. Right, identical model colored as a function of the domains.

CHAPTER 7

CONCLUSION

The diverse projects within this Ph.D can be categorized into distinct phases focused on the study of mitofusins: the TM domain of Fzo1, the amphipathic helix of the Mfn1 HR1 domain, and the overall structure of the yeast mitofusin Fzo1. A significant portion of the Ph. D duration was dedicated to investigate the TM domain of Fzo1. Through this study, structural insights on this TM domain was acquired, as well as understanding of the MARTINI force-fields. With this knowledge, we were able to test the MARTINI force-fields on amphipathic helices (AH) systems and assess their predictive accuracy in peptide-membrane interactions. This first work on AH was followed by a thorough characterization of the AH of the HR1 domain of the human mitofusin Mfn1, carried out using all-atom simulations. These structural analyses of various mitofusins domains allowed us to propose various functional roles associated to these domains. finally, we also studied the overall structure of Fzo1 using the AlphaFold tool, described in Chapter 6. In depth analysis of monomeric, dimeric and tetrameric conformations involving yeast and human mitofusins with their fusion partners was carried out.

7.1 Production of a TM domain structure fitting mitofusins small loops

Chapter 3 focused on the TM domain of Fzo1. When the first model of Fzo1 was produced in 2017 [1], the PREDDIMER webserved was used in order to produce multiple conformations of the two TM helices (TM1 and TM2). However the structure produced for Fzo1 TM domain had not been validated through either massive conformational sampling or experimental data. In this chapter, our primary objective was to generate a substantial number of conformations to evaluate and identify the most probable structure. We decided to not investigate the energy of association between these two helices TM1 and TM2 as they are linked by a loop, which induces a close distance between them and significantly modifies the energy of interaction between the helices alone. Additionally, a specific focus was given to Lysine 716, a peculiar residue for a TM region, and given its position in the first helix TM1, this titrable residue is most likely placed in the middle of the membrane. The pKa of the residue changes in the membrane, resulting potentially in a neutral residue at pH = 7. As the hydrophobic center of the membrane is an unfavourable environment for charged residue, we decided to test whether the residue was charged or neutral. Using the MARTINI family of force-fields, numerous conformations were produced for both a charge and neutral Lys716. Parameters such as crossing angles, contacts between the two helices and analysis such as a clustering were used to assess the most representative conformations produced. This sampling revealed that the presence of a protonated Lys716 disrupted stability within the interactions between the helices TM1 and TM2, as well as within the membrane. In fact the protonated state disturbed the integrity of the peptide within the membrane, which often resulted in the surprising event of the peptide exiting the membrane. The neutral Lys716 simulations converged toward one main conformation, which was used for the following refinement steps. As MARTINI2 and MARTINI3 showed similar predictions, the structure produced by the latest version of the force-field was used. A Temperature Replica-exchange was used for a refinement step, during which slight changes were observed in the interactions between

the two helices. An overall hairpin TM structure was found, with the helices presenting an anti-parallel left-handed dimerization. This final structure was confirmed with the tool AlphaFold, by predicting the structure involving a portion of Fzo1 and its partner Ugo1 or by using a custom MSA for AF prediction (see Section 6.4). Minimal interactions were detected involving Lys716; nevertheless, we did observe proximity between the Lys716 of different monomers. This suggests that the residue might play a role in the dimerization process of Fzo1.

In this first result chapter, an hairpin structure of the TM domain was found. This structure is actually quite similar to the structure observed in the paddle domain of BDLP. Furthermore, while Fzo1 presents 10 amino-acids between the two helices, the human homologues Mfn1 and Mfn2 do not have as many residues between TM1 and TM2. The hairpin structure may likely accommodate this specific constraint. In addition, the conformation was predicted by Huang et al. 2017 [134] for both atlastins and Mfns. This hypothesis was explored using the homology method MODELLER [281, 282, 283] and can be observed in Figure 7.1. This preliminary study shows as expected similar structures between the mitofusins, however for both human mitofusins a portion of TM1 and TM2 are predicted as a loop. These observations strongly suggest a need to reexamine the alignment used for the prediction. A T-REMD simulation could also be conducted for these novel models, much like the Fzo1-TM procedure, to assess its robustness and sample the most prominent structure.



Figure 7.1: Homology modeling of mitofusins transmembrane domains. (A) Sequence alignment of the TM domains of mitofusins Fzo1, Mfn1 and Mfn2. The TM domains are in yellow. The flanking residues before and after the TM domains are in orange. The same color scheme is conserved in the snapshots. (B) Fzo1 TM domain model produced in Section 3. (C) Mfn1 TM domain produced using the homology modeling method MODELLER (v10.4) [281, 282, 283]. (D) Mfn2 TM domain produced using the homology modeling method MODELLER (v10.4) [281, 282, 283].

Finally, an experimental protocol could be implemented for this section of the protein. As we predicted Fzo1 Lys716 as neutral in a membrane environment, it would be of interest to calculate this value experimentally, using titration experiments. This value could be predicted as well using simulations, with

the method explored by Maccallum et al. in 2003 [204], or using pH-replica exchange simulation, as studied by Panahi et al. in 2015 [206]. NMR experiments could be considered to solve the structure of these domains, which was initially planned at the start of the Ph.D project. These experiments would have determined the protonation state of Lys716 as well.

7.2 A first preliminary study of Mfn1-AH

Chapter 5 focused on the Mfn1-AH as well, using all-atom simulations. The study focused on an in-depth investigation of the behavior and interactions of Mfn1-AH with the membrane, using regular simulations and a T-REMD (REMD-helix). These simulations revealed some levels of AH induced disturbance as well as a more stable binding of the peptide in a membrane with PE than a full PC membrane. Furthermore, despite the high temperature conditions, the interactions with the membrane were maintained, demonstrating the robustness of Mfn1-AH bonding. Nonetheless, in the REMD-folding simulations where Mfn1-AH initiated in an unfolded state within the solvent, it was observed that the peptide exhibited reduced tendency for spontaneous docking. The very different results between REMD-helix and REMD-folding raises questions on the conditions favorable for the insertion of the peptide in the membrane. It was suggested that the helix played a significant role in preserving interactions between HR1 and the membrane, but less in the embedding itself. Furthermore, in the context of the protein itself, the AH would not be fully unfolded and would be linked to the membrane through the TM domain anchored to the membrane. In fact, a starting α -helix structure of the peptide might indeed facilitate embedding. To test this hypothesis, it would be interesting reproduce the protocol of the REMD-folding, with Mfn1-AH constrained to an α -helix structure. Further research is necessary to deepen our understanding of these mechanisms and their implications in cellular processes.

In fact, new all-atom regular simulations need to be run, as there is not enough sampling from our current simulations. Longer simulations, with more lipids for each layers are in fact necessary to study the packing defects, as well as the protrusions as a function of distances to the AH. Furthermore, in order to test with computer simulations the fusion inducing properties of Mfn1-AH, we would have to simulate the latter peptide in a two membrane environment. A similar protocol, involving the full HR1 domain and/or the TM domain could be implemented as well, following a method similar to the one introduced by Risselada et al. [154]. This protocol could be easily implemented using coarse-grained simulations. However, the latest version of the MARTINI force-field, MARTINI3, shows strong limitations, which will have to be overcome if we want to be able to build a protocol with this version of the force-field. The MARTINI2 version could however be tested in the meantime.

Finally, conducting *in vitro* studies on the peptide to evaluate its fusion abilities, as well as its binding to the membrane, is imperative. These experiments are currently carried out with our collaborator David Taresté.

7.3 This Ph.D work gave us valuable insights on the MARTINI3 force-field

The various analysis performed for the first project (Section 3) were able to build a strong basis for skills within the study of protein-membrane systems, as well as within the two MARTINI force-fields. While dimerizations of TM1 and TM2 showed similarities between the versions 2 and 3 of the MARTINI force-field, the first limitations of the MARTINI3 force-field were observed as well in this chapter, as TM1 was displaying the peculiar behavior of exiting the membrane. Furthermore, it's worth to note that this project reaffirmed the necessity for a refinement step for interactions predicted by MARTINI. In fact, as shown by Lamprakis and collaborators [238], the MARTINI3 force-field does not sample the experimentally evaluated interface of TM dimers as the global minimum, emphasizing the need for a critical evaluation of the models produced by MARTINI3. In most cases studied by Lamprakis et al., the predicted energies underestimated the experimentally calculated free energy of dimerization, which would explain how the dimerisation of Fzo1 TM1 and TM2 did not prevent TM1 exiting of the membrane.

Chapter 4 focused on the AH-membrane interactions, testing various lipid compositions. The main goal was to compare the AH-membranes interactions of the MARTINI2 and MARTINI3 force-fields. The first AH studied was the cell-penetrating peptide called penetratin. This peptide is known to enter cells either through endocytosis or translocation within the membrane. The capacity of the peptide to interact and bind to negatively charged membranes has been experimentally documented and investigated, while no interactions were shown with neutral membranes such as POPC [260]. Here, we studied the peptide interaction with POPC, POPG and POPS membranes. While the MARTINI2 force-field showed the peptide interacting with all three phospholipids, the MARTINI3 simulations showed opposite behavior of the peptide with neutral and anionic lipids. In fact, MARTINI3 reproduced the experimentally observed result: no binding was observed with PC membranes, while binding throughout the simulations involving anionic lipids. However, we were not able to draw any conclusions on the translocation mechanism of the peptide. The second AH studied is the amphipathic helix located in the HR1 domain of Mfn1. The overall HR1 domain was shown to interact with the membrane and induce fusion, and it is assumed that the AH contained herein participates in the interactions. The AH portion of the domain has only been studied in the context of the overall domain. Outside of the context of either the domain or the protein, the proposed membrane perturbation and fusion inducing capabilities of the peptide has not yet been investigated. With this peptide, the interactions predicted were again very different between the two force-fields: irreversible binding with MARTINI2, while barely any interactions were observed in the MARTINI3 simulations. However, the peptide was observed to interact more with an anionic membrane. These outcomes suggested by MARTINI3 are in direct contradiction with the experimental data related to Mfn1-AH [135]. The partitioning of the residues in the membrane was studied for both AH, and as expected, apolar residues were the most embedded residues of the sequences.

This Chapter clearly demonstrated that MARTINI3 has corrected the overestimation of hydropho-

bicity observed in the MARTINI2 force-field. However, as shown in Chapters 3 and 4, the newest version MARTINI presents a number of shortcomings. First, an underestimation of TM-membrane and AH-membrane interactions was observed in the first two results chapters. This new behavior could be explained by the change in backbone bead described in Section 2.2. In fact, the helices are not described by a neutral bead in MARTINI3, as all of the backbone is composed of polar beads, promoting hydrophilic interactions. MARTINI developers are currently working on this issue. Furthermore, very different dynamics within the membranes were observed: a decrease of membrane thickness was observed in penetratin simulations, as well as an increase of area per lipids, protrusions and packing defects in all MARTINI3 systems studied in both Chapters 3 and 4. In addition, the DOPE effect on membrane thickness and APL is opposed to the tendency observed in all-atom and MARTINI2 simulations. These significant alteration in lipid behavior and protein-membrane interactions should be taken into careful consideration. The membrane behavior could be studied further using membrane only systems with more lipids per leaflet and by confronting the results against all-atom simulations and experimental data. The current protocol lack sampling necessary to correctly assess these membrane dynamics parameters (which explains the error bars, which should be smaller).

The all-atom simulations proposed in chapter 5 provide results opposed to the AH-membrane interactions predicted by the MARTINI3 simulations in Chapter 4. In fact, Mfn1-AH stays binded to the membrane throughout the 300 ns regular simlations and the 500 ns of the 35 replica of REMD-helix, while the MARTINI3 simulations show the peptide exiting the membrane within the first ns. Furthermore, the REMD-folding did show interactions of the peptide with the membrane, as well as one replica partitioning into the membrane. It is crucial to emphasize as well that the area per lipid and the packing defect constant π demonstrated values much more aligned with the MARTINI2 simulations than the MARTINI3 of Section 4. These results show that the membrane dynamics simulated with the MARTINI2 force-field are more consistent to the all-atom force-fields, underlining the need for further refinement and validation of the MARTINI3 force-field for accurate membrane simulations. If we want to simulate new membrane systems, as suggested before for Mfn1-AH, the MARTINI2 force-field might be more appropriate, given the MARTINI3 limitations outlined.

While improving the protein-protein interactions is the goal of the MARTINI3 version, it is important that the protein-membrane interactions and the membrane dynamics are not neglected. Parameters such as membrane thickness, area per lipid and packing defects should be focused on in the future versions of the force-field. However it might not be possible to change the protrusion values, as lipid molecules in a coarse-grained representation is less flexible than in an all-atom representation. Finally, a multi-scale approach, combining CG and AA simulations (as described in Chapter 3), could be more appropriate in certain cases of protein simulations.

7.4 A new cross-type cis-dimer is unveiled by AlphaFold predictions

Chapter 6 focused on yeast and human mitofusins overall structure, through the use of AlphaFold. A first screening of the monomeric conformations was performed. The Fzo1 monomer exhibited significant disparities with the first homologue model built in 2017 [1]: the HRN domain was placed underneath the GTPase domain, and HR1/2 did not present any hinges breaking the continuous coiled-coil, contrary to what was expected from the BDLP homologue [68]. The absence of hinges in the coiled-coil domains are observed for the human mitofusins Mfn1/2 as well. Furthermore, AF demonstrated poor prediction skills of mitofusins TM domain. In fact, Fzo1 TM domain was predicted partially as intrinsically disordered, and Mfn1/2 showed dissociated TM helices, with TM1 presenting an important kink. However, it was later shown that a prediction of Fzo1 with a custom MSA, which exhibited a strong conservation of the TM domain, indeed assembled the two TM helices as anticipated in Section 3. Additionally, it converged towards analogous interactions predicted in this same chapter. As this protocol showed interesting results in the TM domain of Fzo1, it would be interesting to test the same protocol for both Mfn1 and Mfn2. This would require to create a custom MSA for each of the human proteins, ensuring that the MSAs are highly conserved on the TM section of each mitofusins.

Second, oligomers of mitofusins and their fusion partners were produced. These oligomers showed a new unexpected cross type of cis-dimers, involving contacts between the coiled-coil structures, involving the HR2 domain for the closest contacts. In addition, these contacts appeared to be induced by the inclusion of the mitochondrial solute carriers Ugo1 (yeast) and SLC25A46 (human). Surprisingly, the latter proteins induced a more compact conformation of the mitofusins TM domain. While it was possible, through oligomerization with Ugo1, to obtain two helices TM1 and TM2 interacting with one another for Fzo1, such predictions was not achieved for the human mitofusins Mfn1/2. In fact, a kink in TM1 involving the conserved arginine (see Supplementary Figure S3.9) was almost consistently observed in our models. It is noteworthy that the positioning of Ugo1 appeared to be the inverse of SLC25A46. It would be interesting to explore a biased docking approach, such as HADDOCK [270], incorporating Fzo1 and Ugo1, with Ugo1 positioned in the "correct" orientation for further investigation. Testing the protocol of the custom MSA could help determining the most suitable model for these mitofusins. Nevertheless, AF has generated a range of potential dimers, including some that are trans-dimers, which could potentially facilitate membrane tethering and fusion. The precise interactions between the mitofusins and between mitofusins and their mitochondrial solute carriers was assessed in this chapter. Multiple salt bridges and polar interactions were revealed, which could serve as a basis for future experimental validation of the models, using cross linking-mass spectrometry and mutagenesis as demonstrated by Boopathy et al. in 2023 [276] or by De Vecchis et al. in 2017 [1]. However, as said before in Chapter 6, the structure of Fzo1 was partially solved by our collaborator Philippe Meyer, revealing that the position of the GTPase domain as well as HRN domain was in fact correctly predicted by AF. The mutagenesis conducted to

evaluate the 2017 model [1] has largely supported the validity of the Fzo1 model.

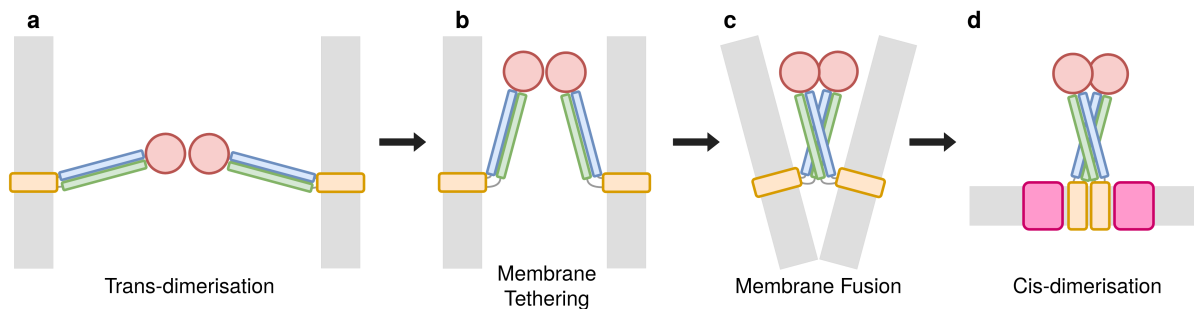


Figure 7.2: Proposed mechanism based on AF models. The mitofusins are schematized, with the main domains represented as rectangle or circles: the orange boxes represent the TM domain, the blue and green long rectangle represent respectively HR1 and HR2 domains, and the red circle is the GTPase domain. The solute carrier partner (either Ugo1 or SLC25A46) is represented as a pink square. In light grey stripes are represented the membranes. **(a)** Trans-dimerization of mitofusins through the GTPase domain. **(b)** Conformational changes mainly occurring between the HR and TM sections, but the GTPase domain might need reorganization as well. These drive the mitofusins and membranes closer to one another. **(c)** Conformational changes leading to the cross-type dimers and membrane fusion. **(d)** The initial trans-dimer is now a post-fusion cis-dimer. Here is shown Ugo1, which was suggested to stabilize the cross-type cis-dimer in Section 6.

As the models produced by AF are validated by the available experimental data, we decided to focus on the potential mechanism that could arise from these structures. From this variety of possible oligomeric mitofusins conformations, we are able to propose a mitofusin induced fusion mechanism, showed in Figure 7.2. Given that AlphaFold exclusively generated open conformation models, we opted to suggest a mechanism that doesn't require a transition between open and closed conformations. Here the membrane tethering starts with the trans-dimerization of the mitofusins (similar to the human mitofusins model presented in Figure 6.3D and E), which can drive the two membrane closer together upon two conformational rearrangement : (i) a first one mainly located onto the base of the TM domain (Figure 7.2b), and (ii) a second one mainly involving the coiled-coil structures and leading to the cross-type dimer as well as the full membrane fusion (Figure 7.2c). The events triggering the conformational changes from (a) to (b), and from (b) to (c) are unknown. However we could speculate that Ugo1/SLC25A46 and GTP/GDP binding/unbinding participates in inducing those conformational changes. A final conformational rearrangement involving the TM domain will occur during the various steps of membrane fusion (Figure 7.2d). The precise structural rearrangement of the molecules from one conformation to an other is still unknown; however, it is possible to assess the possible movements of AF mitofusins models through normal mode analysis. Furthermore, this mechanism does not show the potential effect of the mitofusin on the membrane behavior itself, through its HR and TM domains. In fact, it is still complicated to assess if AF can produce any conformation of the mitofusin allowing for the HR1 domain to interact with the membrane. The amphipathic helix of Mfn1 revealed in 2018 [135] is in fact not accessible to the solvent and available for binding to the membrane in the AF model. Finally, the solute carrier partner is represented in the final step of the proposed mechanism, as a stabilizer of the cross-type dimer. However,

the protein could be involved earlier in the mitofusin fusion mechanism. Furthermore, Ugo1 was placed upside down to SLC25A46.

7.5 What's next ?

These agreements of the AF models with our TM domain predictions and the experimentally solved structure puts in perspective the models first produced for Fzo1. The open conformation could in fact be more similar to the AF model. However, besides the BDLP structure, we have very few information in regards to the closed conformation of mitofusins. So far, the BDLP structure (see Section 1.3.2 and Figure 1.14) as well as the BDLP homology based models of Fzo1 (see Section 1.4.3 and Figure 1.22) predict two loops called hinges 1a and 1b breaking the helix structure of HR1 and HR2. This local structure could be questioned, and a possible bend of the helix or loss of structure upon conformational transition in this section of the two heptad repeat domains cannot be excluded.

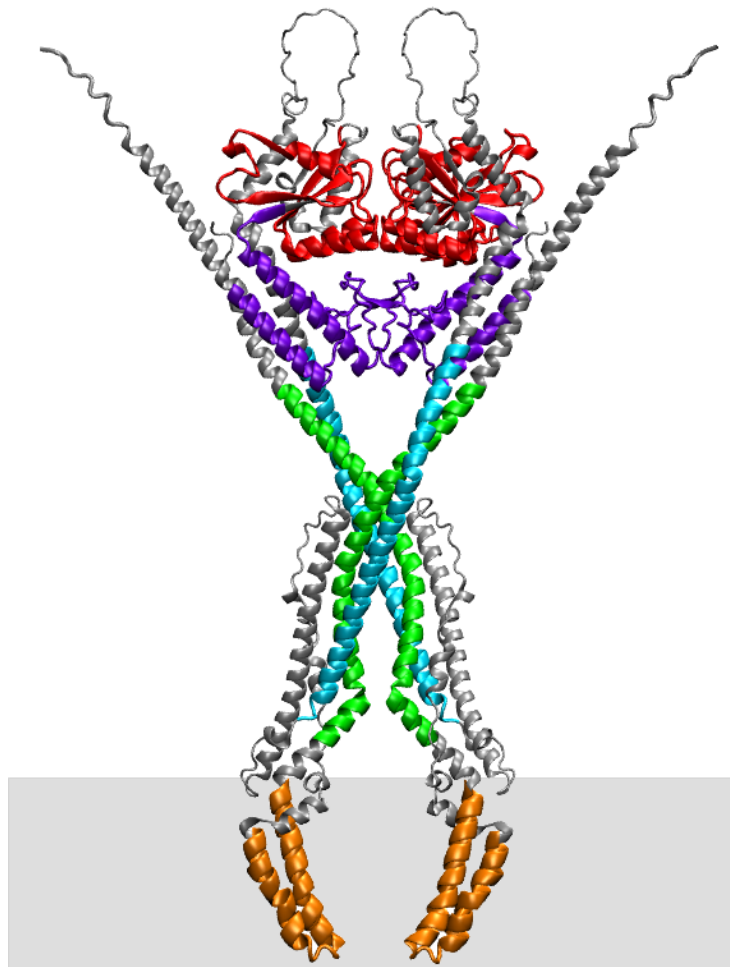


Figure 7.3: **Updated cis-dimer model of Fzo1.** The domains are colored as function of the domains (see Figure 6.1B). The Fzo1 dimer was extracted from the $2 \times \text{Fzo1}[60-855] + 2 \times \text{Ugo1}[100-502]$. The TM domains built in the model $2 \times \text{Mfn1}[1-741] + 2 \times \text{SLC25A46}[1-418]$ were extracted and replaced the initial TM structure of the dimer.

With the various information produced in this Ph.D and the generation of a partial structure from collaborators, we have been able to produce an updated model of the full structure of Fzo1 (Figure 7.3), as well as a new fusion mechanism (Figure 7.2). Based on these models produced, a protocol similar to what Risselada and collaborators established in 2011 for the SNARE proteins [154] could be applied. In fact, coarse-grained simulation involving two monomers of Fzo1 placed on two different membranes could be performed: the goal would be to observe fusion of the two tethered membranes. These prospective avenues hold promise for further unraveling the intricate mechanisms underlying mitochondrial fusion.

BIBLIOGRAPHY

- [1] Dario De Vecchis, Laetitia Cavellini, Marc Baaden, Jérôme Hénin, Mickaël M. Cohen, and Antoine Taly. A membrane-inserted structural model of the yeast mitofusin fzo1. *Scientific Reports*, 7(1):10217, 2017.
- [2] Astrid Brandner, Dario De Vecchis, Marc Baaden, Mickael M. Cohen, and Antoine Taly. Physics-based oligomeric models of the yeast mitofusin fzo1 at the molecular scale in the context of membrane docking. *Mitochondrion*, 49:234–244, 2019.
- [3] Benedikt Westermann. Mitochondrial fusion and fission in cell life and death. *Nat. Rev. Mol. Cell Biol.*, 11(12):872–884, 2010.
- [4] Siv GE Andersson and Charles G Kurland. Origins of mitochondria and hydrogenosomes. *Current Opinion in Microbiology*, 2(5):535–541, 1999.
- [5] Michael W Gray, Gertraud Burger, and B Franz Lang. Mitochondrial evolution. *Science*, 283(5407):1476–1481, 1999.
- [6] Michael W Gray. Mitochondrial evolution. *Cold Spring Harbor Perspectives in Biology*, 4(9):a011403, 2012.
- [7] Yoko Shibata, Junjie Hu, Michael Kozlov, and Tom Rapoport. Mechanisms shaping the membranes of cellular organelles. *Annual review of cell and developmental biology*, 25:329–54, 02 2009.
- [8] George E Palade. An electron microscope study of the mitochondrial structure. *The Journal of Histochemistry and Cytochemistry*, 1(4):188–211, 1953.
- [9] Juan Llopis, J Michael McCaffery, Atsushi Miyawaki, Marilyn G Farquhar, and Roger Y Tsien. Measurement of cytosolic, mitochondrial, and golgi ph in single living cells with green fluorescent proteins. *Proceedings of the National Academy of Sciences*, 95(12):6803–6808, 1998.
- [10] Carmen A. Mannella. Structure and dynamics of the mitochondrial inner membrane cristae. *Biochimica et Biophysica Acta (BBA) - Molecular Cell Research*, 1763(5):542–548, 2006. Mitochondrial Dynamics in Cell Life and Death.

- [11] Felix Vogel, Christoph Bornhövd, Walter Neupert, and Andreas S Reichert. Dynamic subcompartmentalization of the mitochondrial inner membrane. *The Journal of Cell Biology*, 175(2):237–247, 2006.
- [12] Juergen Bereiter-Hahn. Behavior of mitochondria in the living cell. *International Review of Cytology*, 122:1–63, 1990.
- [13] Robert W Gilkerson, Jean M Selker, and Roderick A Capaldi. The cristal membrane of mitochondria is the principal site of oxidative phosphorylation. *FEBS Letters*, 546(2-3):355–358, 2003.
- [14] Estela Area-Gomez, Cristina Guardia-Laguarta, Eric A Schon, and Serge Przedborski. Mitochondria, oxphos, and neurodegeneration: cells are not just running out of gas. *Journal of Clinical Investigation*, 129(1):34–45, 2019.
- [15] Nikolaus Pfanner and Andreas Geissler. Versatility of the mitochondrial protein import machinery. *Nature Reviews Molecular Cell Biology*, 2(5):339–349, 2001.
- [16] Xinnan J Chen and Ronald A Butow. The organization and inheritance of the mitochondrial genome. *Nature Reviews Genetics*, 6(11):815–825, 2005.
- [17] Walter Neupert and Johannes M Herrmann. Translocation of proteins into mitochondria. *Annual Review of Biochemistry*, 76:723–749, 2007.
- [18] Naoto Taguchi, Naotada Ishihara, Atsushi Jofuku, Toshihiko Oka, and Katsuyoshi Mihara. Mitotic phosphorylation of dynamin-related gtpase drp1 participates in mitochondrial fission. *Journal of Biological Chemistry*, 282(15):11521–11529, 2007.
- [19] Naotada Ishihara, Masatoshi Nomura, Atsushi Jofuku, Hiroyuki Kato, Shun-ichi Suzuki, Kazuhiro Masuda, Hidenori Otera, Yoichi Nakanishi, Ikuya Nonaka, Yu-ichi Goto, Naoto Taguchi, Hironobu Morinaga, Mitsuyo Maeda, Ryota Takayanagi, Shigefumi Yokota, and Katsuyoshi Mihara. Mitochondrial fission factor drp1 is essential for embryonic development and synapse formation in mice. *Nature Cell Biology*, 11(8):958–966, 2009.
- [20] Kathrin Altmann, Martin Frank, Dietbert Neumann, Stefan Jakobs, and Benedikt Westermann. The class v myosin motor protein, myo2, plays a major role in mitochondrial motility in *saccharomyces cerevisiae*. *The Journal of Cell Biology*, 181(1):119–130, 2008.
- [21] Hsiuchen Chen, Anne Chomyn, and David C Chan. Disruption of fusion results in mitochondrial heterogeneity and dysfunction. *J Biol Chem*, 280(28):26185–26192, 2005.
- [22] Hsiuchen Chen, Marc Vermulst, Yen-Yu E Wang, Anne Chomyn, Tomas A Prolla, J Michael McCaffery, and David C Chan. Mitochondrial fusion is required for mtdna stability in skeletal muscle and tolerance of mtdna mutations. *Cell*, 141(2):280–289, 2010.
- [23] Zheng Li, Kenichi Okamoto, Yasunori Hayashi, and Morgan Sheng. The importance of dendritic mitochondria in the morphogenesis and plasticity of spines and synapses. *Cell*, 119:873–887, 2004.
- [24] Vladimir P Skulachev. Mitochondrial filaments and clusters as intracellular power-transmitting cables. *Trends in Biochemical Sciences*, 26(1):23–29, 2001.

- [25] Antonio Federico, Elena Cardaioli, Paola Da Pozzo, Patrizia Formichi, Gian Nicola Gallus, and Elena Radi. Mitochondria, oxidative stress and neurodegeneration. *J Neurol Sci*, 322(1-2):254–262, Nov 2012.
- [26] Robert S Balaban, Shino Nemoto, and Toren Finkel. Mitochondria, oxidants, and aging. *Cell*, 120(4):483–495, 2005.
- [27] Tomoko Ono, Kotoyo Isobe, Kazuto Nakada, and Jun-Ichi Hayashi. Human cells are protected from mitochondrial dysfunction by complementation of dna products in fused mitochondria. *Nature Genetics*, 28(3):272–275, 2001.
- [28] Congcong He and Daniel J. Klionsky. Regulation mechanisms and signaling pathways of autophagy. *Annual Review of Genetics*, 43:67–93, 2009.
- [29] Gilad Twig, Alvaro Elorza, Anthony J A Molina, Hibo Mohamed, Jakob D Wikstrom, Gil Walzer, Linsey Stiles, Sarah E Haigh, Steve Katz, Guy Las, Joseph Alroy, Min Wu, Bénédicte F Py, Junying Yuan, Jude T Deeney, Barbara E Corkey, and Orian S Shirihai. Fission and selective fusion govern mitochondrial segregation and elimination by autophagy. *EMBO J*, 27(2):433–446, 2008.
- [30] Charleen T Chu. Mechanisms of selective autophagy and mitophagy: Implications for neurodegenerative diseases. *Neurobiology of Disease*, 122:23–34, 2019.
- [31] Guo Chen, Guido Kroemer, and Oliver Kepp. Mitophagy: An emerging role in aging and age-associated diseases. *Frontiers in Cell and Developmental Biology*, 8:200, 2020. Published 2020 Mar 26.
- [32] Der-Fen Suen, Kristi L Norris, and Richard J Youle. Mitochondrial dynamics and apoptosis. *Genes & Development*, 22(12):1577–1590, 2008.
- [33] Rie Sugioka, Shigeomi Shimizu, and Yoshihide Tsujimoto. Fzo1, a protein involved in mitochondrial fusion, inhibits apoptosis. *Journal of Biological Chemistry*, 279(50):52726–52734, 2004.
- [34] Werner Kühlbrandt. Structure and function of mitochondrial membrane protein complexes. *BMC Biology*, 13:89, 2015.
- [35] Erwin Zinser, Constanze D. M. Sperka-Gottlieb, Evelyn-V. Fasch, Sepp D. Kohlwein, Fritz Paltauf, and Gunther Daum. Phospholipid Synthesis and Lipid Composition of Subcellular Membranes in the Unicellular Eukaryote *Saccharomyces cerevisiae*. *Journal Of Bacteriology*, 173(6):2026–2034, 1991.
- [36] Constanze D.M. Sperka-Gottlieb, Albin Hermetter, Fritz Paltauf, and Guenther Daum. Lipid topology and physical properties of the outer mitochondrial membrane of the yeast, *Saccharomyces cerevisiae*. *Biochimica et Biophysica Acta (BBA)*, 946(2):227–234, 1988.
- [37] Anton I.P.M. de Kroon, Daniele Dolis, Andreas Mayer, Roland Lill, and Ben de Kruijff. Phospholipid composition of highly purified mitochondrial outer membranes of rat liver and *Neurospora crassa*. Is cardiolipin present in the mitochondrial outer membrane? *Biochimica et Biophysica Acta (BBA) - Biomembranes*, 1325(1):108–116, 1997.

- [38] Dominique Ardail, Jean-Paul Privats, Marguerite Egret-Charlierg, Christiane Levratg, Fabienne Lerme, and Pierre Louisot. Mitochondrial Contact Sites, lipid composition and dynamics. *The Journal Of Biological Chemistry*, 265(31):18797–18802, 1990.
- [39] Renate Simbeni, Liza PonSQ, Erwin Zinser, Fritz Paltauf, and Gunther Dauml. Mitochondrial Membrane Contact Sites of Yeast: characterization of lipid components and possible involvement in intramitochondrial translocation of phospholipids. *The Journal Of Biological Chemistry*, 266(16):10047–10049, 1991.
- [40] Friedrich Paltauf and Gottfried Schatz. Promitochondria of Anaerobically Grown Yeast. Lipid Composition. *PNAS*, 8(1):1252–1259, 1969.
- [41] Charles E. Martin, Chan-Seok Oh, and Yide Jiang. Regulation of long chain unsaturated fatty acid synthesis in yeast. *Biochimica et Biophysica Acta (BBA) - Molecular and Cell Biology of Lipids*, 1771(3):271–285, 2007.
- [42] Gerrit van Meer, Dennis R Voelker, and Gerald W Feigenson. Membrane lipids: where they are and how they behave. *Nature reviews Molecular cell biology*, 9(2):112–124, 2008.
- [43] Jan Dudek. Role of cardiolipin in mitochondrial signaling pathways. *Frontiers in Cell and Developmental Biology*, 5:90, 2017.
- [44] A E Rusiñol, Z Cui, M H Chen, and J E Vance. A unique mitochondria-associated membrane fraction from rat liver has a high capacity for lipid synthesis and contains pre-golgi secretory proteins including nascent lipoproteins. *Journal of Biological Chemistry*, 269(44):27494–27502, 1994.
- [45] Marta Giacomello, Aswin Pyakurel, Christina Glytsou, and Luca Scorrano. The cell biology of mitochondrial membrane dynamics. *Nature Reviews Molecular Cell Biology*, 21(4):204–224, 2020. Epub ahead of print.
- [46] Nadav Shai, Eden Yifrach, Carlo W.T. van Roermund, Nir Cohen, Nir Cohen, Nir Cohen, Chen Bibi, Lodewijk IJlst, Laetitia Cavellini, Julie Meurisse, Ramona Schuster, Lior Zada, Muriel Mari, Fulvio Reggiori, Adam L. Hughes, Adam L. Hughes, Mafalda Escobar-Henriques, Mickael M. Cohen, Hans R. Waterham, Ronald J.A. Wanders, Maya Schuldiner, and Einat Zalckvar. Systematic mapping of contact sites reveals tethers and a function for the peroxisome-mitochondria contact. *Nature Communications*, 2018.
- [47] Marc Fransen, Celien Lismont, and Paul A. Walton. The peroxisome-mitochondria connection: How and why? *International Journal of Molecular Sciences*, 2017.
- [48] Reinhard Jahn, Thorsten Lang, and Thomas C. Südhof. Membrane fusion. *Cell*, 112(4):519–533, 2003.
- [49] Leonid V. Chernomordik and Michael M. Kozlov. Mechanics of membrane fusion. *Nat Struct Mol Biol*, 15(7):675–683, 2008.
- [50] Leonid V. Chernomordik and Michael M. Kozlov. Protein-lipid interplay in fusion and fission of biological membranes. *Annual Review of Biochemistry*, 72(1):175–207, 2003. PMID: 14527322.

- [51] Michael M. Kozlov, Sergey L. Leikin, Leonid V. Chernomordik, Vladislav S. Markin, and Yuri A. Chizmadzhev. Stalk mechanism of vesicle fusion. intermixing of aqueous contents. *Eur Biophys J*, 17(3):121–129, 1989.
- [52] Lydie Vamparys, Romain Gautier, Stefano Vanni, W. F. Drew Bennett, D. Peter Tieleman, Bruno Antonny, Catherine Etchebest, and Patrick F. Fuchs. Conical lipids in flat bilayers induce packing defects similar to that induced by positive curvature. *Biophys J*, 104(3):585–593, 2013.
- [53] Vladimir S. Malinin, Peter Frederik, and Barry R. Lentz. Osmotic and curvature stress affect peg-induced fusion of lipid vesicles but not mixing of their lipids. *Biophys J*, 82(4):2090–2100, 2002.
- [54] Yu A Chen and Richard H. Scheller. Snare-mediated membrane fusion. *Nat Rev Mol Cell Biol*, 2(2):98–106, 2001.
- [55] Dirk Fasshauer, R. Bryan Sutton, Axel T. Brunger, and Reinhard Jahn. Conserved structural features of the synaptic fusion complex: Snare proteins reclassified as q- and r-snares. *Proc Natl Acad Sci U S A*, 95(26):15781–15786, 1998.
- [56] Jason B. Bock, Hugo T. Matern, Andrew A. Peden, and Richard H. Scheller. A genomic perspective on membrane compartment organization. *Nature*, 409(6822):839–841, 2001.
- [57] Richard B. Sutton, Dirk Fasshauer, Reinhard Jahn, and Axel T. Brunger. Crystal structure of a snare complex involved in synaptic exocytosis at 2.4 a resolution. *Nature*, 395(6700):347–353, 1998.
- [58] Reinhard Jahn and Richard H. Scheller. Snares — engines for membrane fusion. *Nat Rev Mol Cell Biol*, 7(8):631–643, 2006.
- [59] Klaus M Fiebig, Luke M. Rice, Elizabeth Pollock, and Axel T. Brunger. Folding intermediates of snare complex assembly. *Nature Structural Biology*, 6:117–123, 1999.
- [60] John J. Skehel and Don C. Wiley. Receptor binding and membrane fusion in virus entry: the influenza hemagglutinin. *Annual Review of Biochemistry*, 69:531–569, 2000.
- [61] Donald J. Benton, Andrea Nans, Lesley J. Calder, Jack Turner, Ursula Neu, Yi Pu Lin, Esther Ketelaars, Nicole L. Kallewaard, Davide Corti, Antonio Lanzavecchia, Steven J. Gamblin, Peter B. Rosenthal, and John J. Skehel. Influenza hemagglutinin membrane anchor. *Proceedings of the National Academy of Sciences*, 115(40):10112–10117, 2018.
- [62] Debra M. Eckert and Peter S. Kim. Mechanisms of viral membrane fusion and its inhibition. *Annual Review of Biochemistry*, 70(1):777–810, 2001. PMID: 11395423.
- [63] Gerrit J. K. Praefcke and Harvey T. McMahon. The dynamin superfamily: universal membrane tubulation and fission molecules? *Nature Reviews Molecular Cell Biology*, 5(2):133–147, 2004.
- [64] Rajesh Ramachandran and Sandra L. Schmid. The dynamin superfamily. *Current Biology*, 28(8):R411–R416, 2018.
- [65] Harry H. Low and Jan Löwe. A bacterial dynamin-like protein. *Nature*, 444:766–769, 2006.

- [66] Marc Bramkamp. Structure and function of bacterial dynamin-like proteins. *Biological Chemistry*, 393(11):1203–1214, 2012.
- [67] Joshua S Chappie, Sharmistha Acharya, Marilyn Leonard, Sandra L Schmid, and Fred Dyda. G domain dimerization controls dynamin’s assembly-stimulated gtpase activity. *Nature*, 465(7297):435—440, May 2010.
- [68] Harry H. Low, Carsten Sachse, Linda A. Amos, and Jan Löwe. Structure of a bacterial dynamin-like protein lipid tube provides a mechanism for assembly and membrane curving. *J. Cell Biol.*, 139:1342–1352, 2009.
- [69] Jiwei Liu, Jeffrey K. Noel, and Harry H. Low. Structural basis for membrane tethering by a bacterial dynamin-like pair. *Nature Communications*, 9:3345, 2018.
- [70] James Winsor, David D Hackney, and Tina H Lee. The crossover conformational shift of the gtpase atlastin provides the energy driving er fusion. *Journal of Cell Biology*, 216(5):1321–1335, 2017.
- [71] Liming Yan, Sha Sun, Wei Wang, Juanming Shi, Xiaoyu Hu, Shiyan Wang, Dan Su, Zihe Rao, Junjie Hu, and Zhiyong Lou. Structures of the yeast dynamin-like gtpase sey1p provide insight into homotypic er fusion. *Journal of Cell Biology*, 210(6):961–972, 2015.
- [72] Joshua S Chappie and Fred Dyda. Building a fission machine—structural insights into dynamin assembly and activation. *Journal of Cell Science*, 126(13):2773–2784, 2013.
- [73] Jason A Mears, Laura L Lackner, Shunming Fang, Elena Ingerman, Jodi Nunnari, and Jenny E Hinshaw. Conformational changes in dnm1 support a contractile mechanism for mitochondrial fission. *Nature structural & molecular biology*, 18(1):20–26, 2011.
- [74] Christopher A Francy, Ryan W Clinton, Chris Fröhlich, Colleen Murphy, and Jason A Mears. Cryo-em studies of drp1 reveal cardiolipin interactions that activate the helical oligomer. *Scientific Reports*, 7(1):10744, 2017.
- [75] Xiaodong Cheng, Kuangcai Chen, Bin Dong, Meek Yang, Seth L Filbrun, Yong Myoung, Teng-Xiang Huang, Yan Gu, Gufeng Wang, and Ning Fang. Dynamin-dependent vesicle twist at the final stage of clathrin-mediated endocytosis. *Nature Cell Biology*, 23(8):859–869, 2021.
- [76] Joshua S. Chappie, Jason A. Mears, Shunming Fang, Marilyn Leonard, Sandra L. Schmid, Ronald A. Milligan, Jenny E. Hinshaw, and Fred Dyda. A pseudoatomic model of the dynamin polymer identifies a hydrolysis-dependent powerstroke. *Cell*, 2011.
- [77] Marijn G. J. Ford and Joshua S. Chappie. The structural biology of the dynamin-related proteins: New insights into a diverse, multitalented family. *Traffic*, 2019.
- [78] Martin L Rennie, Siri A McKelvie, Esther M Bulloch, and Richard L Kingston. Transient dimerization of human mxa promotes gtp hydrolysis, resulting in a mechanical power stroke. *Structure*, 22(10):1433–1445, 2014.
- [79] Frank Bürmann, Nina Ebert, Suey van Baarle, Marc Bramkamp, and Marc Bramkamp. A bacterial dynamin-like protein mediating nucleotide-independent membrane fusion. *Molecular Microbiology*, 2011.

- [80] Lijun Guo, Marc Bramkamp, and Marc Bramkamp. Bacterial dynamin-like protein dyna mediates lipid and content mixing and shows phospholipid specificity. *bioRxiv*, 2018.
- [81] Detlef D. Leipe, Yuri I. Wolf, Feng Zhang, Eugene V. Koonin, and L. Aravind. Classification and evolution of p-loop gtpases and related atpases. *Journal of Molecular Biology*, 2002.
- [82] Takumi Koshiba, Scott A. Detmer, Jens T. Kaiser, Hsiuchen Chen, J. Michael McCaffery, and David C. Chan. Structural basis of mitochondrial tethering by mitofusin complexes. *Science*, 2004.
- [83] Oliver C Losón, Zhiyin Song, Hsiuchen Chen, and David C Chan. Fis1, mff, mid49, and mid51 mediate drp1 recruitment in mitochondrial fission. *Molecular Biology of the Cell*, 24(5):659–667, 2013.
- [84] Mary Anne Karren, Emily M. Coonrod, Teresa K. Anderson, and Janet M. Shaw. The role of fis1p–mdv1p interactions in mitochondrial fission complex assembly. *The Journal of Cell Biology*, 171:291 – 301, 2005.
- [85] Jonathan R. Friedman, Laura L. Lackner, Matthew West, Jared R. DiBenedetto, Jodi Nunnari, and Gia K. Voeltz. Er tubules mark sites of mitochondrial division. *Science*, 334(6054):358–362, 2011.
- [86] Farida Korobova, Vinay Ramabhadran, and Henry N Higgs. An actin-dependent step in mitochondrial fission mediated by the er-associated formin inf2. *Science*, 339(6118):464–467, 2013.
- [87] Uri Manor, Sadie Bartholomew, Gonen Golani, Eric Christenson, Michael Kozlov, Henry Higgs, James Spudich, and Jennifer Lippincott-Schwartz. A mitochondria-anchored isoform of the actin-nucleating spire protein regulates mitochondrial division. *eLife*, 4:e08828, aug 2015.
- [88] Marlies Messerschmitt, Stefan Jakobs, Frank Vogel, Stefan Fritz, Kai Stefan Dimmer, Walter Neupert, and Benedikt Westermann. The inner membrane protein mdm33 controls mitochondrial morphology in yeast. *Journal of Cell Biology*, 160(4):553–564, 2003.
- [89] Daniel Tondera, Frank Czauderna, Katharina Paulick, Rolf Schwarzer, Jörg Kaufmann, and Ansgar Santel. The mitochondrial protein mtp18 contributes to mitochondrial fission in mammalian cells. *Journal of Cell Science*, 118(14):3049–3059, 2005.
- [90] Erminia Donnarumma, Michael Kohlhaas, Elodie Vimont, and et al. Mitochondrial fission process 1 controls inner membrane integrity and protects against heart failure. *Nature Communications*, 13:6634, 2022.
- [91] Rajesh Ramachandran. Mitochondrial dynamics: The dynamin superfamily and execution by collusion. *Semin. Cell Dev. Biol.*, 76:201–212, 2018.
- [92] Karen G. Hales and Margaret T. Fuller. Developmentally regulated mitochondrial fusion mediated by a conserved, novel, predicted gtpase. *Cell*, 90:121–129, 1997.
- [93] Doron Rapaport, Michael Brunner, Walter Neupert, and Benedikt Westermann. Fzo1p is a mitochondrial outer membrane protein essential for the biogenesis of functional mitochondria in *saccharomyces cerevisiae*. *Journal of Biological Chemistry*, 273(32):20150–20155, 1998.

- [94] Greg J Hermann, John W Thatcher, John P Mills, Karen G Hales, Margaret T Fuller, Jodi Nunnari, and Janet M Shaw. Mitochondrial fusion in yeast requires the transmembrane gtpase fzo1p. *Journal of Cell Biology*, 143(2):359–373, 1998.
- [95] Takayuki Kanazawa, Mauro D Zappaterra, Ayako Hasegawa, Ashley P Wright, Erin D Newman-Smith, Karolyn F Buttle, Kent McDonald, Carmen A Mannella, and Alexander M. van der Blik. The *c. elegans* opa1 homologue eat-3 is essential for resistance to free radicals. *PLoS genetics*, 4(2):e1000022, 2008.
- [96] Ansgar Santel and Margaret T Fuller. Control of mitochondrial morphology by a human mitofusin. *Journal of Cell Science*, 114(5):867–874, 2001.
- [97] Naotada Ishihara, Yuka Eura, and Katsuyoshi Mihara. Mitofusin 1 and 2 play distinct roles in mitochondrial fusion reactions via GTPase activity. *Journal of Cell Science*, 117(26):6535–6546, 2004.
- [98] Manuel Rojo, Frédéric Legros, Danielle Chateau, and Anne Lombès. Membrane topology and mitochondrial targeting of mitofusins, ubiquitous mammalian homologs of the transmembrane GTPase fzo. *J. Cell. Sci.*, 115:1663–1674, 2002.
- [99] Stefan Fritz, Doron Rapaport, Elisabeth Klanner, Walter Neupert, and Benedikt Westermann. Connection of the mitochondrial outer and inner membranes by fzo1 is critical for organellar fusion. *J. Cell Bio.*, 152:683–692, 2001.
- [100] Shelly Meeusen, Rachel DeVay, Jennifer Block, Ann Cassidy-Stone, Sarah Wayson, J. Michael McCaffery, and Jodi Nunnari. Mitochondrial inner-membrane fusion and crista maintenance requires the dynamin-related gtpase mgm1. *Cell*, 127(2):383–395, 2006.
- [101] G. McQuibban, S. Saurya, and M. Freeman. Mitochondrial membrane remodelling regulated by a conserved rhomboid protease. *Nature*, 423:537–541, 2003.
- [102] S. Cipolat, O. Martins de Brito, B. Dal Zilio, and L. Scorrano. Opa1 requires mitofusin 1 to promote mitochondrial fusion. *Proceedings of the National Academy of Sciences of the United States of America*, 101(45):15927–15932, 2004.
- [103] Valentina Del Dotto, Prashant Mishra, Sara Vidoni, Mario Fogazza, Alessandra Maresca, Leonardo Caporali, J. Michael McCaffery, Martina Cappelletti, Enrico Baruffini, Guy Lenaers, David Chan, Michela Rugolo, Valerio Carelli, and Claudia Zanna. Opa1 isoforms in the hierarchical organization of mitochondrial functions. *Cell Reports*, 19(12):2557–2571, 2017.
- [104] Alexander Malsburg, Gracie Sapp, Kelly Zuccaro, Alexander Appen, Frank Moss, Raghav Kalia, Jeremy Bennett, Luciano Abriata, Matteo Peraro, Martin Van der Laan, Adam Frost, and Halil Aydin. Structural mechanism of mitochondrial membrane remodelling by human opa1. *Nature*, 08 2023.
- [105] Sarah Nyenhuis, Xufeng Wu, Marie-Paule Strub, Yang-In Yim, Abigail Stanton, Valentina Baena, Zulfeqhar Syed, Bertram Canagarajah, John Hammer, and Jenny Hinshaw. Opa1 helical structures give perspective to mitochondrial dysfunction. *Nature*, 620, 08 2023.

- [106] Edith D. Wong, Jennifer A. Wagner, Sidney V. Scott, Voytek Okreglak, Timothy J. Holewinski, Ann Cassidy-Stone, and Jodi Nunnari. The intramitochondrial dynamin-related GTPase, Mgm1p, is a component of a protein complex that mediates mitochondrial fusion. *Journal of Cell Biology*, 160(3):303–311, 02 2003.
- [107] Sevan Mattie, Jan Riemer, Jeremy G. Wideman, and Heidi M. McBride. A new mitofusin topology places the redox-regulated c terminus in the mitochondrial intermembrane space. *The Journal of Cell Biology*, 217:507 – 515, 2018.
- [108] Hiromi Sesaki and Robert E. Jensen. UGO1 Encodes an Outer Membrane Protein Required for Mitochondrial Fusion. *Journal of Cell Biology*, 152(6):1123–1134, 03 2001.
- [109] Hiromi Sesaki and Robert E. Jensen. Ugo1p links the fzo1p and mgm1p gtpases for mitochondrial fusion*. *Journal of Biological Chemistry*, 279(27):28298–28303, 2004.
- [110] Suzanne Hoppins, Jennifer Horner, Cheng Song, J. Michael McCaffery, and Jodi Nunnari. Mitochondrial outer and inner membrane fusion requires a modified carrier protein. *Journal of Cell Biology*, 184(4):569–581, 02 2009.
- [111] Mickael M Cohen and David Tareste. Recent insights into the structure and function of mitofusins in mitochondrial fusion. *F1000Res*, 7, 2018.
- [112] Ryota Iwasawa, Anne-Laure Mahul-Mellier, Christoph Datler, Evangelos Pazarentzos, and Stefan Grimm. Fis1 and bap31 bridge the mitochondria–er interface to establish a platform for apoptosis induction. *The EMBO Journal*, 30(3):556–568, 2011.
- [113] Marta Giacomello and Luca Pellegrini. The coming of age of the mitochondria-er contact: a matter of thickness. *Cell death and differentiation*, 23, 06 2016.
- [114] Agnese De Mario, Rubén Quintana-Cabrera, Denis Martinvalet, and Marta Giacomello. (neuro)degenerated mitochondria-er contacts. *Biochemical and Biophysical Research Communications*, 483(4):1096–1109, 2017. SI: Neurodegeneration.
- [115] Meng-Ju Wu, Yu-Syuan Chen, Mi Kim, Chao-Ching Chang, Silpa Gampala, Yingsheng Zhang, Yueyang Wang, Chih-Yu Chang, Jer-Yen Yang, and Chun Ju Chang. Epithelial-mesenchymal transition directs stem cell polarity via regulation of mitofusin. *Cell Metabolism*, 29, 12 2018.
- [116] Karthika Singaravelu, Charmaine Nelson, Daniel Bakowski, Olga Martins de Brito, Siaw-Wei Ng, Joseph Di Capite, Trevor Powell, Luca Scorrano, and Anant B. Parekh. Mitofusin 2 regulates stim1 migration from the ca²⁺ store to the plasma membrane in cells with depolarized mitochondria*. *Journal of Biological Chemistry*, 286(14):12189–12201, 2011.
- [117] Hsiuchen Chen and David C. Chan. Mitochondrial dynamics–fusion, fission, movement, and mitophagy–in neurodegenerative diseases. *Hum Mol Genet*, 18:R169–R176, 2009.
- [118] Andrew B. Knott, Guy Perkins, Robert Schwarzenbacher, and Ella Bossy-Wetzel. Mitochondrial fragmentation in neurodegeneration. *Nature Reviews Neuroscience*, 9(7):505–518, 2008.
- [119] S.M.E. Feely, M. Laura, C.E. Siskind, S. Sottile, M. Davis, V.S. Gibbons, M.M. Reilly, and M.E. Shy. Mfn2 mutations cause severe phenotypes in most patients with cmt2a. *Neurology*, 76(20):1690–1696, 2011.

- [120] Stephan Z"uchner, Irina V Mersiyanova, Maria Muglia, Neda Bissar-Tadmouri, Jennifer Rochelle, Ece L Dadali, Mario Zappia, Eva Nelis, Antonella Patitucci, Jan Senderek, et al. Mutations in the mitochondrial gtpase mitofusin 2 cause charcot-marie-tooth neuropathy type 2a. *Nat Genet*, 36(5):449–451, 2004. Erratum in: *Nat Genet*. 2004 Jun;36(6):660. Battaloglu E [corrected to Battaloglu E].
- [121] Francesca Bombelli, Tanya Stojkovic, Odile Dubourg, Andoni Echaniz-Laguna, Sophie Tardieu, Karine Larcher, Patrizia Amati-Bonneau, Philippe Latour, Olivier Vignal, Cécile Cazeneuve, Alexis Brice, and Eric Leguern. Charcot-marie-tooth disease type 2a: from typical to rare phenotypic and genotypic features. *JAMA neurology*, 71(8):1036–1042, 2014.
- [122] Victoria H Lawson, Beverly V Graham, and Kevin M Flanigan. Clinical and electrophysiologic features of cmt2a with mutations in the mitofusin 2 gene. *Neurology*, 65(2):197–204, 2005.
- [123] Keshav K Singh and Josephine S. Modica-Napolitano. Special issue: Mitochondria in cancer. *Seminars in Cancer Biology*, 47:iv–vi, 2017. Mitochondria in Cancer.
- [124] Poorva Ghosh, Chantal Vidal, Sanchareeka Dey, and Li Zhang. Mitochondria targeting as an effective strategy for cancer therapy. *International Journal of Molecular Sciences*, 21(9), 2020.
- [125] Sergey Pustynnikov, Francesca Costabile, Silvia Beghi, and Andrea Facciabene. Targeting mitochondria in cancer: current concepts and immunotherapy approaches. *Translational Research*, 202:35–51, 2018.
- [126] Alessandro Allegra, Vanessa Innao, Andrea Gaetano Allegra, and Caterina Musolino. Relationship between mitofusin 2 and cancer. *Advances in Protein Chemistry and Structural Biology*, 116:209–236, 2019.
- [127] Fatemeh Darvish Moghaddam, Peyman Mortazavi, Saeed Hamed, Mohammad Nabiuni, and Nas-taran Hassanzadeh Roodbari. Apoptotic effects of melittin on 4t1 breast cancer cell line is associated with up regulation of mfn1 and drp1 mrna expression. *Anticancer Agents Med Chem*, 20(7):790–799, 2020.
- [128] Zhong Zhang, Ting-E Li, Min Chen, and et al. Mfn1-dependent alteration of mitochondrial dynamics drives hepatocellular carcinoma metastasis by glucose metabolic reprogramming. *British Journal of Cancer*, 122:209–220, feb 2020.
- [129] Rehman Jalees, Zhang Hannah J, Toth Peter T, Zhang Yanmin, Marsboom Glenn, Hong Zhigang, Salgia Ravi, Husain Aliya N, Wietholt Christian, and Archer Stephen L. Inhibition of mitochondrial fission prevents cell cycle progression in lung cancer. *FASEB J.*, 26(5):0892–6638, 2012. PMID: 22321727.
- [130] Ahn Sung Yong, Song Jiwon, Kim Yu Cheon, Kim Myoung Hee, and Hyun Young-Min. Mitofusin-2 promotes the epithelial-mesenchymal transition-induced cervical cancer progression. *Immune Netw*, 21, 2021.
- [131] Xiaofei Cheng, Yanqing Li, and Fanlong Liu. Prognostic impact of mitofusin 2 expression in colon cancer. *Translational Cancer Research*, 11(10), 2022.
- [132] Luca Simula, Francesca Nazio, and Silvia Campello. The mitochondrial dynamics in cancer and immune-surveillance. *Seminars in Cancer Biology*, 47:29–42, 2017. Mitochondria in Cancer.

- [133] Dario De Vecchis, Astrid Brandner, Marc Baaden, Mickael M. Cohen, and Antoine Taly. A molecular perspective on mitochondrial membrane fusion: From the key players to oligomerization and tethering of mitofusin. *J. Membr. Biol.*, 252(4):293–306, 2019.
- [134] Xiaofang Huang, Xin Zhou, Xiaoyu Hu, Amit S. Joshi, Xiangyang Guo, Yushan Zhu, Quan Chen, William A. Prinz, and Junjie Hu. Sequences flanking the transmembrane segments facilitate mitochondrial localization and membrane fusion by mitofusin. *Proceedings of the National Academy of Sciences*, 114(46):E9863–E9872, 2017.
- [135] Frédéric Daste, Cécile Sauvanet, Andrej Bavdek, James Baye, Fabienne Pierre, Rémi Le Borgne, Claudine David, Manuel Rojo, Patrick Fuchs, and David Tareste. The heptad repeat domain 1 of mitofusin has membrane destabilization function in mitochondrial fusion. *EMBO reports*, 19(6), 2018.
- [136] Juan S Bonifacino and Benjamin S Glick. The mechanisms of vesicle budding and fusion. *Cell*, 116(2):153–166, January 2004.
- [137] Tobias Brandt, Laetitia Cavellini, Werner Kühlbrandt, and Mickaël M Cohen. A mitofusin-dependent docking ring complex triggers mitochondrial fusion *in vitro*. *eLife*, 5:e14618, jun 2016.
- [138] Alexander Abrams, Robert Hufnagel, Adriana Rebelo, Claudia Zanna, Neville Patel, Michael Gonzalez, Ion Campeanu, Laurie Griffin, Saskia Groenewald, Alleene Strickland, Feifei Tao, Fiorella Speziani, Lisa Abreu, Rebecca Schüle, Leonardo Caporali, Chiara Morgia, Alessandra Maresca, Rocco Liguori, Raffaele Lodi, and Julia Dallman. Mutations in *slc25a46*, encoding a *ugo1*-like protein, cause an optic atrophy spectrum disorder. *Nature genetics*, 47, 07 2015.
- [139] Yu-Lu Cao, Shuxia Meng, Yang Chen, Jian-Xiong Feng, Dong-Dong Gu, Bing Yu, Yu-Jie Li, Jin-Yu Yang, Shuang Liao, David C Chan, and Song Gao. Mfn1 structures reveal nucleotide-triggered dimerization critical for mitochondrial fusion. *Nature*, 542:372–376, 2017.
- [140] Liming Yan, Yuanbo Qi, Xiaofeng Huang, and et al. Structural basis for gtp hydrolysis and conformational change of *mfn1* in mediating membrane fusion. *Nat Struct Mol Biol*, 25:233–243, 2018.
- [141] Yu-Jie Li, Yu-Lu Cao, Jian-Xiong Feng, Yuanbo Qi, Shuxia Meng, Jie-Feng Yang, Ya-Ting Zhong, Sisi Kang, Xiaoxue Chen, Lan Lan, Li Luo, Bing Yu, Shoudeng Chen, David C Chan, Junjie Hu, and Song Gao. Structural insights of human mitofusin-2 into mitochondrial fusion and *cmt2a* onset. *Nature Communications*, 10(1):4914, 2019.
- [142] Fabian Anton, Gunnar Dittmar, Thomas Langer, and Mafalda Escobar-Henriques. Two deubiquitylases act on mitofusin and regulate mitochondrial fusion along independent pathways. *Molecular Cell*, 49(3):487–498, 2013.
- [143] Antonietta Franco, Richard N. Kitsis, Julie A. Fleischer, Evripidis Gavathiotis, Opher S. Kornfeld, Guohua Gong, Nikolaos Biris, Ann Benz, Nir Qvit, Sara K. Donnelly, Yun Chen, Steven Menerick, Louis Hodgson, Daria Mochly-Rosen, and Gerald W. II Dorn. Correcting mitochondrial fusion by manipulating mitofusin conformations. *Nature*, 540(7631):74–79, 2016.
- [144] Małgorzata Beręsewicz, Anna Boratyńska-Jasińska, Łukasz Charzewski, Maria Kawalec, Dagmara Kabzińska, Andrzej Kochański, Krystiana A. Krzyśko, and Barbara Zabłocka. The effect

of a novel c.820c>t (arg274trp) mutation in the mitofusin 2 gene on fibroblast metabolism and clinical manifestation in a patient. *PLOS ONE*, 12(1):1–25, 01 2017.

- [145] Romain Gautier, Amélie Bacle, Marion L. Tiberti, Patrick F. Fuchs, Stefano Vanni, and Bruno Antony. Packmem: A versatile tool to compute and visualize interfacial packing defects in lipid bilayers. *Biophysical Journal*, 115(3):436–444, 2018.
- [146] Per Larsson and Peter M. Kasson. Lipid tail protrusion in simulations predicts fusogenic activity of influenza fusion peptide mutants and conformational models. *PLoS Comput Biol*, 9(3):e1002950, 2013.
- [147] Mukarram A.Tahir, Reid C.Van Lehn, S.H. Choi, and Alfredo Alexander-Katz. Solvent-exposed lipid tail protrusions depend on lipid membrane composition and curvature. *Biochimica et Biophysica Acta (BBA) - Biomembranes*, 1858(6):1207–1215, 2016.
- [148] Yuliya Smirnova, Siewert Marrink, Reinhard Lipowsky, and Volker Knecht. Solvent-exposed tails as prestalk transition states for membrane fusion at low hydration. *Journal of the American Chemical Society*, 132:6710–8, 05 2010.
- [149] Chetan S. Poojari, Katharina C. Scherer, and Jochen S. Hub. Free energies of membrane stalk formation from a lipidomics perspective. *Nature Communications*, 12(1):6594, 2021.
- [150] Yuliya G. Smirnova, Herre J. Risselada, and Martin Müller. Thermodynamically reversible paths of the first fusion intermediate reveal an important role for membrane anchors of fusion proteins. *Proceedings of the National Academy of Sciences*, 116(7):2571–2576, 2019.
- [151] Peter M Kasson, Nicholas W Kelley, Nina Singhal, Marija Vrljic, Axel T Brunger, and Vijay S Pande. Ensemble molecular dynamics yields submillisecond kinetics and intermediates of membrane fusion. *Proceedings of the National Academy of Sciences*, 103(32):11916–11921, 2006.
- [152] Volker Knecht and Siewert-Jan Marrink. Molecular dynamics simulations of lipid vesicle fusion in atomic detail. *Biophysical Journal*, 92(12):4254–4261, 2007.
- [153] Hiroshi Noguchi and Masako Takasu. Fusion pathways of vesicles: A brownian dynamics simulation. *Journal of Chemical Physics*, 2001.
- [154] Herre Jelger Risselada, Carsten Kutzner, and Helmut Grubmüller. Caught in the act: Visualization of snare-mediated fusion events in molecular detail. *ChemBioChem*, 12(7):1049–1055, 2011.
- [155] Herre Risselada and Helmut Grubmüller. How snare molecules mediate membrane fusion: Recent insights from molecular simulations. *Current opinion in structural biology*, 22:187–96, 02 2012.
- [156] Anton A. Polyansky, Anton O. Chugunov, Pavel E. Volynsky, Nikolay A. Krylov, Dmitry E. Nolde, and Roman G. Efremov. Preddimer: a web server for prediction of transmembrane helical dimers. *Bioinformatics*, 30:889–890, 2014.
- [157] Yuji Sugita and Yuko Okamoto. Replica-exchange molecular dynamics method for protein folding. *Chemical Physics Letters*, 314(1):141–151, 1999.
- [158] John Jumper, Richard Evans, Alexander Pritzel, et al. Highly accurate protein structure prediction with alphafold. *Nature*, 596:583–589, 2021.

- [159] Minkyung Baek, Frank DiMaio, Ivan Anishchenko, Justas Dauparas, Sergey Ovchinnikov, Gyu Rie Lee, Jue Wang, Qian Cong, Lisa N. Kinch, R. Dustin Schaeffer, Claudia Millán, Hahn-beom Park, Carson Adams, Caleb R. Glassman, Andy DeGiovanni, Jose H. Pereira, Andria V. Rodrigues, Alberdina A. van Dijk, Ana C. Ebrecht, Diederik J. Opperman, Theo Sagmeister, Christoph Buhlheller, Tea Pavkov-Keller, Manoj K. Rathinaswamy, Udit Dalwadi, Calvin K. Yip, John E. Burke, K. Christopher Garcia, Nick V. Grishin, Paul D. Adams, Randy J. Read, and David Baker. Accurate prediction of protein structures and interactions using a three-track neural network. *Science*, 373(6557):871–876, 2021. Publisher: American Association for the Advancement of Science.
- [160] Ron Dror, Morten Jensen, David Borhani, and David Shaw. Perspectives on: Molecular dynamics and computational methods: Exploring atomic resolution physiology on a femtosecond to millisecond timescale using molecular dynamics simulations. *The Journal of general physiology*, 135:555–62, 06 2010.
- [161] Siewert J Marrink, H Jelger Risselada, Serge Yefimov, D Peter Tieleman, and Alex H De Vries. The martini force field: coarse grained model for biomolecular simulations. *The journal of physical chemistry B*, 111(27):7812–7824, 2007.
- [162] Luca Monticelli, Senthil K Kandasamy, Xavier Periole, Ronald G Larson, D Peter Tieleman, and Siewert-Jan Marrink. The martini coarse-grained force field: extension to proteins. *Journal of chemical theory and computation*, 4(5):819–834, 2008.
- [163] Djurre H. de Jong, Gurpreet Singh, W. F. Drew Bennett, Clement Arnarez, Tsjerk A. Wassenaar, Lars V. Schäfer, Xavier Periole, D. Peter Tieleman, and Siewert J. Marrink. Improved parameters for the martini coarse-grained protein force field. *Journal of chemical theory and computation*, 9(1):687–697, 2012.
- [164] Paulo C. T. Souza, Roberto Alessandri, Julien Barnoud, and et al. Martini 3: a general purpose force field for coarse-grained molecular dynamics. *Nature Methods*, 18:382–388, 2021.
- [165] Celine Anezo, Alex Vries, Hans-Dieter Holtje, D Tieleman, and Siewert Marrink. Methodological issues in lipid bilayer simulations. *The Journal of Physical Chemistry B*, 107, 09 2003.
- [166] Tom Darden, Darrin York, and Lee Pedersen. Particle mesh ewald: An $n\log(n)$ method for ewald sums in large systems. *The Journal of Chemical Physics*, 98(12):10089–10092, 1993.
- [167] Ulrich Essmann, Lalith Perera, Max L. Berkowitz, Tom Darden, Hsing Lee, and Lee G. Pedersen. A smooth particle mesh ewald method. *The Journal of Chemical Physics*, 103(19):8577–8593, 1995.
- [168] P. P. Ewald. Die Berechnung optischer und elektrostatischer Gitterpotentiale, January 1921.
- [169] Wendy D. Cornell, Piotr Cieplak, Christopher I. Bayly, Ian R. Gould, Kenneth M. Merz, David M. Ferguson, David C. Spellmeyer, Thomas Fox, James W. Caldwell, and Peter A. Kollman. A second generation force field for the simulation of proteins, nucleic acids, and organic molecules. *Journal of the American Chemical Society*, 117:5179–5197, 1995.
- [170] Jeffery B. Klauda, Richard M. Venable, J. Alfredo Freites, Joseph W. O’Connor, Douglas J. Tobias, Carlos Mondragon-Ramirez, Igor Vorobyov, Alexander D. MacKerell, and Richard W. Pastor.

- Update of the charmm all-atom additive force field for lipids: Validation on six lipid types. *The Journal of Physical Chemistry B*, 114(23):7830–7843, 2010. PMID: 20496934.
- [171] R.W Hockney, S.P Goel, and J.W Eastwood. Quiet high-resolution computer models of a plasma. *Journal of Computational Physics*, 14(2):148–158, 1974.
- [172] Berk Hess. P-lincs: A parallel linear constraint solver for molecular simulation. *Journal of Chemical Theory and Computation*, 4(1):116–122, 2008. PMID: 26619985.
- [173] Herman Berendsen, J.P.M. Postma, Wilfred van Gunsteren, AD DiNola, and J.R. Haak. Molecular-dynamics with coupling to an external bath. *The Journal of Chemical Physics*, 81:3684, 10 1984.
- [174] Giovanni Bussia, Davide Donadio, and Michele Parrinello. Canonical sampling through velocity rescaling. *J. Chem. Phys.*, 126:014101–014107, 2007.
- [175] M. Parrinello and A. Rahman. Polymorphic transitions in single crystals: A new molecular dynamics method. *J. Appl. Phys.*, 52:7182–7190, 1981.
- [176] David Van Der Spoel, Erik Lindahl, Berk Hess, Gerrit Groenhof, Alan E Mark, and Herman JC Berendsen. Gromacs: fast, flexible, and free. *Journal of Computational Chemistry*, 26(16):1701–1718, 2005.
- [177] Mark James Abraham, Teemu Murtola, Roland Schulz, Szilárd Páll, Jeremy C Smith, Berk Hess, and Erik Lindahl. Gromacs: High performance molecular simulations through multi-level parallelism from laptops to supercomputers. *SoftwareX*, 1:19–25, 2015.
- [178] Sunhwan Jo, Taehoon Kim, Vidyashankara G. Iyer, and Wonpil Im. Charmm-gui: A web-based graphical user interface for charmm. *Journal of Computational Chemistry*, 29:1859–1865, 2008.
- [179] William H. Press, Saul A. Teukolsky, William T. Vetterling, and Brian P. Flannery. *Numerical Recipes 3rd Edition: The Art of Scientific Computing*. Cambridge University Press, USA, 3 edition, 2007.
- [180] William Humphrey, Andrew Dalke, and Klaus Schulten. VMD – Visual Molecular Dynamics. *Journal of Molecular Graphics*, 14:33–38, 1996.
- [181] Xavier Daura, Karl Gademann, Bernhard Jaun, Wilfred F. Seebach, Dieter ans van Gunsteren, and Alan E. Mark. Peptide folding: When simulation meets experiment. *Angew. Chem. Int. Ed.*, 38:236–240, 1999.
- [182] Jaakko Uusitalo, Helgi Ingólfsson, Parisa Akhshi, D. Tieleman, and Siewert Marrink. Martini coarse-grained force field: Extension to dna. *Journal of Chemical Theory and Computation*, 11:150723135724002, 07 2015.
- [183] Ryan Bradley and Ravi Radhakrishnan. Coarse-grained models for protein-cell membrane interactions. *Polymers*, 5:890–936, 09 2013.
- [184] Austin C. Stark, Casey T. Andrews, and Adrian H. Elcock. Toward optimized potential functions for protein–protein interactions in aqueous solutions: Osmotic second virial coefficient calculations using the martini coarse-grained force field. *Journal of Chemical Theory and Computation*, 9(9):4176–4185, 2013.

- [185] Matti Javanainen, Hector Martinez-Seara, and Ilpo Vattulainen. Excessive aggregation of membrane proteins in the martini model. *PLOS ONE*, 12(11):1–20, 11 2017.
- [186] Philipp S. Schmalhorst, Felix Deluweit, Roger Scherrers, Carl-Philipp Heisenberg, and Mateusz Sikora. Overcoming the limitations of the martini force field in simulations of polysaccharides. *Journal of Chemical Theory and Computation*, 13(10):5039–5053, 2017. PMID: 28787166.
- [187] Yoshiharu Mori and Yuko Okamoto. Generalized-ensemble algorithms for the isobaric–isothermal ensemble. *Journal of the Physical Society of Japan*, 79(7):074003, 2010.
- [188] Alexandra Patriksson and David van der Spoel. A temperature predictor for parallel tempering simulations. *Physical chemistry chemical physics : PCCP*, 10:2073–7, 05 2008.
- [189] Ayori Mitsutake, Yuji Sugita, and Yuko Okamoto. Replica-exchange multicanonical and multicanonical replica-exchange monte carlo simulations of peptides. i. formulation and benchmark test. *The Journal of Chemical Physics*, 118(14):6664–6675, 2003.
- [190] Koji Yoshida, Toshio Yamaguchi, and Yuko Okamoto. Replica-exchange molecular dynamics simulation of small peptide in water and in ethanol. *Chemical Physics Letters*, 412(4):280–284, 2005.
- [191] Heiko Nymeyer, Thomas B Woolf, and Angel E Garcia. Folding is not required for bilayer insertion: replica exchange simulations of an alpha-helical peptide with an explicit lipid bilayer. *Proteins*, 59(4):783–790, Jun 2005.
- [192] L Steven Johnson, Sean Eddy, and Elon Portugaly. Johnson ls, eddy sr, portugaly e.. hidden markov model speed heuristic and iterative hmm search procedure. *bmc bioinformatics* 11: 431. *BMC bioinformatics*, 11:431, 08 2010.
- [193] Michael Remmert, Andreas Biegert, Andreas Hauser, and Johannes Söding. Hhblits: Lightning-fast iterative protein sequence searching by hmm-hmm alignment. *Nature methods*, 9:173–5, 12 2011.
- [194] Yu-Lu Cao, Shuxia Meng, Yang Chen, Jian-Xiong Feng, Dong-Dong Gu, Bing Yu, Yu-Jie Li, Jin-Yu Yang, Shuang Liao, David C. Chan, and Song Gao. Mfn1 structures reveal nucleotide-triggered dimerization critical for mitochondrial fusion. *Nature*, 542:372–376, 2017.
- [195] Liming Yan, Yuanbo Qi, Xiaofang Huang, Caiting Yu, Lan Lan, Xiangyang Guo, Zihe Rao, Junjie Hu, and Zhiyong Lou. Structural basis for gtp hydrolysis and conformational change of mfn1 in mediated membrane fusion. *Nat. Struct. Mol.*, 25:233–243, 2017.
- [196] E. D. Wong, J. A. Wagner, S. W. Gorsich, J. M. McCaffery, J. M. Shaw, and J. Nunnari. The dynamin-related GTPase, mgm1p, is an intermembrane space protein required for maintenance of fusion competent mitochondria. *J. Cell Biol.*, 151(2):341–352, 2000.
- [197] Christian Frezza, Sara Cipolat, Olga Martins de Brito, Massimo Micaroni, Galina V. Beznoussenko, Tomasz Rudka, Davide Bartoli, Roman S. Polishuck, Nika N. Danial, Bart De Strooper, and Luca Scorrano. OPA1 controls apoptotic cristae remodeling independently from mitochondrial fusion. *Cell*, 126(1):177–189, 2006.

- [198] Manfred Lindau, Benjamin A. Hall, Alan Chetwynd, Oliver Beckstein, and Mark S. P. Sansom. Coarse-Grain Simulations Reveal Movement of the Synaptobrevin C-Terminus in Response to Piconewton Forces. *Biophysical Journal*, 103(5):959–969, September 2012.
- [199] Jing Han, Kristyna Pluhackova, Dieter Bruns, and Rainer A. Böckmann. Synaptobrevin transmembrane domain determines the structure and dynamics of the snare motif and the linker region. *Biochimica et Biophysica Acta (BBA) - Biomembranes*, 1858(4):855–865, 2016.
- [200] Jan-Dirk Wehland, Antonina S. Lygina, Pawan Kumar, Samit Guha, Barbara E. Hubrich, Reinhard Jahn, and Ulf Diederichsen. Role of the transmembrane domain in snare protein mediated membrane fusion: peptide nucleic acid/peptide model systems. *Mol. BioSyst.*, 12:2770–2776, 2016.
- [201] Madhurima Dhara, Antonio Yarzagaray, Mazen Makke, Barbara Schindeldecker, Yvonne Schwarz, Ahmed Shaaban, Satyan Sharma, Rainer A Böckmann, Manfred Lindau, Ralf Mohrmann, and Dieter Bruns. v-snare transmembrane domains function as catalysts for vesicle fusion. *eLife*, 5:e17571, jun 2016.
- [202] Erik E. Griffin and David C. Chan. Domain interactions within fzo1 oligomers are essential for mitochondrial fusion. *J. Biol. Chem.*, 281(24):16599–16606, 2006.
- [203] Amita R Sahoo, Paulo CT Souza, Zhiyuan Meng, and Matthias Buck. Transmembrane dimers of type 1 receptors sample alternate configurations: Md simulations using coarse grain martini 3 versus alphafold2 multimer. *Structure*, 31(6):735–745, 2023.
- [204] Justin L. MacCallum, W. F. Drew Bennett, and D. Peter Tieleman. Distribution of amino acids in a lipid bilayer from computer simulations. *Biophysical Journal*, 94(9):3393–3404, 2008.
- [205] Nicholas J. Gleason, Vitaly V. Vostrikov, Denise V. Greathouse, and Roger E. Koeppe. Buried lysine, but not arginine, titrates and alters transmembrane helix tilt. *Proceedings of the National Academy of Sciences*, 110(5):1692–1695, 2013.
- [206] Afra Panahi and Charles L. III Brooks. Membrane environment modulates the pka values of transmembrane helices. *The Journal of Physical Chemistry B*, 119(13):4601–4607, 2015. PMID: 25734901.
- [207] UniProt Consortium. UniProt: a worldwide hub of protein knowledge. *Nucleic acids research*, 47(D1):D506–D515, 2018.
- [208] Daniel WA Buchan and David T Jones. The PSIPRED protein analysis workbench: 20 years on. *Nucleic acids research*, 47(W1):W402–W407, 2019.
- [209] David T Jones. Protein secondary structure prediction based on position-specific scoring matrices. *Journal of molecular biology*, 292(2):195–202, 1999.
- [210] Anders Krogh, BjoÈrn Larsson, Gunnar Von Heijne, and Erik LL Sonnhammer. Predicting transmembrane protein topology with a hidden Markov model: application to complete genomes. *Journal of molecular biology*, 305(3):567–580, 2001.
- [211] E. L. Sonnhammer, G. von Heijne, and A. Krogh. A hidden markov model for predicting transmembrane helices in protein sequences. *Proc Int Conf Intell Syst Mol Biol*, 6:175–182, 1998.

- [212] Bertrand Néron, Hervé Ménager, Corinne Maufrais, Nicolas Joly, Julien Maupetit, Sébastien Letort, Sébastien Carrere, Pierre Tuffery, and Catherine Letondal. Mobylye: a new full web bioinformatics framework. *Bioinformatics*, 25(22):3005–3011, 2009.
- [213] Yifei Qi, Helgi I. Ingólfsson, Xi Cheng, Jumin Lee, Siewert J. Marrink, and Wonpil Im. Charmm-gui martini maker for coarse-grained simulations with the martini force field. *J. Chem. Theory and Comput.*, 11(9):4486–4494, 2015.
- [214] Berk Hess, Henk Bekker, Herman J. C. Berendsen, and Johannes G. E. M. Fraaije. LINCS: A linear constraint solver for molecular simulations. *Journal of Computational Chemistry*, 18(12):1463–1472, 1997.
- [215] Ilario G. Tironi, René Sperb, Paul E. Smith, and Wilfred F. van Gunsteren. A generalized reaction field method for molecular dynamics simulations. *J. Chem. Phys.*, 102(13):5451–5459, 1995.
- [216] Cyrus Chothia, Michael Levitt, and Douglas Richardson. Helix to helix packing in proteins. *Journal of Molecular Biology*, 145:215–250, 1981.
- [217] Naveen Michaud-Agrawal, Elizabeth J. Denning, Thomas B. Woolf, and Oliver Beckstein. MDAnalysis: A toolkit for the analysis of molecular dynamics simulations. *Journal of Computational Chemistry*, 32(10):2319–2327, 2011.
- [218] Richard J. Gowers, Max Linke, Jonathan Barnoud, Tyler J. E. Reddy, Manuel N. Melo, Sean L. Seyler, Jan Domański, David L. Dotson, Sébastien Buchoux, Ian M. Kenney, and Oliver Beckstein. MDAnalysis: A python package for the rapid analysis of molecular dynamics simulations. *Proceedings of the 15th Python in Science Conference*, pages 98–105, 2016.
- [219] Hadley Wickham. *ggplot2: Elegant Graphics for Data Analysis*. Springer-Verlag New York, 2016.
- [220] Jing Huang, Sarah Rauscher, Grzegorz Nawrocki, Ting Ran, Michael Feig, Bert L. de Groot, Helmut Grubmüller, and Alexander D. MacKerell. CHARMM36m: An improved force field for folded and intrinsically disordered proteins. *Nat Methods*, 14(1):71–73, 2017.
- [221] Tsjerk A. Wassenaar, Kristyna Pluhackova, Rainer A. Böckmann, Siewert J. Marrink, and D. Peter Tieleman. Going backward: A flexible geometric approach to reverse transformation from coarse grained to atomistic models. *Journal of Chemical Theory and Computation*, 10(2):676–690, 2014. Relation: <https://www.rug.nl/> Rights: University of Groningen, Groningen Biomolecular Sciences and Biotechnology Institute.
- [222] Shuichi Miyamoto and Peter A Kollman. Settle: An analytical version of the shake and rattle algorithm for rigid water models. *Journal of computational chemistry*, 13(8):952–962, 1992.
- [223] Richard Evans and et al. Protein complex prediction with alphafold-multimer. *biorxiv*, 2021.
- [224] Milot Mirdita, Konstantin Schütze, Yuki Moriwaki, Lim Heo Heo, Sergey Ovchinnikov, and Martin Steinegger. Colabfold: Making protein folding accessible to all. *Nature Methods*, 2022.
- [225] F Sherman, G Fink, and J Hicks. *Methods in yeast genetics: a laboratory course manual*, 1987.
- [226] Christiane Volland, Daniele Urban-Grimal, Gerard Geraud, and Rosine Haguenaue-Tsapis. Endocytosis and degradation of the yeast uracil permease under adverse conditions. *Journal of Biological Chemistry*, 269(13):9833–9841, 1994.

- [227] Robert S Sikorski and Philip Hieter. A system of shuttle vectors and yeast host strains designed for efficient manipulation of dna in *saccharomyces cerevisiae*. *Genetics*, 122(1):19–27, 1989.
- [228] Mickael M Cohen, Elizabeth A Amiott, Adam R Day, Guillaume P Leboucher, Erin N Pryce, Michael H Glickman, J Michael McCaffery, Janet M Shaw, and Allan M Weissman. Sequential requirements for the gtpase domain of the mitofusin *fzo1* and the ubiquitin ligase *scfmdm30* in mitochondrial outer membrane fusion. *Journal of cell science*, 124(9):1403–1410, 2011.
- [229] Bettina Brosig and Dieter Langosch. The dimerization motif of the glycophorin a transmembrane segment in membrane: importance of glycine residues. *Protein Sci.*, 7:1052–1056, 2008.
- [230] Pierre Hubert, Paul Sawma, Jean-Pierre Duneau, Jonathan Khao, J  ler  me Dominique H  nin, Bagnard, and James Sturgis. Single-spanning transmembrane domains in cell growth and cell-cell interactions: More than meets the eye? *Cell Adh Migr*, 4:313–324, 2010.
- [231] R. F. S. Walters and W. F. DeGrado. Helix packing motifs in membrane proteins. *Proc. Natl. Acad.*, 103:13658–13663, 2006.
- [232] Shao-Qing Zhang, Daniel W. Kulp, Chaim A. Schramm, Marco Mravic, Ilan Samish, and William F. DeGrado. The membrane- and soluble-protein helix-helix interactome: similar geometry via different interactions. *Structure*, 23:527–541, 2015.
- [233] Fr  d  ric Pincet, Luc Lebeau, and Sophie Cribier. Short-range specific forces are able to induce hemifusion. *European Biophysics Journal*, 30:91–97, 2001.
- [234] Per Larsson and Peter M Kasson. Lipid tail protrusion in simulations predicts fusogenic activity of influenza fusion peptide mutants and conformational models. *PLoS Computational Biology*, 9(3):e1002950, 2013.
- [235] Claire Fran  ois-Martin, Am  lie Bacle, James E. Rothman, Patrick F. J. Fuchs, and Fr  d  ric Pincet. Cooperation of conical and polyunsaturated lipids to regulate initiation and processing of membrane fusion. *Frontiers in Molecular Biosciences*, 8, 2021.
- [236] Filip Rolland, Joris Winderickx, and Johan M Thevelein. Glucose-sensing and-signalling mechanisms in yeast. *FEMS yeast research*, 2(2):183–201, 2002.
- [237] Juana M Gancedo. Yeast carbon catabolite repression. *Microbiology and molecular biology reviews*, 62(2):334–361, 1998.
- [238] Christos Lamprakis, Ioannis Andreadelis, John Manchester, Camilo Velez-Vega, Jos   S. Duca, and Zoe Cournia. Evaluating the efficiency of the martini force field to study protein dimerization in aqueous and membrane environments. *Journal of Chemical Theory and Computation*, 17(5):3088–3102, 2021.
- [239] Mariano A. Ostuni, Patricia Hermand, Emeline Saindoy, No  lline Guillou, Julie Guellec, Audrey Coens, Claude Hattab, Elodie Desuzinges-Mandon, Anass Jawhari, Soria Iatmanen-Harbi, Olivier Lequin, Patrick Fuchs, Jean-Jacques Lacapere, Christophe Combadi  re, Fr  d  ric Pincet, and Philippe Deterre. Cx3cl1 homo-oligomerization drives cell-to-cell adherence. *Scientific Reports*, 10(1):9069, Jun 2020.

- [240] Verity Jackson, Julia Hermann, Christopher J Tynan, Daniel J Rolfe, Robin A Corey, Anna L Duncan, Maxime Noriega, Amy Chu, Antreas C Kalli, E Yvonne Jones, et al. The guidance and adhesion protein flrt2 dimerizes in cis via dual small-x3-small transmembrane motifs. *Structure*, 30(9):1354–1365, 2022.
- [241] Azadeh Alavizargar, Annegret Elting, Roland Wedlich-Soldner, and Andreas Heuer. Lipid-mediated association of the slg1 transmembrane domains in yeast plasma membranes. *The Journal of Physical Chemistry B*, 126(17):3240–3256, 2022.
- [242] Mariana Valério, Diogo A. Mendonça, João Morais, Carolina C. Buga, Carlos H. Cruz, Miguel A.R.B. Castanho, Manuel N. Melo, Cláudio M. Soares, Ana Salomé Veiga, and Diana Lousa. Parainfluenza fusion peptide promotes membrane fusion by assembling into oligomeric porelike structures. *ACS Chemical Biology*, 17(7):1831–1843, 2022. PMID: 35500279.
- [243] J. Karl Spinti, Fernando Neiva Nunes, and Manuel N. Melo. Room for improvement in the initial martini 3 parameterization of peptide interactions. *Chemical Physics Letters*, 819:140436, 2023.
- [244] Ainara Claveras Cabezudo, Christina Athanasiou, Alexandros Tsengenes, and Rebecca C. Wade. Scaling protein-water interactions in the martini 3 coarse-grained force field to simulate transmembrane helix dimers in different lipid environments. *bioRxiv*, 2023.
- [245] Z. Lin, H. Akin, R. Rao, B. Hie, Z. Zhu, W. Lu, N. Smetanin, R. Verkuil, O. Kabeli, Y. Shmueli, A. Dos Santos Costa, M. Fazel-Zarandi, T. Sercu, S. Candido, and A. Rives. Evolutionary-scale prediction of atomic-level protein structure with a language model. *Science*, 379(6637):1123–1130, Mar 2023.
- [246] M. Graille, S. Sacquin-Mora, and A. Taly. Best Practices of Using AI-Based Models in Crystallography and Their Impact in Structural Biology. *J Chem Inf Model*, Jun 2023.
- [247] Fabian Anton, Julia M. Fres, Astrid Schauss, Benoît Pinson, Gerrit J. K. Praefcke, Thomas Langer, and Mafalda Escobar-Henriques. Ugo1 and Mdm30 act sequentially during Fzo1-mediated mitochondrial outer membrane fusion. *Journal of Cell Science*, 124(7):1126–1135, 04 2011.
- [248] Holger A. Scheidt, Katja Kolocaj, David B. Konrad, James A. Frank, Dirk Trauner, Dieter Langosch, and Daniel Huster. Light-induced lipid mixing implies a causal role of lipid splay in membrane fusion. *Biochimica et Biophysica Acta (BBA) - Biomembranes*, 1862(11):183438, 2020.
- [249] Stefano Vanni, Lydie Vamparys, Romain Gautier, Guillaume Drin, Catherine Etchebest, Patrick F.J. Fuchs, and Bruno Antonny. Amphipathic lipid packing sensor motifs: Probing bilayer defects with hydrophobic residues. *Biophysical Journal*, 104(3):575–584, 2013.
- [250] D. Langosch, M. Hofmann, and C. Ungermann. The role of transmembrane domains in membrane fusion. *Cellular and Molecular Life Sciences*, 64(7):850, Feb 2007.
- [251] Mohamed M Elsutohy, Veeren M Chauhan, Robert Markus, Mohammed Aref Kyyaly, Saul JB Tandler, and Jonathan W Aylott. Real-time measurement of the intracellular ph of yeast cells during glucose metabolism using ratiometric fluorescent nanosensors. *Nanoscale*, 9(18):5904–5911, 2017.

- [252] Shailendra S. Rathore, Yinghui Liu, Haijia Yu, Chun Wan, MyeongSeon Lee, Qian Yin, Michael H. B. Stowell, and Jingshi Shen. Intracellular Vesicle Fusion Requires a Membrane-Destabilizing Peptide Located at the Juxtamembrane Region of the v-SNARE. *Cell Reports*, 29(13):4583–4592.e3, December 2019.
- [253] Sandro Bottaro and Kresten Lindorff-Larsen. Biophysical experiments and biomolecular simulations: A perfect match? *Science*, 361(6400):355–360, Jul 2018.
- [254] Helgi I Ingólfsson, Cesar A Lopez, Jaakko J Uusitalo, Djurre H de Jong, Srinivasa M Gopal, Xavier Periole, and Siewert J Marrink. The power of coarse graining in biomolecular simulations. *Wiley Interdisciplinary Reviews: Computational Molecular Science*, 4(3):225–248, May 2014.
- [255] Zack Jarin, James Newhouse, and Gregory A. Voth. Coarse-grained force fields from the perspective of statistical mechanics: Better understanding of the origins of a martini hangover. *Journal of Chemical Theory and Computation*, 17(2):1170–1180, 2021. PMID: 33475352.
- [256] Sriraksha Srinivasan, Valeria Zoni, and Stefano Vanni. Estimating the accuracy of the martini model towards the investigation of peripheral protein–membrane interactions. *Faraday Discuss.*, 232:131–148, 2021.
- [257] Niek van Hilten, Kai Steffen Stroh, and Herre Jelger Risselada. Efficient quantification of lipid packing defect sensing by amphipathic peptides: Comparing martini 2 and 3 with charmm36. *Journal of Chemical Theory and Computation*, 18(7):4503–4514, 2022. PMID: 35709386.
- [258] F. Emil Thomasen, Francesco Pesce, Mette Ahrensback Roesgaard, Giulio Tesei, and Kresten Lindorff-Larsen. Improving martini 3 for disordered and multidomain proteins. *Journal of Chemical Theory and Computation*, 18(4):2033–2041, 2022. PMID: 35377637.
- [259] F. Emil Thomasen, Tórrur Skaalum, Ashutosh Kumar, Sriraksha Srinivasan, Stefano Vanni, and Kresten Lindorff-Larsen. Recalibration of protein interactions in martini 3. *bioRxiv*, 2023.
- [260] P. Gehan, S. Kulifaj, P. Soule, J.B. Bodin, M. Amoura, A. Walrant, S. Sagan, A.R. Thiam, K. Ngo, V. Vivier, S. Cribier, and N. Rodriguez. Penetratin translocation mechanism through asymmetric droplet interface bilayers. *Biochimica et Biophysica Acta (BBA) - Biomembranes*, 1862(11):183415, 2020.
- [261] R. Gautier, D. Douguet, B. Antonny, and G. Drin. Heliquest: a web server to screen sequences with specific α -helical properties. *Bioinformatics*, 24:2101–2102, 2008.
- [262] S. Buchoux. Fatslim: a fast and robust software to analyze md simulations of membranes. *Bioinformatics*, 33:133–134, 2016.
- [263] Stefano Vanni, Hisaaki Hirose, Helene Barelli, Bruno Antonny, and Romain Gautier. A sub-nanometre view of how membrane curvature and composition modulate lipid packing and protein recruitment. *Nature communications*, 5:4916, 09 2014.
- [264] Manuel Gimenez-Andres, Alenka Copic, and Bruno Antonny. The many faces of amphipathic helices. *Biomolecules*, 8:45, 07 2018.
- [265] Guillaume Drin, Jean-François Casella, Romain Gautier, Thomas Boehmer, Thomas Schwartz, and Bruno Antonny. A general amphipathic-helical motif for sensing membrane curvature. *Nature structural & molecular biology*, 14:138–46, 03 2007.

- [266] M Schiffer and AB Edmundson. Use of helical wheels to represent the structures of proteins and to identify segments with helical potential. *Biophysical journal*, 7(2):121—135, March 1967.
- [267] David S. Eisenberg, R M Weiss, and Thomas C. Terwilliger. The helical hydrophobic moment: a measure of the amphiphilicity of a helix. *Nature*, 299:371–374, 1982.
- [268] Joachim Seelig. Thermodynamics of lipid-peptide interactions. *Biochimica et biophysica acta*, 1666(1-2):40—50, November 2004.
- [269] Claire François-Martin, Amélie Bacle, James Rothman, Patrick Fuchs, and Frédéric Pincet. Cooperation of conical and polyunsaturated lipids to regulate initiation and processing of membrane fusion. *Frontiers in Molecular Biosciences*, 8:763115, 10 2021.
- [270] Cyril Dominguez, Rolf Boelens, and Alexandre Bonvin. Haddock: a protein-protein docking approach based on biochemical or biophysical data. 01 2003.
- [271] Stephen Altschul, T.L. Madden, A Shaffer, J.H. Zhang, and Zheng Zhang. Gapped blast and psi-blast: A new generation of protein database search programs. 25:3389–3402, 09 1997.
- [272] Stephen Altschul, John Wootton, E Gertz, Richa Agarwala, Aleksandr Morgulis, Alejandro Schaffer, and Yi-Kuo Yu. Protein database searches using compositionally adjusted substitution matrices. *The FEBS journal*, 272:5101–9, 11 2005.
- [273] Cédric Notredame, Desmond G Higgins, and Jaap Heringa. T-coffee: a novel method for fast and accurate multiple sequence alignment. Edited by j. thornton. *Journal of Molecular Biology*, 302(1):205–217, 2000.
- [274] Fábio Madeira, Matt Pearce, Adrian R N Tivey, Prasad Basutkar, Joon Lee, Ossama Edbali, Nandana Madhusoodanan, Anton Kolesnikov, and Rodrigo Lopez. Search and sequence analysis tools services from embl-ebi in 2022. *Nucleic acids research*, 50(W1):W276—W279, July 2022.
- [275] Claudio Mirabello, Björn Wallner, Björn Nystedt, Stavros Azinas, and Marta Carroni. Unmasking alphafold: integration of experiments and predictions in multimeric complexes. *bioRxiv*, 2023.
- [276] Sivakumar Boopathy, Camila Makhlouta Lugo, Bridget E. Luce, Julie McDonald, Pusparanee Hakim, Jackeline Ponce, Beatrix M. Ueberheide, and Luke H. Chao. Identification of slc25a46 interaction interfaces with mitochondrial membrane fusogens mfn2 and opa1. *bioRxiv*, 2023.
- [277] Jana Schuettpelez, Alexandre Janer, Hana Antonicka, and Eric A Shoubridge. The role of the mitochondrial outer membrane protein slc25a46 in mitochondrial fission and fusion. *Life Science Alliance*, 6(6), 2023.
- [278] Janos Steffen, Ajay A. Vashisht, Jijun Wan, Joanna C. Jen, Steven M. Claypool, James A. Wohlschlegel, and Carla M. Koehler. Rapid degradation of mutant slc25a46 by the ubiquitin-proteasome system results in mfn1/2-mediated hyperfusion of mitochondria. *Molecular Biology of the Cell*, 28(5):600–612, 2017. PMID: 28057766.
- [279] Edmund R. S. Kunji, Martin S. King, Jonathan J. Ruprecht, and Chancievan Thangaratnarajah. The slc25 carrier family: Important transport proteins in mitochondrial physiology and pathology. *Physiology*, 35(5):302–327, 2020. PMID: 32783608.

- [280] Alexandre Janer, Julien Prudent, Vincent Paupe, Somayyeh Fahiminiya, Jacek Majewski, Nicolas Sgarioto, Christine Rosiers, Anik Forest, Zhen-Yuan Lin, Anne-Claude Gingras, Grant Mitchell, Heidi McBride, and Eric Shoubridge. Slc25a46 is required for mitochondrial lipid homeostasis and cristae maintenance and is responsible for leigh syndrome. *EMBO Molecular Medicine*, 8:e201506159, 07 2016.
- [281] Andrej Sali and Tom Blundell. Comparative protein modelling by satisfaction of spatial restraints. *Protein Struct Distance Anal.*, 64, 01 1994.
- [282] Marc Marti-Renom, Ashley Stuart, Andras Fiser, Roberto Sanchez, Francisco Melo, and Andrej Sali. Comparative protein structure modeling of genes and genomes. *Annual review of biophysics and biomolecular structure*, 29:291–325, 02 2000.
- [283] Benjamin Webb and Andrej Sali. Comparative protein structure modeling using modeller. *Current protocols in bioinformatics / editorial board, Andreas D. Baxevanis ... [et al.]*, 54:5.6.1–5.6.37, 06 2016.